Javier Martínez Cesteros

Development of a low cost pressure sensitive mat: application to stability and posture measurement

Director/es

Plaza García, Imaculada
Medrano Sánchez, Carlos T.

Tesis Doctoral

DEVELOPMENT OF A LOW COST PRESSURE SENSITIVE MAT: APPLICATION TO STABILITY AND POSTURE MEASUREMENT

Autor

Javier Martínez Cesteros

Director/es

Plaza García, Imaculada
Medrano Sánchez, Carlos T.

UNIVERSIDAD DE ZARAGOZA
Escuela de Doctorado

Programa de Doctorado en Ingeniería Electrónica

2023

Development of a low cost pressure sensitive mat: application to stability and posture measurement

AUTHOR:

JAVIER MARTÍNEZ CESTEROS

SUPERVISORS:

INMACULADA PLAZA GARCÍA AND CARLOS T. MEDRANO SÁNCHEZ

Programa de Doctorado en Ingeniería Electrónica

2023

Acknowledgements

Finally, I would like to thank my friends and family for all the support they have provided to me; especially, during my doctoral candidate period.

Abstract

Tactile sensors have found application in many fields such as robotics, video games, rehabilitation or health. In this study several prototypes of Pressure Sensitive Mats (PSMs) have been manufactured. The mat size is 32x32 cm^2 and the number of sensors is 16x16. The sensitive layer is based on Velostat, a piezoresistive material which is readily available. Their low cost contrasts with the high price of most commercial solutions, making them impractical for use in hospitals, primary care centers or many research groups. Two applications of the prototypes are shown in the document.

Our prototypes improve in several aspects a previous version manufactured in our research group. They are manufactured using standard techniques for Printed Circuit Boards, so that they are almost ready for mass production. Concerning the Microcontroller (µC) based Data Acquisition System, up to 165 Hz sampling frequency can be achieved, which is a value already suitable for many studies. This improvement has been possible thanks to: i) A re-design of the data transfer process, which is now in binary format; ii) A change from Bluetooth to Universal Serial Bus; iii) Fast code execution using low level functions. Besides, a fine tuning of the µC Analog to Digital Converter (ADC) has allowed its input impedance to reach several MΩ, closer to an ideal value. In addition, this kind of Resistive Sensor Arrays present crosstalk. In this thesis, a fast implementation of an algorithm to eliminate it has been coded, achieving real time performance. The uncertainty due to the algorithm has also been characterized. Moreover, the sensor output conductance versus pressure is better understood now thanks to a series of detailed experiments with a pneumatic platform. A joint model of hysteresis (Modified Prandtl-Ishlinskii) and creep (as a sum of first order linear time invariant systems) has been fitted to the data. The model explains the hysteresis and the temporal trend of the output, although there is a large variability in the output as a function of time that the model still does not capture com-

pletely. Two other piezoresistive materials have also been tested, showing higher non linear effects than Velostat.

The first application concerns human balance studies in which the PSM has been compared with a reference instrument, the Force Platform, in a set of experiments with humans. The Center of Pressure trajectories from both instruments are highly correlated, but it is evident that the mat provides a lower trajectory spread. We have found that the measurement improves if crosstalk is removed and if the sensor output model is taken into account. More specifically, the model leads to up to a 37% improvement in trajectory distance depending on the kind of experiment compared with a naive approach in which conductance and pressure are supposed to be proportional. For the model to be practical, a scaling factor is introduced to extrapolate the results obtained in the pneumatic platform for a small-sized array to the large mat. In this regard, calibration of large mats deserve further research. Increasing mat resolution has also been found to be an aspect for future improvement.

The second application concerns posture monitoring. In particular, an exploratory study has been conducted to relate spine posture to the pressure on a meditation cushion in sitting meditation. Interest in meditation has grown in recent years and there is evidence that it has some health benefits. One key aspect of meditation is uprightness, straightening the back. How to sit is very important for novice practitioners. Wearing sensors is not very comfortable and practical, so that we have studied whether or not the spine posture can be recovered from pressure images, inspired by previous literature that performed similar analysis for bedridden patients. A device based on five inertial sensors has been built as a reference system to be attached to a set of volunteers in sitting meditation, while a prototype of our PSM has been attached to the meditation cushions. Given that we are working with pressure images and the inherent difficulty of the task, a Machine Learning approach has been considered based on previous Deep Learning systems that work well for object recognition. The system has been adapted in the form of a Convolutional Neural Network. It is able to predict back angles rather well (R^2 higher than 0.75) provided that data from the volunteer under study is in the training set. However, the performance when this condition is not fulfilled decreases dramatically. The role of sex, height or weight should be investigated in the future to overcome this problem and to make this system practical

for everyday use. [1]

Resumen

Los sensores táctiles tienen aplicaciones en muchos campos tales como robótica, videojuegos, rehabilitación o salud. En este estudio varios prototipos de Esterillas Sensibles a la Presión (PSM por sus siglas en inglés) han sido fabricadas. El tamaño de las esterillas es de 32x32 cm^2 y el número de sensores es de 16x16. La capa sensible a la presión está basada en Velostat, un material piezoresistivo que se puede adquirir fácilmente. Su reducido precio contrasta con el alto coste de la mayoría de soluciones comerciales, lo que las hace poco prácticas para su uso en hospitales, centros de atención primaria o muchos grupos de investigación. En esta tesis se muestran dos aplicaciones de los prototipos desarrollados.

Nuestros prototipos mejoran en diversos aspectos una versión previa fabricada en nuestro grupo de investigación. Se fabrican empleando técnicas convencionales mediante Placas de Circuito Impreso, de forma que están casi listos para la producción en masa. Con respecto al Sistema de Adquisición de Datos basado en Microcontrolador (µC), se ha conseguido alcanzar hasta 165 Hz de frecuencia de muestreo, siendo un valor ya adecuado para muchos estudios. Esta mejora ha sido posible gracias a: i) Un rediseño del proceso de transferencia de datos, el cual ahora es en formato binario; ii) Un cambio de Bluetooth a USB; iii) Un código de ejecución rápida utilizando funciones de bajo nivel. Además, un ajuste fino del Conversor Analógico Digital del µC ha permitido que su impedancia de entrada alcance varios MΩ, aproximándose al valor ideal. Además, este tipo de matrices de sensores resistivos presenta diafonía ("crosstalk"). En esta tesis, una implementación rápida de un algoritmo para eliminarlo ha sido codificada, alcanzando la ejecución en tiempo real. La incertidumbre debida al algoritmo también ha sido caracterizada. Asimismo, la conductancia de salida del sensor frente a la presión ahora se comprende mejor gracias a una serie detallada de experimentos con una plataforma neumática. Un modelo conjunto de histéresis (Prandtl-Ishlinskii Modificado) y "creep" (como una suma de sistemas de primer

orden lineales e invariantes en el tiempo) ha sido ajustado a los datos. El modelo explica la histéresis y la tendencia temporal de la salida, aunque hay una gran variabilidad en la salida como función del tiempo que el modelo todavía no captura completamente. Otros dos materiales piezoresistivos también han sido probados, mostrando mayores efectos no lineales que el Velostat.

La primera aplicación desarrollada en la tesis se refiere a estudios de estabilidad humana donde la PSM ha sido comparada con un instrumento de referencia, la plataforma de fuerza, en un conjunto de experimentos con personas. Las trayectorias del Centro de Presión provenientes de ambos instrumentos están altamente correladas, pero es evidente que la esterilla proporciona una amplitud inferior de la trayectoria. Hemos descubierto que la medida mejora si el "crosstalk" es eliminado y si el modelo de salida del sensor es tenido en cuenta. Más específicamente, el modelo conduce hasta un 37% de mejora en la distancia entre trayectorias, dependiendo del tipo de experimento, comparado con el planteamiento simplista en el que conductancia y presión se suponen proporcionales. Para que el modelo resulte práctico, un factor de escalado es introducido para extrapolar los resultados obtenidos en la plataforma neumática con una matriz de tamaño reducido a la esterilla de mayores dimensiones utilizada en las pruebas de estabilidad. En este aspecto, la calibración de esterillas grandes merece investigación adicional. Incrementar la resolución de la esterilla también ha mostrado ser un aspecto de mejora futura.

La segunda aplicación se refiere a la monitorización de la postura. En particular, un estudio exploratorio se ha llevado a cabo para relacionar la postura de la columna vertebral con la presión sobre un cojín de meditación en meditación sedente. El interés en la meditación ha crecido en los últimos años y hay evidencias de que aporta beneficios a la salud. Un aspecto clave en la meditación es la verticalidad, manteniendo recta la espalda. Cómo sentarse es muy importante para principiantes. Llevar sensores no es muy cómodo ni práctico, así que hemos estudiado si la postura vertebral puede ser recuperada a partir de las imágenes de presión, inspirados por la literatura previa que realizaba análisis similares para pacientes encamados. Un dispositivo basado en cinco sensores inerciales ha sido desarrollado como sistema de referencia, que se coloca en la espalda de un conjunto de voluntarios durante la meditación sedente, mientras que un prototipo de nuestra PSM ha sido acoplado al cojín de meditación. Dado que estamos trabajando con imágenes de presión y la dificultad inherente a la tarea, se uti-

lizan técnicas de Aprendizaje Automático, en concreto a partir de un sistema de Aprendizaje Profundo que funcionaba bien en el reconocimiento de objetos. El sistema ha sido adaptado en la forma de una Red Neuronal Convolucional y es capaz de predecir los ángulos de la espalda bastante bien (R2 superior a 0.75) para voluntarios cuyos datos se encuentran en el conjunto de entrenamiento. Sin embargo, si esta condición no se cumple las prestaciones decrecen considerablemente. El rol del sexo, altura o peso debería ser investigado en el futuro para afrontar este problema y hacer este sistema práctico para el uso diario. [2]

Contents

List of Figures

List of Tables

List of Algorithms and Codes

Acronyms and terms

Chapter 1

Introduction

1.1 Context and motivation

In addition to facilitating our daily tasks, technology is also helpful to improve our health. This improvement is present both in medical equipment found in hospitals and in small devices of common use (thermometers, pulsometers, oximeters, pedometers, ...). Nowadays, the technologies applied to health are widely extended, having these sensoring functions embedded in our smartphones and smartwatches [183]. These tools enable users to monitor their health, allowing them to avoid risks and prevent diseases [30]. Besides, they also increase their efficiency, accuracy and usability with research in this field.

In recent years there has been an increase in the presence of wearable devices and smart fabrics [27]. Tactile sensors are among the sensors used in these devices. Tactile sensors are those sensors capable of measuring the interaction that occurs between the sensor and the environment by means of physical contact between them [64].

These sensors allow measuring the force exerted on a contact surface, but there are situations in which the pressure distribution on several points is the outcome of interest. For this purpose, several tactile sensors are grouped into an array structure. These devices are usually no more than 1 mm thick, with lengths that can reach even meters (beds, walkways). In an array, each cell detects the normal force exerted on its surface to obtain a pressure image of the entire assembly. In this document the term cell will be used to name each of the units in an array of sensors.

This type of devices has a wide range of applications. For instance, they are used to provide tactile feedback to robotic arms, facilitating the manipulation of objects [80]. They can also be used to classify finger positions [128]. They are also used in touch screens [246]. With respect to health applications, they have been used to monitor sleeping [134] and to measure the pressure exerted on jaws [105] (figure 1.1).
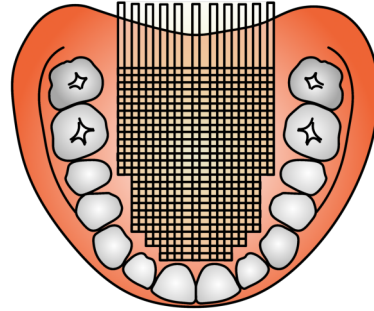
Figure 1.1: Tactile sensor sheet on a humans jaw. Based on [105]

For some applications to measure pressure on seats, beds or on the floor, the name mat is often used, and the arrays are called Pressure Sensitive Mats (PSMs). Although there is an increasing use of PSMs in last years with many applications [123], there are still several problems that are currently being investigated. A major problem would be the high cost of commercial solutions, although there are more affordable alternatives like the prototypes shown in [230, 233]. Besides, PSMs have the disadvantage of reduced measurement accuracy. This can affect its usability in some situations and it is also present in commercial solutions, even though it is more noticeable in more affordable devices [147, 167].

1.2   Goals

The overall objective of the thesis is to develop a low-cost PSM showing potential applications in the field of healthcare. Specifically, we will look for applications in two different contexts: stability characterization and posture monitoring. The prototypes developed are based on standard technologies and commercial materials. As expected in these systems, pressure measurements are unreliable. Therefore, we will try to overcome some of the limitations they present. This leads us to set the following specific objectives:

- Prototypes: Improving a previous prototype developed in our research group. This improvement refers to data acquisition (speed, reliability), sensor response modeling to compensate for some non-linear effects as well as the post-processing to recover each of the cell resistances that form the array (numerical resolution of the crosstalk problem and measurement uncertainty).

– Human stability characterization: improving the measurement of the Center of Pressure (CoP) in human balance tests.

– Posture monitoring: showing the relation between the pressure image on a seat and the spine posture in sitting meditation. Modern Machine Learning (ML) techniques will be used to discover that relation.

1.3   Contributions

The contributions of this thesis can be summarized as follows:

- The scanning frequency of the previous prototype has been increased from 10 Hz to a maximum of 165 Hz. This is relevant for balance studies. Moreover, new prototypes have been built using manufacturing processes more suitable for mass production. Finally, it has been shown that the piezoresistive material used in our prototypes, Velostat, presents less non-linear effects than other low-cost candidates. Its creep and hysteresis response has been modeled. Up to our knowledge, this deep analysis and modeling of Velostat is a novelty of our research.

- The post-processing required to remove crosstalk is much faster now. Parallel implementations of the algorithms developed in our group [150] have been developed together with C versions. Thus, real-time operation is now possible making our algorithms more useful.

- Uncertainty in the measurement after crosstalk removal has also been characterized. Besides, it has been shown that the algorithms used in the post-processing can be extended to other kind of circuits that are very common in Resistive Sensor Arrays (RSAs). These are also novel ideas introduced in our research.

- The CoP obtained from PSM has been compared with a reference instrument, a Force Platform (FP). Several aspects have been found to be relevant for improving the CoP trajectory. One of them is the compensation for creep and hysteresis, which is a novelty of our study.

- ML techniques have been utilized to predict spine posture from the pressure images obtained with a PSM on a meditation cushion. The results are

good provided that the system has been trained with data that includes the person who sits on the cushion, even though the spine is not in contact with the PSM directly. This aspect is different from previous studies.

1.4 Structure of this document

Chapter 2 presents the prototype manufactured previously in the group. It was used in the first set of experiments. Meanwhile, several improvements were implemented. They include a faster and more reliable data transfer to the Personal Computer (PC) via Universal Serial Bus (USB) and new versions of the PSM based on flexible Printed Circuit Board (PCB). A comparison between several low cost piezoresistive materials is also shown considering experiments related to variability, drift, creep and hysteresis. A model of creep and hysteresis for Velostat has been developed. On the other hand, the group had developed a software solution for the crosstalk problem in RSAs, i.e., a post-processing after a complete scan of the array. In this chapter, the uncertainty associated to this procedure is shown. Moreover, an implementation to reduce the computing time of the algorithm is shown.

Chapter 3 is devoted to balance studies focusing on CoP trajectories. The experimental protocol and their evaluation are explained. An FP was used as a reference instrument. Two set of experiments are described. The first one is a preliminary study using the previous prototype limited to a low sampling frequency. In the second one the CoP trajectory was captured with an improved prototype (sampling frequency 100 Hz) and the measurement was further improved using the compensation of hysteresis and creep.

Chapter 4 shows the application for posture measurement. Two different devices were used in this study. On the one hand, a set of inertial sensors was used to determine the posture of the spine. We have implemented a system based on a previously published paper. On the other hand, one of our improved prototypes was fixed on a meditation cushion to determine a pressure image. We will describe the protocol in which volunteers adopt a meditation posture while wearing the inertial sensors and sitting on the indicated cushion. We will develop ML techniques to relate the pressure exerted on the seat to the posture of the spine.

General conclusions of the thesis and future lines of research are considered

in chapter 5.

A list of publications derived from the thesis, the proof of some equations, some preliminary analyses that can be the seed of future studies, and supplementary materials are given in the appendices.

Given that several applications are developed in this thesis together with new PSM designs, chapters 2, 3 and 4 include their own state of the art, focusing on the concepts required in each chapter.

Chapter 2

Prototype of a Pressure Sensitive Mat

I N this chapter the PSMs manufactured for this thesis are described. We first review commercial products and academic studies related to our prototypes, together with issues concerning non-linear effects of piezoresistive materials and circuits used in Data Acquisition Systems (DAQs) for RSAs. Then, the previous prototype developed in our group is presented. This is the starting point of the thesis. Then, the new prototypes are presented highlighting the improvements. Some aspects regarding the improved prototypes require an explanation in detail due to their complexity, so that separate sections are devoted to them.

2.1 State of the art

2.1.1 Commercial products

There are several companies that offer large area tactile sensors. For instance:

- Tekscan®: It is likely to be the company most cited in articles using tactile sensors for health applications. It offers several products. Among them there are several models of PSMs. The model Tekscan® 5315 with 2016 cells (1 cells/cm², 42.67 cm x 48.87 cm)[2] cost €12,419 in 2019. It has been used in studies like [32, 45].

- GAITRite®: Their products include Walkways devices, which are very long

mats so that a person can walk on them, mainly in a straight line [216]. The Walkway with 18,432 cells (0.62 cells/cm², 500 cm x 90 cm) is sold by €6,000 [4].

- BodiTrak: It presents some PSM devices. Among them, we can find the BodiTrak2 Lite with 1,024 cells (0.62 cells/cm² 45.72 cm x45.72 cm), which is sold in [1] by €3,250. An example of one of its devices appears in [141].

- RSscan (Materialise Footscan®): The footscan® model is 0.5 m large with 4,096 cells (2.58 cells/cm² 48.8 cm x 32.5 cm) [5]. There is no price available, although it should be similar to the previous ones in which contacting the company is required to get a quota.

- SensingTex©: It is the most affordable one of the models we have found. The Seating Mat has 256 cells (0.25 cells/cm², 32 cm x 32 cm), with a cost around €500 [21]. It has been used in [236]

2.1.2 Research studies

The previous commercial solutions present a high cost. For this reason, some authors have opted to develop cheaper academic prototypes. Due to the high quantity of sensors and materials that can be used for pressure sensing, our search is focused on those with a piezoresistive principle of operation, which have an electrical behavior that it is easier to model and generalize.

If we look for studies on piezoresistive materials, we can find different types of works:

- Analyzing their use as components in fibers and textiles [37, 48, 100, 118, 132, 137, 162, 250, 251]

- Studying the behavior of materials as antennae [35, 99],

- Implementing sensors [51, 75, 101, 104, 193, 217, 219] for their characterization,

- Arranged in isolated sensor strips [220] or as an array of strips [98, 130, 135, 180]. In this case, uses are mainly medical: embedded into prosthetic sockets for amputees [98], identifying knee joint motion patterns [130] or designing and implementing gloves with sensors, in order to analyze manipulation and recognize hand gestures [135, 180].

- In matrix form [74, 84, 127, 136, 150, 170, 210, 225]

Paying special attention to strip or matrix geometries, it can be indicated:

- In the strips, the size and number of sensors is variable:

    - 6 modules of 47.5 mm (length), 30 mm (width) and 3 mm (thickness). Jamming layers are also included with dimensions: 42.5 mm (length), 18 mm (width) and 0.2 mm (thickness) [220].

    - 10 flexible sensors. Each sensing zone had the following dimensions: 50 mm long and 15 mm wide [130].

    - 12 sensitive elements of Velostat with a diameter of 5 mm. Electrode plates 2 mm in diameter were positioned 20 mm apart from one another [98].

    - Or a mix of sensors for a single device: five strips of 2 sensors of Velostat (20x20 mm), and one 4x4 sensor matrix [135].

The matrix forms also vary in terms of number of sensors and size, but the most usual sensor side is near 10 x 10 mm [74, 127, 225], although it is possible to find larger (15x30 mm [84], 25x50 [136]) or lower dimensions (7x7 mm [210]).

Number of sensors is variable, from the smallest: 3x3 [225], 3x4 [84] to the largest (16x16 [150] or 32x32 [210]), going through intermediate sizes 7x4 [136], 8x10 [127], 9x9 [100] or 10x14 [74].

Biggest mats present sizes of 320x320 mm (256 nodes [150]), 210x297 mm (140 nodes [74]). Suprapto et al. [210] designed their 32x32 matrix (1024 nodes) with cells of 7x7 mm sensor size and 10 mm distance between sensors.

As far as the manufacturing process is concerned, prototypes are normally home made using different structures:

- Only one layer for electrodes and interconnections [84, 170].

- With different layers of materials. According to the description of the authors (see figure 2.1):

    - Three layers:

        * Medrano et al. developed a mat of 2 outer layers of a flexible grid printed with a 3D printer which conductive lines and a piezoresistive sheet of Velostat, placed in the middle [150].

* Suprapto et al. used three main layers which were a top electrode, Velostat, and bottom electrode respectively [210].

* Vehec et al. glued the Velostat on the bottom side of the top foil. A separator foil was placed between the top and the bottom foil. The bottom foil was made on polyester film (see figure 2.1), while the top foil used polyimide film [225]

– Four layers: a) upper contact layer with horizontal sensor arrays b) middle pressure-sensitive electrically resistive layer c) lower contact layer with vertical sensor arrays and d) bottom protective and anti-slippery layer [127]

– Five layers:

* Fajingbesi et al. design used: a) Bamboo substrate b) Column electrode c) Velostat d) Row electrode e) Bamboo substrate [74],

* Liu et al. developed a mat with: The top and bottom laminating layer, the Velostat sheet, and 2 bars of conductive fabric connectors to other electronic components [136].

Analyzing the materials used, we often find low-cost pressure-sensitive materials such as Velostat [51, 74, 75, 84, 98, 127, 135, 136, 147, 150, 180, 193, 210, 217, 219, 225] also known by its other commercial name, the Linqstat [51, 104, 225]. Other materials sensitive to pressure are EeonTex [75, 132], X-static [48], Elastane [35, 118, 162, 220], Shieldex [37, 99, 100, 170] or Spandex [101, 130, 137, 250, 251].

2.1.3 Non-linear response of the materials

Academic prototypes are usually more affordable than commercial ones. This is due to the use of low-cost materials. But these materials present strong non-ideal responses, which make it difficult to obtain accurate measurements, and require a processing step to try to recover values closer to the true pressure. In these materials' conductance (inverse of the resistance) is more or less proportional to pressure. However, this is only a very crude approximation of the true conductance vs. pressure curve. Several non linear effects are reviewed in the next paragraphs. The output of the sensor is taken to be its conductance, g.

Before proceeding with the review of the main non-linear effects, it is important to point out that a small sized array was built to characterize the sensor
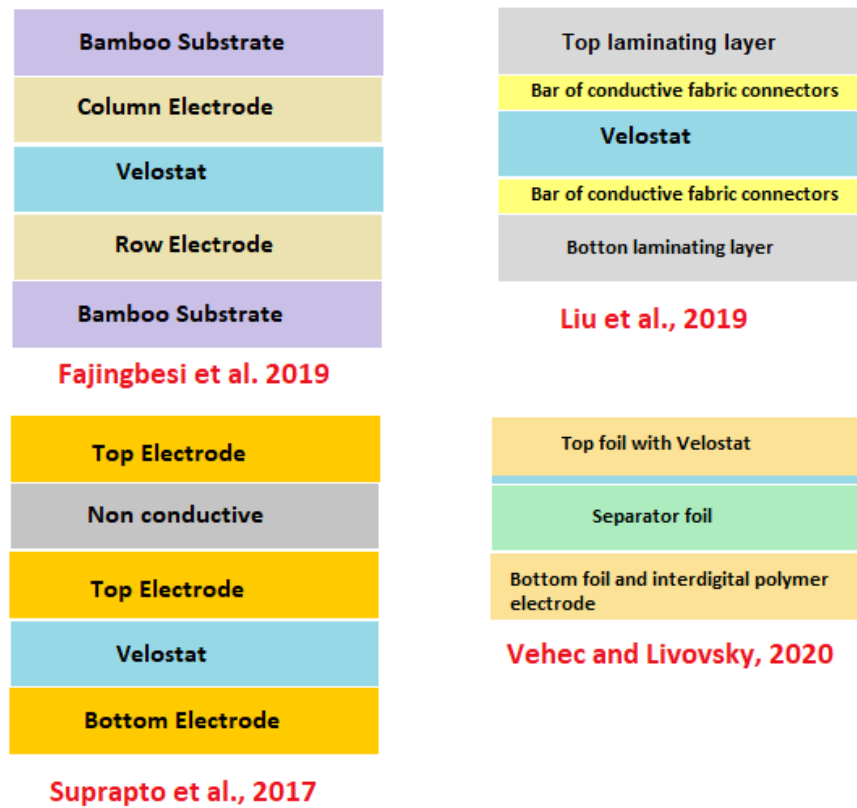
Figure 2.1: Decomposition of the layers according to some authors ([74, 136, 210, 225]).

response in this thesis. Thus, an output per cell was recorded. The discussion below takes into account this fact when a quantitative value has to be obtained.

One problem with these materials is the lack of repeatability [124]. By lack of repeatability we mean the difference in sensor output between experiments carried out under the same conditions. In the case of pressure sensors, it corresponds to the difference between the values measured when the same pressure is exerted under similar conditions.

To test the repeatability of a pressure sensor, cycles with the same pressure values are usually applied to the sensor, and the results obtained in each cycle are compared [92, 249]. In an ideal condition, the same value is obtained at the sensor output in all cycles. But in the real case, small variations occur between measurements. These variations are higher in the case of using low-cost materials. In order to quantify this variation, we use the Standard Deviation (SD). This parameter can be normalized by dividing it by the mean of the values obtained

in the cycles. The result is the Coefficient of Variation (CV) [92].

In this thesis, a set of consecutive load/unload cycles has been applied to characterize variability. For each cycle, the average of the last part of the sensor output has been obtained under the load condition. Thus, a value per cycle and per cell is obtained, and from them the CV squared is obtained according to the following equation(2.1):

$$Variability(g) = CV^2 = \frac{(std(\bar{g}[t_e - \Delta t : t_e]_{cycle,cell}))^2}{(mean(\bar{g}[t_e - \Delta t) : t_e]_{cycle,cell}))^2} \tag{2.1}$$

where g refers to the sensor output, the bar over, $\bar{g}$, indicates average and Δt is the time in which the average is taken. This time is taken just before the end time, t_e, of the load pulse (i.e., g values are averaged from $t_e - \Delta t$ to t_e for each pulse and for each cell).

It is worthy pointing out that a value per cell and pulse is obtained, and then the SD is calculated over that set of values. Thus, the variance calculated in the numerator of equation 2.1 includes two sources: the difference with respect to the cycle number and the differences coming from cell variability. From a practical point of view, we think that it is more relevant to get this more complete variability in order to compare materials for real use.

Another non-ideal behavior affecting the pressure measurement is drift. In this document the notation of [164] is adopted so that creep and drift do not refer to the same phenomenon. Drift corresponds to the high frequency fluctuations that occur in the value obtained from a measurement. These fluctuations are seen in the repeated variation of the measured value in short periods of time when maintaining the same pressure applied on the sensor.

To measure drift, a pressure value is applied and kept constant over a period of time. In order to be able to measure the fluctuations, a set of non-overlapping short time windows of the sensor output are first extracted. Since the windows are short the influence of other non linear effects on the drift measurement is reduced. For a given window, the fluctuation has a quantitative value obtained after calculating the measurement SD in that window. This value is denoted as $\sigma_{window,cell}$ because there is value per cell and per short window. To obtain the final drift, the average of the window fluctuations is computed and normalized by dividing by the average measured conductance according to equation 2.2 in a

similar way to [165]:

$$Drift(g) = \frac{mean(\sigma_{window,cell})}{g_{mean}} \tag{2.2}$$

where the mean is taken over both windows and cells.

Yet another non-ideal behavior is creep [24, 124, 164, 165, 231]. Creep refers to the continuous change effect that a measurement suffers, as its value continues to increase over time when a constant force is applied.

For creep characterization in pressure sensors, a constant pressure is applied for an intermediate to long period of time. The slope of the measured conductance is quantified and then normalized with respect to the average of the conductance over that time period [238]. Thus, we have characterized it using equation 2.3.

$$Creep(g) = \frac{\left|slope(g[(t_e - \Delta T/2) : t_e])\right|}{\bar{g}[(t_e - \Delta T/2) : t_e]} \tag{2.3}$$

where g is the sensor output, the bar over, $\bar{g}$, refers to the average, and the calculation is done from the time $t_e - \Delta T/2$ to t_e, being t_e the end time of the constant pressure period and ΔT its total width. The first half of the load pulse is discarded to avoid short term effects. The slope is obtained by fitting a line in the selected window. Given that there are several cells in the matrix, a creep value is first obtained for each cell and then the final creep that we will show is the average over cells.

Finally, hysteresis [125, 156, 184] is another typical non-linear effect that appears in piezoresistive materials. A piezoresistive sensor with hysteresis shows different output depending on the previous pressure trajectory to which it has been subjected. Thus, if the pressure increases from a minimum value to a maximum value and then decreases from the maximum to the minimum, the sensor output does not follow the same path. The trajectory for increasing pressures is below the trajectory associated to decreasing pressures. A hysteresis cycle is then formed. In order to characterize this phenomenon, known upward and downward pressures are usually applied repeatedly [156, 197]. In our case, the cycles averaged over cells are first obtained. Then a quantitative value of hysteresis is calculated as the maximum difference between the two paths of the sensor output normalized by the full scale output following this equation.

$$Hysteresis(g) = \frac{max\left(\left|g_{up} - g_{down}\right|\right)}{max(g) - min(g)} \tag{2.4}$$

where g is the average (over cells) output and g_{up} and g_{down} refer to the averaged (over cells) output with increasing and decreasing pressures respectively.

Modeling and compensating for hysteresis and creep

In the previous subsection, simple parameters were defined to characterize non-linear effects. However, more refined models of these effects are required if one wants to get rid of them.

In this subsection, some relevant previous studies that try to compensate for creep and hysteresis are reviewed. In the field of piezoelectric actuators this type of compensation is commonly considered [90, 190]. A model of the hysteresis and dynamic behavior of the actuator is needed in order to carry out such a compensation. Once the model is known, the simplest control strategy is a feedforward operation in which the inverse model is in series with the piezo-actuated stage [90, 120]. Thus, in the context of piezoactuators, if a given output is desired, y_d, and the system has a model $y = M([u])$, the desired trajectory y_d is first passed through the inverse model to get a control input, u, (in the digital control side), and then the piezoactuator physical behavior recovers $y_d = M([u]) = M(M^{-1}([y_d]))$. Following this approach the influence of creep and hysteresis can be minimized.

These ideas can be borrowed from the piezoactuated stages literature and applied to the current context of tactile sensors. If the sensor response is known, schematically as $y = M([x])$, then the inverse model can be used to recover the input for a given output time series, see figure 2.2. For piezoresistive sensors, it is considered that y is the conductance and x is the applied pressure. The behavior of these materials show strong effects depending on the previous value of pressures, so that the value of y depends on all the previous values of x, which is often represented by brackets $[x]$.

In this way, several authors have considered hysteresis compensation in tactile sensors as in [198]: the sensor output was modeled with a Generalized Prandt-Ishlinskii model achieving an error reduction from 7.20% to 1.51% in the pressure estimated by the sensor for an input range of 206 kPa. In [60] the model considered was a Preisach hysteresis model for a silicon piezoresistive sensor and a large error decrease was also found. A specific hysteresis model for a piezoresistive sensor on a PCB was developed in [196]. Moreover, finding a different model for each cell in the 16x16 matrix was found to improve the resulting pressure
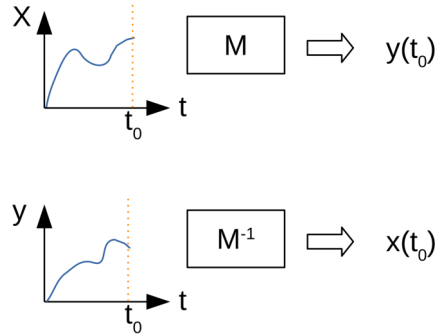
Figure 2.2: Recovering pressure from conductance in a piezoresistive sensor.

images dramatically. Thus, not only non-linear sensor response was reduced but also mismatching between different cells. In [122] a piezoresistive sensor was used in a system to estimate the rotation angle of a wrist. The error in the angle was shown to decrease when the hysteresis was compensated, in this case with a Modified Prandtl-Ishlinskii (MPI) model. Concerning creep, it was corrected in a plantar pressure measurement system [34]. The system was based on boots with a commercial system in which capacitive sensors are integrated into the insoles. Creep was modeled with a second order polynomial over time. Therefore, the total output had an increase over time and the increasing percentage was used to correct the output of each sensor. The corrected force under several parts of the feet was in agreement with previous values reported in fatigue studies. In a foam with optical pressure sensors developed by Chacko et al. [56], the strain was modeled as a constant term and an exponential term. It was shown that this model was better than power law time dependent functions.

2.1.4 Data acquisition circuits

This subsection is largely based on our article [149] from which several excerpts are extracted (© 2022 IEEE).

Basic circuit: the crosstalk problem

When a large set of sensitive cells are placed in an array it is not practical to set individual lines for each one. To limit the number of connections, a single cell of the array is conventionally addressed using a row-column selection device (analog Multiplexer (mux)/Demultiplexer (demux)). The most basic circuit is shown in figure 2.3. The mux/demux selects a cell and the resistance is connected to a

voltage divider circuit whose output voltage is measured by an Analog to Digital Converter (ADC) (in the figure the ADC and the mux/demux control lines are integrated in a Microcontroller (µC)).
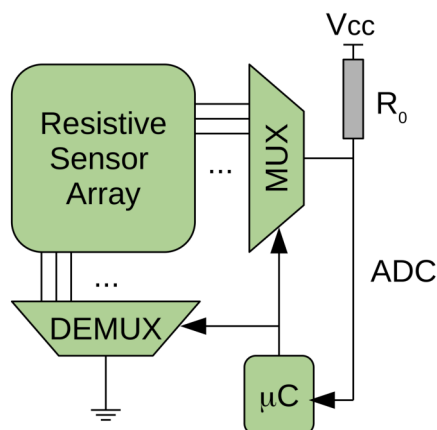
Figure 2.3: Schematic view of a basic reading circuit for resistive sensor arrays.

However, the basic data acquisition configuration suffers from the problem of crosstalk [200, 239]: when a cell is addressed the current not only flows through it but also through other elements because row and column connections are shared. This alters largely the measurement. For PSMs the crosstalk is visually very apparent since there seems to be pressure exerted on regions where there are no objects on them. This is why this effect is sometimes called ghost or phantom effect. An example is shown in figure 2.4, in which row 3 is connected to V_{ref} via a resistor and column A to ground. Thus, a voltage divider circuit is formed with the aim of measuring r_{3A} from the value of the voltage at node 3 (row 3 would be connected to the ADC). However, the current not only flows through r_{3A} and there are many paths for it as the one shown in red. In fact, the quantity that can be measured is not r_{3A} but the equivalent resistance between nodes 3 and A, which we indicate as R_{3A}. In this document we use the notation r_{ip}/g_{ip} to refer to the resistance/conductance of a single cell located at row i column p, and R_{ip}/G_{ip} for the equivalent resistance/conductance between the same pair of nodes.

Circuits for solving the crosstalk problem

Several solutions have been proposed to solve the crosstalk problem partially or completely. They have been reviewed in [239]. For instance the Inserting Diode
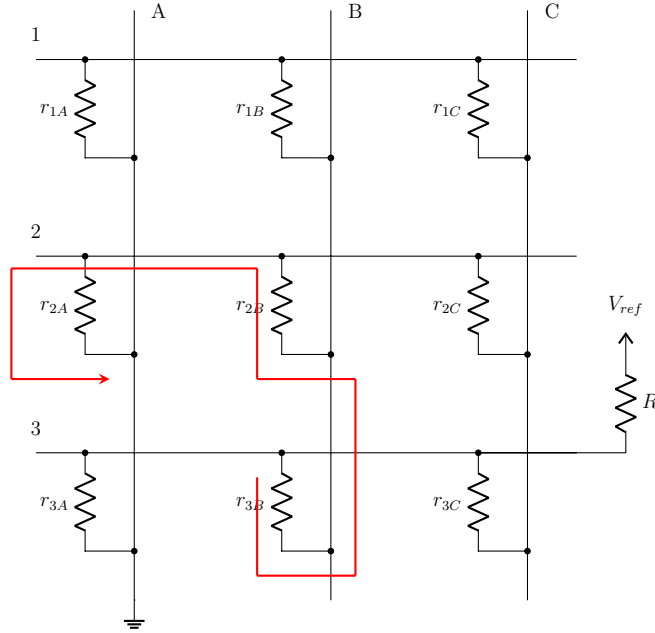
Figure 2.4: Example of a 3x3 RSA: cell 3A is being addressed. The red line shows one of the current paths that do not pass through r_{3A} ([149] © 2022 IEEE).

Method [206, 239] proposes inserting a diode in series with every sensitive cell. Thus, parasitic currents are blocked by the unidirectional conductivity of diodes.

Other more refined strategies using operational amplifiers have also been considered. The role of rows and columns could be interchanged but we consider in this document that, generally speaking, the scanning is performed by powering a row and then reading the columns at once (parallel readout mode) or sequentially (single readout mode). The matrix size is denoted as $N_R \times N_C$. Thus, in parallel readout mode a single row is addressed each time and all the columns are read in parallel. In a typical configuration [119], the selected row is connected to a given voltage, V_{ref}, and all the others to ground. The columns are connected to an Operational Amplifier (OA) with a negative feedback resistor whose value can be set to provide the desired output range for an expected input range of sensor resistances. The negative OA node acts as a virtual ground. Therefore, non-scanned cells are connected between ground and virtual ground and there is no current flowing on them. This is the basis of Zero Potential Method (ZPM). For ideal components, a ZPM circuit eliminates the primary crosstalk in the array. Buffers or switches can be used to select rows, sometimes together with voltage followers. In turn, every column needs an OA and the corresponding ADC. The combination of capacitive feedback and an Field Programmable Gate Array (FPGA) is an

alternative to perform several conversions simultaneously [169]. However, if the components are not ideal there is still some remaining crosstalk. The non ideal behavior includes: output resistance of buffer or switches, offset voltage, bias current, and finite gain of OAs. These issues were addressed in [96],[94]: by adding a row and a column with known resistors, it is shown that the cell resistances can be obtained from a combination of measured output voltages that eliminates the effect of non ideal components. The disadvantage of parallel readout methods is the number of components required to implement them: buffer or switches, each one with its own control line, and the number of OAs and ADCs. Thus, the size and complexity of the circuit can become large. Power can also be an issue, not only because of the power required by the components, but also because cell resistances are connected between V_{ref} and ground in the typical configurations, so that the current is limited only by their value and the resistance of the buffer or switch. An additional limiting resistance per row could be set to reduce power. However, if the designer has no constraints on power, size, cost and space, a parallel readout mode is the best solution, achieving also the highest sampling rate.

On the other hand, if the readout mode is single, the number of components is reduced at the expense of increasing the scanning time. For a selected row, each column must be selected too in this mode. The Voltage Feedback Method (VFM) and the ZPM are among the most popular approaches. There are several variants, but the basic circuits are shown in figures 2.5a and 2.5b respectively [95, 239]. The VFM [240] tries to set the same voltage level in the terminals of cells in the rows that are not being addressed. In this way, no current will flow through them and the primary crosstalk is eliminated. An OA together with a voltage divider circuit sets the same voltage at the input of non addressed rows as in the output of the selected column. The current in the non-selected columns of the selected row is diverted through the OA. Again, the non ideal behavior of components generates relevant errors. Thus, some modifications have been proposed like the Improved Isolated Drive Feedback Circuit with Compensation (IIDFCC) [241]: a suitable selection of resistor values in the voltage divider circuit (the average value of the internal mux resistances) has been shown to greatly reduce the crosstalk effect due to the switch internal resistances. With respect to ZPM, it can be adapted to single mode readout, see figure 2.5b. Each column requires a switch that can connect either to ground or to the OA. If the components were ideal this solution

would remove crosstalk. However, the non ideal behavior is often relevant and large errors can appear. Hidalgo et al. [138] proposed a modification called Quasi Zero Potential Method (QZPM) in which row and column switches connect either to ground or to the so-called connecting node, which in turn connects to an OA configured as an inverter amplifier. In QZPM the RSA is in fact powered only through the voltage at the positive input of the OA, which establishes the same potential (ideally) at the negative input node. It is shown that the cell resistances can be deduced taking into account the effect of the internal switch resistance, R_m, after an extended set of measurements has been performed: either row-column pairs ($N_R \cdot N_C$ measurements), a single column (N_C measurements), a single row (N_R measurements), or pairs of columns ($N_C \cdot (N_C - 1)/2$ measurements) are connected to the connecting node. In comparison with the traditional ZPM method, the scanning time is larger but ZPM cannot cope with non ideal switches, $R_m \neq 0$, which give rise to errors.

Post-processing solutions to crosstalk: Inverse of Equivalent Conductance Method

The crosstalk problem can also be addressed by means of a post-processing of a pressure image. In [243] a smoothing algorithm based on Gibbs sampling was proposed. It tended to bring values of suspicious pixels close to the average of the neighbor sites. However, this algorithm only tackled mechanical coupling and not the coupling between separated sites. Cheng et al. [58] used a large mat for activity recognition. A crosstalk effect was acknowledged and a kind of image processing algorithm was proposed. However, neither the crosstalk origin nor the details of the algorithm were discussed in length.

An algorithm based on a circuit analysis of the kind circuit shown in figure 2.3 has been proposed in our group [149, 150]. It is called Inverse of Equivalent Conductance Method (IECM). As stated above, the basic circuit shown in figure 2.4 allows measuring the equivalent resistance between the selected row and column pair, not the desired cell resistance. Thus, the problem is to find the cell resistances, which are the quantities we are interested in, from the set of equivalent resistances after a scan of the whole array, which are the quantities that can be obtained in the measurement. This can be stated as an optimization problem. For the sake of clarity, the IECM approach [150] is outlined in this subsection. The notation used through the document is also introduced.
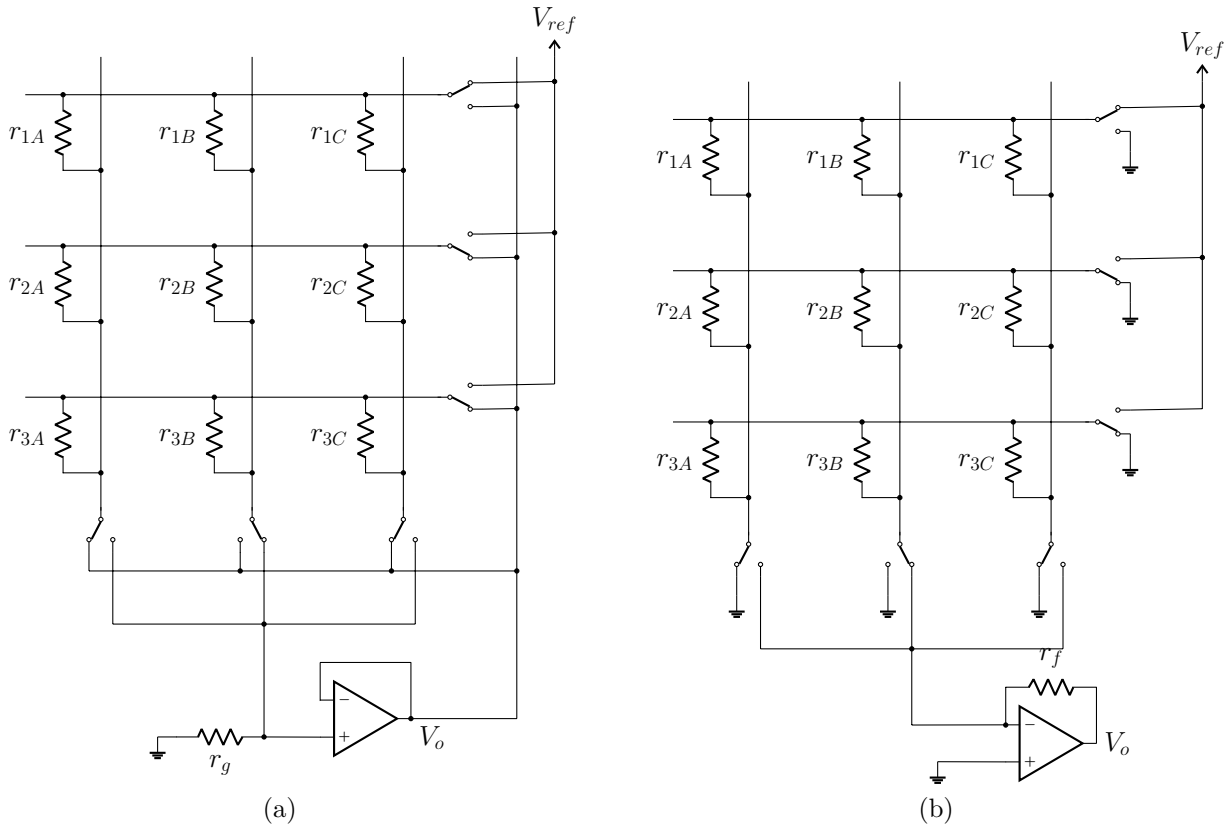
Figure 2.5: (a) Circuit configuration of VFM for a 3x3 array. Cell 1B is being addressed; (b) Circuit configuration of ZPM for a 3x3 array. Cell 1B is being addressed.

From a formal point of view, the equivalent conductance between nodes 3 and A can be found by solving the circuit of figure 2.6 in which a current is injected between them. Given that there is a different circuit for each row-column pair, we introduce the following notation: $V_{ip,j}$ refers to the voltage at node j in the circuit used to find the equivalent resistance value between row i and column p. Once the circuit is solved, the equivalent conductance is $G_{3A} = \frac{I_{ref}}{V_{3A,A} - V_{3A,3}}$ or, in general:

$$G_{ip} = \frac{I_{ref}}{V_{ip,p} - V_{ip,i}} \tag{2.5}$$

I_{ref} is just a multiplicative constant in the circuit solution that can be set to 1 in the implementation.

Without loss of generality, we consider row 1 as ground. The circuit for row i and column p can be solved using Kirchhoff's laws that lead to a linear matrix
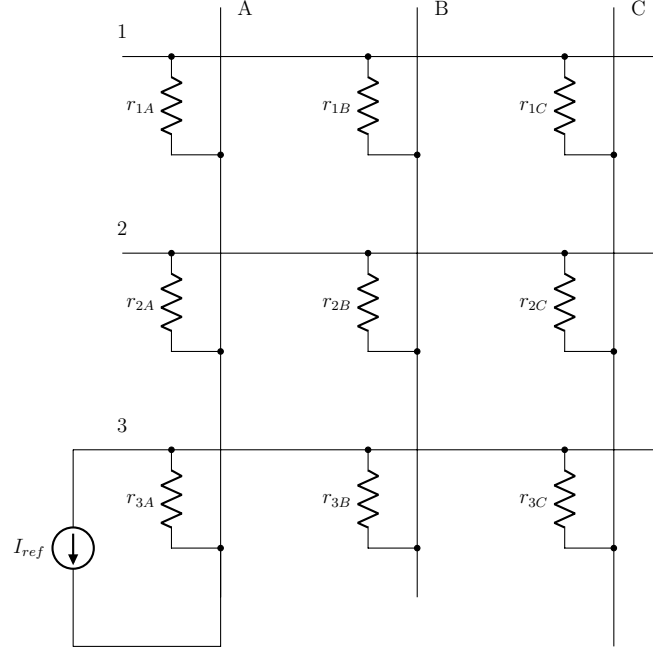
Figure 2.6: Theoretical circuit to determine the equivalent resistance between row 3 and column A in a 3x3 array ([149] © 2022 IEEE).

equation:

$$\mathbf{C}\mathbf{V}_{ip} = \mathbf{I}_{ip} \tag{2.6}$$

where the matrix $\mathbf{C}$ has physical dimension of conductance, and the notation $\mathbf{V}_{ip}$ refers to the voltage solution in vector form and $\mathbf{I}_{ip}$ to the current injected in vector form.

For instance in the circuit shown in figure 2.6, the nodes are ordered as: 2, 3, A, B, C. Thus, the matrix $\mathbf{C}$ is:

$$\mathbf{C} = \begin{pmatrix} g_{2,} & 0 & -g_{2A} & -g_{2B} & -g_{2C} \\ 0 & g_{3,} & -g_{3A} & -g_{3B} & -g_{3C} \\ -g_{2A} & -g_{3A} & g_{,A} & 0 & 0 \\ -g_{2B} & -g_{3B} & 0 & g_{,B} & 0 \\ -g_{2C} & -g_{3C} & 0 & 0 & g_{,C} \end{pmatrix} \tag{2.7}$$

where the shorthand notations $g_{i,} = \sum_p g_{ip}$ and $g_{,p} = \sum_i g_{ip}$ have been used. For instance: $g_{3,} = g_{3A} + g_{3B} + g_{3C}$.

Finally, the vector $\mathbf{I}_{3A}$ would be $\mathbf{I}_{3A} = (0, -I_{ref}, I_{ref}, 0, 0)^T$.

It should be noted that the matrix $\mathbf{C}$ does not depend on the row-column pair

under consideration in equation 2.6. It is the corresponding intensity vector, $\mathbf{I}_{ip}$, the quantity that reflects the row-column nodes connected by the current source.

Therefore, if the cell conductances are known, the equivalent conductances can be found with the following steps for each row-column pair:

- Solving the circuit to find the equivalent resistance value of the row-column pair under consideration (similar to figure 2.6).

- Applying equation 2.5.

The general relation between those two sets of conductances is represented in a short notation as $\mathbf{G} = \mathbf{F}(\mathbf{g})$ and each component is denoted as $G_{ip} = F_{ip}(\mathbf{g})$. In [150] a software solution is proposed. It aims to invert the relation, that is, formally to do the following operation:

$$\mathbf{g} = \mathbf{F}^{-1}(\mathbf{G}) \tag{2.8}$$

In [150] several numerical algorithms have been proposed to solve this inverse relation. The most useful ones are the following:

- A least-squares approach. The elements of $\mathbf{g}$ can be found by minimizing the following cost function:

$$\|\mathbf{G}_{exp} - \mathbf{F}(\mathbf{g})\|^2 = \sum_{i,p} \|G_{exp,ip} - F_{ip}(\mathbf{g})\|^2 \tag{2.9}$$

The cell conductances are also subjected to an additional constraint $0 \leq g_{ip}$. In equation 2.9, $G_{exp,ip}$ are the quantities measured after a complete scan of the RSA.

The least-squares Least Squares (LSQR) approach is the most accurate one, although it is slow in general. A standard numeric package was used (scipy.optimize.least_squares [226]) in the Python implementation.

- A fixed point formulation of equation 2.8 is also possible. The conductances are iteratively found using this equation [150]:

$$\mathbf{g}_{n+1} = \mathbf{g}_n + \beta(\mathbf{G}_{exp} - \mathbf{F}(\mathbf{g}_n)) \tag{2.10}$$

where β is a damping factor that has to be chosen to balance speed and convergence.

Fixed point iterations are faster and for many practical purposes the accuracy is enough.

Comparison and selection of methods

In the mat prototypes presented in this document, the basic data acquisition circuit has been implemented, see figure 2.3. Crosstalk is removed in a post-processing step with IECM. In this subsection, it is argued why this choice is reasonable.

Contrary to most previous studies, IECM provides a software solution to the problem of crosstalk. The key point to apply IECM is to be able to measure the equivalent resistance of an RSA when a row-column pair is selected. In the circuit shown in figure 2.4 a voltage divider circuit is used, but a configuration with an OA is also possible. For the purpose of the current discussion, we focus on the voltage divider option. With respect to previous studies the configuration belongs to the group of single mode readout circuits. Table 2.1 presents a summary of characteristics of state-of-the-art methods. The voltage divider limits the current in the circuit, which is important in portable devices. This is in contrast to the original ZPM and VFM methods, or parallel readout methods [96]. With respect to QZPM, the proposed circuit has simpler and smaller components and less PCB paths. For instance, column selection requires an $N_C : 1$ mux with their $log_2(N_C)$ control lines, while in QZPM N_C analog switches are required, each one with its own control line. The switches are commonly named as single pole double throw switches or $2 : 1$ mux. A similar consideration could be done for the rows. Thus, the proposed configuration is a minimal hardware solution. As for the manufacturing requirements of the acquisition circuit, it would allow reducing as much as possible the requirement of components and minimizing the number of control lines required. Even low-end μCs are likely to have the required number of digital outputs. All together, this would lead to a data acquisition system of minimal cost and space. Besides, QZPM requires extra measurements compared with the traditional $N_R \cdot N_C$ readings and makes the system slower.

Thus, IECM allows keeping the circuit to its minimum complexity and cost, with a reduced power consumption. Given that low-cost is a requirement of the prototypes, in this thesis IECM and the basic circuit configuration are used.

Besides, it is worth indicating the relevance of the IECM drawbacks. In this thesis, it will be shown that the large resistance values cannot be recovered with accuracy. However, they correspond to lower values of pressure with no influence on a CoP for instance. Thus, the main drawback is not relevant. The post-processing time required is neither an issue since real-time results are not required in this thesis, because we are not developing a commercial product. Anyway, it will be shown that real-time could be achieved when the algorithms are implemented in C. Besides, the non-ideal behavior of mux/demux characterized by their non-zero internal resistance is also easily addressed in our prototype by means of a previous calibration step. This is possible because the DAQ system is always an independent box that is plugged into a connector of the mat. Thus, the calibration is carried out following several steps. If the mat is not connected, the configuration is equivalent to an array of infinite resistances. Furthermore, if the mat is not connected but a pair row-column is short-circuited with a cable this is equivalent to setting a single cell with zero resistance while the others are infinite. In this case, if a reading of the DAQ is carried out, the internal resistance of the mux/demux can be deduced. The value can be subtracted later once it is known. Thus, the calibration proceeds by short-circuiting sequentially all row-column pairs and obtaining the internal resistance of the mux/demux channels (in fact, it has been checked that all the channels have the same value for practical purposes). Anyway, for future applications, ZPM or QZPM are not completely discarded since their hardware requirements are not very high. A deep analysis of economic costs should be performed[1].

Given said that, optimization approaches can be useful for other circuits. In appendix C it is shown that IECM has the potential to be adapted to QZPM in a general framework of optimization methods. QZPM assumes that the switch resistance is known, while they can be estimated by the algorithm too if the adapted IECM is utilized. This shows that this kind of methods are worth to be studied for dealing with crosstalk in RSAs.

---

[1]In [72] the cost of a ZPM circuit was estimated to be €18 higher than the basic circuit used in this thesis for a 16x16 array

Table 2.1: Comparison of methods [149] © 2022 IEEE.

Method	Readout Time	Readout Mode	# OA	Selection Components	# Control Lines	Current
IIDFCC [241]	$2 \cdot (N_R \cdot N_C)$	Single	1	$N_R + N_C$ (2:1 MUX)	$N_R + N_C$	V_{ref}/R'
QZPM [138]	$N_C \cdot (N_R + (N_C + 1)/2) + N_R$	Single	1	$N_R + N_C$ (2:1 MUX)	$N_R + N_C$	$< V_{ref}/R$
proposed	$N_R \cdot N_C$	Single	0	1 (N_R:1 MUX) + 1 (N_C:1 MUX)	$log_2(N_R \cdot N_C)$	$< V_{ref}/R$
Improved ZPM-I [96]	$N_R + 1$	Parallel	$N_C + 1$	$N_R + 1$ Buffer	$N_R + 1$	V_{ref}/R'
Improved ZPM-II [96]	$N_R + 2$	Parallel	$N_C + 1$	$N_R + 1$ Buffer	$N_R + 1$	V_{ref}/R'

R is a known resistor set by the designer that limits the current and R' is the series between the output resistance of the buffer and the equivalent resistance of the RSA.
R' can be low, so that power can be high in the first and in the last 2 methods presented in the table. Buffer role can also be played by switches or 2:1 MUX.

2.2   PSM Prototypes

2.2.1   Previous prototype

A first prototype of PSM was developed previously in our group. It consists of three layers (see figure 2.7). The first layer is made of an insulating material Thermoplastic Polyurethane (TPU) [12]. It serves as a mechanical base and was built using a 3D printer. Adhesive copper tape, 7 mm width, is used to build horizontal lines on one side of the TPU layer.

The second layer is in fact composed of three sheets of Velostat. This is the material sensitive to pressure. The sheets cover the whole area.

The third layer is just similar to the first one but rotated 90°. In this way the copper lines are vertical and orthogonal to the lines in the first layer.

Either regular tape or Kapton® is used in the common areas that are out of the main array to avoid short circuits between copper lines. The last part of the lines is open to solder cables.

Crossing points between the copper lines in the first and the third layers are associated to the sensitive cells of the PSM. Each one has a sensitive area of 7 mm x 7 mm. The mat size is 32 cm x 32 cm and there are 16 copper tracks in each side, so that a matrix of 16x16 cells is formed. Thus, the resolution is $0.25 \, cells/cm^2$.

Copper lines are soldered to a female connector in which the DAQ circuit can be plugged. The DAQ system is inside a Polylactic Acid (PLA) box which has also been built with a 3D printer. The circuit is similar to many previous studies [129, 244] and its schematic is presented in figure 2.8. It is a circuit based on a pair of mux / demux to select row or columns (section 2.1.4), in which two muxs [9] 16:1 have been used: One is used for row selection the other for column selection. The selected row is connected to the reference voltage (V_{ref}) through

(a) First Layer

(b) Velostat and First layer

(c) Rows and columns with Kapton®

(d) Positioning of last layer
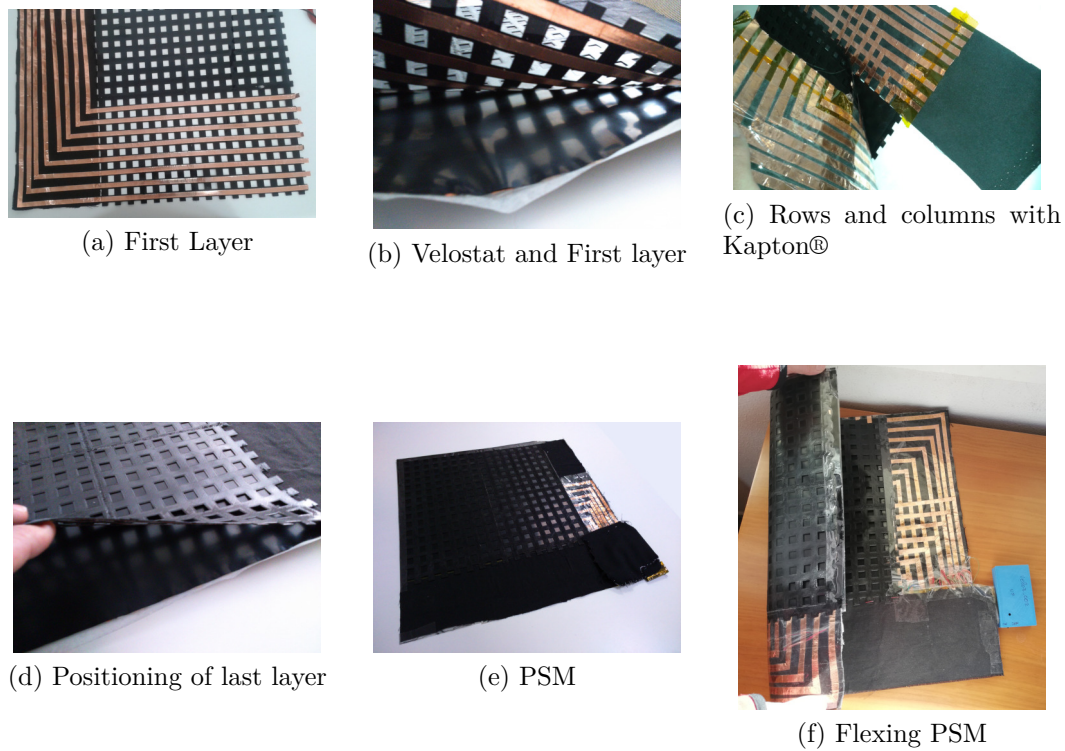
(e) PSM

(f) Flexing PSM

Figure 2.7: Prototype of PSM: (**a**) First layer of the PSM; (**b**) First layer with unfolded sheet of Velostat; (**c**) Inclusion of the insulator; (**d**) Positioning of the last layer; (**e**) Fully mounted PSM; (**f**) Flexing of the PSM.

a resistor $R_o = 2.2k\,\Omega$. A voltage divider circuit between the sensor array and R_o is formed and the middle point is connected to an ADC, see figure 2.3. The ADC is integrated into an STM32F103C8T6 µC [18], which is also used to control muxs. The ADC has 12 bits resolution. It turned out that the mux resistance and the ADC input resistance were far from ideal. They were estimated for each box independently (typical values $R_{ADC} = 123k\,\Omega$ and $R_{mux} = 145\,\Omega$). The µC is also connected to a Bluetooth module that sends data to a PC in text format. In the PC side a program written in Processing was developed to receive data, storing in and visualizing data as images for debugging purposes. Bluetooth transmission is the bottleneck of the system that limits the data transfer and therefore the sampling frequency of the PSM. The whole PSM is scanned at 10 Hz (in the test we performed the maximum value that can be reached was about 15 Hz).

Since this first prototype was based on a flexible base, it can be adapted to
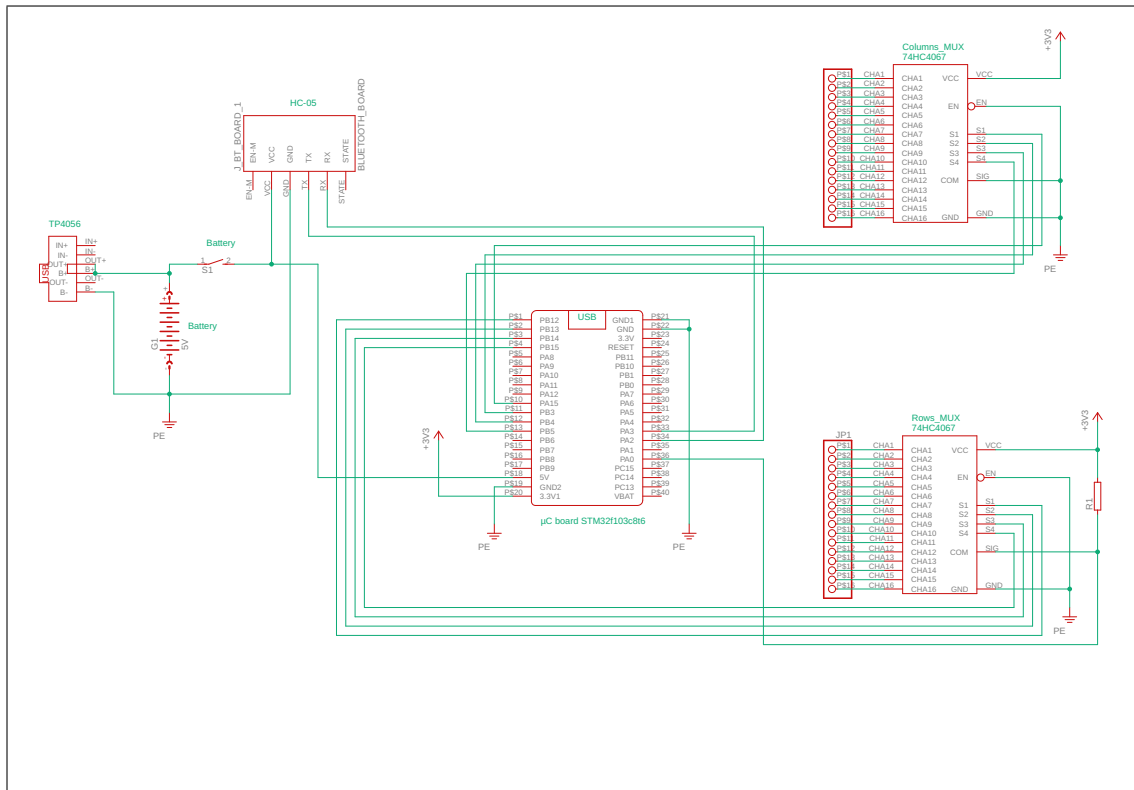
Figure 2.8: Schematic of the DAQ of the PSM

any irregular surface. It can also be folded for transportation.

Velostat costs less than €5/m², about €4.20/m², and the estimated cost of the materials used for manufacturing the PSM is around €100.

2.2.2 Improved prototype

The previous prototype has a very low cost because it is based on low cost materials and manufactured in our own laboratory. However, its size is larger than the printing area of our 3D printer. So each support, in the first and third layers, has to be printed in four pieces independently and then glued together afterwards. Adding copper lines (adhesive copper tape) has to be done manually too. This is a tedious procedure, hard to be redone if some mistake happens. Due to these reasons, a new version of the prototype was built. In the new prototype, the materials cost is higher, but the work force required is decreased considerably. The process can be automatized and parallelized.

In the new prototype, flexible PCB based on Kapton® [111] are used instead of the flexible TPU layers manufactured with a 3D printer. In this way, the copper

lines and the electrodes are integrated in the same PCB. It is possible to test several electrode variants. An alternative was based on circular electrode shapes, shown in figure 2.9b. In this case, the structure has also three layers as in the previous prototype figure 2.9d. Sensitive units are formed in the crossing points of vertical and horizontal lines. A single Velostat sheet is included in the middle of two flexible PCBs. Thus, the electrode itself (plain variant) is a sandwich structure made of copper-Velostat-copper. This is the same as in the previous prototype except that the electrode shape is circular and the lines can be placed with higher accuracy in the PCB design software. Another alternative is based on an interdigital electrode shape (interdigital variant, figures 2.9a and 2.9c). In this case the two terminals of each sensitive cell are integrated into a single flexible PCB. A single sheet of Velostat is placed on top of it. The advantage of this configuration is that it requires only a PCB, and thus the cost can be reduced from €280 to €200. The interdigital electrode presents a higher resistance under the same pressure, which seems reasonable because the contact area of the plain electrode is clearly higher. A view of the PSM with a protection fabric is shown in figure 2.9e.

PCBs were manufactured by an external commercial company. Thus, in the new prototype cells are homogeneous and copies could be manufactured easily for mass production.

Flexible PCBs cannot be folded as much as the TPU based PSMs, but they can still be rolled up and adapted to irregular surfaces. In addition, they are lighter.

Improving the DAQ circuit.

DAQ circuit was also improved. In the first version, the µC was programmed using the Integrated Development Environment (IDE) STM32CubeIDE [17], which allows debugging code and uses a Hardware Abstraction Layer (HAL) to facilitate programming µCs. However, an external programmer is required (see appendix E). The official programmer is rather expensive [16] although there are cheaper non official versions (€3, [115]).

The popular STM32F103C8T6 development board known as BluePill [115] was used in our prototypes. It has several peripheral devices. The board can be programmed using the programmer pins, connecting them to the pins of Serial Wire Debug (SWD).
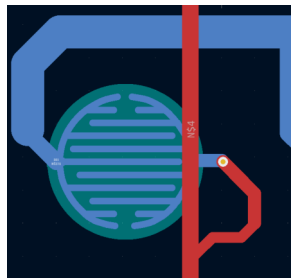
(a) Interdigital electrode of PSM

(b) Plain electrode of PSM
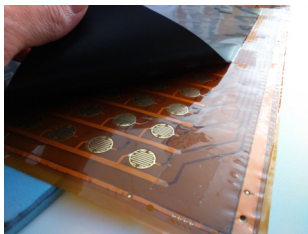
(c) Interdigital electrode in a manufactured PSM
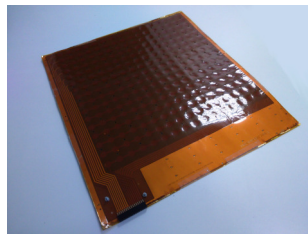
(d) manufactured PSM with plain electrode

(e) PSM covered by fabric

Figure 2.9: Prototype of PSM: (**a**) Interdigital electrode of PSM; (**b**) Plain electrode of PSM; (**c**) PSM with unfolded sheet of Velostat and interdigital electrode; (**d**) PSM with plain electrode made of Kapton®; (**e**) Kapton® PSM covered by a fabric.

However, during the µC programming process, the STM32CubeIDE was not always able to send information correctly both under Windows or Linux operating systems. Moreover, STM32CubeIDE requires the generation of a project file with a configuration for each application. This makes working with files very annoying. Besides, data transfer under Linux was often blocked. This prevented the use of Linux for some parts of the development even though the frameworks were supposed to be available for all the operating systems.

Therefore, we opted to install the Arduino bootloader in the development board. In this way the Arduino IDE could be used to program it. This IDE has also some very useful basic functions [7].

Programming the µC with the Arduino bootloader can be performed with the FTDI232 module (USB to Serial UART) [13]. The board also presents a USB module that can be utilized for data communication. The integrated USB can

also be used to program the board. Installing the bootloader was first required, see appendix E. In this way, the programmer is only needed in the first step to upload the bootloader. Afterwards, new programs can be uploaded to the board with a direct connection to a PC with a USB cable.

In the first prototype, data were sent as text strings. Given that a 12 bit ADC can reach a value of 4095 (a four digit number) each cell could imply the transmission of up to 40 bits including the digits and a separator character. This was improved by sending data in binary format. In this way each of the 4096 levels of the ADC can be sent with two characters (char in C) [7], so that only 16 bits per cell were sent. In our case, the data was sent in a little-endian codification because the family of μC works with this format, although their utilization depends on the compiler optimization. The code 2.1 shows the binary sending process.

```
1   void send_msg(uint16_t *cell_v){
2     // Send data in binary
3     setPin(debugPin);
4     Serial.flush();
5     Serial.write(INIT);
6     Serial.write(INIT);
7
8     for(int ii=0;ii<N_CELLS;ii++){
9       Serial.write(lowByte(cell_v[ii]));
10      Serial.write(highByte(cell_v[ii]));
11    }
12
13    #if(USE_VERIF)
14      calc_n_send_verif(cell_v, &verif_val);
15    #endif
16    clrPin(debugPin);
17  }
```

Code 2.1: Sending data in binary. INIT refers to an initialization char.

Reliability is increased by reducing the frame length, because sending fewer characters per pressure image reduces the possibility of failure. Besides, especial characters like tabs, spaces, or line feeds are eliminated; they could give rise to some problems with some codifications. To check the transmission of a full pressure image, an additional signature is sent, like a kind of parity (Code 2.1). If the signature is not right, the PC stores -1 as the values of ADC reading values. Thus, erroneous pressure images can be detected in the post-processing and data sampling can be preserved.

```
1  void calc_n_send_verif(uint16_t *cells_v, uint16_t *verif){
2    *verif = 0;
3    for(int i=0; i<N_CELLS; i++){
4      *verif = *verif + cells_v[i];
5    }
6    *verif = *verif % ADC_MVAL;
7
8    //Send
9    Serial.write(lowByte(*verif));
10   Serial.write(highByte(*verif));
11 }
```

Code 2.2: Calculation and sending verification bytes

Data transmission is no more implemented via a Bluetooth connection. Instead, a USB cable is used in the improved prototype version although the Bluetooth module is still available. This solution allows increasing the data transmission rates from 115200 bits/s (Bluetooth) to 1 Mbit/s (USB). These numbers are stable transmission rates, not maximal values.

Concerning the PSM, sending data via USB in binary format enables a full scan of it to be sent at 75 Hz, while with the Bluetooth module only 15 Hz could be reached in our tests.

In addition, controlling the mux is now more efficient. A set of agile macros has been coded to set digital levels. They do not perform some checks as the popular `digitalWrite()` function in Arduino does, following [143]. The function that updates the mux control lines checks them at the bit level and updates the µC ports (code 2.3). Since this function is called many times, its improvement has also a great influence in the maximum scanning frequency.

```
1  // Set Clear and Toggle digital ports
2  //We can add the port C with another if; in our case not necessary
3  #define setPin(b) ( (b)<16 ? GPIOA_BASE->BSRR |=(1<<(b)) : GPIOB_BASE->
       BSRR |=(1<<(b−16)) )
4  #define clrPin(b) ( (b)<16 ? GPIOA_BASE->BRR |=(1<<(b)) : GPIOB_BASE->BRR
       |=(1<<(b−16)) )
5  #define tglPin(b) ( (b)<16 ? GPIOA_BASE->ODR ^=(1<<(b)) : GPIOB_BASE->
       ODR ^=(1<<(b−16)) )
6  //Port C b>31
7  #define setPinC(b) GPIOC_BASE->BSRR |=(1<<(b−19))
8  #define clrPinC(b) GPIOC_BASE->BRR |=(1<<(b−19))
9
10 int row_Pins[N_ROW_MuxPins] = {PB12, PB13, PB14, PB15}; // From LSB to MSB
```

```
11  int col_Pins[N_COL_MuxPins] = {PA15, PB3, PB4, PB5}; // From LSB to MSB
12
13  // Set MUX
14  void set_Mux(int *pins_vec, unsigned short dec_val, byte n_bits){
15    unsigned short highPinsA=0, lowPinsA=0, highPinsB=0, lowPinsB = 0;
16    for(byte i_mux=0; i_mux<n_bits; i_mux++){
17      if(pins_vec[i_mux]<16){
18        highPinsA += (bitRead(dec_val, i_mux)) << (pins_vec[i_mux]) ;
19        lowPinsA += (not bitRead(dec_val, i_mux)) << (pins_vec[i_mux]);
20      }else{
21        highPinsB += (bitRead(dec_val, i_mux)) << (pins_vec[i_mux]−16) ;
22        lowPinsB += (not bitRead(dec_val, i_mux)) << (pins_vec[i_mux]−16);
23      }
24    }
25    GPIOA_BASE−>BSRR |= highPinsA;
26    GPIOA_BASE−>BRR |= lowPinsA;
27    GPIOB_BASE−>BSRR |= highPinsB;
28    GPIOB_BASE−>BRR |= lowPinsB;
29  }
```

Code 2.3: Setting of Mux control lines

Another improvement is related to time management. The sampling period is now guaranteed by means of timer controlled by an Interrupt Request (IRQ). In the previous prototype, the sampling period was rather low, 10 Hz, so it was not necessary to control the sampling event with high accuracy. The interruption has been configured at a low level, leading to a more agile execution [8, 10]. High level functions of Arduino have been avoided to remove unnecessary overhead. Inside the interruption routine, a complete scan of the PSM is carried out, i.e., selecting the 256 cells and reading their values.

It is worth highlighting that the μC has a default 72 MHz working clock frequency, but this value had to be lowered to 48 MHz to send data via USB. If not, IRQ from USB can interfere with the timer IRQ. The most accurate timer of the μC has been selected, Timer2. It enables reaching the desired frequencies without truncation. The timer configuration is presented in 2.4.

```
1  void config_timer2(void) {
2    //timer 2 setup
3    TIMER2_BASE−>PSC = 8000;  //48MHz/8000=6000 Hz
4    TIMER2_BASE−>ARR = 40−1;  //6000/40=150Hz
5    TIMER2_BASE−>CNT = 0;     //Clear Counter
6    timer_attach_interrupt(TIMER2, 0, handler_tim2);  //Handler of timer 2
```

```
7   TIMER2_BASE−>CR1 |= 0x0001;  //Enable timer 2
8 }
9
10 //timer 2 interrupt
11 void handler_tim2(void){
12   GPIOC_BASE−>ODR ^= 0x2000;  //toggle PC13 (LED)  1<<13=1*2**13=8192=0
       x2000
13   read_cells(cell_val);
14   send_flag=1;
15 }
```

Code 2.4: Timer Interruption Configuration and Handler

ADC configuration was another issue to be refined. This device can work with increased or decreased conversion times, but a lower conversion time should imply a lower input impedance too. Nonetheless, in the previous prototype it was tested that the input impedance was rather low despite the fact that the HAL default configuration was set for high conversion times (low conversion rates). Thus, to increase the conversion speed the ADC has been configured as shown in code 2.5. The configuration is based on low level functions that do not perform so many checks and the sampling time is set to 13.5 ADC clock cycles.

```
1 const int8_t  analogPin = PA0;
2 uint16_t adcValue;
3
4 void config_ADCs(void){
5   rcc_set_prescaler(RCC_PRESCALER_ADC, RCC_ADCPRE_PCLK_DIV_4);
6   int  pinMapADCin = PIN_MAP[analogPin].adc_channel;
7   //adc_set_sample_rate(ADC1, ADC_SMPR_1_5);   //ADC_SMPR_1_5  = 0,58uS/
       sample. Faster but Rin low.
8   adc_set_sample_rate(ADC1, ADC_SMPR_13_5);    //ADC_SMPR_13_5 = 1.08uS,
       Rin>10Kohm
9   adc_set_reg_seqlen(ADC1, 1);
10   ADC1−>regs−>SQR3 = pinMapADCin;
11   ADC1−>regs−>CR2 |= ADC_CR2_SWSTART;
12 }
13
14 void read_cells(uint16_t *c_val){
15   // Scaning of rows
16   for(unsigned short i_row=0; i_row<N_ROWS; i_row++){
17     set_Mux3(row_Pins, N_ROWS−i_row−1, N_ROW_MuxPins);
18     // Scaning of cols
19     for(unsigned short i_col=0; i_col<N_COLS; i_col++){
```

```
20      set_Mux3(col_Pins, i_col, N_COL_MuxPins);
21      delay_us(1);
22      setPin(debugPin2);
23
24      adcValue=ADC1->regs->DR;
25      ADC1->regs->CR2 |= ADC_CR2_SWSTART;
26      while((ADC1->regs->SR & ADC_SR_EOC) == 0){;}
27      adcValue=ADC1->regs->DR;
28
29      c_val[i_col+i_row*N_COLS] = adcValue;//analogRead(analogPin);
30      clrPin(debugPin2);
31    }
32  }
33 }
```

Code 2.5: ADC Configuration and Usage

Taking into account all the previous improvements, the PSM sampling frequency has been increased from 10 Hz in the previous prototype (maximum of 15 Hz) to 100 Hz in the new prototype (165 Hz maximum). Moreover, the ADC input resistance is now about 6.9 $M\Omega$, which is ideal for practical purposes in our application.

Fast IECM implementation: Python and C

The post-processing required to remove crosstalk, IECM, was first implemented in Python [150], as explained in section 2.1.4. For real circuits with noise it was verified that a LSQR approach or a fixed point iterative solutions (equation 2.8) were suitable.

The LSQR approach was implemented with the Scipy library [226], (section 2.1.4). The library function can perform the optimization with constraints and a given numerical error can be set as input parameter for termination. The constraints were used to force the conductance to be positive quantities. On the other hand, fixed point iterations were implemented with our own code.

The fixed point equations are clearly faster than the LSQR, but even in this case, with about 1 min per volunteer and 100 pressure images per second, the post-processing of a balance experiment can take a non negligible amount of time. Increasing processing speed was a very beneficial goal. The Python module devoted to multiprocessing [76] was selected to implement a parallel version of the IECM method. It is more convenient than the Python threading module because

it implements a true parallel execution in the Central Processing Unit (CPU) and creates new copies of the variables allocating memory for them. Thus, each subprocess can modify the variables in an independent way and there is no need to synchronize parallel executions of the code. The process management is carried out by means of a Pool object. In this way, when a set of pressure images has to be post-processed, each subprocess is in charge of processing only some of them, executing the same code. Incoming images are assigned to different subprocesses.

Using this parallelization technique allows decreasing a lot of computing times, but it is still an annoying process if a large quantity of data is to be processed (for instance from several volunteers in a balance test experiment).

To further speed processing times, a C implementation has been developed, both in sequential and parallel versions. The GSL library was used to perform matrix operations and to perform least square optimization [73]. The fixed point algorithm was translated to C. Since it was implemented with our own code, the results are exactly the same as in the Python version. However, the least square optimization was not exactly the same because input parameters and perhaps internal details of GSL implementation are different from those of the Python version. For fair comparison, the number of iterations in the GSL implementation was set to reduce the ghost effect to the same levels as in the Python LSQR implementation using some of our test images. Besides, in GSL it was not possible to include constraints. Instead, forcing conductances to be positive was achieved by using their logarithm in the minimization. In this way, the conductance value comes from an exponential operation of an optimized parameter. Therefore, they are never negative.

The parallel C implementation is shown in figure 2.10. It is based on a pool of processing threads. The main program is in charge of capturing data and sending them to a queue. Each time a new frame arrives, it adds the new frame to the queue and sends a signal to the pool of threads. If one of the threads is not busy, it removes the frame from the queue and process it to remove crosstalk. After processing it sends the processed frame to the output queue. In figure it is considered that another single thread can remove the processed frames from the output queue for storing it or perform some fast operation like calculating a center of pressure, while for visualization many of the frames could be just discarded. The implementation follows the ideas of producer/consumer models and a thread pool and it uses mutex and conditional variables following parallel programming

Table 2.2: Processing speed (in fps)

Language Method	Python	C
LSQR Serial	0.042	1.285
LSQR Parallel (4 Threads)	0.055	4.831
Fixed Point Serial	6.061	76.923
Fixed Point Parallel (4 Threads)	**8.264**	**294.118**

techniques to share data between threads and synchronize them [163].
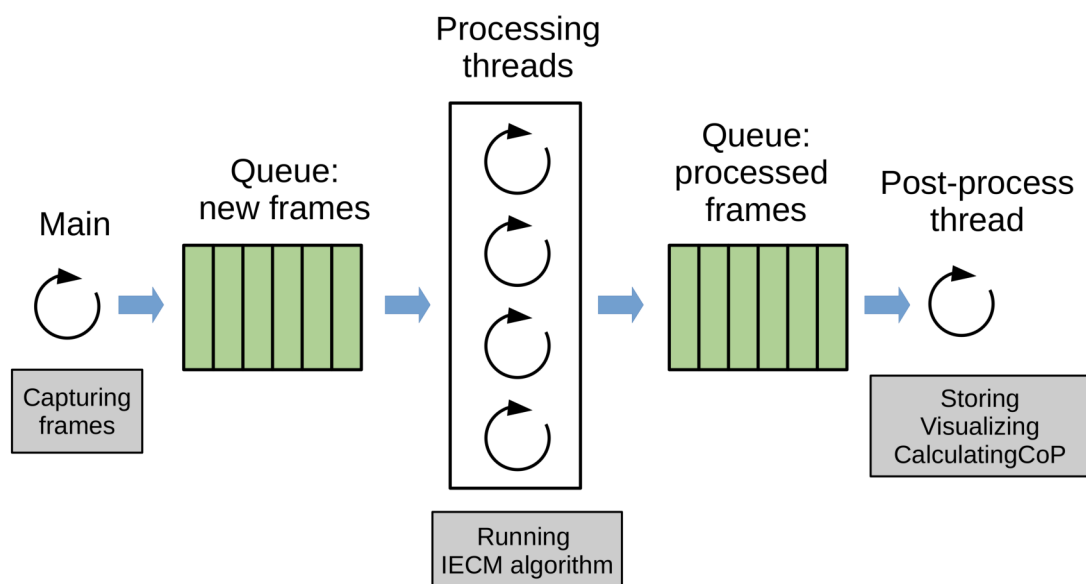
Figure 2.10: Schematic view of the parallel C implementation of IECM.

Processing times of different implementations can be seen in table 2.2, measured as frames per second. The programs were run in an Intel® Core™ i7-8700 CPU @ 3.20GHz. It is worth highlighting that the faster implementation is far faster than the current best sampling frequency of the PSM, with a factor almost two between them. Thus, real time processing is possible. The programs used four threads/subprocesses because most computers now posses at least such a number of physical cores.

Other improvements

Our current knowledge about PSMs have led to further enhancements of the previous prototype. They concern a far better characterization and modeling of

the sensor response to pressure and an estimation of the uncertainty measurement provided by the PSM. Nonetheless, they require a deeper analysis and more formal mathematical background. Therefore, we have decided to present them in separate subsections to explain them in detail.

2.2.3   Summary table of PSM prototypes.

To sum up, the characteristics of the three PSM prototypes that have been used in the thesis are shown in table 2.3. The name will be used as a reference in the document. 3D_Velo3_Blue and Kdigit_Velo_100 were used in balance tests, while Kplain_Velo_150 was used in the posture monitoring experiments.

Table 2.3: Summary of prototipes used in the thesis. Nº layers refers to the number of layers of piezoresistive material.

Identifying name	electrode type	material	communication	freq	nº layers	PCB type
3D_Velo3_Blue	plain	Velostat	Bluetooth	10 Hz	3	ABS 3D
Kplain_Velo_150	plain	Velostat	USB	150 Hz	1	Kapton®
Kdigit_Velo_100	interdigital	Velostat	USB	100 Hz	1	Kapton®

2.3   Uncertainty characterization in IECM.

Ideally, any measurement should provide not only a single value but also its uncertainty, i.e. an interval in which the true value of the physical magnitude is likely to be found [25, 26, 33]. This uncertainty might not be always presented, but a professional equipment should provide it. Being able to estimate the uncertainty of our PSM prototype is also an improvement over our previous studies. However, this topic deserves further explanations so that this specific subsection is devoted to it.

In this thesis, an analysis of the uncertainty associated to IECM has been developed. There are good reasons to carry out such analysis. Formally, the relation between the cell conductances and the measured (equivalent) conductances is shown in equation 2.8, $\mathbf{g} = \mathbf{F}^{-1}(\mathbf{G})$. If the measured conductances have some uncertainty, then the solutions found in this equation have also an uncertainty. Given that a rather complex algorithm is required to find $\mathbf{g}$ coming from a large

set of experimental measurements, it is worth studying whether the values obtained are reliable or not. In this section, this question is going to be answered. This section is largely based on our article [149] from which several excerpts are extracted (© 2022 IEEE).

2.3.1   Propagating uncertainty

From a technical point of view, the problem we are dealing with is that of propagating uncertainty. For small and uncorrelated uncertainties, the law of propagation of uncertainty [25] can be set as:

$$\sigma_{g_{jq}} = \sqrt{\sum_{i,p} \left(\frac{\partial g_{jq}}{\partial G_{ip}} \right)^2 \sigma_{G_{ip}}^2} \tag{2.11}$$

where the symbol σ_x is used for the standard deviation of a given quantity x, as a measure of its uncertainty.

The key quantities that have to be obtained to calculate the influence on $\mathbf{g}$ are the partial derivatives:

$$\frac{\partial g_{jq}}{\partial G_{ip}} \tag{2.12}$$

We have not obtained directly $\frac{\partial g_{jq}}{\partial G_{ip}}$. However, in the appendix C it is shown that:

$$\frac{\partial G_{ip}}{\partial g_{jq}} = \frac{(V_{ip,j} - V_{ip,q})^2}{(V_{ip,p} - V_{ip,i})^2} \tag{2.13}$$

The indices (i, p) or (j, q) refer to the physical row-column position in an RSA (the voltage notation has been explained in section 2.1.4). For the purpose of the next reasoning, it is convenient to see $\mathbf{g}$ or $\mathbf{G}$ as single vectors, flattening the physical indices into a single mathematical index. Therefore, we represent the set of partial derivatives as $\frac{\partial \mathbf{G}}{\partial \mathbf{g}}$, which can be seen as a matrix. For instance, in a 16x16 RSA, there are 256 cell conductances and 256 equivalent conductances. Thus, the matrix $\frac{\partial \mathbf{G}}{\partial \mathbf{g}}$ is a 256x256 matrix representing the partial derivatives of each equivalent conductance with respect to each cell conductance. Following the theory of partial derivatives, the required quantities, $\frac{\partial \mathbf{g}}{\partial \mathbf{G}}$, can be obtained as:

$$\frac{\partial \mathbf{g}}{\partial \mathbf{G}} = \left(\frac{\partial \mathbf{G}}{\partial \mathbf{g}}\right)^{-1} \tag{2.14}$$

To sum up, the partial derivatives required in equation 2.11 can be obtained by first calculating the set of partial derivatives in equation 2.13, and then obtaining the inverse matrix, equation 2.14. It should be highlighted that all the voltages required in equation 2.13 are obtained when running IECM. Equation 2.11 also requires the quantities $\sigma_{G_{ip}}$. In this document, we refer to them as the noise model. They represent the noise of the measurement system.

If the uncertainties are not small, simulation is required to quantify the confidence interval for any given quantity [25]. The circuit has to be solved for different values of $\mathbf{G}$ inside an interval, and the set of outcomes, $\mathbf{g}$, can be characterized statistically by an SD for instance or any other parameter.

In the next subsections, results concerning uncertainty will be given in two different contexts: one with simulated values and the other one with values measured from a real RSA.

2.3.2   Experiments with simulated noise

The starting point of these simulations is a known value of an RSA ($\mathbf{g}$). Then $\mathbf{G}$ is calculated. Afterwards, we proceed by adding noise to $\mathbf{G}$ and using IECM to find $\mathbf{g}$ with a least-squares approach. This has been repeated $1,000$ times so that a value of standard deviation for each cell can be obtained [26]. These standard deviations can be compared with those obtained from the law of propagation of uncertainty. The general procedure carried out in this section is graphically explained in figure 2.11.

Although this subsection is entitled as "simulated noise", the noise model and some of the initial $\mathbf{g}$ are close to true values since they are taken from experiments (see section 2.3.3). More specifically, the noise model corresponds to a gaussian distribution with relative standard deviation as shown in figure 2.12. In the figure the points correspond to measured noise in a real DAQ system for some known values of resistance. For intermediate values, linear interpolation has been used.

In the first case we present, the initial value of $\mathbf{g}$ is a set of 16x16 conductances randomly selected between $1e-5$ and $1e-2$ S, which correspond to resistances in the range $100\,\Omega$ to $100\,k\Omega$. Figure 2.13 shows the relative noise figure for both, the simulations and the uncertainty propagation equation 2.11.
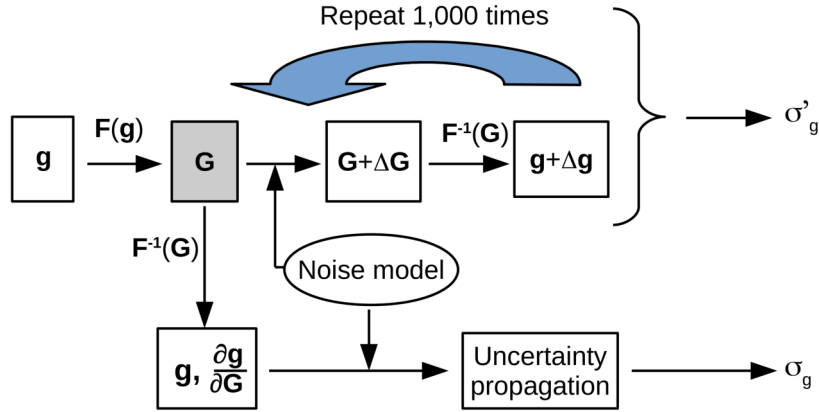
Figure 2.11: Schematic view of the process to obtain uncertainty from simulations, σ'_g, and the comparison with uncertainty propagation equation, σ_g ([149] © 2022 IEEE).
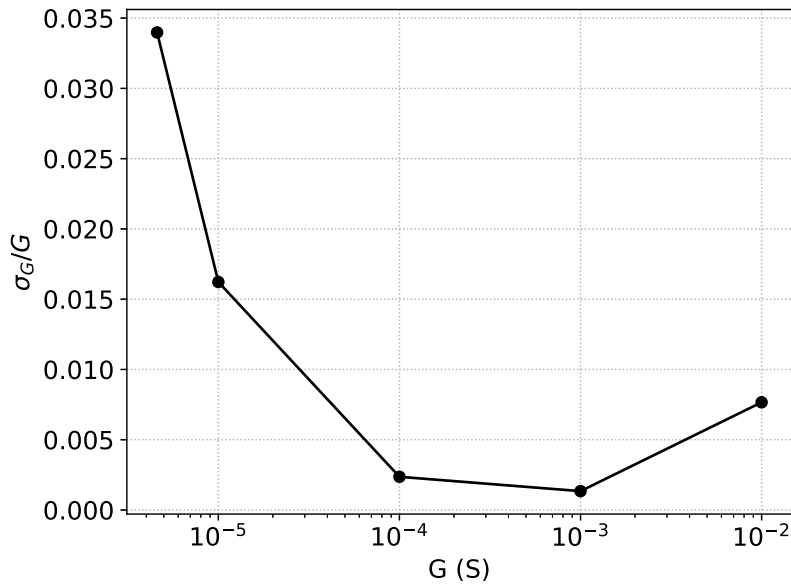
Figure 2.12: Relative standard deviation of the noise model used ([149] © 2022 IEEE).

For lower conductances, the uncertainty propagation equation tends to overestimate the simulation, while for higher conductances, it gives the same results as the simulations with overlapping points in the figure. This behavior can be explained because equation 2.11 is not exact and comes from a linear approximation [25, 113]. Thus, it is not surprising that it deviates from true values in the range in which uncertainty is larger. In addition, the relative uncertainty increases for low values of conductance, which are not reliable. It is not hard to imagine sit-

uations in which this can happen. For instance, let us consider a 2x2 array (like
in figure 2.14a) composed of 10 kΩ in cell $(1, A)$ and three 100 Ω resistors in the
other three cells. In this case, the equivalent resistance between nodes 1 and A is
easily obtained as a parallel combination of 10 kΩ and 300 Ω (see figure 2.14b),
which is roughly 300 Ω. For any other row-column pair the equivalent resistance
would be the parallel combination of 100 Ω and $10, 200Ω$ using a similar reason-
ing. That value is about 100 Ω. Therefore, the largest resistor has little influence
on the measurements and thus it is harder to be recovered from them.
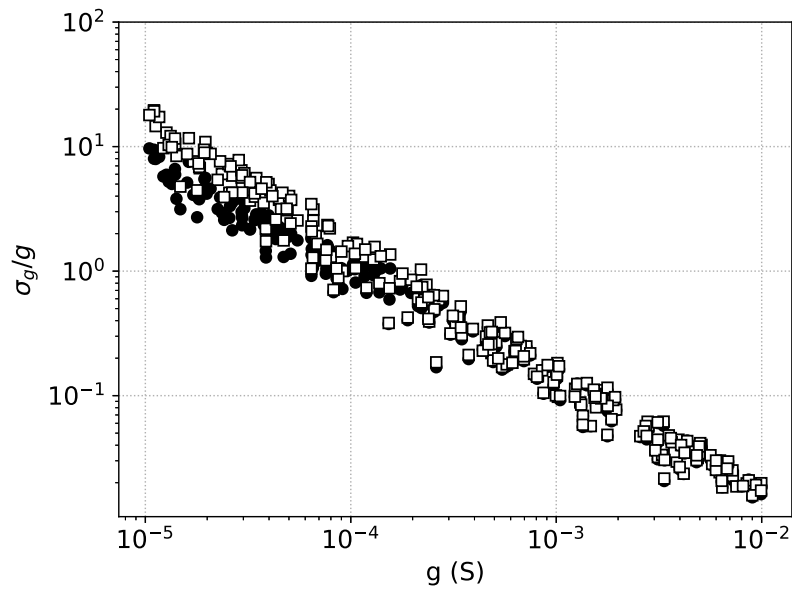
Figure 2.13: Relative uncertainty as a function of conductance for a random
array of conductances. Squares represent the values from uncertainty propagation
equation, circles from simulation ([149] © 2022 IEEE).

In the second case, the values of **g** come from the measurements of a Velostat-
based PSM, our fist prototype, with a person standing on it [150]. Figure 2.15
shows the conductance map and the results of the uncertainty estimation. In
this case the uncertainty propagation equation and the simulation give almost
the same results, even though the former shows a tendency to overestimate un-
certainty values in the very low conductance range. Low conductances are not
reliable at all, while for conductances above a value about $1e - 4$ the uncertainty
is less than 10 % (in other words, resistances lower than a few kΩ can be recovered
with that precision).

In the third case, the values of **g** come from the same PSM with a person
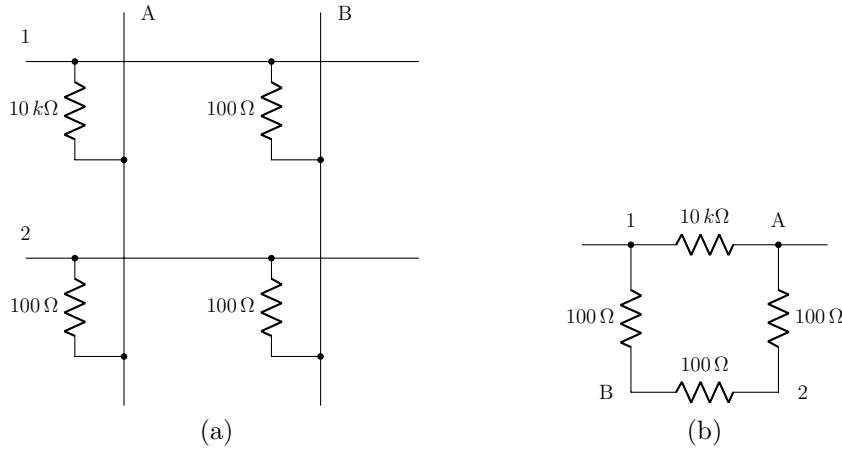
Figure 2.14: a) Example of a 2x2 array; b) The equivalent resistor seen from nodes $(1, A)$ ([149] © 2022 IEEE).

in semi-tandem stance. In this case, the values of conductance before processing showed a clear ghost effect, while after the processing there is almost no pressure in the top right part, shown in figure 2.16a, where no foot is in contact with the mat. The results are similar to the previous case but with some minor differences: The spread of the values seems larger in this case and the tendency for uncertainty overestimation of equation 2.11 is even more clear.

2.3.3   Noise in a real RSA

In this case, we built a PCB with a female socket to plug resistors, see figure 2.17. The connections reproduced a 6x6 RSA. The PCB has also a connector to plug our DAQ system developed for our PSMs, based on the circuit shown in figure 2.3. Although the circuit is built for a 16x16 array, there is no problem if a smaller RSA is plugged. The rest of the captured RSA values, indices from 7 to 16, appear to be as infinite resistances. Thus, the pressure images can be just cropped to the relevant 6x6 area.

The first step was to determine the noise model. For that purpose, a known single test resistor was placed in a cell and the rest of connections were left open. In this way, an ideal situation was achieved: measuring the equivalent resistance was the same as measuring the cell resistance, all other being infinite. Then, we acquired data for about 30 s (300 samples) and extracted the standard deviation. An example of the voltage values measured for a test resistor of 1 kΩ is presented in figure 2.18. Discrete jumps are clearly seen, corresponding to changes in the
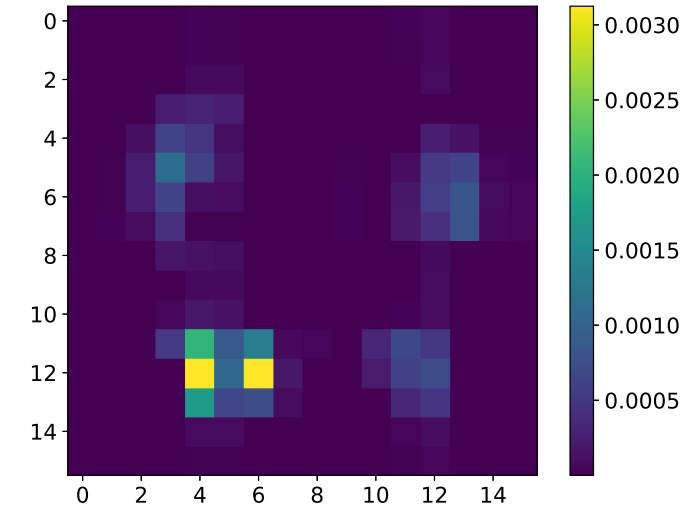
(a)
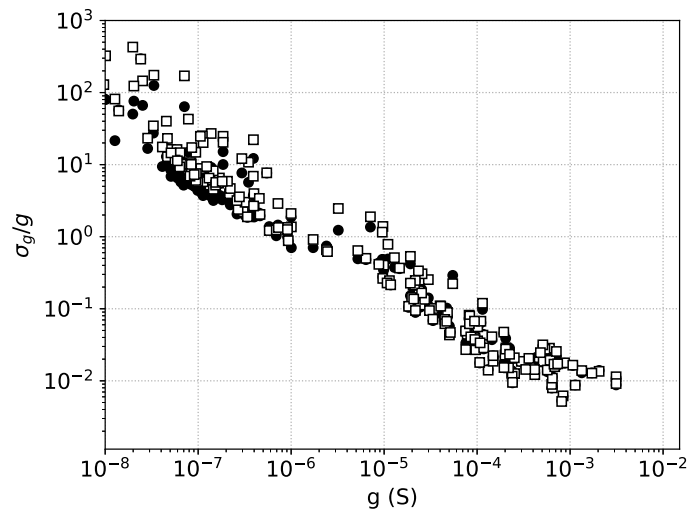
(b)

Figure 2.15: Conductance map of a PSM (person in standing position, top figure), and relative uncertainty (bottom figure). Squares represent the values from uncertainty propagation equation, circles from simulation ([149] © 2022 IEEE).

ADC readings of a few units. The global results are shown in table 2.4 for each value of resistance. It can be seen that the noise is almost constant, around ±1 mV. This corresponds to about ±1.24 LSB in the system. Therefore, it seems that the intrinsic quantification error is a large portion of the uncertainty in the system. It is likely that the noise would be larger in another environment but, given that our system is composed of a simple PCB and that it was not tested

(a)

(b)
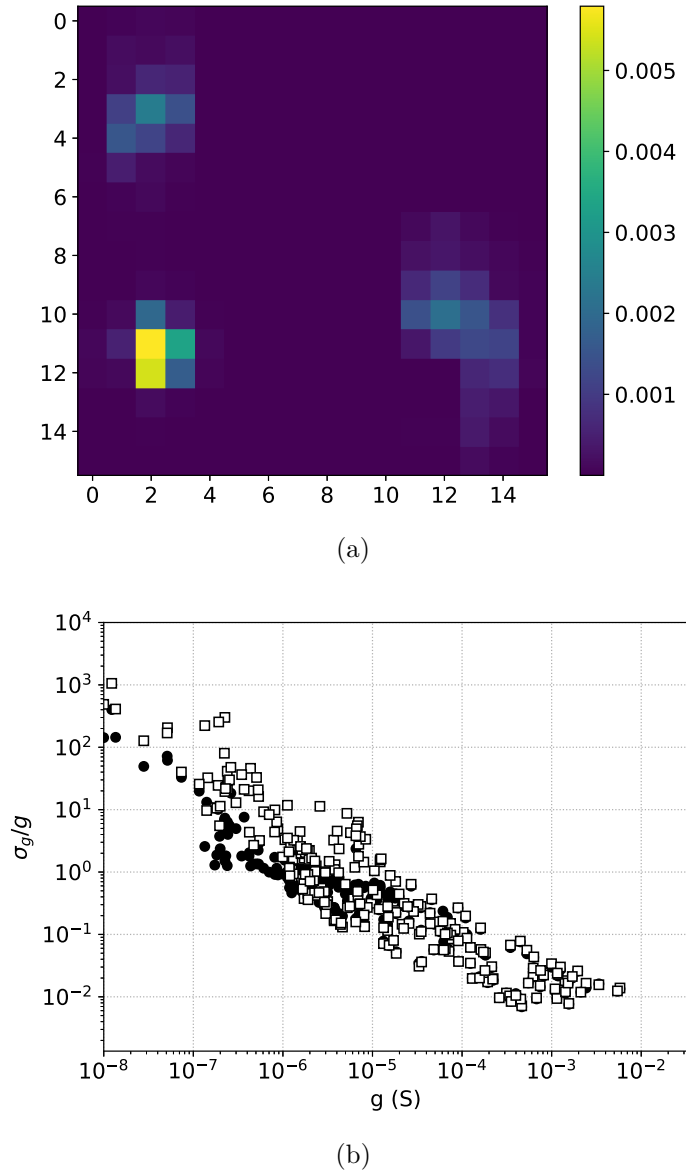
Figure 2.16: Conductance map of a PSM (person in semi tandem, top figure), and relative uncertainty (bottom figure). Squares represent the values from uncertainty propagation equation, circles from simulation ([149] © 2022 IEEE).

in a noisy environment, the measured noise may be lower than the typical value found on µC applications. The results presented in figure 2.12 are derived from the values in table 2.4 just by expressing them in relative terms.

Once determined the noise model, we measured the noise with different configuration of the 6x6 RSA using resistors of 100 Ω, 1 kΩ, 10 kΩ and 100 kΩ. The procedure to obtain the experimental uncertainty and the estimation obtained
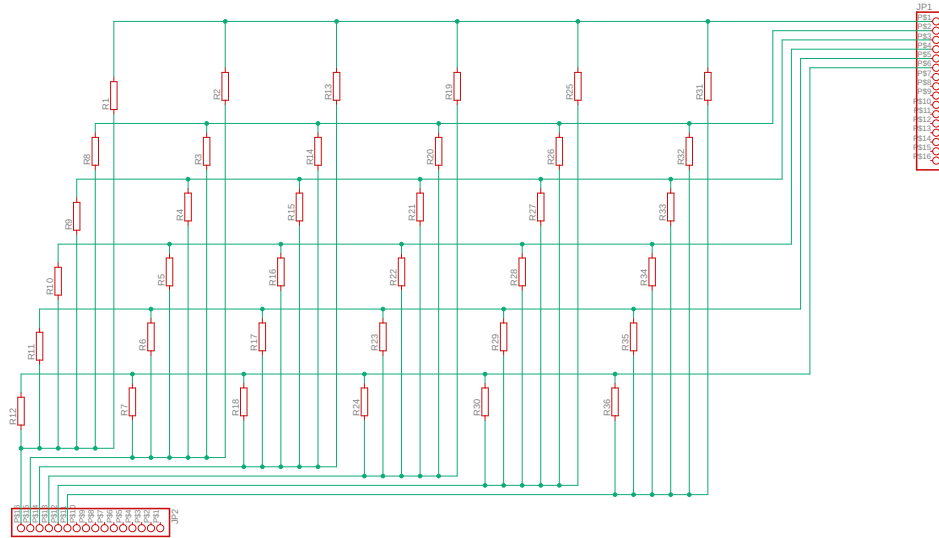
(a) 6x6 Schematic
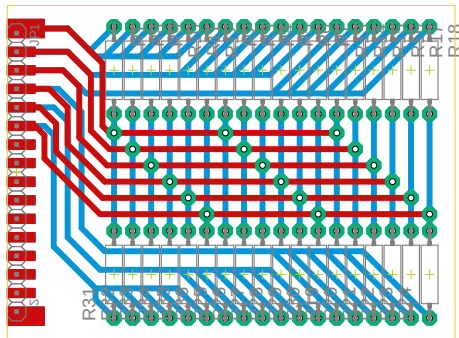
(b) 6x6 PCB
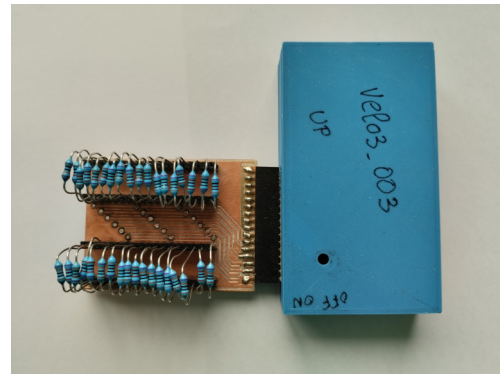
(c) 6x6 circuit

Figure 2.17: PCB employed to measure the noise in the system: (**a**) Schematic of the prototyping board to plug a 6x6 resistor array; (**b**) PCB layout of the same board; (**c**) Manufactured PCB with resistors and the DAQ box plugged.

from the uncertainty propagation equation is very similar to the one shown in figure 2.11. The difference is that instead of adding noise in the computer to an
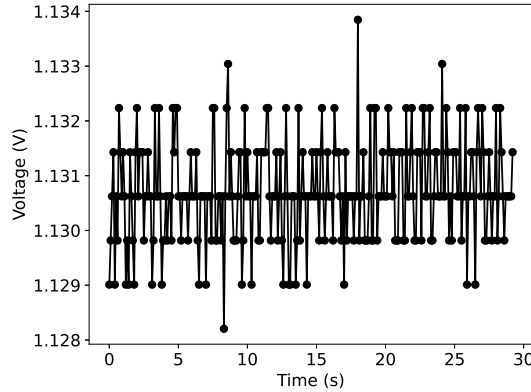
Figure 2.18: Measured voltage for a test resistor of 1 kΩ showing the noise level in the system ([149] © 2022 IEEE).

Table 2.4: Measured voltage noise level for various test resistors and the associated uncertainty in the conductance deduced from the voltage divider circuit. The noise is characterized in terms of standard deviations (σ_v for voltage, σ_g for conductance) [149] © 2022 IEEE.

Resistance Ω	σ_v (mV)	σ_g (S)
100	1.0	7.7e-5
1,000	0.9	1.3e-6
10e3	1.1	2.4e-7
100e3	1.1	1.6e-7
220e3	1.1	1.6e-7

initial $\mathbf{G}$, in this section we just took several measurements of the same configuration in static conditions (about 30 s, 300 samples), getting several $\mathbf{G}$ values and then several values of $\mathbf{g}$ using IECM. In this way the experimental uncertainty could be determined. On the other hand, from a value of $\mathbf{G}$ (in fact, we took the median), we derived $\mathbf{g} = \mathbf{F}^{-1}(\mathbf{G})$ using IECM and the derivatives $\frac{\partial \mathbf{g}}{\partial \mathbf{G}}$, from which uncertainty propagation can be applied to obtain the expected uncertainty.

Two different configurations were tested. In the first configuration, the resistors were randomly selected, see figure 2.19a. In the second configuration we tested a case with a strong ghost effect, in which three corners are filled with 100 Ω resistor and the rest with higher values (illustrated in figure 2.20a). The general trend of the results is similar to the cases shown in section 2.3.2. However, a graph like figures 2.15b and 2.16b is not very helpful because the points overlap due to the presence of a discrete set of resistance values. Therefore, in this section, we represent only bar plots showing the cell values that can be determined

with a relative precision better or close to 10%. They correspond to 100 Ω and 1 kΩ resistors. The bar plots in figures 2.19b and 2.20b show the value of conductance and the relative uncertainty obtained from the measurements and from the uncertainty propagation equation. In general, they agree reasonably well with some tendency to overestimation for 1 kΩ resistors ($1e-3$ S conductance) and underestimation for 100 Ω resistors ($1e-2$ S conductance) in the case in which there is strong ghost effect.

2.3.4   Conclusions

In this section we have proven an equation to find the sensitivity of cell conductances $\mathbf{g}$ with respect to equivalent conductance measurements $\mathbf{G}$ in an RSA when using IECM to eliminate the crosstalk problem. This leads to the possibility of estimating the uncertainty using the law of uncertainty propagation. We have tested this with simulated and real RSA. The uncertainty propagated is very close to the simulated and experimental ones for low values of resistance, which are the ones that can be obtained with a reasonable reliability. For higher resistances, the propagation equation tends to overestimate the uncertainty, but the main outcome is clear: they cannot be obtained reliably.

IECM is a software solution to the problem of crosstalk in RSAs. It has an advantage in terms of reduction of electronic components, which is very important for large arrays. A consequence of the results of this section is that the largest resistance values cannot be obtained in this way reliably, while the lowest resistance values present far less uncertainty. The importance of this characteristic of IECM depends on the application. For a PSM, the uncertainty in large values of resistance (low values of conductance) does not imply too much change in terms of pressure exerted on the mat. This is due to the approximate proportionality between conductance and pressure in many sensitive materials. It would be rather irrelevant to find a center of pressure or an object shape. Nevertheless, this might not be the case for other sensors that are based on an RSA model. With the extension of IECM proposed in this section, it can detect the situations in which the results are not reliable.

(a)

(b)
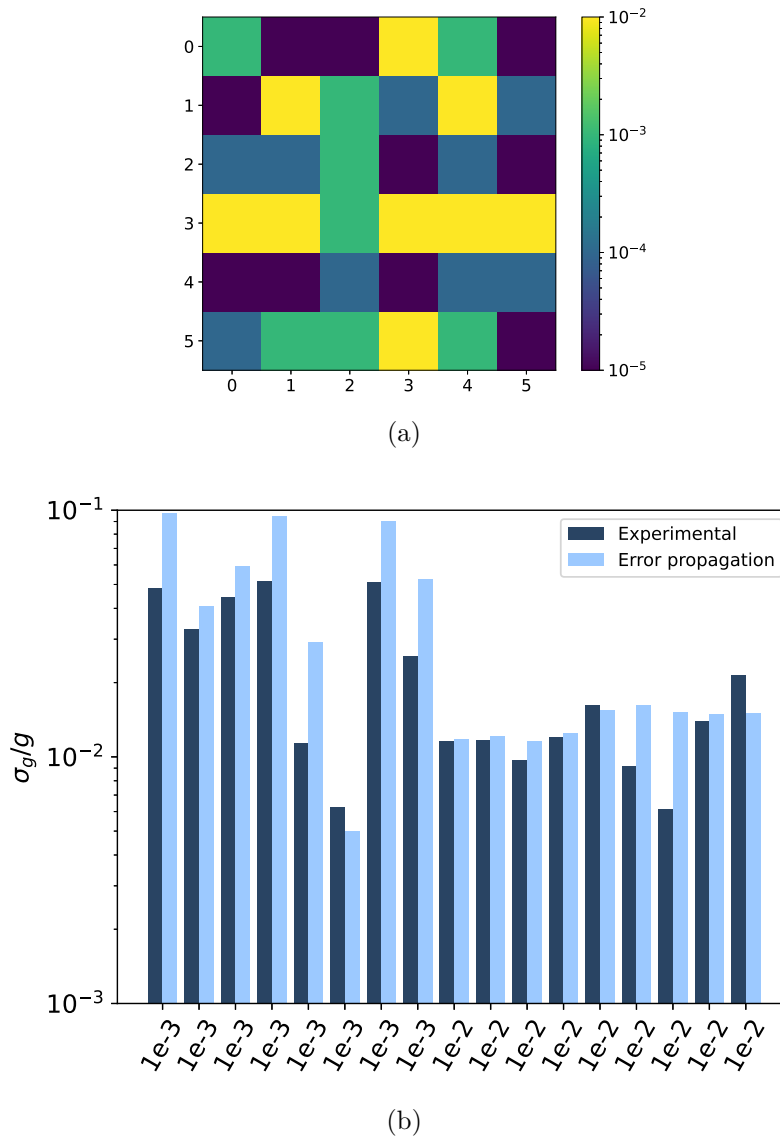
Figure 2.19: a) Conductance map of a 6x6 RSA with random resistances and b) relative uncertainty of the highest conductance cells (bottom), in which dark blue is the experimental uncertainty and the light blue the value obtained from the uncertainty propagation equation. Labels in x-axis represent the conductance in S of the corresponding cells [149] © 2022 IEEE.

2.4 Characterizing and comparing piezoresistive materials

Although Velostat is likely to be the most popular low cost piezoresistive material, there are other alternatives available in the market. Thus, a possible improvement

(a)

(b)
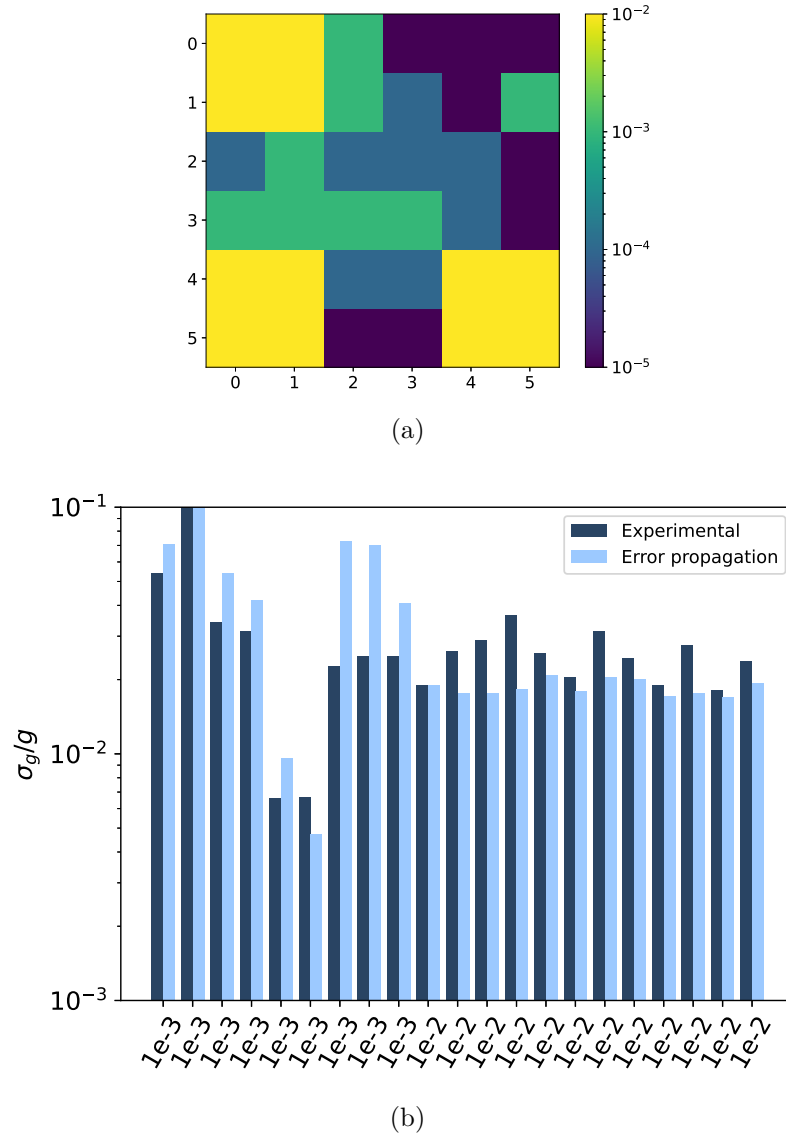
Figure 2.20: a) Conductance map of a 6x6 RSA that would show strong ghost effect if not corrected and b) relative uncertainty of the highest conductance cells (bottom), in which dark blue is the experimental uncertainty and the light blue the value obtained from the uncertainty propagation equation. Labels in x-axis represent the conductance in S of the corresponding cells [149] © 2022 IEEE.

option was to select a material whose response to pressure had less non-linear effects, see section 2.1.2. The experiments and selection requires a more lengthy discussion. This is why a specific section has been devoted to this topic.

Three materials have been selected for a controlled experiment in which a small-sized array is subjected to a set of pressure patterns: Velostat [6], EeonTex [70] and Ex-static [11].

2.4.1   Experimental set-up

The controlled experiments were performed in a pneumatic platform by researchers of the Electronics Department, University of Malaga, who are collaborating with our group in the study. The commercial device has been described in [53, 197]. It allows applying a uniform pressure on a surface. It is a Tekscan® PB100E with a Pneumax 171E2N.T.D.0009 regulator. It has an active area of 127 mm x 311 mm with a maximum thickness of the samples of 1.55 m. The applied pressures go from 0 to 100 PSI (680.47 kPa) with a resolution of 1% of the span.

Three PCBs have been developed, each one for a different material (see figure 2.21). They include 10 interdigital electrodes. A simplified DAQ circuit was developed for them. It is based on an ATMEGA4809 μC in the Arduino Board Nano Every, see schematic on figure 2.22. The μC is in charge of multiplexing the 10 sensors. The mux output is connected to a voltage divider circuit. The voltage is measured by the μC ADC. In this case each sensor has a different line (ground is common) so there is no crosstalk.

The system is connected to a PC via USB, which also powers the circuits. Sending data is started from the computer side by sending an 's' char (start) in utf-8 codification. Then acquisition starts and a LED in the board blinks. Reading the 10 sensors values and sending their data from the board to the PC in text format is done every 500 ms. The acquisition ends when the PC sends an 'f' (finish) char to the board.

2.4.2   Protocol

Material characterization was carried out by repeatedly applying load and unload cycles, which have been classified into three kinds of tests: fast cyclic tests, long tests and hysteresis tests. The experiments allow quantifying non linear effects, as explained in section 2.1.3. Nonetheless, it should be pointed out that it is very difficult to design experiments in which a single non-linear effect is observed and the others are ruled out. For instance, creep can last for hours or days and it is not practical to perform such long cycles in which even the pneumatic platform is not able to keep the same pressure level. Thus, in all the experiments all the non-linear effects are present to a greater or lesser extent.

The main goal of the fast cyclic test is to characterize repeatability. Pressure is applied for two minutes, then the material is free from pressure for the next

(a) Velostat PCB

(b) EeonTex PCB

(c) Ex-static PCB

(d) Back of PCB

(e) Design of DAQ Box

(f) DAQ system connected with Box
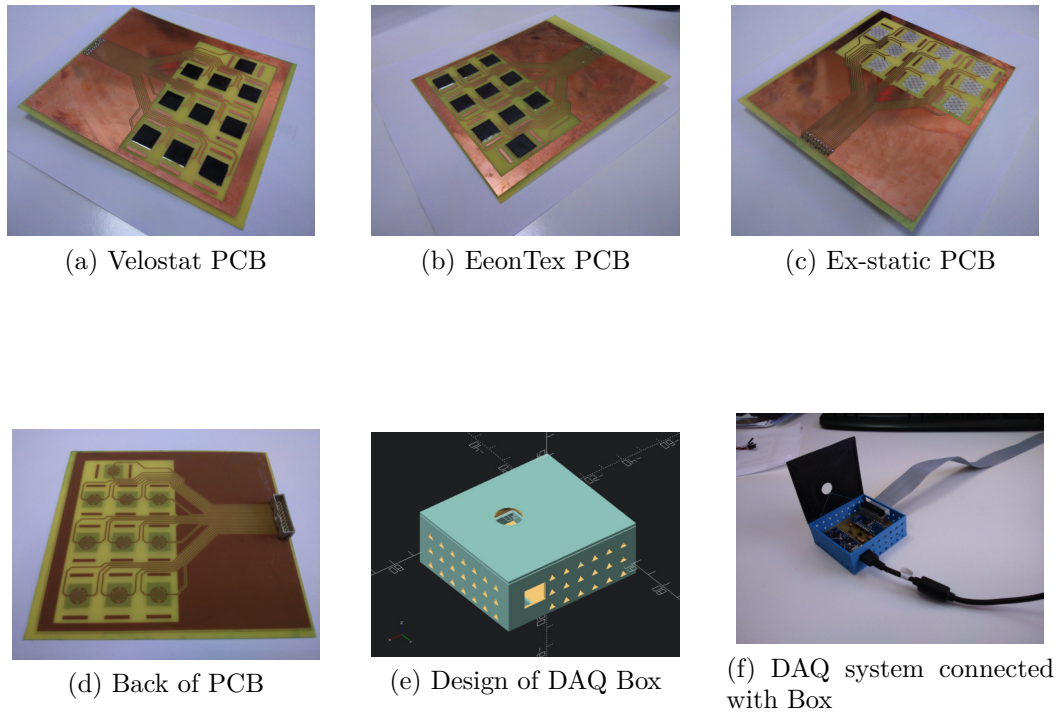
Figure 2.21: PCBs and DAQ used for comparing the materials: (**a**) Velostat PCB; (**b**) Eeontex PCB; (**c**) Ex-static PCB; (**d**) Back part of the PCBs; (**e**) OpenScad box design for the DAQ; (**f**) DAQ system connected inside PLA Box.

two minutes. These load/unload process is repeated 20 times (illustrated in figure 2.23).

The set of load/unload cycles has been carried out for two different pressures, 5 psi (34.47 kPa) and 15 psi (103.42 kPa). The material was kept uncompressed for a minimum period of 80 min between the application of 5 and 15 psi cycles in order to try to make independent measures. Each PCB with its own sensitive material was subjected to the same test procedure.

The long test tries to characterize creep and drift. A staircase of pressure values is applied to the PCB. Each step lasts 25 min. The system starts from 0 psi, then goes up to 5 psi, 15 psi, 30 psi and then down to 15 psi, 5 psi and 0 psi as shown in figure 2.24.

The hysteresis tests include two different applied pressure series, one with descendent maximum values and the other with ascendant minimum values. In
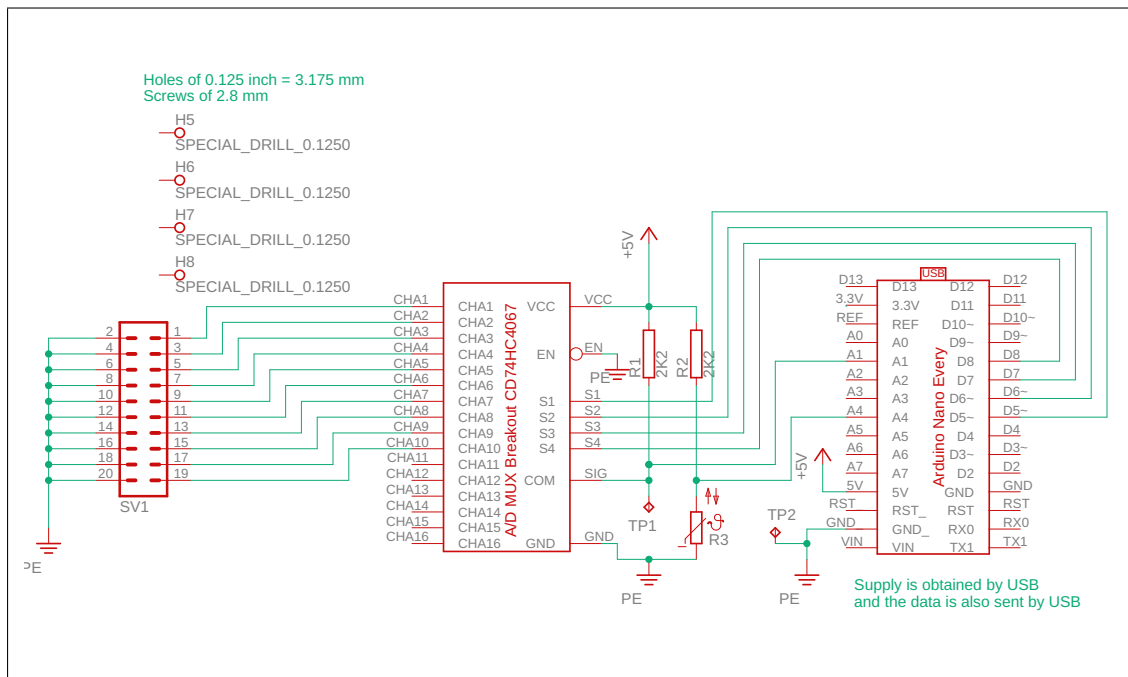
Figure 2.22: Schematic of the DAQ system used for the material characterization.
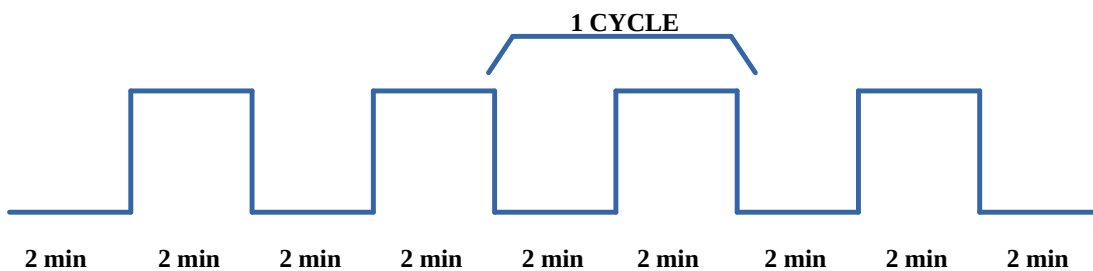
Figure 2.23: Fast ciclic pressure pulses.
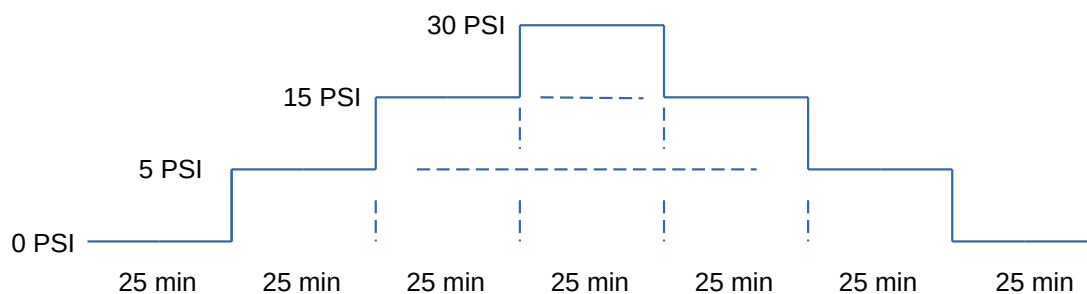
Figure 2.24: Long time applied pressure.

both cases the system starts from 0 psi and changes in steps of 2 psi up to the maximum value of the cycle. Each step lasts 6 s to allow pressure to become stable. In the descendent cycles, each cycle reaches a maximum value 4 psi lower

than the previous one. In the ascendant cycles, the minimum of the cycle is 4 psi higher each time, although the system always return to zero pressure after performing a hysteresis cycle in the upper part of the conductance vs. pressure diagram.

In other words, the set of applied pressures is the following:

1. Descendent hysteresis tests:
   $0 \to 32 \to 0 \to 28 \to 0 \to 24 \to 0 \to 20 \to 0 \to 16 \to 0 \to 12 \to 0 \to 8 \to 0 \to 4 \to 0$

2. Ascendant hysteresis tests:
   $0 \to 32 \to 4 \to 32 \to 0 \to 32 \to 8 \to 32 \to 0 \to 32 \to 12 \to 32 \to 0 \to 32 \to 16 \to 32 \to 0 \to 32 \to 20 \to 32 \to 0 \to 32 \to 24 \to 32 \to 0 \to 32 \to 28 \to 32 \to 0$

The process is better understood with the help of figures 2.25 and 2.26.
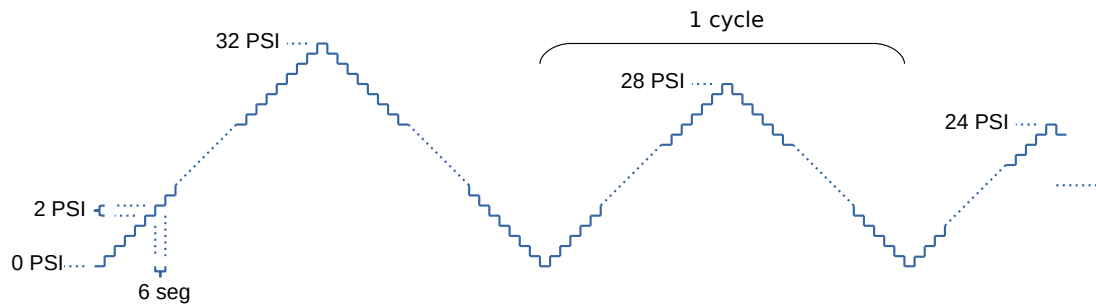
Figure 2.25: Pressure applied in descendent hysteresis tests.
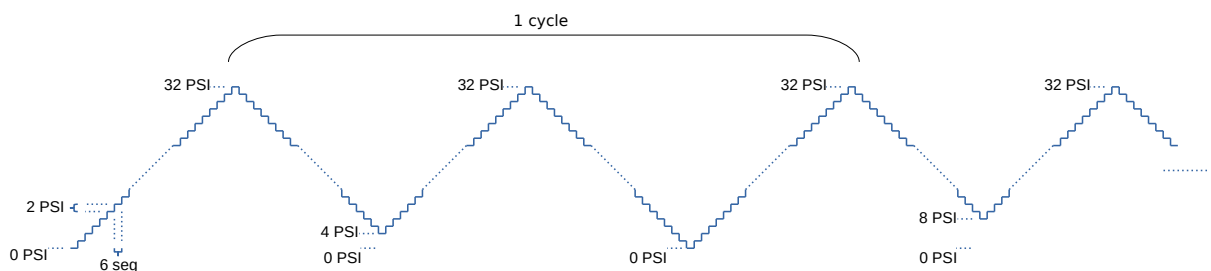
Figure 2.26: Pressure applied in ascendant hysteresis tests.

The set of descendent/ascendant hysteresis cycles were repeated ten times. When quantifying hysteresis with a single value, the repetitions were averaged in order to reduce the influence of other effects.

The maximum value of pressure in the experiments is 32 psi. This value is higher than values reported in the literature for pressure exerted when standing on a single leg, which will be the worst situation considered in this thesis. No more than 20 psi have been found for peak values in previous studies [89, 191, 210]

2.4.3   Results and material selection

The numerical characterization of variability follows equation 2.1 using data from the fast cyclic tests, with $\Delta t = 30$ s in this case (the total pulse time is 2 min). For an ideal material, the outputs of all the cycles and of all the cells should be the same, which is not the case in this experiment.

With respect to variability, EeonTex and Velostat behave much better than Ex-static, see table 2.5. EeonTex and Velostat present very similar values at 5 psi but differ clearly at 15 psi, in which EeonTex outstands. The general aspect of sensor output as a function of the sample is shown in figure 2.27. It is noticeable that the two sources of variability, pulse repetition and cell, cannot be neglected and both contribute to the final result shown in table 2.5. If the pulse repetitions are also averaged, like in figure 2.28, it is again clear that Ex-static is the worse material.

Table 2.5: Variability of the materials. The best value is highlighted in bold.

Pressure Material	15 PSI	5 PSI	Mean
EeonTex	**0.067**	0.103	**0.085**
Ex-Static	0.152	0.217	0.185
Velostat	0.123	**0.094**	0.108

Long tests are used to calculate creep and drift. Creep is calculated using equation 2.3. Each load value was kept constant for 25 min, so that $\Delta T = 25$ min in the equation.

In figures 2.29 and 2.30 the sensor output as a function of sample number is shown (full test or high pressure part respectively). Creep and drift effects are noticeable. Creep is higher in EeonTex as can be deduced from table 2.6 and figure 2.31. The behavior of Ex-static and Velostat is more similar, but Ex-static has a large creep variation depending on the applied pressure, see figure 2.31. At first, one could think that this effect can be neglected because the values shown

(a) Velostat variability

(b) EeonTex variability

(c) Ex-static variability
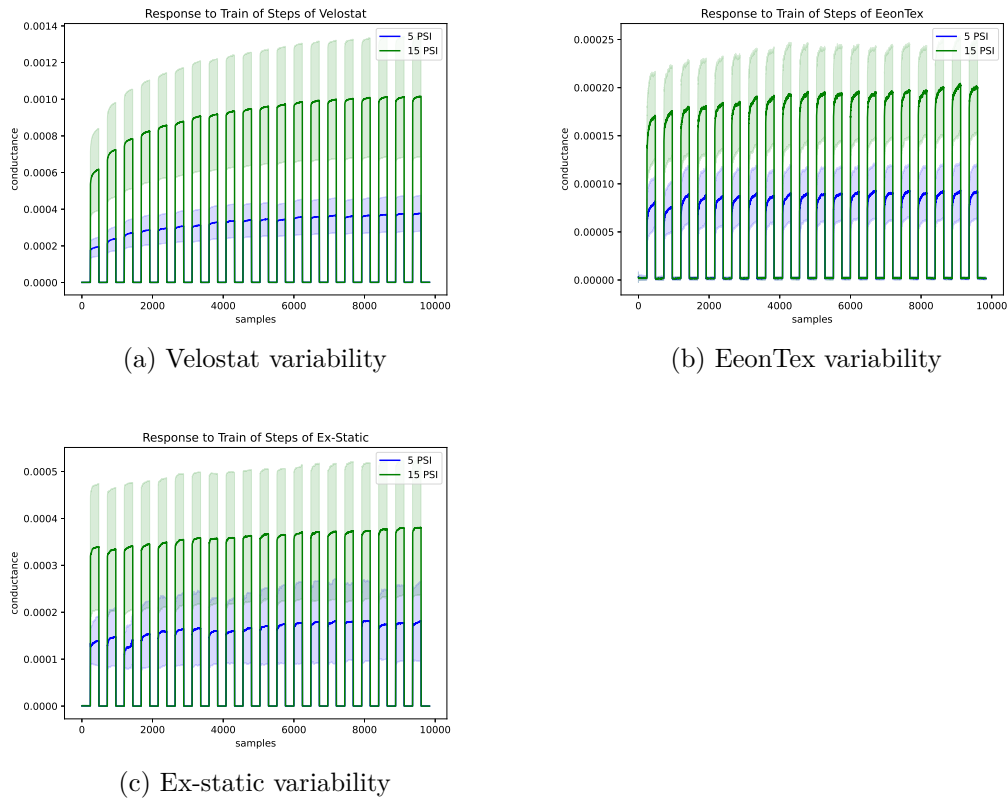
Figure 2.27: Output of fast cyclic test (lines represent average over cells, shadow part the associated SD): (**a**) Velostat; (**b**) Eeontex; (**c**) Ex-static.
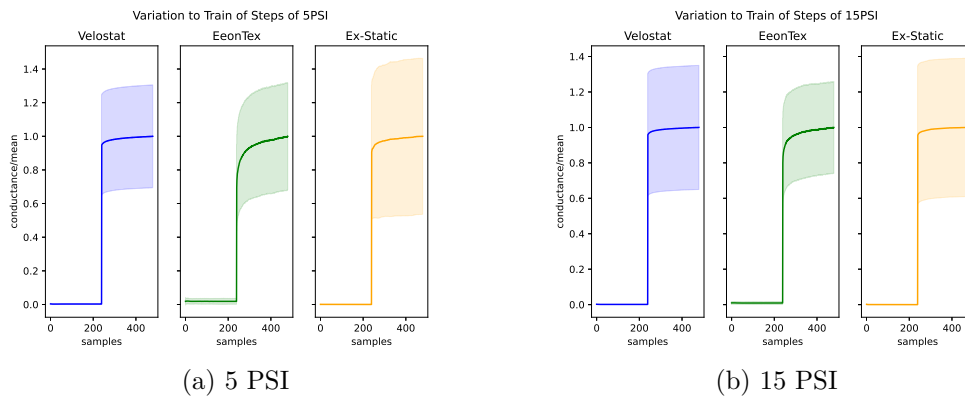
(a) 5 PSI

(b) 15 PSI

Figure 2.28: Response to step pulse. The lines show average over cells and over pulses and the shadow the associated SD: (**a**) 5 PSI; (**b**) 15 PSI.

are very low. However, it has to be taken into account that the effect is shown per second. But creep can last for hours and it can be relevant for some experiments.

The creep has also an asymmetric behavior very noticeable in Velostat. When
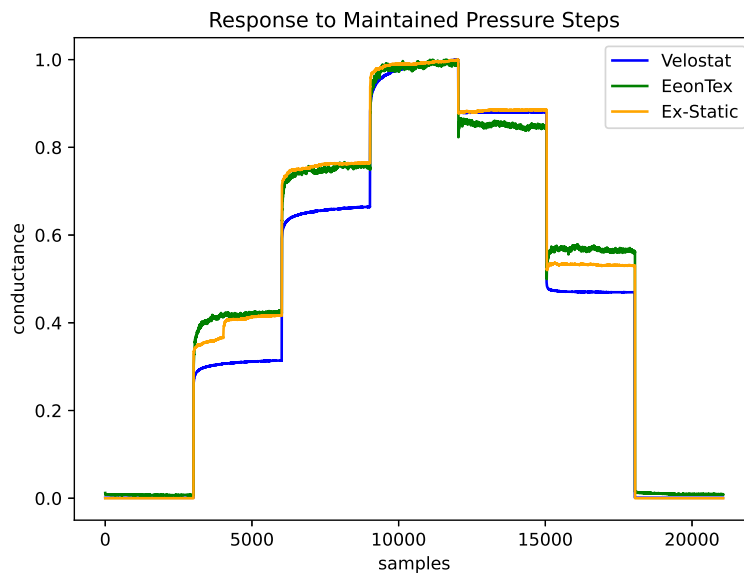
Figure 2.29: Creep response by material (averaged over cells). For comparison purposes the measurements have been normalized.
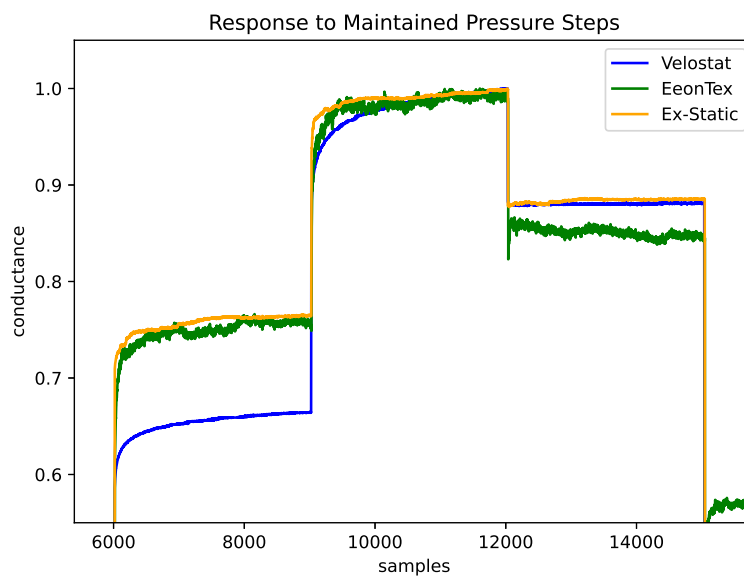
Figure 2.30: Top part of the Creep response by material (averaged over cells). For comparison purposes the measurements have been normalized.

the sensor has been subjected to a pressure and the load is decreased, creep is far lower. For instance in table 2.6 the creep values before and after 30 psi has been reached are very different, far lower in the second part of the experiment

(see values at 15 psi on the left or on the right of 30 psi in table 2.6). This has been found in the literature previously and can also be related to the fact that creep in tactile sensors can sometimes be reduced if a pre-load step is performed [53, 235].

Table 2.6: Creep values (in s⁻¹). The best value is highlighted in bold.

Pressure Material	Creep				
	2) 5 PSI	3) 15 PSI	4) 30 PSI	5) 15 PSI	6) 5 PSI
EeonTex	2.61e-05	2.85e-05	2.63e-05	2.37e-05	2.98e-05
Ex-Static	3.30e-05	**4.42e-06**	**1.30e-05**	2.17e-06	1.32e-05
Velostat	**1.76e-05**	1.45e-05	1.84e-05	**1.53e-06**	**2.37e-06**
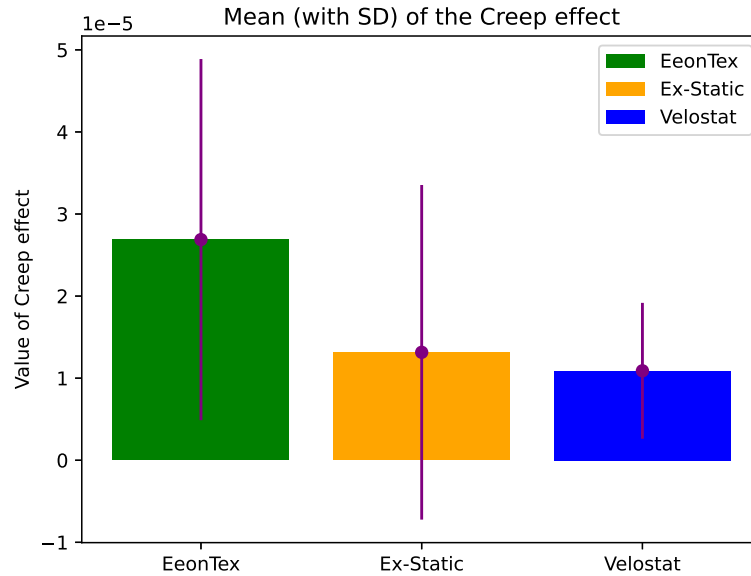
Figure 2.31: Overall effect of the creep averaged for all applied pressures and cells. Bars show the associated SD.

Concerning drift, it is also obtained from the long tests. For each value of the applied pressure, the first half part is discarded to remove short term effects that follows the change in applied pressure. Then, drift is calculated as explained in the paragraph above equation 2.2. The window size that we have taken is 30 s, which is the same window duration as in the variability experiment.

Comparing the materials, Ex-static and Velostat show much less drift than EeonTex. Overall, the best behavior with respect to drift corresponds to Velostat, see table 2.7 and figure 2.32. Even though the values are lower than 1%, for EeonTex they are noticeable even visually, shown in figure 2.30. Thus, EeonTex is the worse concerning both drift and creep.

Table 2.7: Drift values. The best value is highlighted in bold.

Pressure Material	Drift				
	2) 5 PSI	3) 15 PSI	4) 30 PSI	5) 15 PSI	6) 5 PSI
EeonTex	1.05e-02	7.31e-03	6.84e-03	6.53e-03	9.14e-03
Ex-Static	2.59e-03	1.41e-03	**8.66e-04**	9.60e-04	2.15e-03
Velostat	**1.42e-03**	**9.22e-04**	8.71e-04	**9.18e-04**	**6.70e-04**
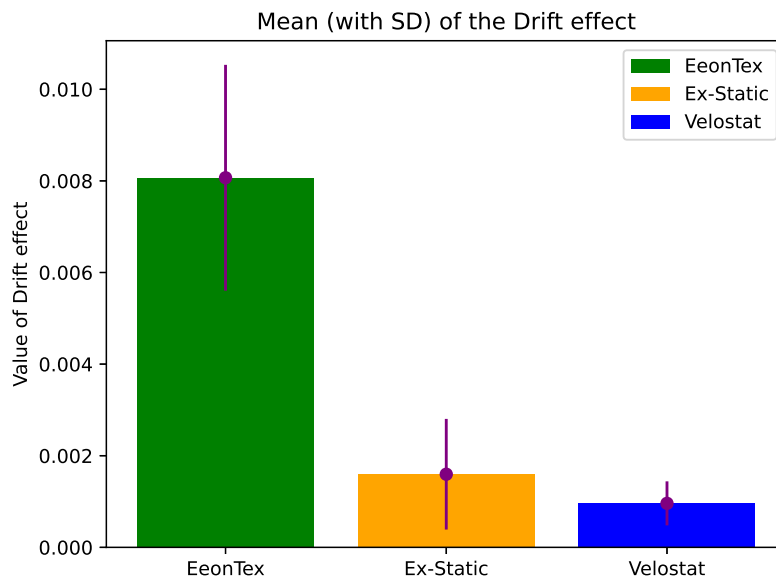
Figure 2.32: Overall effect of the drift averaged over cells and pressures. Bars show the associated SD.

With respect to hysteresis, it is visually very apparent as shown in figure 2.33. Velostat is the material that presents less hysteresis. The numerical results confirm this visual evaluation, see tables 2.8 and 2.9. In average, table 2.10, the hysteresis value of Velostat is about 33% less than the other two materials, which are very close. For the ascendant cycles and high pressures, the hysteresis values

might be very high, but this is because they are divided by a low number, see equation 2.4, so that small experimental errors may have a large impact.

Table 2.8: Hysteresis of the ascendant cycles. The best value is highlighted in bold.

Cycle Material	0) 4 PSI	1) 8 PSI	2) 12 PSI	3) 16 PSI	4) 20 PSI	5) 24 PSI	6) 28 PSI
EeonTex	0.254	0.214	0.192	0.269	0.430	0.560	0.662
Ex-Static	0.263	0.341	0.369	0.333	0.375	**0.435**	**0.550**
Velostat	**0.121**	**0.110**	**0.114**	**0.121**	**0.209**	0.469	0.785

Table 2.9: Hysteresis of the descendent cycles. The best value is highlighted in bold.

Cycle Material	0) 4 PSI	1) 8 PSI	2) 12 PSI	3) 16 PSI	4) 20 PSI	5) 24 PSI	6) 28 PSI	7) 32 PSI
EeonTex	0.170	0.201	0.213	0.204	0.200	0.189	0.188	0.187
Ex-Static	**0.075**	0.167	0.222	0.226	0.230	0.223	0.223	0.234
Velostat	0.081	**0.107**	**0.110**	**0.107**	**0.104**	**0.101**	**0.104**	**0.127**

Table 2.10: Average hysteresis of the materials. The best value is highlighted in bold.

Material	EeonTex	Ex-Static	Velostat
Hysteresis	0.276	0.284	**0.185**

A radar chart with all the non-linear effects considered has been created, see figure 2.34. In this radar chart the effect of creep has been multiplied by a time of 25 min, which is the period of the load condition in long tests. Besides, none of the experiments with volunteers in this thesis will last longer than that period. In this way all the axes are relative measures and the comparison between them is meaningful.

Hysteresis, variability and creep are the non-linear effects that affect these materials to a larger extent. These effects must be taken into account in the selection of sensitive materials, especially in the case of instrumentation devices. In an overall view of the analysis, Velostat would be our choice for the design of
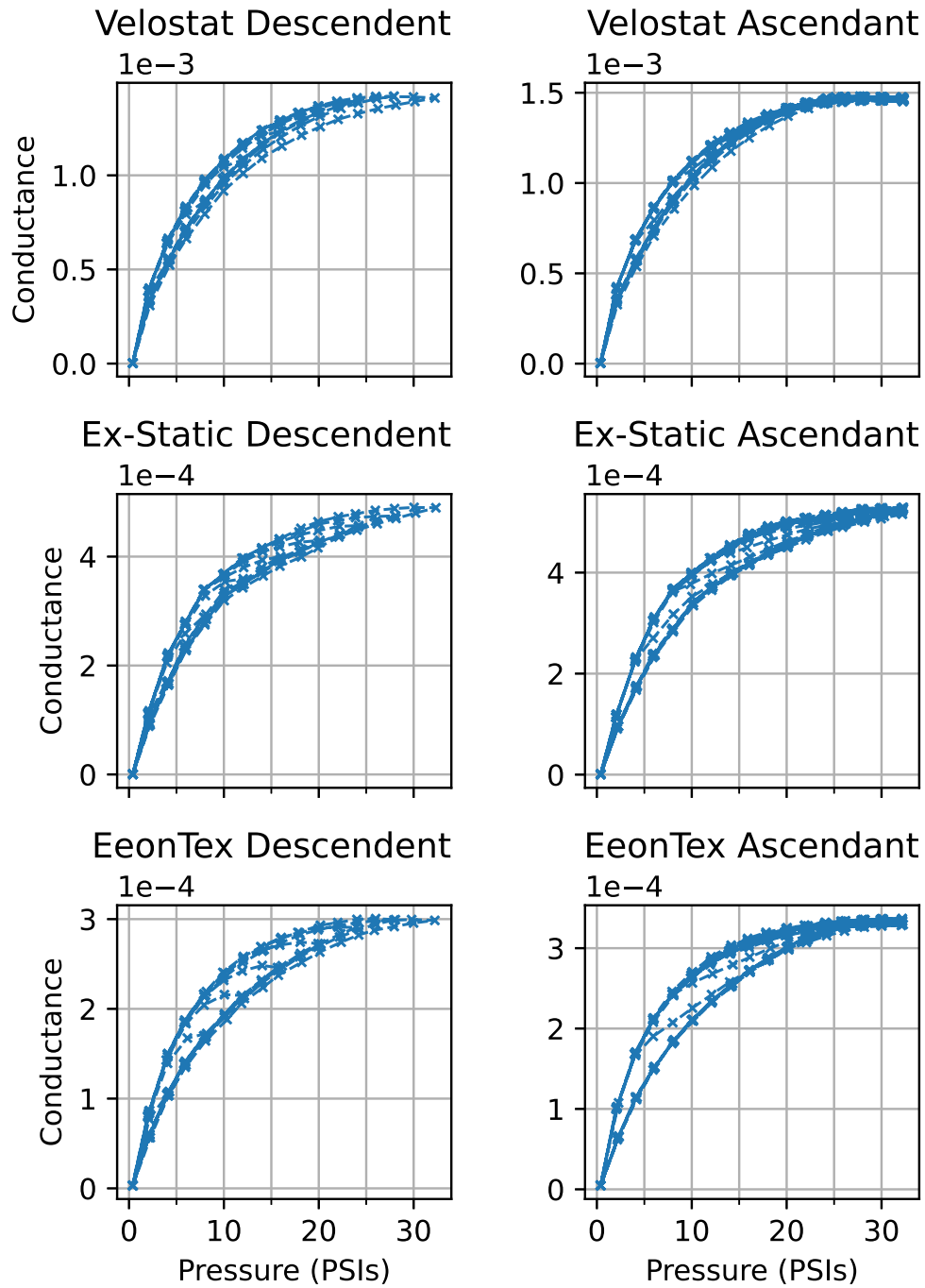
Figure 2.33: Hysteresis (averaged over cells).

PSM among the materials considered in this thesis because it has the lower value of hysteresis, creep and drift. Eeontex is the most repeatable, but it is also the most vulnerable to drift and creep. Ex-static presents a high value of hysteresis as does EeonTex, as well as a high variability.
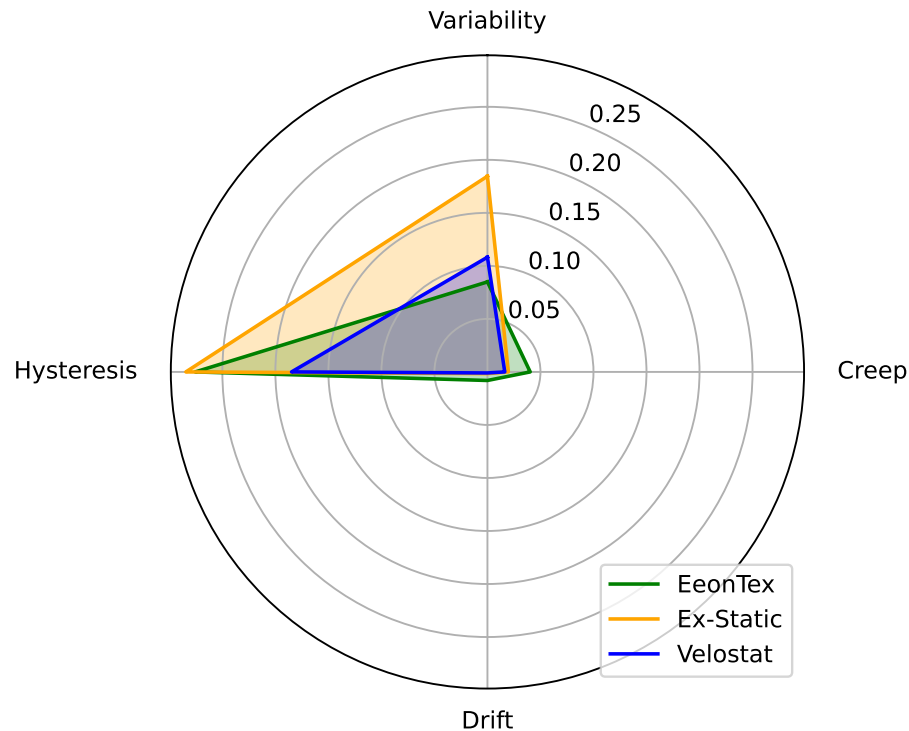
Figure 2.34: Radar chart of the considered non-linear effects in the materials

2.5 Modeling creep and hysteresis in Velostat

Modeling some non-linear effects opens the possibility of compensating for them to obtain a more accurate measurement, thus improving our previous prototypes. However, there is a rather complex mathematical machinery to model creep and hysteresis, so that a specific section is devoted to present the models and the parameters found for Velostat. The data from the hysteresis tests are used in this section because they already show a change with time (repetition), which indicates not only hysteresis but also creep.

2.5.1   Selected models

Hysteresis

In this study an MPI model [91] has been selected to fit the hysteresis in Velostat. It is a phenomenological model based on the concept of operators [90]. There are several reasons for that choice: the inverse model is analytical and the equations can be found in the literature [91]; asymmetric hysteresis is very common in piezoelectric and piezoresistive materials and this model can deal with it; finally, the number of free parameters is relatively small, which is very suitable to find them in optimization processes.

The basic concept for reproducing a hysteresis output is the play operator. In this document we consider the variant adapted for positive signals, the One-Side Play (OSP) operator. Let $p(t)$ be the input signal (pressure) for t in $[0, t_M]$. The signal is supposed to be monotone in a set of subintervals, $[t_i, t_{i+1}]$, with $0 < t_1 < t_2 < \cdots < t_M$. Then an OSP operator with threshold r provides an output, $y_r(t)$, given by the following equation:

$$y_r(0) = F_r[p](0) = f_r(p(0), 0)$$
$$y_r(t) = F_r[p](t) = f_r(p(t), y_r(t_i)) \tag{2.15}$$

for $t_i < t \le t_{i+1}$, with

$$f_r(x, y) = max(x - r, min(x, y)) \tag{2.16}$$

A weighted sum of OSP operators is taken to provide the desired sensor output with hysteresis, g_h (conductance). Moreover, a polynomial term is added to model asymmetric hysteresis:

$$g_h(t) = a_1 \, p(t) + a_2 \, p^2(t) + a_3 p^3(t) + \sum_{i=1}^{N} b_i F_{r_i}[p](t) \tag{2.17}$$

The authors of the original paper [91] considered only odd polynomials. However, the fit quality without the second order term was clearly worse with our data, so that we have decided to include it.

The number of OSP operators has been set to $N = 6$ with equally distributed thresholds defined as $r_i = (i-1)/N$ (assuming that the input is normalized). This

or similar numbers are typical in previous studies. To reduce the parameters of the model, the weights are not independent but follow an equation that is also found in the literature [197]:

$$b_i = \rho\, e^{(-\tau\, r_i)} \tag{2.18}$$

where ρ and τ are the two parameters that define the exponential decreasing function.

In order to define the inverse of an MPI model, it is convenient to divide the output into two addends [91]:

$$g_h(t) = P[p](t) + F[p](t) \tag{2.19}$$

where $P[p](t) = a_2\, p^2(t) + a_3 p^3(t)$ and $F[p](t) = a_1\, p(t) + \sum_{i=1}^{N} b_i F_{r_i}[p](t)$. In this way, $F[p](t)$ includes both the linear term and the hysteresis.

A key property is that the inverse of $F[p](t)$ is also an MPI model [91]:

$$F^{-1}[u](t) = \hat{a}_1\, u(t) + \sum_{j=1}^{N} \hat{b}_j F_{\hat{r}_j}[u](t) \tag{2.20}$$

where:

$$\hat{a}_1 = \frac{1}{a_1}$$

$$\hat{b}_j = -\frac{b_j}{\left(a_1 + \sum_{i=1}^{j-1} b_i\right)\left(a_1 + \sum_{i=1}^{j} b_i\right)}$$

$$\hat{r}_j = a_1\, r_j + \sum_{i=1}^{j-1} b_i(r_j - r_i) \tag{2.21}$$

Figure 2.35 presents the flow chart that can be applied to compute the total inverse model [91]. Therefore, $p(t)$ can be calculated from $g_h(t)$ with the following equations that are computed at each time step:

$$u(t) = g_h(t) - P[p](t) = g_h(t) - (a_2\, p^2(t) + a_3\, p^3(t))$$

$$p(t) = F^{-1}[u](t) \tag{2.22}$$
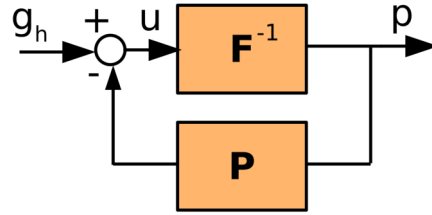
Figure 2.35: Signal flow chart of the inverse hysteresis operation.

Creep

Modeling creep is also based on the idea of operators. A single creep operator is equivalent to a first order system [90, 190] and the total creep can be represented as a weighted sum of creep operators [109, 155, 208].

More specifically each creep operator is associated to a parameter l_i in such a way that the output at time $t_k = k\,T$ is established as:

$$y_{c,i}(t_k) = e^{-l_i\,T} y_{c,i}(t_{k-1}) + (1 - e^{-l_i\,T}) p(t_{k-1}) \tag{2.23}$$

where T is the sampling period.

$C[p](t)$, the total creep, is calculated using the following equation:

$$g_c(t_k) = C[p](t_k) = \sum_{i=1}^{N_c} w_i\, y_{c,i}(t_k) \tag{2.24}$$

where w_i are the weights and N_c the number of creep operators.

In this study two creep operators have been used. The number has been found by trial and error, being slightly better than using a single creep operator or more than two. Increasing their number did not improve the fit and it is not recommended to augment unnecessarily the model complexity. Besides, many creep models include a constant term proportional to the input. In our case it is already included in the linear term of the hysteresis model. Anyway, it could be considered as a creep operator in the limit $l_i \to \infty$.

Joint Creep and Hysteresis Modeling

The direct joint model is graphically represented in figure 2.36a. The direct model is obtained as the sum of hysteresis and creep [155], i.e., the output is obtained by adding equations 2.17 and 2.24. On the other hand, the same concepts considered

in figure 2.35 can be applied in the inverse of the joint model, shown in figure 2.36b. From a formal point of view, the output is still computed as $p(t) = F^{-1}[u](t)$, where $F^{-1}[u](t)$ has been defined in equation 2.20. The difference with the inverse model of the hysteresis is that the creep has to be subtracted as well to compute $u(t)$, as follows:

$$u(t) = g(t) - P[p](t) - C[p](t) \tag{2.25}$$

where $P[p](t)$ has been defined in equation 2.19, and $C[p](t)$ has been defined in equation 2.24.

Thus, the inverse model can be used to recover the applied pressure, $p(t)$, from the measured conductance, $g(t)$.
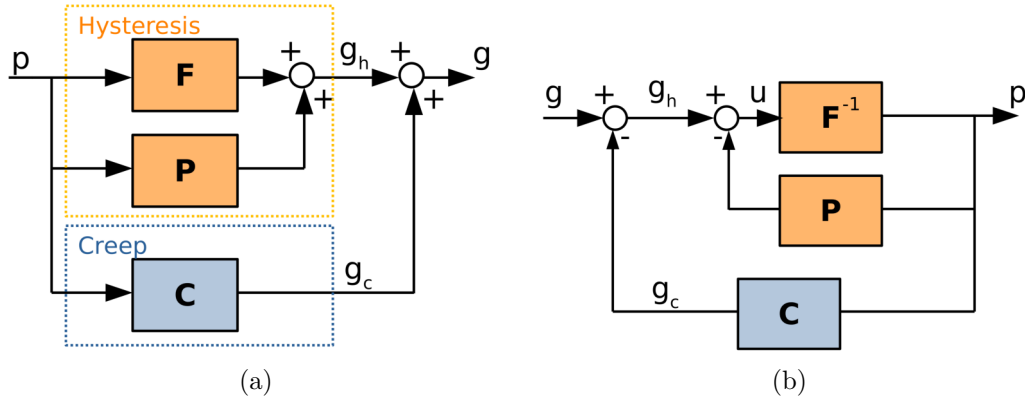
Figure 2.36: a) Signal flow chart of the joint hysteresis and creep model and b) its inverse.

Parameter identification

Summing up, the joint model requires a set of parameters: ρ, τ, a_1, a_2, a_3, l_i and w_i. Identifying them can be stated as a minimization problem with constraints in a relatively large dimensional space. The cost function is related to the typical sum of squares error. Let p_t be a temporal series of pressures and $g_{exp,t}$ the associated conductance of the sensor measured in the experiment. If the model predicts an output $g_{m,t}$, the cost function to be minimized is denoted as SSE_N and defined as:

$$SSE_N = \frac{\sum\limits_{t=1}^{N_t} (g_{exp,t} - g_{m,t})^2}{N_t} \tag{2.26}$$

where N_t is the number of points in the temporal series, which for convenience is dividing the sum of squares error.

In our case, there are two kinds of experiments, descendent and ascendant hysteresis cycles. They can be considered as independent because there was a long period of unload condition between them, around 11 days. Thus, in fact the average of SSE_N over the two kinds of experiments has been considered as a target function.

Finding the parameters is not an easy task. It is typical to use some stochastic search algorithm. Thus, in this paper we have adopted a simulated-annealing algorithm [185] for searching the parameter space. Some trials were done with other more refined strategies for optimization, but the results of the classical simulated-annealing were far better. Therefore, only the best parameters found with it are presented and the issue of improving the search will be considered for future studies.

2.5.2 Results and discussion

Model optimization results are shown in figures 2.37 and 2.38: the former presents the descendent hysteresis cycles, the latter presents the ascendant hysteresis cycles. The applied pressure pattern was repeated ten times in each kind of experiment. It is apparent from the figures that the sensor hysteresis cycles change over time, i.e., as a function of the repetition. Therefore, the model has to include such a dependence. The creep model introduced in section 2.5.1 is the way to give a trend in the output as shown in figures 2.37b and 2.38b. Two of the repetitions of the pressure pattern are also shown to observe the model fit with some detail.

The quality of the model fit is variable. The first repetition is rather bad in both descendent and ascendant cycles, see figures 2.37c and 2.38c. The fit quality is better for the next repetitions, shown in figures 2.37d and 2.38d although in the last repetitions of the ascendant cycles, see figure 2.38b, the fit is not very good again (and in fact the conductance seems to decrease globally).

The irregular fit quality is also apparent if the inverse model is applied. The ultimate goal of modeling the sensor output would be to recover the true pressure from the measurements, as seen in figure 2.39, in which the applied pressure and the pressure recovered from the conductance is shown (descendent experiment). The general view in figure 2.39a reveals a bad prediction for the first repetition. The next repetitions seem to be predicted with a far better accuracy, see figures
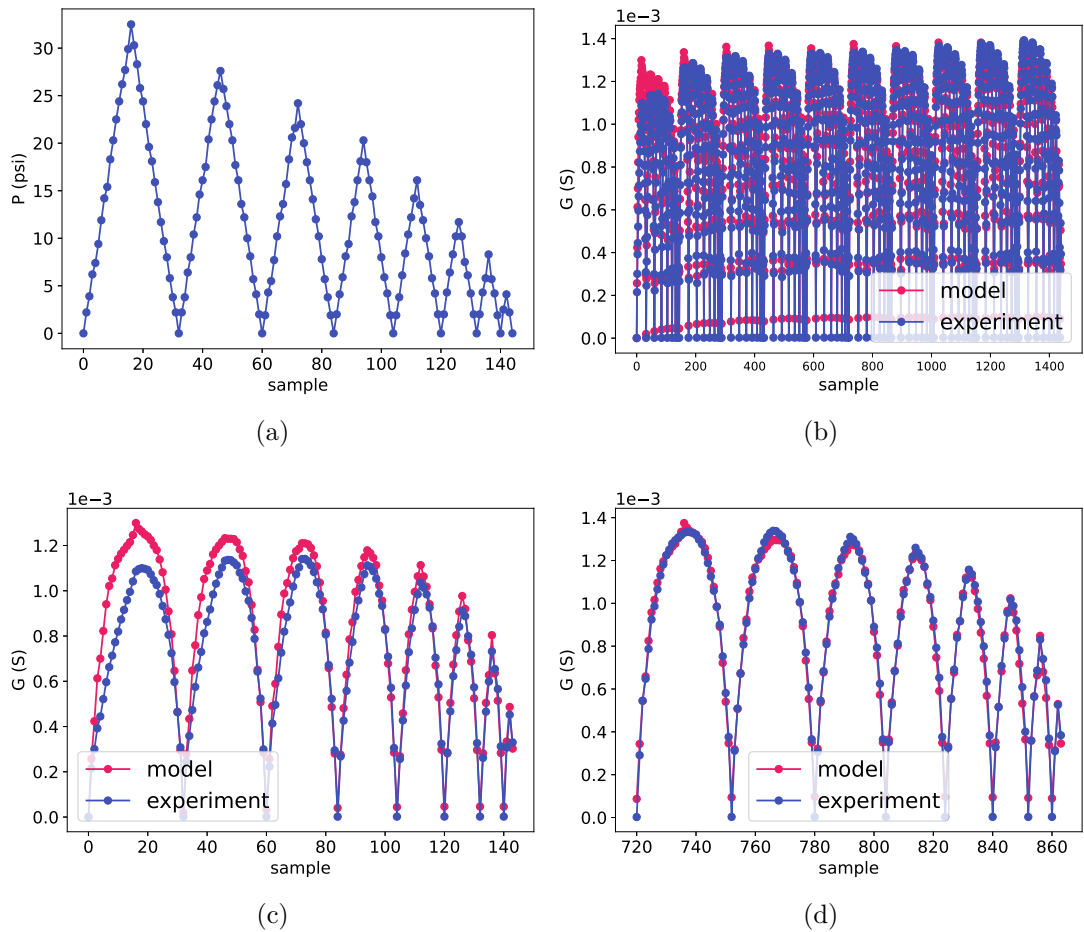
Figure 2.37: Descendent hysteresis cycles: a) Applied pressure pattern (one repetition); b) General view of the output in the ten repetitions; c) First repetition d) Sixth repetition.

2.39c and 2.39d. The higher deviations of the curve shapes are associated to higher pressures.

The model parameters are shown in table 2.11.

2.6 Conclusions

In this chapter, the advances in our prototype have been described. The improved prototypes could be easily manufactured for mass production with a reduced manual work required. They can be scanned at frequencies higher than 100 Hz, which can be required in many applications. To achieve this high sampling frequency, the µC configuration had to be fine tuned and a binary data transmission had to
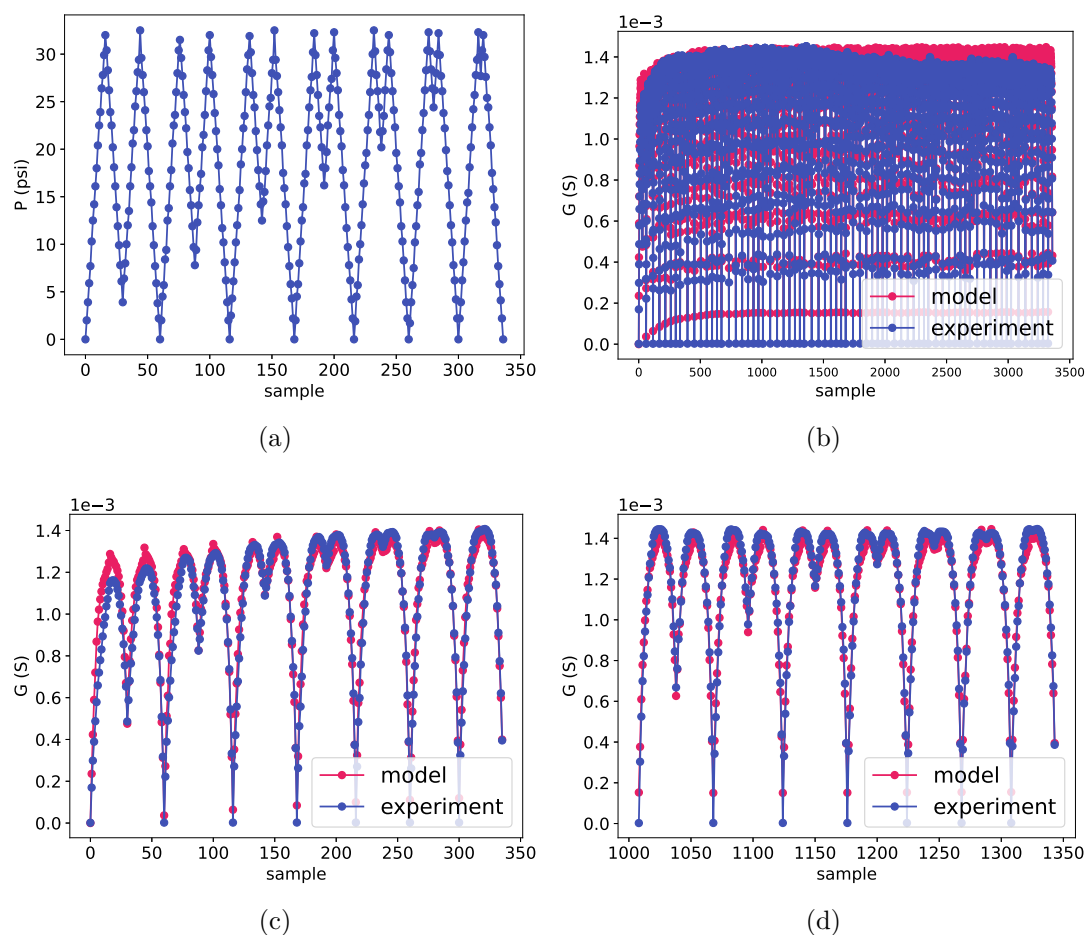
Figure 2.38: Ascendant hysteresis cycles: a) Applied pressure pattern (one repetition); b) General view of the output in the ten repetitions; c) First repetition d) Fourth repetition.

be devised, changing also from Bluetooth to USB.

On the computer side, the crosstalk removal algorithm can now operate in real time thanks to a parallelized C implementation. Besides, equations to estimate the uncertainty in the measured cell conductances after running this algorithm have been developed and the uncertainty can be estimated in our PSM. The result is reasonable and the higher resistances in the array can not be recovered reliably, but this is not a problem in our applications because they correspond to very low pressures. Besides, it has been proven that the principles in which IECM is based can be applied to other DAQ circuits commonly found in the literature, like the QZPM, in which it can be applied to find not only cell resistances but also switch resistances (ideally zero), see appendix C. This opens a new line of
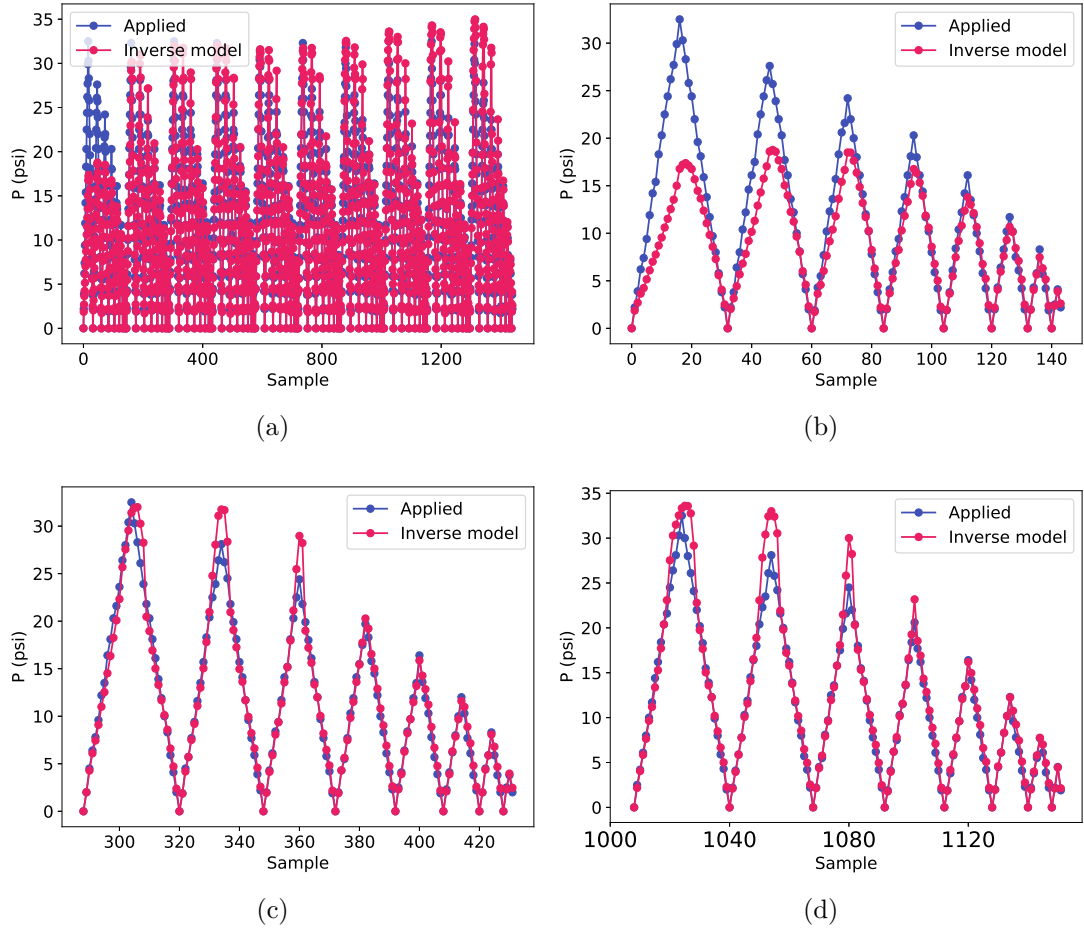
Figure 2.39: Applied pressure and recovered pressure using the inverse model: a) General view; b), c) and d) first, third and eighth repetition respectively.

Table 2.11: Model parameters.

Parameter	Value	Unit
ρ	$1.64e-4$	S/psi
τ	0.269	psi^{-1}
a_1	$1.01e-4$	S/psi
a_2	$-5.32e-6$	S/psi^2
a_3	$7.37e-8$	S/psi^3
l_1	$8.25e-4$	s^{-1}
l_2	$5.26e-6$	s^{-1}
w_1	$8.42e-6$	S/psi
w_2	$1.90e-6$	S/psi
SSE_N	$2.74e-9$	S^2

research.

Finally, a very complete characterization of the sensor output for three materials has been presented. Up to our knowledge, no previous study has performed such a deep analysis of three low cost piezoresistive materials, Velostat being one of them. This material is very common in previous research. It is shown that it presents less non-linear effects than the other two candidates analyzed. Besides, a model of hysteresis and creep in Velostat has been found, which is also a novelty of this thesis. It captures several characteristics of the sensor response, but there is still room for improvement because the hysteresis cycles change a lot from the first to the last repetition for repetitive tests, while the model fit is far better in the intermediate ones. Theoretically, this model can be used to recover pressure with a higher accuracy. However, the model has been found for a small sized array due to the space limitations of the pneumatic device, and its application to a real case in which the PSM prototypes are used deserves further comments as it will be explained in detail in chapter 3.

Chapter 3

Testing human balance: Center of Pressure measurements

ESTING balance is very common in clinical practice. Thus, providing objective measurements of balancing abilities is of great importance to complement subjective functional tests or questionnaires. This document is focused on quantifying postural control in static upright stance. In particular, the CoP displacement is a widely accepted quantitative measure in this kind of tests. The reference instrument for CoP measurement is the FP.

However, FP are usually bulky, heavy and expensive (typical FPs cost thousands of euros, the most affordable ones cost just under a thousand euros). Therefore, research has been conducted to find alternatives to characterize postural control in standing position. A PSM is also an option to determine stability. Besides, the problem of determining accurately CoP displacements using low cost piezoresistive materials is a research challenge because overcoming their limitations is not an easy task. Studies on low cost PSMs are worth to be carried out because they have multiple advantages. They are affordable instruments with a reduced complexity in the manufacturing process. Thus, they would be available for many research teams and medical centers. Moreover, they are flexible, lightweight and transport-friendly, which allows their use in irregular surfaces like seats, backrests, and beds.

This chapter is divided into several sections. In section 3.1 the state of the art is presented, indicating a brief reference to the use of CoP and FP in health research, as well as a review of the main results of previous studies that used PSMs to characterize stability. Section 3.2 presents the experimental protocol,

the data processing performed and the system evaluation. Two series of experiments were performed with different prototypes. The experiments are similar, but some relevant differences are highlighted. The data processing methods are also different because the hysteresis and creep compensation has been only performed in the second set of experiments and the second prototype allowed recovering a smoother CoP trajectory. Section 3.3 presents the results and discussion, and section 3.4 the conclusions of this chapter.

3.1   State of the art

The CoP is the projection of the body center of gravity to the ground [222], and the time displacement of this projection is its trajectory. It is conventionally measured using an FP [192]. Therefore, this device is found in many studies concerning a wide range of populations and applications: older people [66, 131, 171, 182], infants [68], diabetic subjects [146], children with cerebral palsy [42], or athletes [41].

FPs measure ground reaction forces [41]. The most basic FP would contain a single sensor force, and give a single measurement. However, most FP include several sensors in different orientations [3, 23, 117]. These sensors are usually located at each corner of the rectangular shape. This enables obtaining 3D information. Moreover, the CoP and the moment around each of the axes can also be obtained. Most common sensor technologies are load cells and piezoelectric sensors, although load cells are likely to be the most robust and spread.

A PSM is also an option to determine stability. A PSM intends to cover relatively large areas allowing the pressure to be measured on seats, beds, or on the floor. Several studies have compared commercial PSMs with FPs. In [32] an AMTI® FP and a commercial plantar pressure system (Tekscan® Strideway Plantar Pressure Mat) were used in quiet standing deadlift trials with eight different weighting conditions. The ground reaction force from the two instruments was recorded. The differences were not statistically significant and the correlation was high ($r = 0.959$) although a small size effect was found. In [85] CoP measurements obtained from MatScan® PSM and AMTI® AccuSway FP were compared in single-legged balance trials with both eyes closed and open. Healthy volunteers participated in the experiment. Several CoP parameters were analyzed: Anterior-Posterior (A-P) and Medial-Lateral (M-L) excursions, total

distance, and area. The correlation was good both considering the parameters themselves ($r > 0.92$) but also considering the differences between eyes open and eyes closed conditions ($r > 0.85$). Moreover, both devices detected large effect sizes between those conditions. However, Bland-Altmann plots revealed a smaller spread of the CoP trajectory measured by the PSM and most of these differences were statistically significant. These differences increased with the displacement of the CoP. For instance, the CoP excursions showed differences ranging from 0.14 cm to 0.42 cm depending on the trial. In [166] the authors compared a commercial pressure sensor, (Nitta C-scan12S), and an FP (Model OR6-5-1000, AMTI®) in quiet standing (eyes open and closed) with healthy subjects. Several parameters of the CoP trajectory were extracted: root mean square, standard deviations along M-L and A-P directions, area of 95% confidence ellipse, mean velocity, total power of the power spectrum density and frequencies containing 50% and 95% of the power (in both directions), and 2D histograms. The Concordance Correlation Coefficient (CCC) ranged from 0.036 to 0.607 depending on the parameter. The authors concluded that the sway amplitudes for the PSM were slightly smaller than those of the FP. In a particular case shown, the values for the standard deviation of the CoP trajectory along the M-L direction were 1.49 and 1.98 mm respectively, while for the A-P direction they were 2.18 and 3.10 mm respectively. Differences between the two instruments were reduced with a postprocessing of CoP signals. A transfer function was found to bring CoP trajectories of the PSM close to those of the FP. It was obtained numerically in the frequency domain. The characteristics of the relation between the CoP trajectory in both devices were rather independent of the subject, sway direction and visual condition. This indicated that a unique filter could be used. After correcting PSM CoP trajectories using the filter, the CCCs were always higher than 0.9. In [42] a Tekscan® HR Mat and an AMTI® FP were used to assess standing balance in typical children and in children with cerebral palsy. The CoP path was analyzed with 21 parameters. Correlation between instruments ranged from 0.509 to 0.992 depending on the parameters and children group. However, statistical differences between them were found in 18 and 16 parameters for typical and cerebral palsy groups respectively. The maximal excursion of the CoP were higher for the FP except for the M-L direction in children with cerebral palsy, in which the average was the same (up to 0.01mm differences). Despite the differences between the instruments, PSM preserved discrimination ability: using a logistic regression 11

out of the 21 parameters were found to significantly predict group membership, although the number increases to 15 if measures from FP were used.

In an overall view of previous comparisons between FPs and PSMs, the studies found a moderate to strong correlation between the instruments for some CoP parameters. However, there are several studies that reveal that PSMs measure a lower spread of the trajectory. Tested PSMs belong mostly to Tekscan®. Thus, they are high end equipments from a leader company. The sample frequency is at least 50 Hz and the resolution is $0.968\,sensels/cm^2$ in the worst case. The evaluation is performed using mainly correlation, although some statistical parameters are sometimes provided. The studies do not compare the CoP itself, but some parameters extracted from it, which are conventionally used in health research [181]. Moreover, only one study tried to mitigate the differences between the instruments. The authors found a filter that related CoP coordinates coming from the two instruments.

In the next section, the experiments developed with our prototypes are presented. The prototypes are low-cost equipment, thus very different from the ones utilized in previous studies. Their resolution is low compared with them ($0.25\,sensels/cm^2$), and the first prototype achieves only a very limited sampling frequency, 10 Hz. A preliminary evaluation of the first prototype was published in [148] from which some excerpts have been taken.

3.2   Measurement protocol, data processing and evaluation

3.2.1   First prototype

In this experiment, our prototype 3D_Velo3_Blue (table 2.3) was compared with a commercial FP and a commercial PSM. The FP was a PS-2141 PASPORT by Pasco [20]. Its measurement range is -1100 N to 4400 N and its resolution is 0.1 N. The FP allows sampling rates up to 2 kHz depending on the interface device. For this study, the measurements were registered at 10 Hz for compatibility with the PSMs. The software provided by the manufacturer allows retrieving CoP trajectory data directly in a file that is transferred via USB. Besides, the commercial Seating Mat from Sensing Tex was tested [22]. According to the documentation, the pressure sensitivity is obtained through a combination of electronic inks and

pastes which are stretchable, elastic and can be printed on materials with special surface preparations. The mat size and number of spots of this product are the same as in our prototype. Each sensitive spot has a diameter of 10 mm and each frame of the PSM was acquired at a frequency of 10 Hz. The conductance versus pressure curve of each sensor follows well a linear dependence. This commercial product is more affordable than many of its competitors. The software provided by the manufacturer was used to acquire, via Bluetooth, the raw data. Then we followed the documentation guidelines to transform them to conductance. Crosstalk effect also appears in Seating Mat and the software includes a compensation option for it.

The PSMs were laid, overlapping, on the FP (shown in figure 3.1). The vertical order of the PSMs was randomly selected for each volunteer (in fact, we checked that there were no significant differences in the PSM output for the two possible positions). The systems were tested with humans to obtain the same kind of pressure images and irregular shapes of feet [150, 191] as in balance studies, which would be the ultimate target application, although in this preliminary study we have only considered healthy subjects. Each participant performed the following eyes-open and barefoot trials on the platforms, with each of these tests performed once per participant:

- Trial single-legged, right leg (Right Leg for short): Volunteers started the trial in single-legged quiet standing (flamingo posture, right leg). Then, they had to control their balance.

- Trial single-legged, left leg (Left Leg for short): The previous trial was repeated, this time controlling their balance on the other leg.

- Trial two-legged with trunk movements (Rotation for short): In the last trial volunteers started in two-legged quiet standing and then swayed while describing circles seen from above. Movements were performed slowly (about half cycle per second).

A chair was placed close to the instruments to allow volunteers to lean on its backrest momentarily if balance was about to be lost. In this way, all the volunteers carried out the tests successfully, remaining single-legged throughout the entire tests. Forty two volunteers participated in the experiment (29 men, 13 women), table 3.1.

Figure 3.1: Experimental set-up with the commercial systems and our prototype, first set of experiments [148].

Table 3.1: Overall characteristics of the participant in the first experiments given as mean (SD) [148].

	Men	Women	Total
No.	29	13	42
Height (m)	1.78 (0.07)	1.64 (0.06)	1.74 (0.09)
Weight (kg)	81.36 (14.21)	58.54 (7.21)	74.30 (16.34)
Age (years)	33.55 (12.47)	26.00 (11.91)	31.21 (12.66)

We selected single-legged trials because they are very common [85, 204]. Besides, as the selected volunteers are healthy, tests involving some difficulty should be performed in order to obtain some relevant variations between subjects and noticeable CoP excursions. Concerning the *Rotation* test, trunk movements are also typical in stability studies [66]. This movement allowed checking the differences between the two instruments for larger CoP displacements.

Each trial lasted 60 s and the three instruments acquired the data simultaneously. However, the instruments were started independently and the signals had to be aligned in a post-processing step. To fully synchronize the signals coming from different instruments, we used the cross-correlation between them. This quantity is supposed to be maximal when the signals are fully aligned. Thus, the cross-correlations of the Cartesian components of the CoP were obtained and the signals were aligned to maximize them. Anyway, the signals were displayed and the initial time was corrected manually when required.

Table 3.2: Models used for our prototype PSM in the first set of experiments. The force platform is included for completeness.

Short name	Comment
FP	Force platform PS-2141, 10 Hz sampling frequency.
PROP	Base model. Crosstalk is removed using IECM. Then, conductance and pressure are supposed to be proportional.
PROP-C	As PROP model but crosstalk is not removed.
PROP-8x8	Reduced resolution. Select only one out of two rows and columns of the original sensor matrix. Then use PROP model.

In this experiment, it was assumed the Conductance versus pressure proportional model (PROP), i.e, conductance and pressure are supposed to be proportional. In addition, some variants of the basic processing for *3D_Velos3_Blue* were performed to study the effect of several limitations of the prototype, see table 3.2. FP is included for completeness. They are explained in the next paragraphs.

Although the elimination of the crosstalk is visually beneficial, it could not be done in real time at the beginning of this PhD period and required an annoying post-processing step. Therefore, we aimed to know whether or not it was relevant for the CoP. For that purpose, the role of the crosstalk elimination was studied by repeating the analysis with the raw values of conductance without further processing. This model is like PROP but without removing crosstalk (PROP-C).

Another aspect to be considered is the resolution of our PSM. We emulated an experiment with an 8x8 mat by selecting only one out of two rows and columns of the original sensor matrix. The results corresponding to this variant are labeled as PROP-8x8. In fact, there are four options: a) Selecting columns $1, 3, 5, \ldots$ and rows $1, 3, 5, \ldots$; b) Selecting columns $1, 3, 5, \ldots$ and rows $2, 4, 6, \ldots$; c) Selecting columns $2, 4, 6, \ldots$ and rows $1, 3, 5, \ldots$; d) Selecting columns $2, 4, 6, \ldots$ and rows $2, 4, 6, \ldots$. The average result of these options is the value shown for PROP-8x8.

Regarding performance, it was evaluated considering two set of parameters. On the one hand, we followed an approach that is commonly used in the literature, i.e., extracting some parameters of the CoP trajectory and then comparing them with those obtained from the FP. More specifically, the standard deviation of the

M-L components of the CoP path, σ_{ML}, and the standard deviation of the A-P components of the CoP path, σ_{AP}, were extracted. Thus, one value of σ_{ML} and one value of σ_{AP} were obtained for each subject, trial performed and instrument. These values are the base for the device comparison. Analyzing the displacements on each axis is very common. In particular, the standard deviation is a typical parameter of the CoP spread [57]. It is simple to calculate and less sensitive to low sampling frequency or to outliers than the maximum range for instance. Therefore, it is suitable for the current study of our first prototype. Besides, it has been used in many previous works [68, 166, 237] and shows good discrimination ability in different groups and pathology subjects [57].

Then, the Pearson's correlation coefficient between the CoP parameters obtained from PSM and FP, r, was calculated. This allows us to compare them with previous studies. However, this coefficient is not very helpful in many situations. For instance, two signals may present a bias between them and yet the correlation can be perfect. In other situation, the two signals may show no bias but can be related by some "gain" factor $\neq 1$. In this case the correlation would be perfect but the instrument outputs are not the same clearly.

Therefore, we have also calculated a figure of merit for the CoP trajectory itself. We have not found it in previous studies, probably because they are focused on clinical research and the trajectory is not used directly. However, we think that the primary outcome of the instrument in balance tests is the CoP path. From a technical point of view, the trajectories derived from a PSM and a FP should be compared. If both trajectories become closer using some processing or modeling, then it is reasonable to expect that any parameter obtained from them will be more similar too.

Thus, given two trajectories, the distance between each pair of points in the $x - y$ plane was considered, d_i, and then we calculated the Lock-step Euclidean Distance (LSED) [213], which it is further divided by the number of points in the trajectory, N_{CoP}, for convenience. The result is called Eu:

$$Eu = \frac{\sqrt{\sum_{i=1}^{N_{CoP}} d_i^2}}{N_{CoP}} \tag{3.1}$$

For a specific discussion concerning the resolution of the PSM, Eu by direction will be considered:

$$Eu_{ML} = \frac{\sqrt{\sum\limits_{i=1}^{N_{CoP}} (x_{FP,i} - x_{PSM,i})^2}}{N_{CoP}}$$

$$Eu_{AP} = \frac{\sqrt{\sum\limits_{i=1}^{N_{CoP}} (y_{FP,i} - y_{PSM,i})^2}}{N_{CoP}} \tag{3.2}$$

where x and y are the coordinates in the M-L and A-P directions respectively and the index FP or PSM refer to the force platform or the mat, respectively.

3.2.2 Second prototype

The protocol was very similar to the one explained in the previous section but with some differences. In this case the commercial PSM, Sensing Mat, was not included because the analysis of the first set of experiments already revealed a worse performance. Thus, only our prototype was on top of the FP during the experiments (prototype Kdigit_Velo_100, 100 Hz sampling frequency, table 2.3).

The volunteers performed three kinds of trials, each performed once, as in the first experiment. The experiments lasted only 30 s, plus a few seconds to start the acquisition programs and step on the instruments. The duration is lower than in the previous experiments because 1 min was sometimes uncomfortable for some people. In this case four male volunteers performed the balance tests. The overall characteristics of the volunteers can be seen in table 3.3.

Table 3.3: Overall characteristics of the participant in the second set of experiments

	Mean	SD
Height (m)	1.75	0.04
Weight (kg)	72.75	10.90
Age (years)	33.75	11.92

The signals from the two devices had a unavoidable delay. The cross-correlation was again used to align them. Anyway, the signals were displayed to check the alignment and a 30 s window extracted for further processing.

The pressure was obtained by applying the inverse model found using the tests

in the pneumatic platform as shown in section 2.5. However, a direct application
of the model has some difficulties that are worth explaining. The PSM size avoids
testing it in the pneumatic platform. This is why a reduced sensor array was built
for the pneumatic system[1]. Thus, the model parameters have been found for a
different array. Despite being manufactured with the same material and electrode
shape, the sensor outputs have a large variability. Even applying the same average
model for all the cells in the small-sized array used in the pneumatic device is
somehow risky. It is typical to perform some equilibration process or even to find
individual models for each cell [152, 196], which is not possible in our case. This
raises the question of the suitability of the given model for the PSM. To overcome
this problem, we propose a heuristic scaling factor for the stability experiments in
which a volunteer stands on the large PSM. Let $p = M(g)$ be the generic model
that relates conductance to pressure. Then the conductance is scaled by a factor
f in such a way that the following equation is fulfilled:

$$\sum_{i=1}^{16} \sum_{j=1}^{16} M(f \cdot g_{i,j}) \cdot A = W \tag{3.3}$$

where $g_{i,j}$ is the conductance measured for each cell, A is the cell area $(4\,cm^2)$,
and W is the weight of the subject performing the experiment.

In fact, the average of the above equation was taken during the 30 s experi-
ment duration. The factor f was found using a brute force search in the interval
$[0.25, 0.75]$. As can be deduced from the extreme values of the interval, the con-
ductance of the PSM was larger than expected considering the outcome obtained
in the experiments with the pneumatic device. If the factor is not introduced,
the model gives pressures that are likely to be unrealistic.

Several model variants are considered in section 3.3 to check the improvement
associated to increasing model complexity. They are presented in table 3.4 for
the sake of clarity. FP is also included for completeness. Concerning the PSM,
results from a naive approach that assumes that conductance is proportional to
pressure will be shown (PROP for short). This assumption is sometimes used
in the literature and gives a reasonable similarity between the shape of the CoP
trajectories derived from PSM and FP, as we checked ourselves with the first
prototype. Besides, two models that compensate hysteresis and creep without

---

[1]The collaboration with the University of Malaga started after the beginning of the PhD
and after the manufacturing of the second prototype and the experimental work with it. It is
reasonable to think of a future PSM that could fit into the pneumatic platform.

Table 3.4: Models used for our prototype PSM in the second set of experiments. The force platform is included for completeness.

Short name	Comment
FP	Force Platform PS-2141. The reference instrument in balance tests. 100 Hz sampling frequency.
PROP	Proportional model. Pressure and conductance are assumed to be proportional in PSM. Crosstalk is first removed using IECM.
CHC	Creep and Hysteresis Compensation model for PSM. Crosstalk is first removed using IECM. Then, the joint model explained in section 2.5 is applied for compensation. No scaling is performed.
SCHC	Scaled Creep and Hysteresis Compensation model for PSM. As CHC but introducing a scaling factor, equation 3.3
SCHC-8x8	Scaled Creep and Hysteresis Compensation model for PSM with an emulated 8x8 resolution (average of all the 8x8 options is taken).

and with scaling factor, Creep and Hysteresis Compensation (CHC) and Scaled CHC (SCHC) respectively will be considered to check the effect of the heuristic scaling, equation 3.3. Then, the issue of resolution is going to be considered, model SCHC-8x8. An 8x8 version of the mat is considered by selecting one out of two rows and columns of the original matrix, as explained for the experiments with the first prototype, section 3.2.

In the second set of experiments we have considered the same evaluation parameters as in the first set, but the number of volunteers is rather small, only 4. So the average for a kind of experiment is a mean of only four values. To mitigate this fact, we will try to draw conclusions from a global view of all the experiments.

3.3   Results and discussion

3.3.1   First prototype

The results of the standard deviation of the trajectory are shown in figure 3.2, separated by kind of trial and direction, M-L or A-P. The values obtained from PSMs are lower compared with the values derived from the FP. This is even more clear for the Seating Mat. This indicates that PSMs estimate a smaller trajectory. This is in keeping with several studies found in previous literature. This is not only valid for averaged values shown in the figures but also for particular cases. When the results are analyzed volunteer by volunteer, the spread measured by the PSM is almost always lower than the spread measured by the FP. In table 3.5 the percentage of volunteers for whom that condition is fulfilled is shown separated by experiment, parameter and PSM variant.

The correlation between the PSM and the FP, considering the standard deviation of the trajectories have also been calculated. The variants PROP, PROP-C and PROP-8x8 are highly correlated with FP for both σ_{ML} and σ_{AP} and the three kinds of trials. The values are higher than 0.85. This kind of values has also been found in the literature previously. On the other hand, the values obtained for Seating Mat are not so good, mostly around 0.5 for the single legged trials.

When comparing our mat *3D_Velo3_Blue*, variant PROP, with the commercial one, Seating Mat, it seems that the commercial one measures an even smaller trajectory. This is true for almost all the volunteers and trials. The percentages of volunteers for who PROP is better than Seating Mat (better means closer to FP) are: for σ_{ML} 97.6%, 85.7% and 100% for the trials Right Leg, Left Leg

Table 3.5: Percentage of volunteers for who the spread of CoP trajectory is lower when measured with a PSM, considering the variants of our prototype and the commercial mat.

	PROP	PROP-C	PROP-8x8	Seating Mat
$\sigma_{ML}(RightLeg)$	100	100	100	97.6
$\sigma_{AP}(RightLeg)$	97.6	100	95.2	100
$\sigma_{ML}(LeftLeg)$	100	100	100	100
$\sigma_{AP}(LeftLeg)$	97.6	100	97.6	100
$\sigma_{ML}(Rotation)$	85.7	100	83.3	100
$\sigma_{AP}(Rotation)$	66.7	100	69.0	100
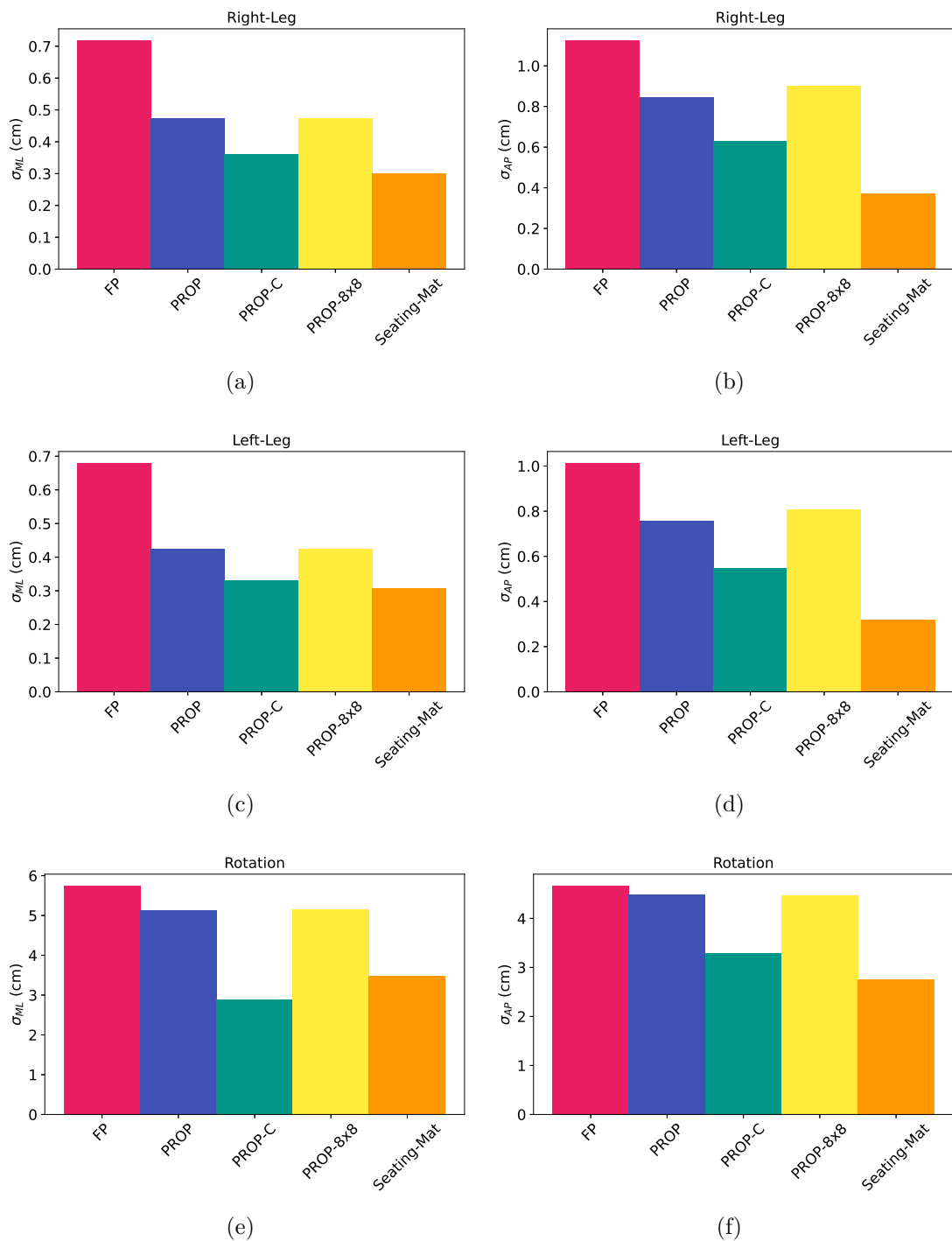
Figure 3.2: CoP standard deviation in the first experiment: a) M-L direction and Right Leg ;b) A-P direction and Right Leg; c) M-L direction and Left Leg ;d) A-P direction and Left Leg; e) M-L direction and Rotation ; f) A-P direction and Rotation.

and Rotation experiments respectively; for σ_{AP} the same percentages are 95.2%, 100% and 100%.

The comparison of PROP with PROP-C is also clear (see figure 3.2). In this case the percentages of volunteers for who PROP is better than PROP-C are: for σ_{ML} 97.6%, 97.6% and 100% for the trials Right Leg, Left Leg and Rotation experiments respectively; for σ_{AP} the percentages are 97.6%, 100% and 100%.

The comparison between PROP and PROP-8x8 is not so evident. In fact, it turns out globally that the spread of the trajectory is larger for PROP-8x8, and thus closer to the true value. The percentages of volunteers for who PROP is better than PROP-8x8 are: for σ_{ML} 42.9%, 52.3% and 33.3% for the trials Right Leg, Left Leg and Rotation experiments respectively; for σ_{AP} the percentages are 11.9%, 14.3% and 50%.

The results concerning the trajectory distance, Eu, are shown in figure 3.3, separated by kind of trial. These results also confirm that Seating Mat is the worse instrument. This is also true not only for the average but also volunteer by volunteer. For instance, the percentages in which PROP is better than Seating Mat (better means lower Eu for the same volunteer) are 90.5%, 95.2% and 100% for the Right Leg, Left Leg and Rotation experiments respectively.

Looking at figures 3.3a and 3.3b it might seem that the differences between PROP and PROP-C are not so large for the single-legged experiments. However, a view of the individual experiments yields clear results on this aspect. PROP is better than PROP-C for a 92.8%, 90.5% and 97.6% of the volunteers for the Right Leg, Left Leg and Rotation experiments respectively.

The comparison between PROP and PROP-8x8 is easier to interpret with respect to Eu. In the three trials, on average PROP is better than PROP-8x8. The percentages in which PROP is better than PROP-8x8 are unequivocal: 100% in all trials.

In a global view of the experiments, the commercial mat Seating Mat is the worse to measure the CoP. The sensor is supposed to be rather linear but despite that the measurement is not very good. We think that this can be due to several reasons. First, this PSM presents a very remarkable crosstalk problem, with phantom objects clearly visible if the circumstances are the suitable ones (for instance when there is pressure in three corners of a rectangle, the fourth one seems to be pressed). In other words, feet pressure images tend to appear like more rectangular in shape. An option of the manufacturer software has been
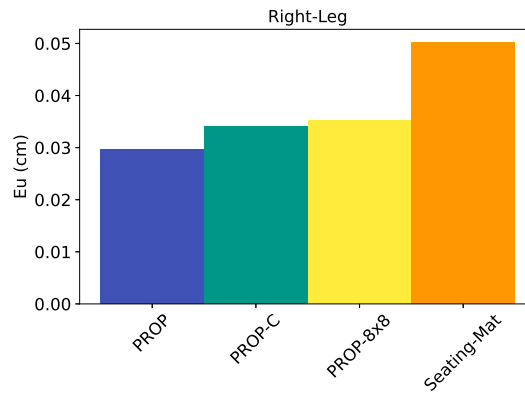
(a)
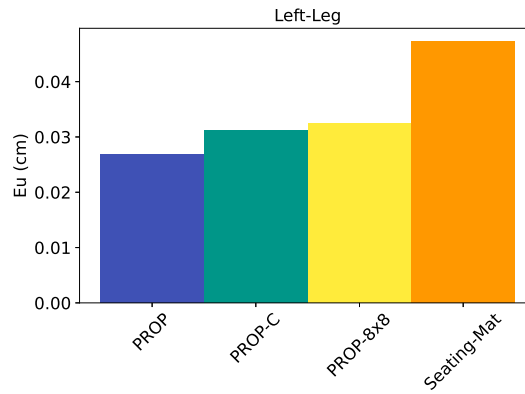
(b)
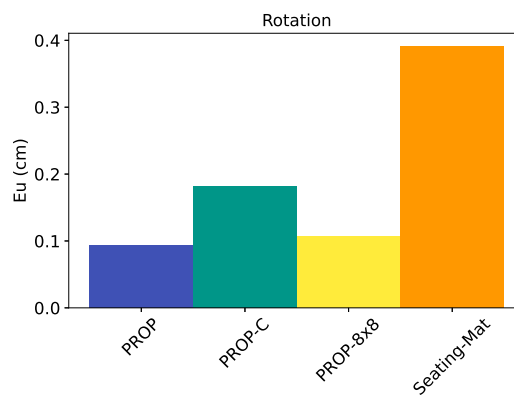
(c)

Figure 3.3: *Eu*, trajectory distance, with respect to FP in the first experiment for three trials: a) Right Leg ;b) Left Leg ;c) Rotation.

activated to remove crosstalk. Digging into the documentation it seems to be a kind of sharpening image processing. However, our experience is that this option

is rather inefficient. Another reason for the bad quality of the Seating Mat results may be that there is no correction for the internal resistance of multiplexers or switches that the DAQ circuit is likely to include. For low cost components this internal resistance cannot be neglected, as we have seen in our own circuits in which they are very similar to sensor resistances for high pressures.

With respect to the processing options considered for our *3D_Velo3_Blue*, not removing crosstalk implies a worse measurement, which is also coherent with the result of the commercial mat. This is clear concerning both the trajectory standard deviations and the distance trajectory (*Eu*).

The effect of resolution might seem controversial. Concerning the trajectory spread as measured by σ_{ML} and σ_{AP}, the lower resolution mat seems to be better. However, the trajectory distance, *Eu*, shows the opposite results. The primary outcome of the experiment is the trajectory, so that we would prefer PROP because the trajectories are closer to FP as indicated by *Eu*. The reason why the spread is higher for PROP-8x8 will be discussed in the second experiment in which the CoP trajectories are analyzed in detail.

3.3.2   Second prototype

The results of the trajectory standard deviations are shown in figure 3.4, separated by kind of trial and direction, M-L or A-P. As in the previous experiment, PSM CoP trajectory spread less than the true trajectory. It should be bear in mind that there are only four volunteers, so that each of the bars in the figure is the average of only four numbers. Anyway, the percentage of volunteers for who PSMs show less spread is almost always 100%, table 3.6, so that the fact that the trajectories derived from PSM are smaller is clear.

The correlation in the second experiment is broadly speaking high with some exceptions. SCHC obtains *r* values always higher than 0.8. However, the correlations of PROP and CHC models for σ_{ML} and the Right Leg experiment are 0.70 and 0.57 respectively. In the SCHC-8x8 option, there are three cases in which the correlation is lower too: 0.66, 0.78, 0.59 for the following parameters: $\sigma_{ML}(RightLeg)$, $\sigma_{ML}(LeftLeg)$ and $\sigma_{AP}(LeftLeg)$. Although the number of volunteers is limited, it seems that SCHC is the model that is able to keep high correlation across all the parameters and trials. On the other hand some cases of the 8x8 reduced resolution version are especially bad, contributing to lowering the average values shown above (let us recall that the 8x8 results are in fact an

Table 3.6: Percentage of volunteers for who the spread of CoP trajectory is lower when measured with the PSM in the second experiment.

	SCHC	CHC	PROP	SCHC-8x8
$\sigma_{ML}(RightLeg)$	100	100	100	100
$\sigma_{AP}(RightLeg)$	100	100	100	75
$\sigma_{ML}(LeftLeg)$	100	100	100	100
$\sigma_{AP}(LeftLeg)$	100	100	100	75
$\sigma_{ML}(Rotation)$	100	100	100	100
$\sigma_{AP}(Rotation)$	100	100	100	100

average over four possibilities as explained in section 3.2).

The comparison in detail between SCHC and PROP gives these results. SCHC is better (better means that the corresponding trajectory standard deviation is closer to that obtained with the FP) for a 100%, 75% and 100% of the volunteers concerning σ_{ML} and the trials Right Leg, Left Leg and Rotation respectively; while for σ_{AP} the same numbers are always 100%. At the risk of insisting, we indicate that just a volunteer is a 25% difference in this experiment.

The comparison between SCHC and CHC reveals that SCHC is better but not a large difference is found: SCHC is better than CHC for 75%, 25% and 50% of the volunteers concerning σ_{ML} and the trials Right Leg, Left Leg and Rotation respectively; while for σ_{AP} the same numbers are 100%, 100% and 25%. That means that SCHC is better in 15 out of 24 cases (24 = 3 trials by 2 parameters by 4 volunteers).

The comparison between SCHC and SCHC-8x8 seems to indicate better values for SCHC-8x8. SCHC is better than SCHC-8x8 for 75%, 50% and 25% of the volunteers concerning σ_{ML} and the trials Right Leg, Left Leg and Rotation respectively; while for σ_{AP} the same numbers are 0%, 0% and 75%. That means that SCHC is better only in 9 out of 24 cases. It might be tempting to conclude that increasing the resolution does not help, and even that a reduced mat resolution would provide results closest to FP. However, this is not true as it will be argued below.

The results of the *Eu* are shown in figure 3.5, separated by kind of trial. SCHC is always the lower in average and CHC the next one with a lower value. The average relative improvement of SCHC with respect to PROP, the model used in the first set of experiments, ranges from 13% to 37% depending on the

(a)

(b)

(c)

(d)

(e)

(f)
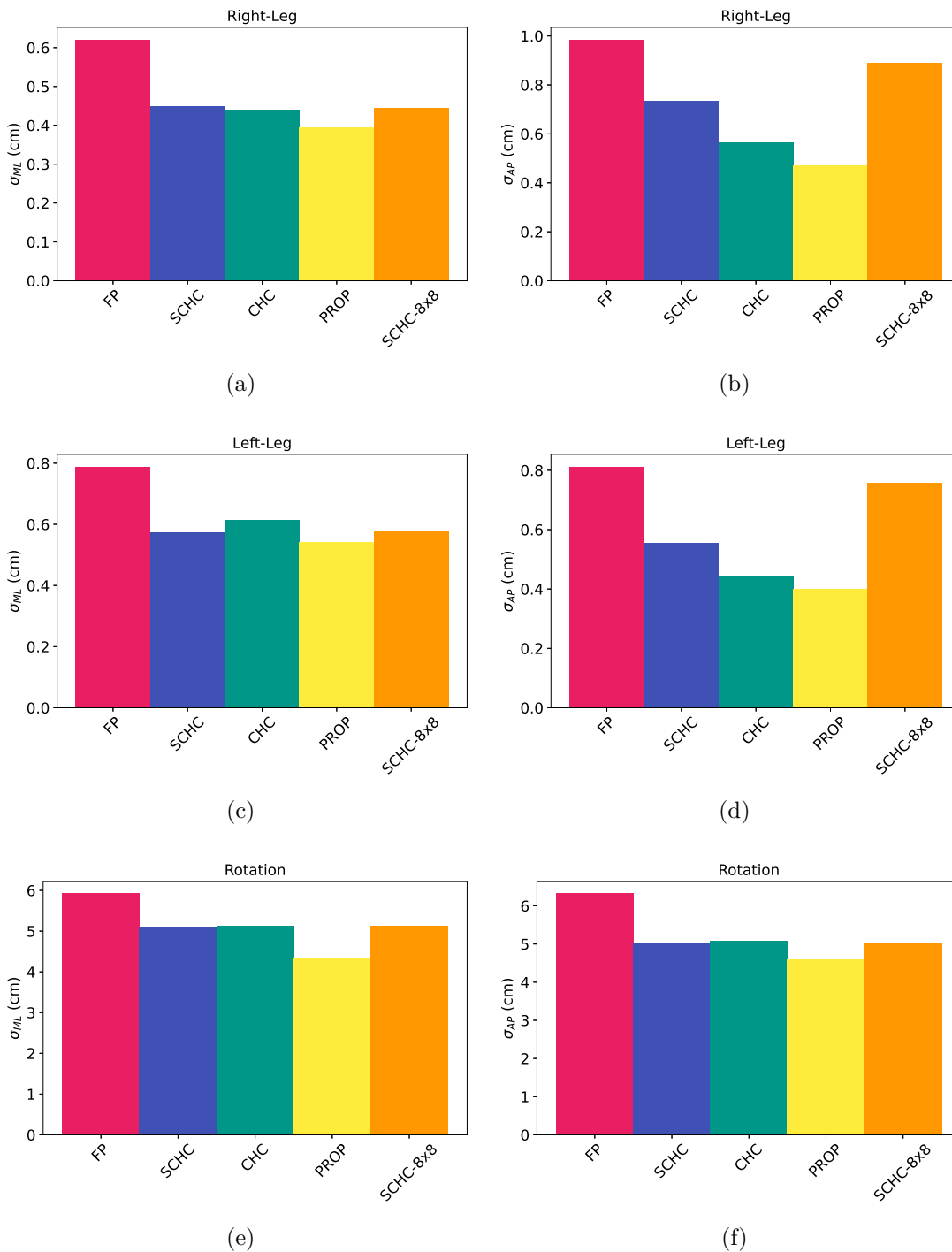
Figure 3.4: CoP standard deviation in the second experiment: a) M-L direction and Right Leg ;b) A-P direction and Right Leg; c) M-L direction and Left Leg ;d) A-P direction and Left Leg; e) M-L direction and Rotation ; f) A-P direction and Rotation.
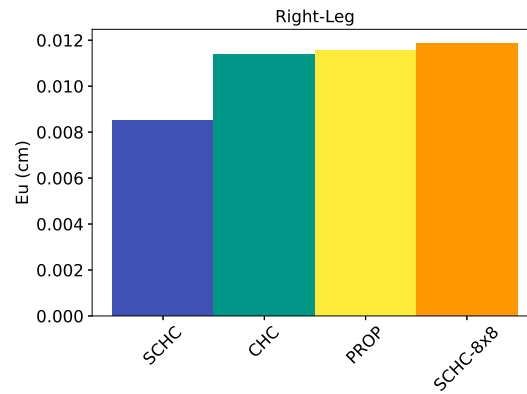
(a)
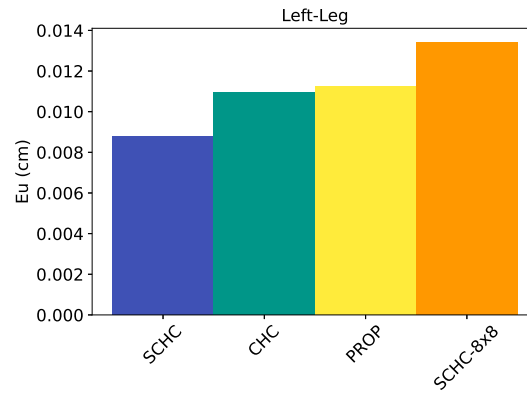
(b)
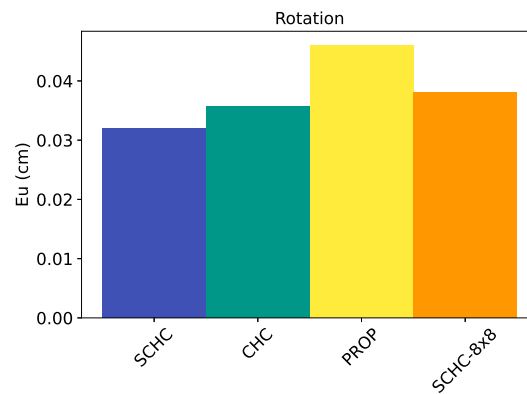
(c)

Figure 3.5: *Eu*, trajectory distance, between the FP and the PSMs in the second set of experiments: a) Right leg experiment; b) Left leg experiment; c) Rotation.

kind of trial.

With respect to *Eu*, the comparison between SCHC and the rest of variants

is very simply stated: it outperforms all of them for all volunteers and kind of trial (100% percentage).

The improvement is also visually noticeable when drawing the CoP coordinates as a function of time. Fig. 3.6 shows one example of the M-L and A-P CoP coordinates given by the FP or the PSM considering the naive PROP approach or the SCHC model found. Even though the correlation between signals seems to be always high, the height of valleys and peaks differs when comparing the FP and the PSM outputs. However, the results of the joint MPI and Creep model allows the peaks and valleys of the predicted PSM output to become closer to the values of FP. The Rotation experiment, shown in figures 3.6a and 3.6b, shows a larger full scale output and the signals look smoother. The SCHC seems better in all the peak and valleys. The larger full scale output is easily understood because there is a large load transfer between the feet, so that the CoP spread is higher than in single legged experiments. For the single legged experiment and M-L direction, look at figure 3.6c, the signals from PROP and SCHC are very similar, but for the A-P direction, see figure 3.6d, SCHC outperforms clearly PROP, which cannot reproduce many of the peak and valleys.

In a global view of the second set of experiments, SCHC is clearly better than PROP model for both, standard deviation and *Eu*. We think that SCHC is better than CHC too because in the primary measure of CoP difference, *Eu*, the results are forceful, although there are cases in which the standard deviations are not so clear. This might be related to an irregular shape of the trajectory as it happens with the 8x8 mat version, as explained below. In fact, we think that SCHC is also better than SCHC-8x8: *Eu* results are convincing. The reason why SCHC-8x8 produces larger σ_{ML} and σ_{AP} (closer to FP) is that the trajectories are irregular, somehow "noisy". A visual inspection of the trajectories is required to explain this. One example is shown in figure 3.7. For single legged experiments and the M-L direction the reduced resolution version might seem better in some parts of the time window. This is seen in figure 3.7a in which in some of the peaks and valleys the 8x8 version is closer to FP. However, trajectories measured by the 8x8 version are more erratic, especially in the A-P direction, see figures 3.7b and 3.7d. This gives rise to an artificial increase of the standard deviations, even though the CoP trajectory itself is further from the true one. This behavior is generally found for all the volunteers and experiments. To further investigate the effect of the resolution, tables 3.7 and 3.8 provide *Eu* values by volunteer
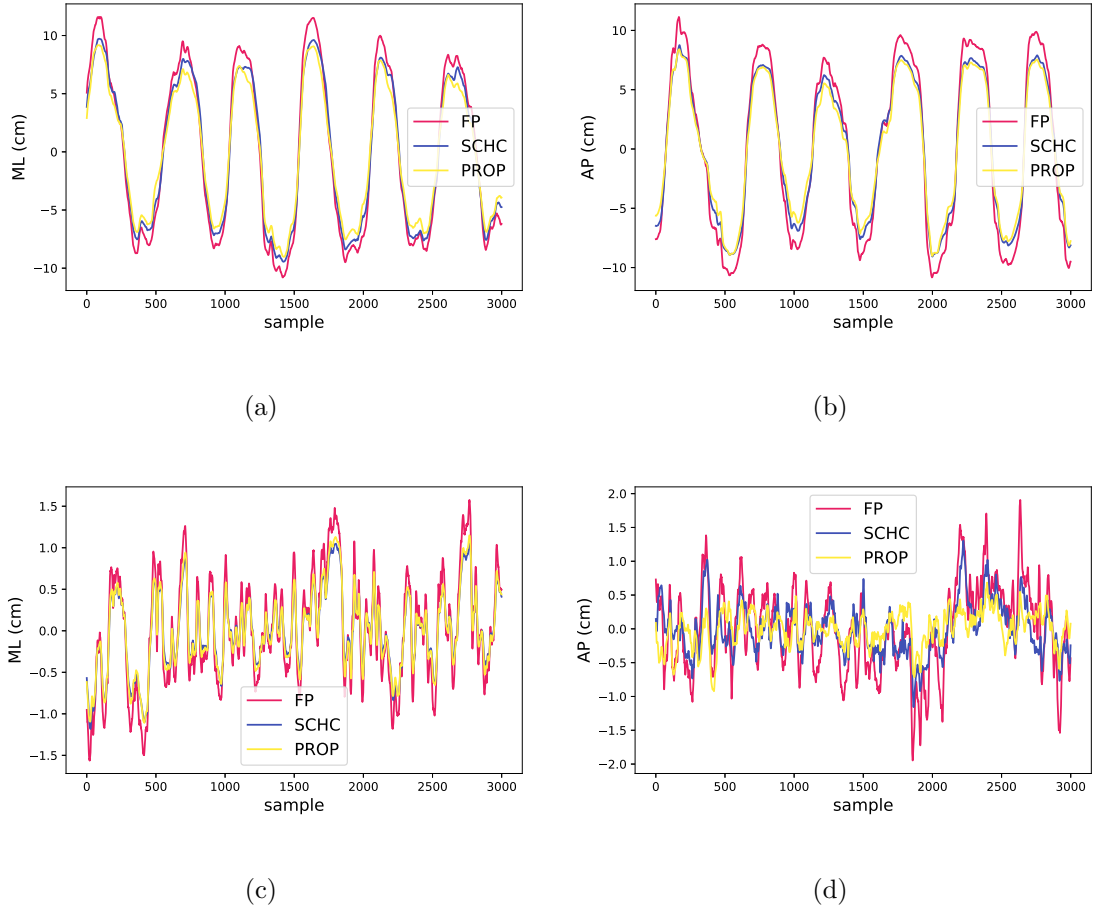
Figure 3.6: Examples of temporal series of CoP coordinates in the second set of experiments comparing FP, PROP and SCHC; a) and b) Rotation experiment (M-L and A-P directions respectively); c) and d) a single legged experiment (M-L and A-P directions respectively).

and by direction, Eu_{ML} and Eu_{AP} respectively, see equation 3.2. For all the volunteers and trials SCHC improves SCHC-8x8 even considering only a single direction of the trajectory. In the single-legged trials the differences between these two variants are proportionally higher for the A-P direction, as could be deduced from those tables, corroborating the visual inspection of the CoP paths.

3.4 Conclusions

In this chapter the use of PSMs for measuring CoP has been studied. A first set of experiments was carried out with a prototype with reduced sampling period

(a)

(b)

(c)

(d)
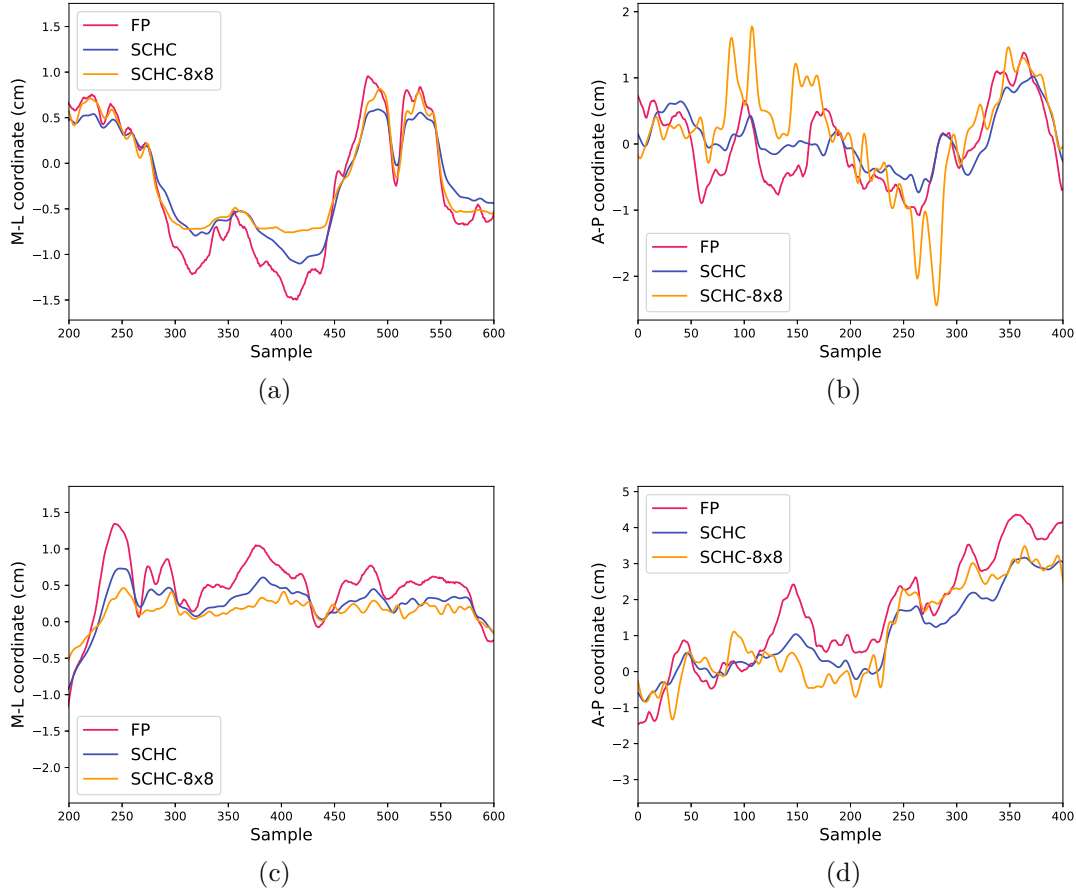
Figure 3.7: Excerpts of temporal series of CoP coordinates comparing FP, SCHC and SCHC-8x8 in single legged experiments for two different volunteers: a) and c) M-L direction; b) and d) A-P direction.

Table 3.7: Eu_{ML}(cm) in the second set of experiments by volunteer ID and trial considering two PSM versions with different resolution.

ID	Right-Leg		Left-Leg		Rotation	
	SCHC	SCHC-8x8	SCHC	SCHC-8x8	SCHC	SCHC-8x8
1	2.8e-3	3.3e-3	4.0e-3	4.5e-3	1.99e-2	2.75e-2
2	5.0e-3	5.7e-3	4.9e-3	5.6e-3	1.99e-2	2.37e-2
3	3.6e-3	4.2e-3	3.7e-3	4.5e-3	1.59e-2	2.07e-2
4	4.3e-3	4.7e-3	6.2e-3	6.5e-3	2.41e-2	2.71e-2

(10 Hz) and no sensor modeling, i.e., conductance and pressure were assumed to be proportional. There is a good correlation between the PSM and the FP, but

Table 3.8: Eu_{AP}(cm) in the second set of experiments by volunteer ID and trial considering two PSM versions with different resolution.

| | Right-Leg | | Left-Leg | | Rotation | |
ID	SCHC	SCHC-8x8	SCHC	SCHC-8x8	SCHC	SCHC-8x8
1	6.9e-3	1.24e-2	7.1e-3	1.25e-2	2.48e-2	2.78e-2
2	9.3e-3	1.19e-2	7.6e-3	1.23e-2	2.51e-2	2.77e-2
3	7.5e-3	1.03e-2	7.8e-3	1.32e-2	2.13e-2	2.75e-2
4	6.2e-3	9.1e-3	6.8e-3	1.08e-2	2.92e-2	3.12e-2

it is also evident that the CoP trajectories are smaller for PSM. It has also been found that eliminating the crosstalk that appears in this kind of sensor matrices is very important to improve the results. It is also important to highlight that the prototype provides better measurements than a commercial PSM, the Seating Mat.

In the second set of experiments the PSM had a far better sampling rate, 100 Hz and a more refined model of sensor output was available. Again, the trajectories derived from PSM are smaller. In this case, it was proved that the model improves the results but that a scaling factor is helpful when extrapolating the model found for a small-sized array to the real PSM. Despite the assumptions and approximations, it seems that the model captures a relevant aspect of the material/electrode response to pressure. In a future research, it would be important to analyze more in detail this kind of extrapolation or to be able to carry out an equilibration or calibration step for large arrays, at least to lower the differences between the cells in the array.

With respect to the resolution of the array, we have concluded that a lower resolution leads to an important increase in the trajectory distance with respect to the FP. Thus, a future improvement would be to increase the resolution of the mat. Anyway, the comparison between the versions of normal or reduced resolution has shown some surprising results. For instance, when comparing standard deviation of the trajectories the lower resolution does not seem to have any effect and presents often better values. It has been required to turn out to the trajectories themselves to realize that the lower resolution mat provides more irregular temporal series. The consequence is that the SD are larger and thus, closest to the values provided by the FP but the quality of the trajectory itself does not increase. We think that including a more direct measure of the

trajectory differences, like Eu, is very helpful in this kind of comparisons and that previous studies that only take into account parameters obtained from the trajectory can miss important aspects.

Chapter 4

Spine posture monitoring

I N this chapter we are going to use one of our prototypes to obtain spinal posture information in sitting meditation. In the subsection on the state of the art we will indicate the growing importance of meditation techniques in the field of health, as well as the importance of maintaining correct spine posture. Ideally, we want to retrieve information about posture from the pressure map on the meditation cushion. The measurement on the cushion itself is much more comfortable for the meditator than having to put a set of sensors on the back (see subsection of the state of the art dedicated to spine posture measurement). In addition, other information such as maximum pressure points can be obtained in the future.

For years, our research group, EduQTech, has been working on the development of technical aids for practicing meditation. This line arose at the request of psychiatrists and psychologists who apply mindfulness meditation as a complementary technique in their medical treatments. It has been developed especially for people living in rural areas or people who cannot attend regular meditation groups. Some of the results include the development of a mobile applications [177], respiration sensors [224] or the use of Inertial Measurement Units (IMUs) for measuring movement in short sessions of mindfulness sitting meditation [188].

In this line of work, the information that the novice practitioner receives about the meditation technique, in particular about how to sit, is very important. However, even in front of the mirror, students often fail to recognize their own failures [201].

Therefore, we have conducted an exploratory study with the aim of predicting posture from pressure maps using ML techniques. This is a complex problem,

because the posture-pressure relationship is not invertible, and it is different from previous work in the literature. We expect that the power of ML techniques will be able to obtain relevant information, despite the numerous sources of uncertainty in the problem, for example: the PSM does not give a reliable measure, the pressure is not measured on the back directly, and part of the weight is applied on the legs, not directly on the cushion. In the state of the art we will also briefly review the basic concepts of ML, as well as previous studies in which the relationship between posture and pressure exerted by the body was investigated in some way. We will also indicate the systems used to measure spine posture.

4.1 State of the art

4.1.1 Meditation as a complementary health technique

Interest in meditation and its implications for physical and mental health has grown strongly in recent decades. Although different attempts to define what is meant by meditation can be found in the literature, it was not until 2004 that an operational definition of meditation in the field of health was published. Cardoso et al. [50] characterized meditation with four operational parameters:

- Specific technique: A technique procedure, clearly defined and regularly practiced is necessary.

- Muscle relaxation somewhere during the process.

- Logic relaxation: involving three aspects: a) Not to intend to analyzing (not trying to explain) the possible psychophysical effects; (b) Not to intend to judging (good, bad, right, wrong) the possible psychophysical effects; (c) Not to intend to creating any type of expectation regarding the process.

- Self-induced state: Self-applied by the individual him/herself (no dependence on the instructor is stimulated).

- Self-focus skill (anchor)

There are many different types of meditation, each with a specific focus or intention. Meditation that involves fixation on a specific mantra, image, feeling, or idea is known as focused attention; meditation that involves fixation on the

present moment is known as mindfulness; and meditation that combines ethical discipline and physical postures, with an emphasis on harmony between the body and mind, is known as yoga [189].

Although numerous works have been published on the impact of meditation on health, some authors have highlighted aspects that has been an impediment to formulating quality studies [145] [110]. For this reason, it has been necessary to consult meta-analyses and metasyntheses (i.e., second-order meta-analysis) to derive a comprehensive estimate of the effect of meditation on health.

Over time, different meta-analyses have linked meditation to health benefits, see for instance [69], [86] or [97]. More recently Sampaio et al. [195] concluded that meditation is classified as a complementary and integrative technique in the area of health. The advances in researches with meditation, the discovery of its potential as an instrument of self-regulation of the human body and its benefits to health have shown that it is a consistent alternative therapy when associated with conventional medical treatments.

Rose, et al. [189] developed a metasynthesis of twenty-eight meta-analyses of randomized controlled trials, which collectively provided 404 meta-analytic effects from over 31,000 participants. They conclude that there was a robust, medium-sized effect of meditation on health when aggregating across meta-analyses. By aggregating data from a relatively large and highly diverse set of meta-analyses, their research provides among the most compelling evidence to date that meditation benefits health.

Sitting meditation

Sitting meditation is perhaps the best known type of meditation. However, many practitioners show poor posture in sitting meditation (see figure 4.1).

In sitting meditation the practitioner is usually asked to "straighten the back." This direction is sometimes illadvised for a better posture [103]. Seen from the side, the spine does not form a straight line, but is slightly curved [201].

The sitting bones provide centeredness and stability in a sitting posture (see Fig. 4.2a). The center of the body vertically above the sitting bones supports the weight of the body, so that the practitioner can feel vertically aligned in a sitting posture with little or no tension in their back (see Fig. 4.2b) [103].

Uprightness is not the form of a particular posture in sitting meditation, but the essence of the posture [103].

Therefore, the aim of this chapter is to investigate whether or not it is pos-
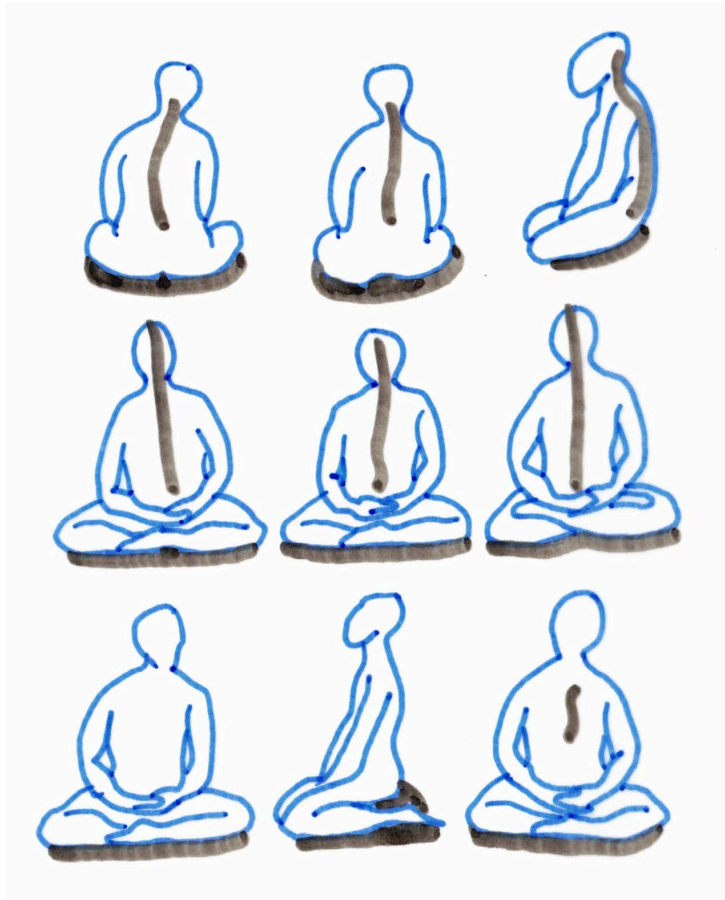
Figure 4.1: Incorrect postures in sitting meditation. Based on [201]

sible to know the meditator's posture during meditation practice. In particular, whether or not the posture of the spine can be recovered from the pressure exerted on the seat (see figures 4.2a and 4.2b).

4.1.2   Machine Learning techniques

In this subsection, the basic concepts of ML are reviewed. The information can be found in classical books like [43, 87], as well as in more applied texts [82].

The goal of ML techniques is for a machine to be able to make a prediction, given an input. In a classification problem the prediction corresponds to a finite set of categories to which the input can belong. In a regression problem the prediction consists of one or more continuous variables.

Generally, data require a preprocessing step before they can serve as input to the prediction systems. In this preprocessing, features that can be useful to the

(a) Correct posture of the tailbones bones during meditation
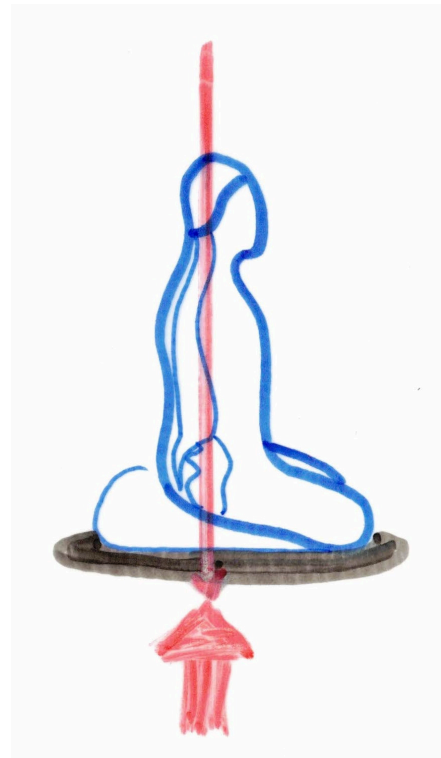
(b) Vertical alignment during sitting meditation.

Figure 4.2: Proper meditation posture: (**a**) Correct posture of the tailbones bones during meditation. Illustrated based on Hye-jeong Yoon [103] (**b**) Vertical alignment during sitting meditation. Illustration inspired by Hye-jeong Yoon [103].

predictor systems are extracted. Feature extraction is a critical step in order for an ML system to function properly. Unfortunately, it is a step that requires prior knowledge, it is often based on trial and error, and it is not always systematic especially for new problems.

ML systems have a number of internal parameters that can be adaptively tuned. For this purpose, in the training stage a training set, i.e. a set of known input and output values, is presented to the ML system leading to the adaptation of the parameters so that the prediction is similar to the known output. This type of learning is called supervised learning and is the one we will refer to in the thesis.

There are numerous techniques available. One of the most popular is neural networks. Figure 4.3 shows an MultiLayer Perceptron (MLP) with a hidden

layer. Each layer receives information from the previous layer, processes it, and its output is exploited by the next layer. Generically, if $\mathbf{x}$ is the input to a neuron, the output, z, has the form:

$$z = \phi(\mathbf{x}^T\mathbf{w} + \mathbf{b}) \tag{4.1}$$

where $\mathbf{w}$ are the neuron weights and $\mathbf{b}$ the bias term. The function $\phi()$ is called activation function and plays an important role in the network.
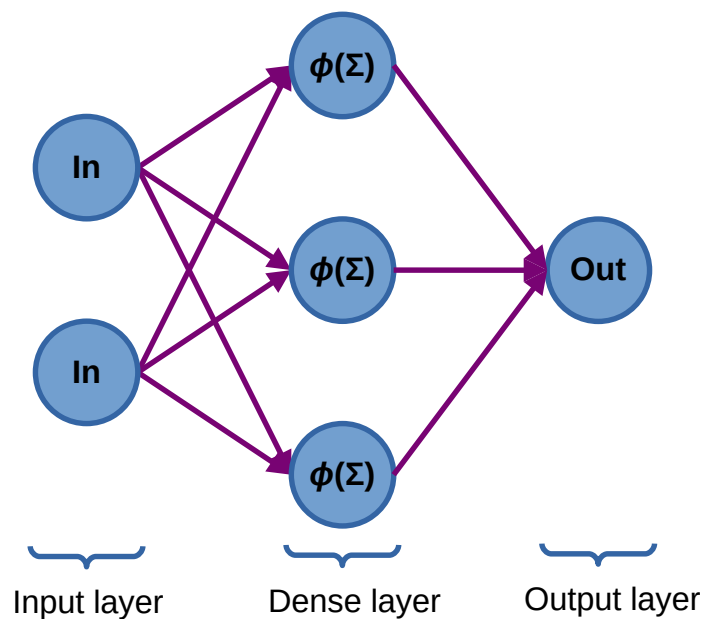
Figure 4.3: Layers diagram in MLP.

To simplify the notation, the input data is often augmented with 1 and the bias is considered as another weight. Thus, the set of weights of all neurons corresponds to the adaptive parameters that need to be found in the training.

One type of ML systems is called Deep Learning. In Deep Learning, greater flexibility and power is achieved because such a structure allows the information from the world to be represented as a set of concepts in which each concept is based on the previous ones. There is no consensus on the depth that is necessary for a system to be considered "deep", but a neural network with several hidden layers would already be an example of a deep system. For instance in object recognition, each layer can represent certain aspects of an input image, and the

recognition of the image is built by the hierarchy of concepts that each layer is capable of representing. In this way, Deep Learning systems often support inputs with much less preprocessing, avoiding the problem of "hand-crafted" feature extraction.

Thus, Deep Learning systems have had remarkable successes in complex fields such as image or speech recognition. One of the most popular structures are the Convolutional Neural Network (CNN) structures. The basic idea of this type of structures is that they include convolutional layers, where neurons in one layer are connected only to nearby neurons in the previous layer (illustrated in figure 4.4). In this way, a hierarchy is formed where the first layers extract low-level features from the image, which are then assembled to form high-level ones.
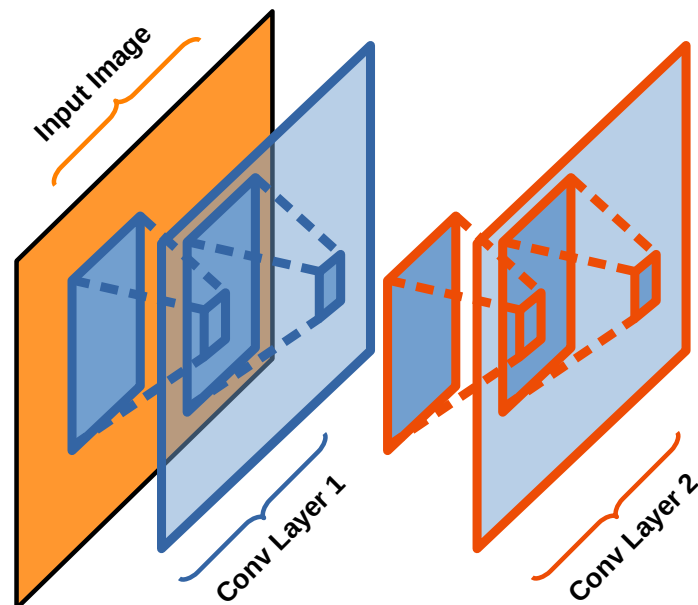
Figure 4.4: Convolutional layers diagram in CNN.

In neural networks, the data set is usually divided into three parts. One is the training data set. It is used to adjust the model parameters. For this purpose, a target function is minimized in the training data set. This target function may decrease with the iterations, but after several training iterations the network loses the ability to generalize, i.e. to succeed with data other than the training data. Therefore, another set of data called validation set is set apart. The validation set can be used to control the error and decide when to stop training if the error in it increases. The validation sets can also be used to decide other characteristics

of the network, called hyperparameters, such as the number of neurons or layers. Finally, the test set is used to estimate the performance of the system. The test set is used neither to train the parameters nor to choose the hyperparameters.

The target function used in this thesis is Mean Squared Error (MSE). If $\hat{\mathbf{y}}_i$ is the model prediction and $\mathbf{y}_i$ the corresponding value in the training set, MSE is defined as:

$$MSE = \frac{1}{N} \sum_{i=1}^{N} \|\hat{\mathbf{y}}_i - \mathbf{y}_i\|^2 \tag{4.2}$$

where N is the number of samples in the training set. The output is represented in bold because it can be multivariable.

Minimizing the MSE is equivalent to maximizing a log-likelihood when the probability of obtaining a value at the output is Gaussian.

Algorithms based on the idea of gradient descent, namely stochastic gradient descent, are used to find the network parameters. The error gradient can be calculated efficiently with the backpropagation method. The basic idea is to move the parameters in the opposite direction of the gradient, with a given proportional factor, the learning rate, that decreases as the iterations increase.

Fortunately, many libraries have been developed that allow neural networks to be implemented with relative ease. On the other hand, minimization is not easy with real data and multi-layered structures. Many problems arise in practice. We will mention those that are of interest in this thesis.

In some cases the number of training data is limited. It can be interesting to obtain more data to improve the training. For this purpose, data augmentation techniques are used to obtain new samples from the previous ones. For example, in a problem of recognizing an object in images, one can rotate the images, change the scale or move the object, so that the system learns to recognize the object in any situation.

It may also happen that the training is slow. This may occur because the changes in the parameters are small. In gradient descent, the parameters move in the opposite direction of the gradient. There are variants that modify this behavior for faster convergence: momentum optimization, Nesterov Accelerated Gradient, AdaGrad, RMSProp, Adam, Nadam. These variants introduce ideas such as the gradient affecting the acceleration of motion in parameter space, rather than velocity; or correcting the gradient to point in a better direction

(decreasing the value in directions of greater variation); or a combination of both.

Another problem that may arise is that of overfitting. The model can be trained with a low level of error, but its generalization capability is poor, i.e., its performance on other data sets worsens significantly. This may be due to the fact that the model is very complex and has more parameters than necessary. To reduce this error, so-called regularization techniques are available. One of the most popular is to add to the objective function a term containing the sum of the squares of the network weights (L_2 regularization) multiplied by a constant. Another technique, equivalent to the previous one in some cases, is weight decay. In general, in the weight decay technique it is sought that the values of the weights do not grow too much. Another regularization technique is the dropout. In each training step, there is a probability that the neuron is ignored during that step and its weights are not updated.

Since in a multilayer neural network it is necessary to calculate the gradients through the layers, there are also numerical problems and the values can become excessively small. There are several options to remedy this, such as switching to activation functions that do not saturate or the batch normalization technique, in which an operation is added just before or after each activation function. The operation takes its input, centers it at zero and normalizes it, resulting in its output. In this way, gradient vanishing problems are avoided since the numerical values are fairly bounded. In practice, these techniques have also helped in the regularization of the network.

Training a system to achieve acceptable performance can be a tedious and complex process. Sometimes, one resorts to using another system that has already been trained for a similar problem to a greater or lesser extent, and to starting from the pre-trained system to reach a reasonable solution in less time.

To measure the performance of an ML system, so-called metrics are used. For classification tasks, the ratio of correct detections over the number of instances (precision) and the ratio of correct detections over the items in that category (recall) are commonly considered. In the case of a system performing regression, MSE, mentioned above, or also the R2 score can be used:

$$R^2 = 1 - \sum_i \frac{\|\mathbf{y}_i - \hat{\mathbf{y}}_i\|^2}{\|\mathbf{y}_i - \bar{\mathbf{y}}\|^2} \tag{4.3}$$

where $\bar{\mathbf{y}}$ is the average value.

For a perfect fit, R^2 is 1.0 The value is zero if the prediction is just the mean value, and can also take negative values.

When the value of a metric is given, it is necessary to indicate whether it refers to the training set, the validation set or the test set. The final performance estimate must be indicated for the test set.

4.1.3   Relation between posture and pressure

The aim of this thesis is to investigate whether or not it is possible to know the meditators posture during meditation practice. In particular, whether or not the posture of the spine can be recovered from the pressure exerted on the seat. To develop this task, we will globally analyze previous studies that use measurements of the pressure exerted on sensors to determine the posture of the spine.

We can find different types of studies, relating the pressure exerted on a mat when sitting with different body parameters. For example, in [153] the rotation of the pelvis is studied, in [133] it is related to the lumbar spine stability and abdominal bracing stability.

Some works have focused on sleep to monitor it (see for example [129]), to know the postures adopted [62, 179], or to investigate which may be the best materials for beds [139] in order to minimize peak body contact pressures.

Other studies use measurements of the pressure exerted when sitting to improve specific aspects. For example, in [174] the effect of backrest inclination of a wheelchair on buttock pressures in spinal cord injured people was analyzed; in [248] the effects of seatback support on collision parameters were studied.

Finally, we have also found studies that analyze exercises, such as in [209] where Sundlholm et al. used a pressure mat to track exercises such as push-ups, squats, or abdominal crunches in order to monitoring them without additional sensors.

However, the studies closest to the objective of our work focus on recognizing sitting postures, usually to give information to the user about bad postures that can hurt him/her (see for instance [49, 151, 202, 211, 214, 244]).

From these studies we can conclude the versatility when using pressure mats, since they can be used both lying on the prototype ([129, 133]), on the floor [209], on a bed [62, 139, 179] or sitting in a chair, installing the mat on the backrest [211, 248] or on the main seat [49, 151, 174, 211, 214, 244].

The pressure mats used can be commercial (we mostly find the Teskcan brand,

as for example in: [133, 139, 174, 214]) or home made prototypes. The number of sensors varies from 256 [211, 244] to more than 2000 elements [133, 179, 209, 248], with others numbers such as 1024 (32x32) [49, 54, 129, 214].

For data collection, the number of subjects ranges from less than 10 ([151, 209, 211, 214]), from 11 to 20 ([62, 133, 139, 153, 179]), from 21 to 30 ([202, 244, 248]) or more than 40 ([49, 174]) with the maximum being 60 [202].

Finally, with regard to data processing, it can be indicated that there are different methods in a global overview:

- Classical statistical methods:

    - Analysis of Variance (ANOVA) [133, 174, 202].

    - Paired t-test [139].

    - Bonferrori test [202].

    - Dunnett and Tukey tests [174].

    - Mann-Whitney U-test [174].

    - General Linear Model [174, 248],

    - Regresion analyses and Multiple regression [133, 153], respectively.

    - Monte Carlo [62].

- Methods closest to ML:

    - Principal Component Analyses [49, 211].

    - Naive Bayes Network [151, 244].

    - Dynamic Time Warping [209, 244].

    - K-Nearest Neighbors (k-NN) classifier [209].

    - Clustering techniques, specifically the Nearest Posture Prototype (NPP) using Sum of Absolute Difference (SAD).

    - CNN architectures [62].

    - Restricted Boltzmann Machine (RBM) [62].

Two studies stand out over the rest, so that they have inspired our work.

In [62], four convolutional layers and a dense layer are used together with a skeleton model. This CNN is employed to obtain joint positions in bedridden patients. The model is applied to two bed positions (supine, seated). It retrieves the positions from the pressure images of the bed. Seventeen volunteers participated in the experiment and a total of 28000 images were recorded. The structure is trained end-to-end and it is able to reconstruct the position of the joints, obtaining an average positioning error of 77 mm. Meanwhile, in [179] subjects are classified from the images obtained by PSMs, in three common sleeping postures. For this, 18 features are extracted, which feed a dense Artificial Neural Network (ANN) with 3 deep layers with 20, 20 and 19 neurons. The tests were performed on 13 volunteers. For the 10-fold cross-validation case accuracy and recall are often above 70%.

Among the articles found, many place the PSM directly on the area of the body from which they wish to extract information and are often used for classification tasks. In our case we would like to retrieve numerical values of spine inclination, which is more difficult than a posture classification. In addition, we try to obtain them indirectly, since we measure only the pressure exerted on the seat with our prototype of the PSM

4.1.4   Spine posture measurement

There is a wide range of measurement techniques for spine posture monitoring. They are listed in table 4.1 together with a list of previous studies that use them. In a global view of them, the proportions shown in the figure 4.5 were obtained.
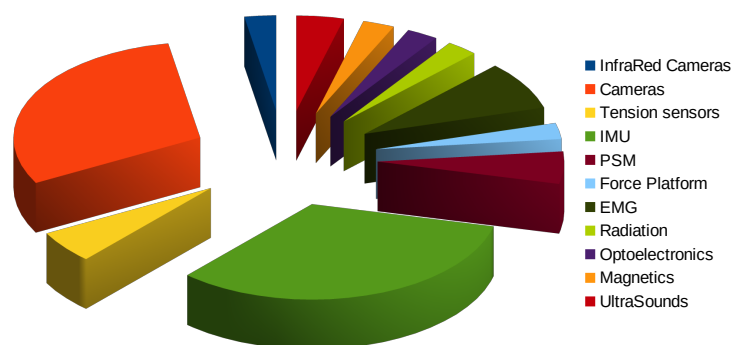
Figure 4.5: Proportion of instruments used for the measurement of the human back.

In view of this analysis, it has been observed that the most common sensors

Table 4.1: Measurement techniques for spine posture monitoring

Sensor type	References
Accelerometers and IMUs	[31, 46, 52, 63, 65, 67, 78, 79, 83, 107, 121, 123, 157, 160, 172, 173, 176, 187, 203, 207, 218, 221, 227, 234]
Camera based	[29, 38, 40, 44, 46, 55, 59, 61, 65, 67, 77, 88, 144, 154, 158, 173, 186, 221, 223, 228, 245, 247]
PSMs	[46, 126, 242, 245]
Optoelectronics	[106, 178]
EMGs	[77, 154, 159, 194, 203, 245]
Radiación (X-Ray)	[71, 81]
Force Platforms	[36, 108]
Stretch Sensors	[107, 228, 229, 247]
InfraRed Cameras	[114, 159]
Magnetic Sensors	[102, 140]
Ultrasounds	[116, 142, 212]

used are inertial sensors (IMUs) and those based on vision systems (cameras). This conclusion has been also drawn in several review papers. Wang et al. [232] stated that accelerometer and IMUs are the most popular sensors used in wearable technology for rehabilitation. In [205] it can also be found that most systems for spine posture are based on IMUs.

Camera based systems present some practical problems: more space is required, occlusions are a major issue, specific software is needed to synchronize cameras and analyze the results, markers are often required, and the cost is high compared with IMUs [187]. On the other hand, the IMUs are the most commonly used sensors and they should not be difficult to synchronize. Despite some difficulties like their modeling and calibration, a system based on IMUs has been chosen to obtain the values considered as the reference for the spine posture.

4.2   Spine posture measurement system

Some previous studies use 3 points for spine modeling [161, 173, 187], others use 5 points [31, 52, 227] and some use 7 points. Although 3 points is technically sufficient, a model with 5 points would yield a more reliable model. Therefore, 5 sensors were used in our study.

The most common vertebrae over which sensors are placed are T1, T12 and S1 [83, 160, 173, 187]. We have placed the sensors over the C7, T4-5, T10-12, L4-5 and S3 vertebrae in a similar way to [31, 227] as can be seen in the figure 4.6

(a) Positioning of the IMUs

(b) Vertebrae on the skin
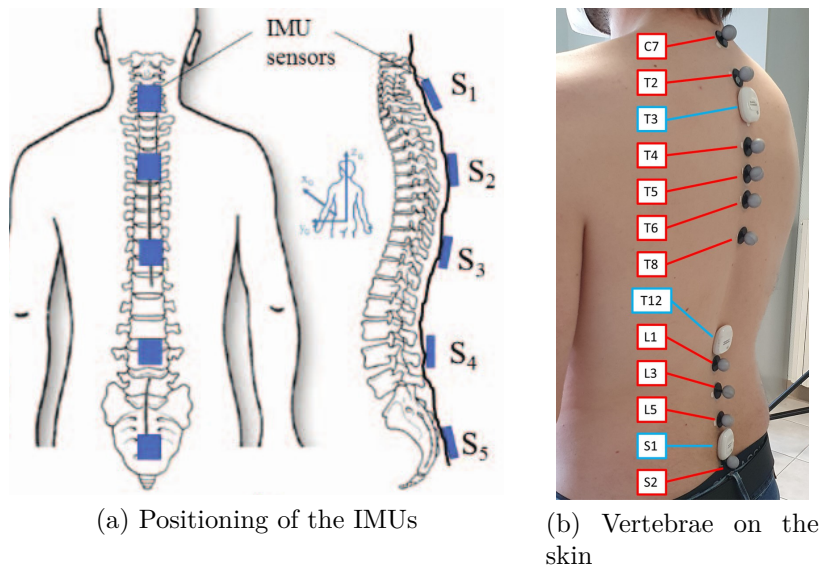
Figure 4.6: Vertebrae on which to position the IMUs: (**a**) Placement of the IMUs, image of [31]; (**b**) Vertebrae on the skin, image of [173].

In [227], a comparison is made between five typical types of IMUs. And among them, the BNO055 [15] is chosen because it features a self-calibration function. This is an important benefit as calibration of the IMUs is a cumbersome and time-consuming process. Therefore, it is also going to be the sensor we select in our work. In addition, the BNO055 has integrated algorithms that allow it to return the absolute orientation obtained by the sensor, thus avoiding complex orientation calculations. Another advantage of the BNO055 is its price. The BNO055 sensor usually has a price between €15 and €30, variable also due to the semiconductor crisis. Other sensors used in the literature, such as ADIS16448 or sensors from Xsen, are clearly higher priced. In contrast, cheaper sensors such as the MPU9xxx lack self-calibration routines or do not provide the orientation directly.

The BNO055 sensor is an integrated sensor, but it is also available on development boards that facilitate prototyping. For this reason, we have chosen to use the sensor on a development board.

For the DAQ circuit, the same development board model and µC as in the PSM prototypes, STM32F103C8T6 [18, 115], has been used. This allows us to reuse the configuration process already performed and the same Arduino bootloader file. In this way programming is very simple, although entering code at a lower level is also possible. Besides, the source files are simplified into a single .ino file and the libraries required in a given project.

The system is connected by USB with the PC where the storage and visualization of the sampled data takes place. In addition to this, the power supply of the system is also obtained by the same USB cable.

To control the IMU BNO055 from the Arduino using the Inter-Integrated Circuit (I²C) communication protocol, there is the Adafruit Unified BNO055 Driver [28] library, which can be installed from the Arduino library manager.

For Arduino I²C communication on the STM32F103C family there are two libraries available: Softwire and Wire. They do not differ much from each other and both present a similar interface. But in our µC [18] only the Softwire library appears to work, while the Adafruit BNO055 version 1.5.2 library uses Wire.

Due to this incompatibility between libraries, the Adafruit BNO055 library has been patched to use the Softire module and a local copy of the modified library local has to be located in the project folder (Code 4.1 displays the output of the diff command between the original and modified library, showing the changes made to the code). In this way, data can be obtained with our µC and the library examples can be run.

```
1  diff −r −−color ./BNO055_original/Adafruit_BNO055.cpp ./BNO055_fixed/
       Adafruit_BNO055.cpp
2  47c48
3  <                             TwoWire *theWire) {
4  −−−
5  >                             SoftWire *theWire) {
6  diff −r −−color ./BNO055_original/Adafruit_BNO055.h ./BNO055_fixed/
       Adafruit_BNO055.h
7  28,29c28,30
8  < #include <Adafruit_I2CDevice.h>
9  < #include <Adafruit_Sensor.h>
10 −−−
11 > #include "Adafruit_BusIO/Adafruit_I2CDevice.h"
12 > #include "Adafruit_BusIO/Adafruit_I2CDevice.cpp"
13 > #include "Adafruit_Sensor.h"
14 281c282,285
```

```
15  >   static SoftWire Wire;
16  283,284c287,288
17  <                    TwoWire *theWire = &Wire);
18  −−−
19  >                    SoftWire *theWire = &Wire);
20  diff −r −−color ./BNO055_original/Adafruit_BusIO/Adafruit_I2CDevice.cpp ./
        BNO055_fixed/Adafruit_BusIO/Adafruit_I2CDevice.cpp
21  10c12
22  < Adafruit_I2CDevice::Adafruit_I2CDevice(uint8_t addr, TwoWire *theWire) {
23  −−−
24  > Adafruit_I2CDevice::Adafruit_I2CDevice(uint8_t addr, SoftWire *theWire) {
25  121,123c122,124
26  <   if (_wire−>write(buffer, len) != len) {
27  −−−
28  >   if (_wire−>write(buffer, len)) {
29  diff −r −−color ./BNO055_original/Adafruit_BusIO/Adafruit_I2CDevice.h ./
        BNO055_fixed/Adafruit_BusIO/Adafruit_I2CDevice.h
30  5c5
31  < #include <Wire.h>
32  −−−
33  > #include <SoftWire.h>
34  10c10
35  <   Adafruit_I2CDevice(uint8_t addr, TwoWire *theWire = &Wire);
36  −−−
37  >   Adafruit_I2CDevice(uint8_t addr, SoftWire *theWire);// = &Wire);
38  30c30
39  <   TwoWire *_wire;
40  −−−
41  >   SoftWire *_wire;
42  diff −r −−color ./BNO055_original/Adafruit_BusIO/Adafruit_SPIDevice.h ./
        BNO055_fixed/Adafruit_BusIO/Adafruit_SPIDevice.h
43  26c26
44  < #elif defined(ESP32) || defined(___ASR6501___) || defined(___ASR6502___)
45  −−−
46  > #elif defined(ESP32) || defined(___ASR6501___)
47  57c57
48  < #if !defined(___ASR6501___) && !defined(___ASR6502___)
49  −−−
50  > #if not defined(___ASR6501___)
```

Code 4.1: Adafruit BNO055 library patch

Another detail that was taken into account during sensor selection is that we

want to read five sensors and the IMUs usually have a limited number of I^{2}C addresses. Specifically, the BNO055 sensor only presents two addresses available in slave mode, 0x28 and 0x29. These addresses are set by connecting the ADR pin of the BNO055 to logic 0 or 1 respectively [15].

Initially, it was proposed to set all sensors to address 0x28. To read one of them, the address would be changed to 0x29 by switching the ADR pin, and that address would always be read. This requires as many digital control pins as sensors. However, this option is not feasible because reading the ADR pin and setting the sensor address occurs at the start of the sensor configuration process, at startup after power-up. Moreover, changing ADR implies losing the calibration.

Another option would be to use an I^{2}C multiplexer such as [19]. This possibility would allow the transmission of information from multiple devices with the same I^{2}C address, but requires the purchase of specific chips, and we had supply problems at the time of developing the system.

It was observed that if the data cable is left open (high impedance) while keeping the clock signal, the sensor calibration is not lost. This makes it possible to multiplex the sensor to be read. This option requires a multiplexer and the wiring of 8 signals (Vcc, GND, Clk, 5x SDA).

Although these options would be functional, the µC used in our DAQ contains three I^{2}C buses. This allows us to employ all five sensors by connecting two to each bus. This option would also require the wiring of 8 signals (Vcc, GND, 3x (Clk and SDA)), but no additional hardware is required as would be the case with multiplexers. Another advantage is that the I^{2}C signals remain connected to the bus, which avoids possible bounces that could delay the reading when changing to or from a high impedance state.

For the attachment of the system to the back, a platform has been developed on which the sensors are embedded, keeping them equidistant from each other. This system has a flat, smooth surface on the side that rests on the back, preventing pinching, maximizing comfort and facilitating the initial self-calibration of the sensors. In order for the sensors to maintain their position on the spine, each sensor is adjusted with an elastic strap around the torso. The wiring of the sensors is done on the back side and they are left loose to avoid interference with the user's mobility. The boxes of each sensor have been designed open to facilitate the freedom of wiring and assembly and disassembly if necessary. Flexible

flat cable has been used for the wiring to give uniformity to the system.

The design of the measurement system has been decided to be modular, which facilitates the replacement of any component in the event of damage to any part, allowing users to continue measuring. The sensor brackets hold the sensors in place by tightening. They have been designed and printed in 3D, adjusting their dimensions to the sensor plate, and correct positioning generates a clicking sound that indicates proper positioning. In addition, the positioning tape passes over the sensor, making it impossible for the sensor to move in the housing.

The modules are spaced 90 mm apart, which we have estimated as an adequate distance to be able to reconstruct the shape of the back, in adults within the variability of heights, sexes and ages (according to [14] the length of the back measures around 66 cm, and according to [47] 57 cm). The sensor brackets are attached to a flexible printed piece, which maintains the distance between sensors but allows the back to move without opposing them, and allows tracking their movement. The sensor is attached to the back with elastic straps that position the sensors and fasten with printed [215] clips for easy placement. Since they are printed, we have been able to adapt the exact size to the strap. The prototype can be seen in figure 4.7.

For the reading of the sensors we use a code similar to the Adafruit BNO055 [28] library examples. Each sensor is read sequentially at a frequency of 10 Hz, using the same interruption as in our PSM. The three modules I^{2}C of our μC are enabled and wired to their associated IMUs. The library functions are used for reading and sending the data in binary format as four-byte numbers (float numbers in Arduino except for the Arduino DUE). The same code of data reception verification is included as the one used by the PSM. The information transmitted corresponds to the orientations of each sensor in the form of Euler angles.

The system sends data through the USB integrated in the board through which it is powered. The PC to which it is connected is in charge of executing a Python script which interprets the data in binary format and stores them in a plain text file as numbers with five decimal places separated by spaces. At the same time that it performs the storage, the adaptation of the spine model of [227] is displayed on the screen.

In [227] a series of equations for modeling spine curvature is presented. They represent the spine as a series of circular arc. These equations include conditions depending on how the inclinations of different sensors occur, giving rise to 14
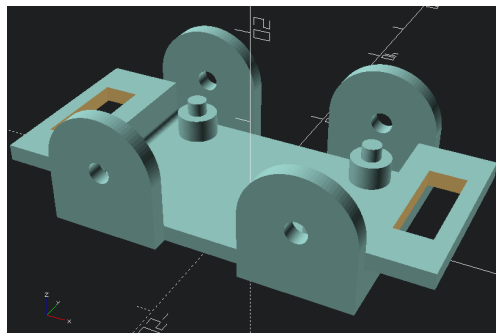
(a) BNO055 Box
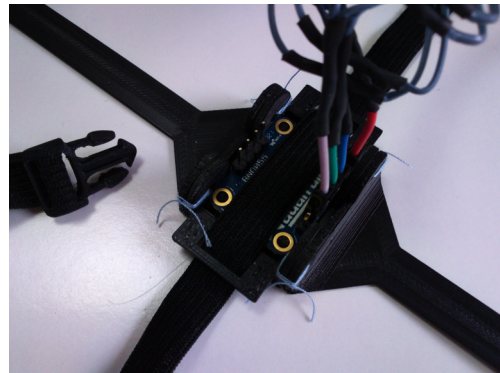
(b) IMU in system
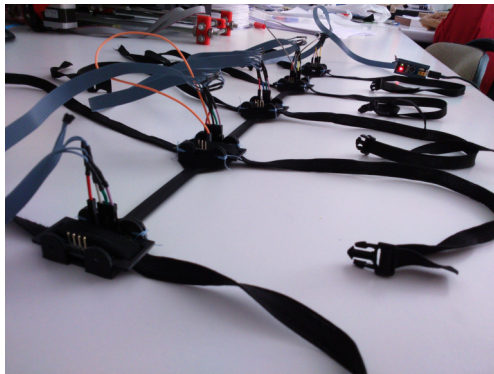
(c) Column IMUs devices
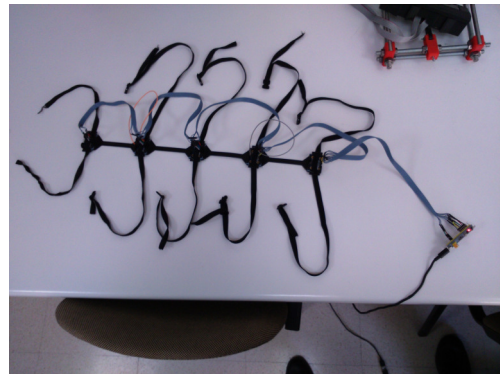
(d) Column Measurement System

Figure 4.7: Spine posture measurement system: (**a**) BNO055 Box;(**b**) IMU connected in system; (**c**) BNO055 senors in system; (**d**) back measurement system.

different cases of curvature. The associated curvatures compose the model in charge of representing the shape of the spine, allowing to represent the posture of the back. Figure 4.8 extracted from [227] shows two cases of different curvatures.

It has been observed that the model proposed by [227] could serve for visual purposes, to detect errors in the initial calibration of the sensors. But this system can be simplified by considering it as a two-dimensional point translation. Considering a two-dimensional coordinate system, translation and rotation matrices can be applied, similar to coordinate transformations in robotics, to obtain the relative position of the different sensors.

In our simplified model, it has been assumed that the junction between two points is similar to a circular arc, which is no more than $\pi/2$ radians. The sensors can obtain the tilt angles referenced to a right-handed orthogonal system. The Z axis is oriented towards the spine (sagittal axis), the Y axis would be oriented
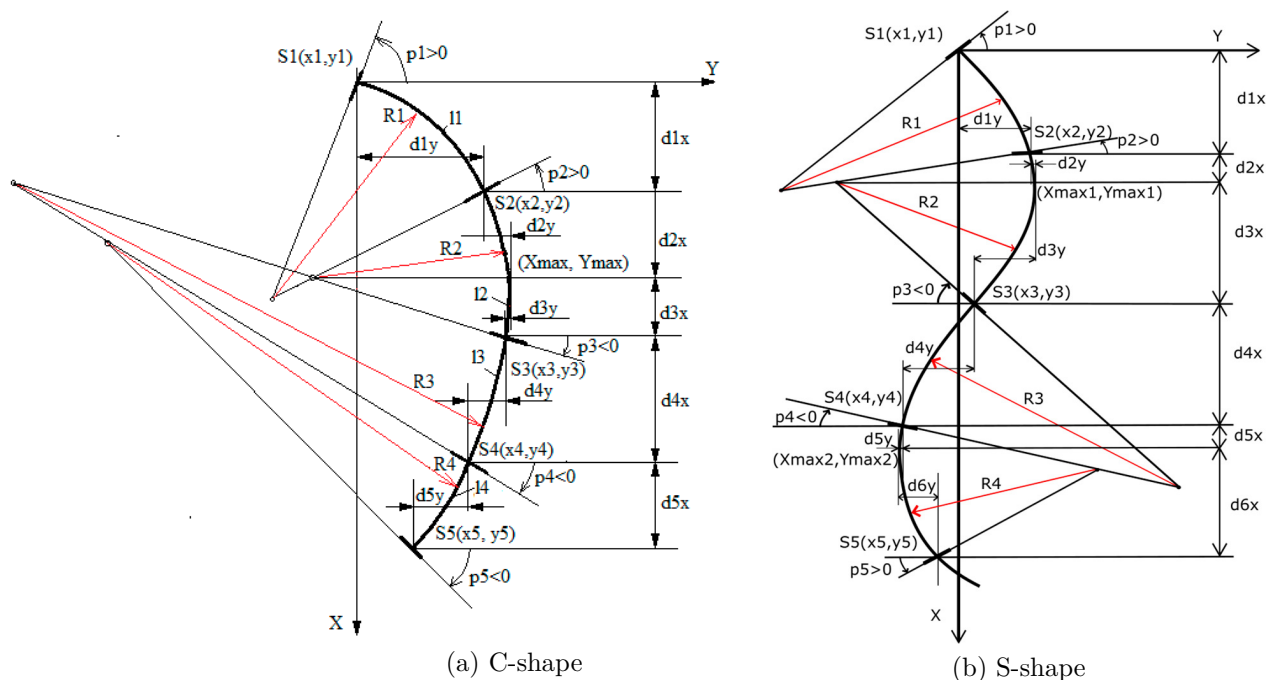
(a) C-shape

(b) S-shape

Figure 4.8: Geometric model of [227]: (**a**) C-shape;(**b**) S-shape.

towards the person's head (longitudinal axis) and the X axis is perpendicular to the person's A-P plane (frontal axis) as shown in figure 4.9a. With the orientation of the sensor around the X-axis, we can obtain the orientation of the spine in the sagittal plane because such orientation is directly the pitch, the 3rd Euler angle.

In our case we have taken as reference the upper sensor, the closest to the head, and depending on whether the angle increment is positive or negative there are only two arc possibilities (concave or convex). Since the distances between sensors are constant, we can obtain the relative position to the next point. Using translation matrices [39], the position and orientation of the next sensor can be calculated as a rotation whose radius is proportional to the angle increase and to the distance between sensors. The translation matrix that allow us to obtain the coordinates of sensor $i + 1$ with respect to sensor i is given by:

(a) Body planes

(b) Spine model
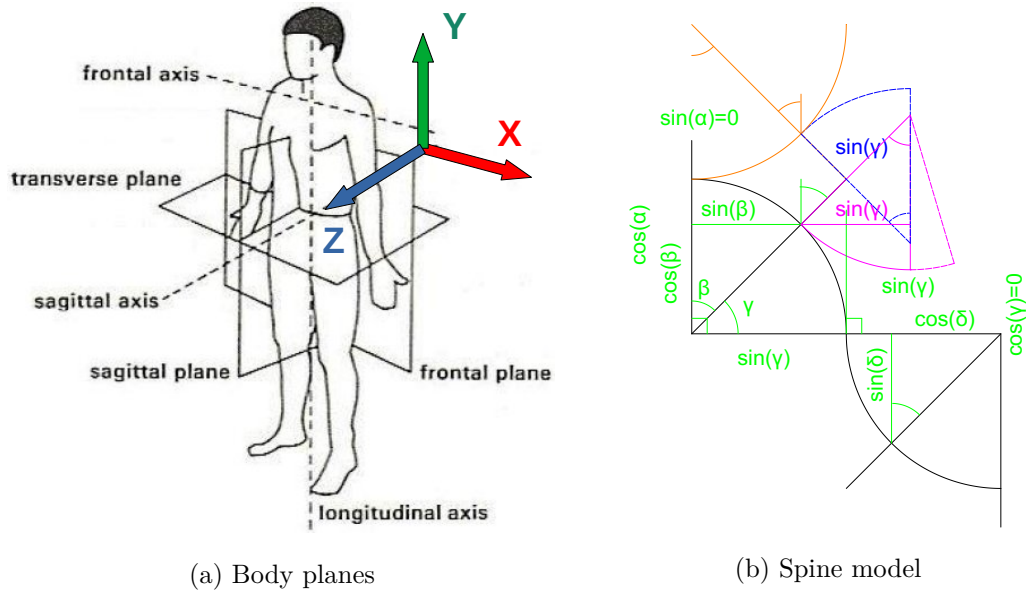
Figure 4.9: Spine reference system: (**a**) Body planes, Image from [199]; (**b**) Body angles reference.

$$\Delta\alpha = \alpha_{i+1} - \alpha_i; \quad C = sign(\Delta\alpha); \quad R_{i,i+1} = |l_{i,i+1}/\Delta\alpha|$$

$$T_i^{i+1} = \begin{pmatrix} 1 & 0 & C * R_{i,i+1} \cdot \sin(\Delta\alpha) \\ 0 & 1 & C * R_{i,i+1} \cdot (1 - \cos(\Delta\alpha)) \\ 0 & 0 & 1 \end{pmatrix} \begin{pmatrix} \cos(\Delta\alpha) & -\sin(\Delta\alpha) & 0 \\ \sin(\Delta\alpha) & \cos(\Delta\alpha) & 0 \\ 0 & 0 & 1 \end{pmatrix}$$

$$(4.4)$$

where $l_{i,i+1}$ is the distance between consecutive sensors and α_i are angles around X for sensor i.

To get the position of a given sensor with respect to sensor 1, equation 4.4 has to be applied sequentially: $\prod_{j=1}^{i} T_j^{j+1}$. The resulting matrix allows obtaining the coordinates of sensor $i + 1$ after multiplying it by the initial vector $(0, 0, 1)^T$, the position of the first sensor [39].

These coordinates have been used to check the orientation visually in the computer, to test the right operation of the sensor system and to debug it.

4.3   Measurement protocol, data processing and evaluation

For user measurements, the spine measurement system and a PSM (Kplain_Velo_150, see table 2.3) placed on a meditation cushion (see figure 4.10a) were used. The PSM was fixed with Velcro straps attached to the cushion and the mat itself, preventing their relative displacement. As the sensors of the spine measurement device have a self-calibrating routine, the sensors are started on a flat table, pointing toward the same direction. Then, they are moved a little until the sensors are calibrated. Finally, they are placed on the user's back. This allows us to know the initial orientation and ensure the operation of the sensors before the test with the user.

Once the spine measurement device has been firmly placed, as shown in figure 4.10, the volunteer sits on the meditation cushion (see figure 4.10c). Then the volunteer is asked to bounce a little to facilitate the signal synchronization in the data processing.

(a) Meditation cushion with PSM on it

(b) Spine measurement device properly attached

(c) Fontal view of the attached device

Figure 4.10: Spine meditation systems: (**a**) Meditation pillow with PSM; (**b**) Back image of meditation volunteer; (**c**) Frontal image of meditation volunteer.

Volunteers are then asked to maintain an appropriate position (straight back) on the cushion for 30 seconds. Then they have to lean forward for 30 s and backwards for other 30 s. Subsequently, volunteers have been asked to repeat the bounces and to slowly rock back and forth (between the three previous postures),

performing several swings. Finally, users are asked to repeat the slow bounces and swings again.

The trial was conducted by 12 participants (5 men, 7 women), who performed the exercise 3 times on different days. Basic data of volunteers can be found on table 4.2.

Table 4.2: Basic data of the meditation volunteers

	mean	SD
age (years)	32	14
weight (kg)	62	9
height (m)	1.68	0.07

Conductance measured by the PSM has been processed to remove crosstalk (section 2.1.4) and subsampled to the sampling frequency of the spine measurement device. If all the angles are added together to get a single value and the cell signals in the PSM are added too to get another single value, there is a clear relation between data obtained from the spine measurement device and data coming from the PSM. Figure 4.11 shows both temporal series. The signals have been scaled to represent them (the scaling means subtracting the average and divide the result by that average).
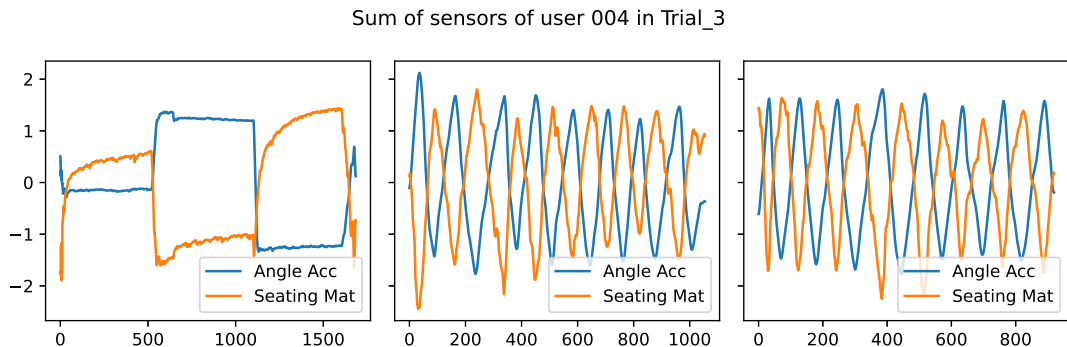
Figure 4.11: Cumulative value of sensors obtained by a volunteer.

Due to the relation obtained between these signals, they have been used for the alignment of otherwise not synchronized data from the mat and the spine measurement device. This is a semi manual process similar to the one explained in section 3.2.1 for balance tests.

It should be noted that despite the relationship found between the data coming from both instruments, the values of the back angles are the ultimate data to

be recovered. Due to the complexity of the problem and to the fact that the PSM obtains pressure images, we resorted to the use of techniques similar to image classification. Therefore, and after some preliminary analysis with other relational techniques (Factor analysis, Principal Components Analysis), a CNN was selected for this regression problem. This structure has been previously used to classify pressure images like in [179].

Each pressure image is normalized, so that the mean is subtracted from each cell of the input image and the result is divided by the SD. The mean and deviation values are taken to be the mean and SD of all the cells of the images in the training set. This normalization process is performed before passing the images to our CNN. In this case it is assumed that the conductance and pressure are proportional.

In the design process of our network we mimicked the structure of the Alexnet [112] network, which features an internal structure of three input convolutional layers followed by three fully connected layers. But our input frames present very small dimensions (16x16). Thus, temporal windows of size 50 have been first extracted (overlapping with stride 1). Each window gives rise to a small video of size 50x16x16, which is then resized as a 50x256 image. Given this flattened image as input to our network it must be able to reconstruct the temporal average value of each of the angles obtained by the spine measurement device. The diagram of the network used can be seen in the figure 4.12.
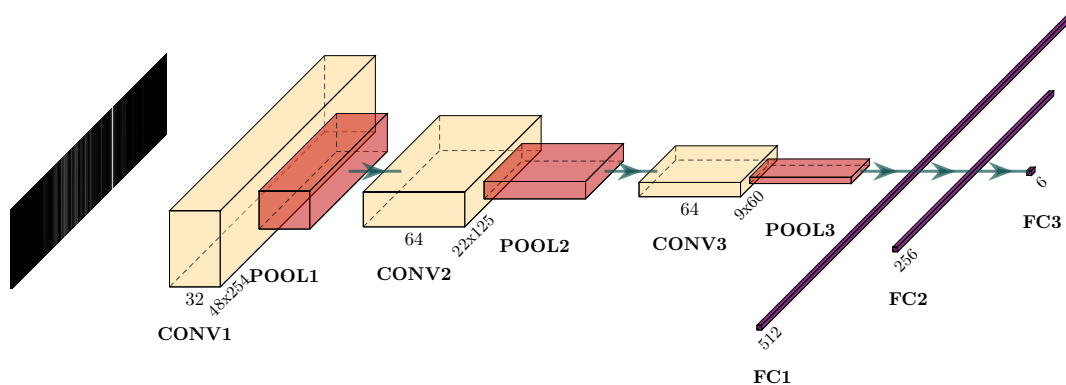
Figure 4.12: CNN diagram

According to the diagram shown, our network has a first convolutional layer

of 32 3x3 filters with Rectified Linear Unit (ReLU) activation function followed by a MaxPooling for 2x2 averaging and stride of 1. This is followed by another convolutional layer of 64 3x3 filters with ReLU activation and another MaxPooling layer for 2x2 averaging and stride of 1. This layer is followed by a third convolutional layer of 64 filters 3x3 ReLU and MaxPooling 2x2. The result of these layers is resized to a vector with 7680 components. This vector is passed to three Dense layers (also named Fully Connected) in a similar way to an MLP. The first layer is dense with 512 neurons and LeakyReLU activation function. The second layer is dense too with 256 neurons and LeakyReLU activation. Finally, the third layer would correspond to the output layer presenting 6 neurons without activation function. The activation functions have been selected in this way because the pressure values do not present negative data (convolutional part) but the angles we wish to obtain can be negative (dense part). The weights of the network have been initialized with respect to the Kaiming criterion [93]. The output of the network presents the estimate of the angles (in radians) together with their sum. An output of 0 means a completely straight spine. The sum has been included in the network output in order to facilitate the training process in view of the relationship between the sum of the cell outputs in the PSM and this value.

The data recorded during the experiment is subjected to the window extraction process as explained above. Then it is divided in train, validation and test data set with about 41000, 3500 and 18000 samples respectively.

Two different options for the partition of the data have been considered. They are summarized in table 4.3. On the one hand, in one of the partitions different subjects are considered in the training, validation and data sets, option Leave Subjects Out (LSO). Nine volunteers are included in the training data, one in the validation set and the remaining three are included in the test set. In this way, the CNN faces data from people who are not in the training set. On the other hand, in the option Keep Subjects In (KSI) the same volunteers are included in the training, validation and test sets, with a proportion of extracted windows as 70 %, 10 % and 20 % respectively.

Several techniques have been used in the training process to reduce the difference between the predictions of the PSM and the values given by the spine measurement device. One of them is the use of normalization and drop out layers (0.2) in the network structure. Data augmentation techniques have also been ap-

Table 4.3: Correspondence of Participants (P) for each option of data partition.

	Train	Validation	Test
Leave Subjects Out (LSO)	P1 to P8	P9	P10 to P12
Keep Subjects In (KSI)	P1 to P12	P1 to P12	P1 to P12

plied: the pressure images have been subjected to rotations ($\pm15°$), displacements (±5 cells), lateral symmetry operations, scaling by a factor 1/2 or 2 and blurring. The aim of this data augmentation would be to make the results obtained more independent of the position on which the user had sat with respect to the PSM, and trying to make the network output not dependent on the user. This is because under all these operations the back will be in the same posture while the pressure image is proportional to the original one just with some translation, rotation, etc.

Concerning the training algorithm, our first option was the classical Stochastic Gradient Descent (SGD). However, according to [168], the Adaptive Moment Estimation (Adam) optimizer would have an improved capacity to find solutions in problems similar the one under study in this document. So that we turned out to Adam, confirming that the results improved. Furthermore, a decay was applied during training to regularize the network, Adaptive Moment Estimation with Weight Decay (AdamW).

The CNN has been trained on the same computer on which the tests of the section 2.2.2 were performed (Intel® Core™ i7-8700 CPU @ 3.20GHz) which has a NVIDIA GeForce GTX 1050 Ti graphic card. The CNN has been implemented in the Python programming language with the Pytorch machine learning library, which has GPU support.

As metrics in the training process, we have applied as a loss function the MSE, equation 4.2, which is the typical function in regression problems as in our case, together with the R2 score of the TorchMetrics package, equation 4.3, which is also typically found to quantify the goodness of fit in regression problems.

4.4 Results and discussion

After training the network, the following results (shown in figures 4.13 and 4.14) are obtained on the validation and test set respectively, KSI training option.

These results indicate the values estimated by our model reconstructions from the PSM readings versus the values of the spine tilt angles. The sensors are numbered from the sensor in the cervical area to the sensor closest to the sacrum. In both figures, the last graph represents the plot of the sensor sum, which is and independent prediction of the CNN. These data show the possibility of reconstructing spine inclinations from pressure maps. However, the results correspond to the option KSI, i.e., when training set contains data from volunteers whose data are also in test set. For such a model to become practical for real case, if a new volunteer is going to use the system a kind of calibration stage would be required. In this stage the new volunteer should perform a series of known movements with the spine measurement system and the PSM together, as it was done in our protocol. The model should be trained again to adapt to possible variations in the pressure maps of the new individual.
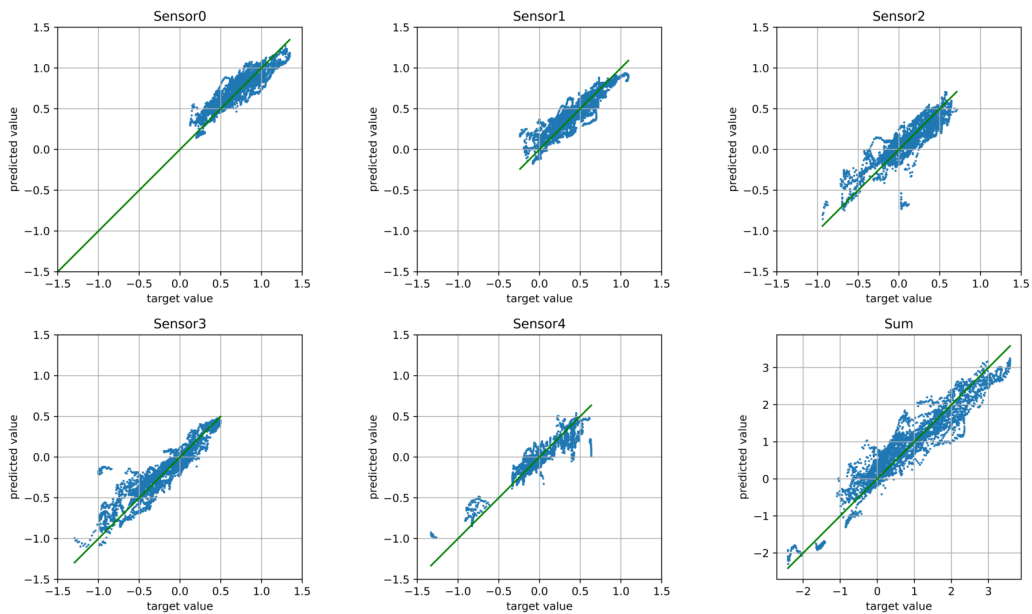
Figure 4.13: Result on the validation set with KSI partition

For the LSO option, the same results are obtained in figures 4.15 y 4.16 for the validation and test sets. The results are not satisfactory and clearly worse than for the other option, KSI. Thus, if a subject is not in the training set, the CNN does not seem to be able to predict the spine posture. Only the sensors 0, 1, and the total sum might resemble to the prediction.

Table 4.4 shows the R2 score. The numerical results confirm the visual inspection of the figures. For KSI the score is good, higher than 0.75 both for test
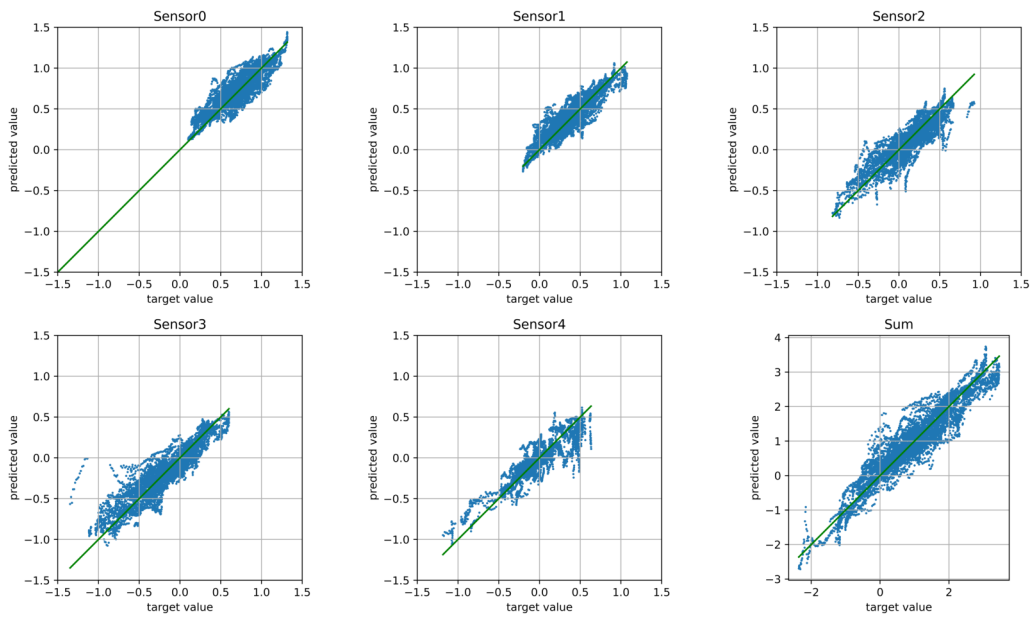
Figure 4.14: Result on the test set with KSI partition.
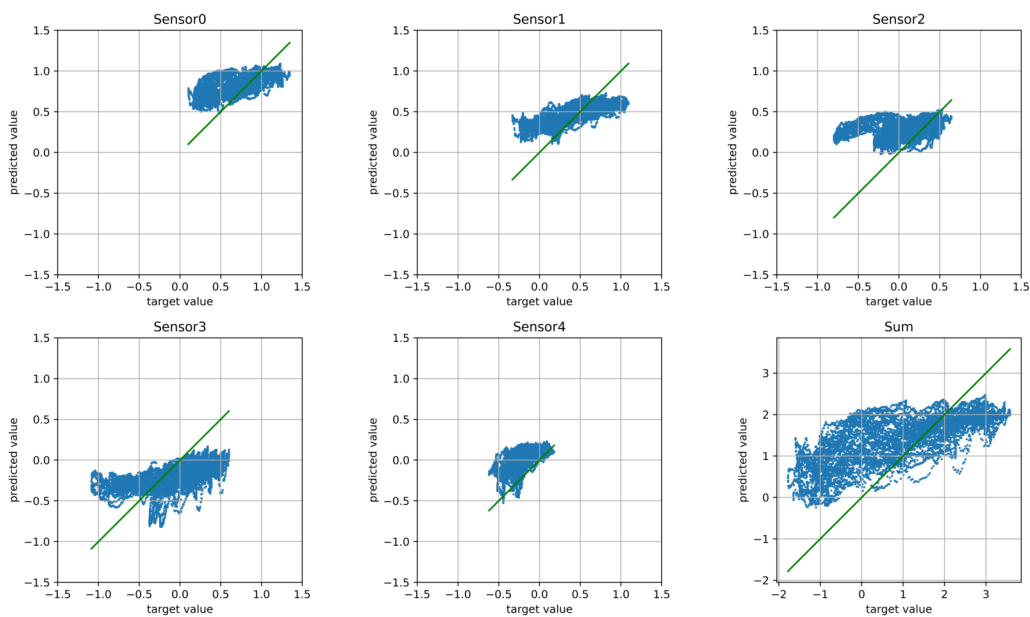
Figure 4.15: Result on the validation set with LSO partition

and validation sets. On the other hand, for the LSO option the value is rather low. For instance, in the test set the R2 score is different from 0 (up to the third decimal place) only for sensors 0, 1 and the sum, but they do not reach even 0.5.
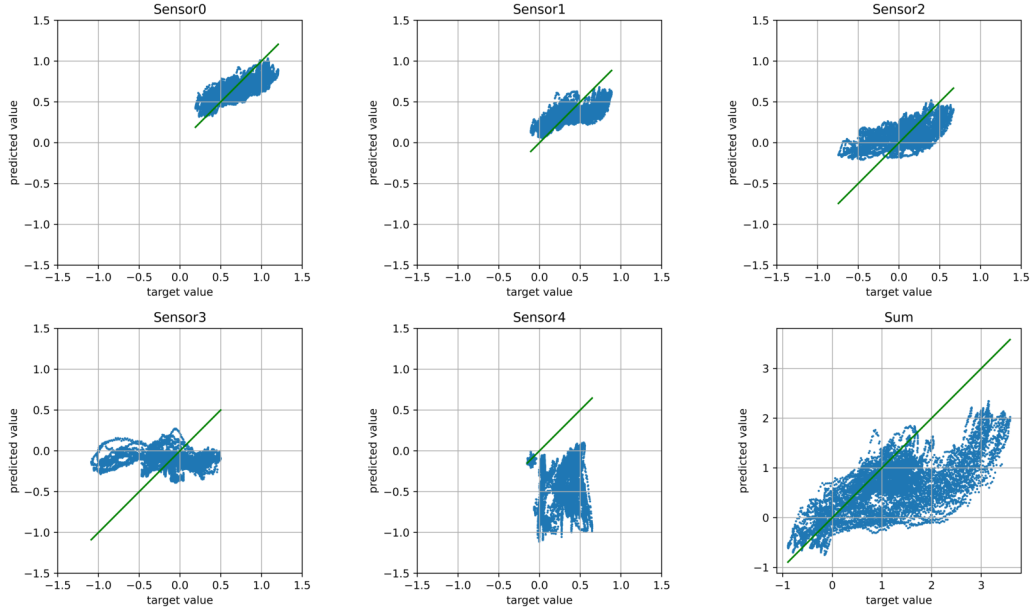
Figure 4.16: Result on the test set with LSO partition

Table 4.4: MSE and R2 scores of the predictions of the spine posture

| | | MSE | R2 score | | | | | |
	Subset		Sensor0	Sensor1	Sensor2	Sensor3	Sensor4	Sum
KSI	Validation	0.036	0.920	0.807	0.764	0.860	0.835	0.881
	Test	0.053	0.913	0.783	0.767	0.848	0.793	0.875
LSO	Validation	0.319	0.184	0.411	-0.372	0.202	-1.025	0.310
	Test	0.428	0.248	0.411	-0.073	-0.004	-2.446	0.253

4.5 Conclusions

We have designed and implemented a measuring device to detect the posture of the spine. The system could be used for the analysis and correction of posture in meditation. If the training data contains information of a person, then the implemented CNN is able to reconstruct the spine tilt angles with an R2 score very reasonable (higher than 0.75 or 0.8 for most angles). This is a remarkable result considering the difficulty of the task: extracting the tilt of the spine in several parts such as the cervical, lumbar or thoracic regions, which are far apart from the PSM that provides the pressure image. However, the performance decreases dramatically when the subject's data under study is not in the training set.

To further improve the performance, especially in the LSO case, there are

several options to test. One option would be to investigate the role of height, weight and other physical parameters in the predictions with a larger sample of volunteers. It might happen that the prediction is better if a person with similar characteristics to those of the subject under study has been taken into account in the training. We could even try to include those characteristics as inputs of the ML system. Another issue to be studied is the sensor location. Since the distance between the sensors is constant, that means that the vertebra on which it is attached depends on the volunteer. This can alter the prediction capacity. It might happen that modeling the spine with a refined geometrical model could help to predict it, instead of using directly the sensor outputs.

Chapter 5

Conclusions and future directions

OW cost prototypes of PSMs have been successfully manufactured. They have been utilized in two health related applications. Thus, the goals of the thesis have been achieved.

The prototypes improve a previous version in relevant aspects. The sampling frequency can reach 165 Hz, which is already suitable for most health studies. Low-level programming of the DAQ system was required to achieve this data transfer rate, in addition to using USB for transmission. The manufacturing process is based on standard techniques so that it is more repetitive and less prone to errors. The DAQ circuit has been kept to the minimum thanks to the IECM crosstalk elimination algorithm that can be run in real time. Besides, a source of uncertainty associated with the noise in the measurement and the IECM algorithm has been characterized. Higher resistances cannot be obtained accurately, but they correspond to very low pressures, which will often be irrelevant. The nonlinear sensor output with the interdigital electrode has been measured and modeled: hysteresis with an MPI model and creep as a sum of first order systems. The model captures the time trend observed in Velostat but only to a certain extent, as the goodness of fit is uneven. However, it has been shown that Velostat shows less nonlinear effects than the other two materials analyzed.

In one of the applications to human balance studies, it has been found that the sensor modeling helps to reduce the differences between the PSM and the FP (up to 37% improvement in trajectory distance with respect to a simple proportional model). However, a conductance scaling factor is required to achieve these results. This scaling factor ensures that the measured pressure is coherent with the weight of the person performing the tests. Resolution is another important factor that

can improve the results, although it is necessary to pay attention to figures of merit directly associated with the CoP trajectories to realize this.

With respect to posture monitoring, an exploratory study has been performed to recover spine posture from pressure images in sitting meditation. The implemented system has shown to accurately predict the tilt angles of the spine (R2 score higher than 0.75) but only provided that the volunteers data have been included in the training set, which limits the application of the system.

There are several open questions for future research. To further improve the prototypes, the resolution should be increased and the sensor modeling improved. With respect to the resolution, it has to be tested whether or not IECM can also run in real time for a larger array. Anyway, other DAQ circuits can remove the main crosstalk but an analysis of economic cost in detail should be carried out. Moreover, other sources of uncertainty in the circuit can be analyzed. With respect to sensor modeling, the main problem of high variability between cells remains. Practical equilibration and calibration techniques for a large mat would be welcome (using a dead weight or a motorized tip to exert pressure are likely to be inaccurate or slow). Furthermore, although a model of hysteresis and creep has been fitted, there are several options available in previous studies of non linear sensor behavior and there is room for improvement. Creep is more complex than the relatively simple model used in this thesis and the current goodness of fit is rather irregular depending on the pressure cycle repetition.

Finally, the exploratory analysis of posture monitoring can be further extended to include variables such as height, weight, sex, etc. in the prediction system to increase the prediction R2 score when the ML system faces a person not included in the training set.

Chapter 6

Conclusiones y perspectivas de futuro

S e han desarrollado completamente varios prototipos de PSMs de bajo coste. Dichos prototipos han sido utilizados en dos aplicaciones relacionadas con el ámbito de la salud. Por ello, los objetivos de la tesis han sido alcanzados.

Los prototipos mejoran una versión previa en aspectos relevantes. La frecuencia de muestreo puede alcanzar 165 Hz, que es ya adecuada para la mayoría de estudios de salud. La programación a bajo nivel del sistema DAQ, junto con el empleo de la transmisión por USB son necesarios para alcanzar este ratio de transferencia de los datos. El proceso de manufactura está basado en técnicas convencionales por lo que es más repetitivo y menos propenso a errores. La complejidad del circuito DAQ ha sido mantenida al mínimo gracias al algoritmo de eliminación de "crosstalk", IECM, que puede ser ejecutado en tiempo real. Además, una fuente de incertidumbre asociada con el ruido de la medida y el algoritmo IECM ha sido caracterizada. Las resistencias elevadas no son obtenidas de forma precisa, pero se corresponden a presiones muy bajas, las cuales suelen ser irrelevantes. La salida no lineal del sensor con el electrodo interdigital ha sido medida y modelada: la histéresis con un modelo MPI y el "creep" como la suma de sistemas de primer orden. El modelo captura la tendencia temporal observada en el Velostat, pero solo hasta cierto punto, ya que la bondad del ajuste es limitada. Sin embargo, se ha observado que el Velostat muestra menos efectos no-lineales que los otros dos materiales analizados.

En una de las aplicaciones al estudio del equilibrio humano, se ha encontrado

que el modelado del sensor ayuda a reducir las diferencias entre la PSM y la FP (hasta el 37% de mejora en la distancia de la trayectoria con respecto al modelo proporcional simple). Sin embargo, un factor de escalado de la conductancia es necesario para alcanzar estos resultados. Este factor de escalado asegura que la presión medida es coherente con el peso de la persona realizando el ensayo. La resolución es otro factor importante que puede mejorar los resultados, aunque es necesario prestar atención a las figuras de mérito directamente asociadas con las trayectorias del CoP para apreciarlo.

Con respecto a la medición de la postura, un estudio exploratorio ha sido realizado para recuperar la postura de la columna vertebral a partir de las imágenes de presión sobre un cojín de meditación. El sistema implementado ha mostrado predecir con precisión los ángulos de inclinación de la columna vertebral (coeficiente R2 mayor que 0.75) pero sólo cuando los datos de los voluntarios han sido incluidos en el conjunto de entrenamiento, lo que limita la aplicación del sistema.

Hay varias cuestiones abiertas para futuras investigaciones. Para una mejora mayor de los prototipos, la resolución debería incrementarse y el modelado del sensor debería ser refinado. Con respecto a la resolución, debe comprobarse si el IECM también puede ser ejecutado en tiempo real para una matriz más grande. De cualquier modo, otros circuitos de DAQ pueden eliminar el componente principal del "crosstalk" pero un análisis detallado del coste económico debería ser realizado. Además, otras fuentes de incertidumbre en el circuito pueden ser analizadas. Con respecto al modelado del sensor, el problema principal de la elevada variabilidad entre celdas persiste. Técnicas prácticas de equilibrado y calibración para una esterilla grande serían bienvenidas (emplear técnicas basadas en pesos muertos o una punta motorizada para ejercer presión es probable que sean inexactas o lentas). Además, aunque un modelo de histéresis y "creep" ha sido ajustado, existen diversas opciones disponibles en estudios previos sobre el comportamiento de sensores no lineales y hay margen para mejoras. El "creep" es más complejo que el modelo relativamente simple empleado en esta tesis y el ajuste actual es bastante irregular dependiendo de la repetición del ciclo de presión.

Finalmente, el análisis exploratorio de la medida de la postura puede ser extendido más para incluir variables tales como altura, peso, sexo, etc. en el sistema de predicción para incrementar el coeficiente R2 de la predicción cuando el sistema de ML se enfrenta a personas no incluidas en el conjunto de entrenamiento.

Appendix A

Publications and projects

A.1   Journal papers

- J. Martínez-Cesteros, C. Medrano-Sánchez, I. Plaza-García, R. Igual-Catalán and S. Albiol-Pérez, "A Velostat-Based Pressure-Sensitive Mat for Center-of-Pressure Measurements: A Preliminary Study," Int. J. Environ. Res. Public Health 2021, 18, 5958. https://doi.org/10.3390/ijerph18115958 (Q2 in PUBLIC, ENVIRONMENTAL & OCCUPATIONAL HEALTH - SCIE, Journal Impact Factor = 4.614).

- J. Martínez-Cesteros, C. Medrano-Sánchez, I. Plaza-García, and R. Igual-Catalán, "Uncertainty Analysis in the Inverse of Equivalent Conductance Method for Dealing With Crosstalk in 2-D Resistive Sensor Arrays," in IEEE Sensors Journal, vol. 22, no. 1, pp. 373-384, 1 Jan.1, 2022, doi: 10.1109/JSEN.2021.3129668 (In 2021: Q1 in INSTRUMENTS & INSTRU-MENTATION - SCIE, Journal Impact Factor = 4.325).

- J. Martínez-Cesteros, C. Medrano-Sánchez, J. Castellanos-Ramos, J.A. Sánchez-Durán, I. Plaza-García, "Creep and Hysteresis Compensation in Pressure Sensitive Mats for Improving Center of Pressure Measurements", sent to IEEE Sensors Journal.

A.2   Conferences:

- C. Medrano-Sánchez, J. Martínez-Cesteros, F. Arcega-Solsona and I. Plaza-García, "The approach to the concept of measurement error in the text-

books of Electronic Instrumentation," 2022 Congreso de Tecnología, Aprendizaje y Enseñanza de la Electrónica (XV Technologies Applied to Electronics Teaching Conference), Teruel, Spain, 2022, pp. 1-7,
doi: 10.1109/TAEE54169.2022.9840680.

- J. Martínez-Cesteros, C. Medrano-Sánchez and I. Plaza-García, Esterilla táctil inteligente de bajo coste para la medida de la estabilidad y la postura, XV Congreso de Tecnología, Aprendizaje y Enseñanza de la Electrónica, Teruel, Spain, 2022 (Panel doctoral).

A.3 Other publications:

A list of publications in which the author has collaborated but not directly associated to the PhD is also included:

- S. Domínguez-Gimeno, C. Medrano-Sanchez, R. Igual-Catalán, J. Martínez-Cesteros, I. Plaza-García, "An Optimization Approach to Eliminate Crosstalk in Zero Potential Circuits for Reading Resistive Sensor Arrays,", Submitted to IEEE Sensors Journal.

- R. Igual-Catalán, M. Abián Vicén, J. Abril Servisé, M. Rahmouni, G. Díaz Fuertes, S. Domínguez Gimeno, J. Martínez Cesteros, C. Medrano Sánchez, "Experiencias interdisciplinares en el aprendizaje de la ingeniería electrónica, eléctrica y química", XV Congreso de Tecnología, Aprendizaje y Enseñanza de la Electrónica, Teruel, Spain, 2022.

A.4 Projects

- Instrumentación Inteligente y Aplicación en Salud (Intelligent Instrumentation and Application on Health), Grant PID2021-125091OB-I00, supported by MCIN/AEI/10.13039/501100011033 and by "ERDF A way of making Europe". From January 1, 2022 to December 31, 2024. Main researchers: F. Vidal and J.A. Hidalgo.

- Education-Quality-Technology (EduQTech), supported by Departamento de Ciencia, Universidad y Sociedad del Conocimiento del Gobierno de Aragón under Grant T49_20R, 2020-2022. Main researcher: C. Medrano.

A.5 PhD Grants

- PhD grant from Spanish "Ministerio de Ciencia, Innovación y Universidades" FPU-18/04282.

- Mobility grant for short stays, EST22/00325, Spanish "Ministerio de Universidades".

Appendix B

Proof of the equation to find the derivative of equivalent conductances with respect to cell conductances

This section is based on the supplementary material of [149] (© 2022 IEEE).

In this supplementary material we derive the equation stated in the document that shows the derivative of the equivalent conductances with respect to cell conductances. This is the equation that supports all the rest of numerical development for finding uncertainty in the cell resistances when using IECM:

$$\frac{\partial G_{ip}}{\partial g_{jq}} = \frac{(V_{ip,j} - V_{ip,q})^2}{(V_{ip,p} - V_{ip,i})^2} \tag{B.1}$$

The notation is explained in the main text of the document, section 2.3.

The starting point of the proof is the equation that relates the equivalent conductance between row i and column p to the voltages of the associated circuit as:

$$G_{ip} = \frac{I_{ref}}{V_{ip,p} - V_{ip,i}} \tag{B.2}$$

where $\mathbf{V}_{ip}$ is the solution of the following equation:

$$\mathbf{C}\mathbf{V}_{ip} = \mathbf{I}_{ip} \tag{B.3}$$

A specific example will also be worked out for some steps of the proof to make it clear. For instance, figure B.1 shows the circuit that should be solved to find the equivalent conductance between row 3 and column A in a 3 x 3 resistor array, for which we could write:

$$G_{3A} = \frac{I_{ref}}{V_{3A,A} - V_{3A,3}} \tag{B.4}$$

It is worth noting a subtlety of the notation used in this appendix. In matrices like $\mathbf{C}$, its derivatives, or vectors like $\mathbf{V}_{ip}$ or $\mathbf{I}_{ip}$, rows and columns are not labeled with consecutive numbers as usual but with the name of the node in the corresponding circuit. For instance in a 3 x 3 RSA the labels are in the set $\{2, 3, A, B, C\}$ (node 1 is ground), see the example in figure B.1 for the matrix $\partial \mathbf{C}/\partial g_{2B}$ that we will use below.

Taking the partial derivative of equation B.2 with respect to a generic g_{jp} leads to:

$$\frac{\partial G_{ip}}{\partial g_{jq}} = -\frac{I_{ref}}{(V_{ip,p} - V_{ip,i})^2} \left(\frac{\partial V_{ip,p}}{\partial g_{jq}} - \frac{\partial V_{ip,i}}{\partial g_{jq}} \right) \tag{B.5}$$

As a specific example, one of the derivatives for a 3x3 RSA would be:

$$\frac{\partial G_{3A}}{\partial g_{2B}} = -\frac{I_{ref}}{(V_{3A,A} - V_{3A,3})^2} \left(\frac{\partial V_{3A,A}}{\partial g_{2B}} - \frac{\partial V_{3A,3}}{\partial g_{2B}} \right) \tag{B.6}$$

Let us work out the first partial derivative in the right hand side of equation B.5. The voltage $V_{ip,p}$ is the row p component of $\mathbf{V}_{ip}$. This vector is the solution of the circuit equation $\mathbf{CV}_{ip} = \mathbf{I}_{ip}$ (see figure B.1 for a specific example), which is formally:

$$\mathbf{V}_{ip} = \mathbf{C}^{-1}\mathbf{I}_{ip} \tag{B.7}$$

The p component can be set as:

$$V_{ip,p} = (\mathbf{V}_{ip})^T \mathbf{1}_p = \mathbf{I}_{ip}^T \mathbf{C}^{-1} \mathbf{1}_p \tag{B.8}$$

where the notation $\mathbf{1}_p$ refers to a column vector in which all the elements are zero except the row p and we have taken into account that $\mathbf{C}$ is symmetric.

Then we use the following equation [175] for the derivative of the inverse of a matrix $\mathbf{Y}$ with respect to a variable x:
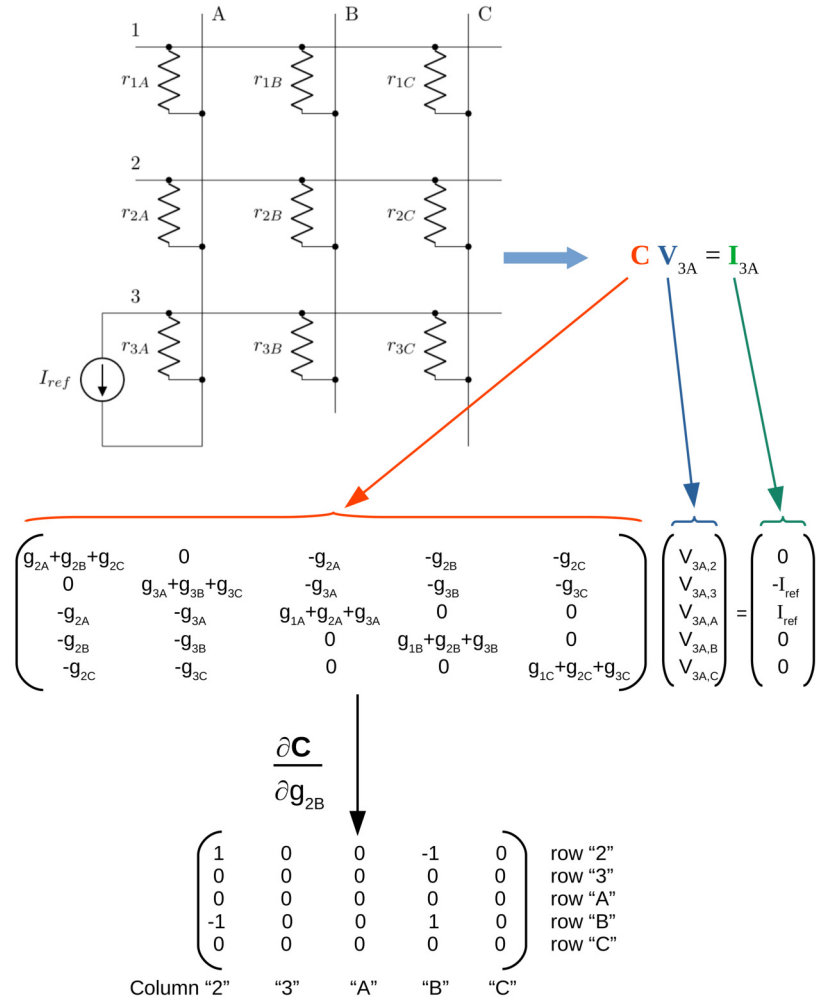
Figure B.1: Example circuit in a 3 x 3 resistive sensor array to calculate the equivalent conductances between nodes 3 and A. Node 1 is taken as ground. [149] (© 2022 IEEE)

$$\frac{\partial \mathbf{Y}^{-1}}{\partial x} = -\mathbf{Y}^{-1}\frac{\partial \mathbf{Y}}{\partial x}\mathbf{Y}^{-1} \tag{B.9}$$

to find the following relation:

$$\frac{\partial V_{ip,p}}{\partial g_{jq}} = -\mathbf{I}_{ip}^T \mathbf{C}^{-1}\frac{\partial \mathbf{C}}{\partial g_{jq}}\mathbf{C}^{-1}\mathbf{1}_p \tag{B.10}$$

Using equation B.7, $\mathbf{I}_{ip}^T\mathbf{C}^{-1} = \mathbf{V}_{ip}^T$, so that the expression can also be set as:

$$\frac{\partial V_{ip,p}}{\partial g_{jq}} = -\mathbf{V}_{ip}^T\frac{\partial \mathbf{C}}{\partial g_{jq}}\mathbf{C}^{-1}\mathbf{1}_p = -\mathbf{V}_{ip}^T\frac{\partial \mathbf{C}}{\partial g_{jq}}\mathbf{C}_p^{-1} \tag{B.11}$$

where we introduce the notation $\mathbf{C}_p^{-1}$ to refer to column p of $\mathbf{C}^{-1}$ since the product $\mathbf{C}^{-1}\mathbf{1}_p$ extracts that column due to the definition of $\mathbf{1}_p$.

In the specific 3x3 RSA example, we are going to calculate the partial derivative of $V_{3A,A}$ with respect to g_{2B}:

$$\frac{\partial V_{3A,A}}{\partial g_{2B}} = -\mathbf{V}_{3A}^T \frac{\partial \mathbf{C}}{\partial g_{2B}} \mathbf{C}^{-1}\mathbf{1}_A \tag{B.12}$$

All the reasoning that follows is applied in this case as shown in figures B.1 and B.2 step by step.

Equation B.11 can be simplified because the matrix $\frac{\partial \mathbf{C}}{\partial g_{jq}}$ turns out to be sparse, with almost all the elements equal to zero. To see this, we must be aware that g_{jq} appears only when the Kirchhoff's current law is applied to node j and its connection to node q, or to node q and its connection to node j. Thus, g_{jq} only enters in the left part of equation B.3 for rows j and q. We could write informally rows j and q of $\mathbf{CV}_{ip}$ respectively as:

$$g_{jq}(V_{ip,j} - V_{ip,q}) + \cdots \tag{B.13}$$
$$g_{jq}(V_{ip,q} - V_{ip,j}) + \cdots \tag{B.14}$$

Thus, the matrix $\frac{\partial \mathbf{C}}{\partial g_{jq}}$ has only some non-zero elements in rows j and q:

$$\left(\frac{\partial \mathbf{C}}{\partial g_{jq}}\right)_{\alpha\beta} = \begin{cases} 1 & \text{if } \alpha = \beta = j \quad \text{or} \quad \alpha = \beta = q \\ -1 & \text{if } \alpha, \beta = j, q \quad \text{or} \quad \alpha, \beta = q, j \\ 0 & \text{otherwise} \end{cases} \tag{B.15}$$

In figure B.1 the matrix $\partial \mathbf{C}/\partial g_{2B}$ is shown as a specific example.

Thus, the product $\frac{\partial \mathbf{C}}{\partial g_{jq}}\mathbf{C}_p^{-1}$ is a vector whose elements are zero except for rows j and q, in which they take the same value, $C_{jp}^{-1} - C_{qp}^{-1}$, except the sign:

$$\frac{\partial \mathbf{C}}{\partial g_{jq}} \mathbf{C}_p^{-1} = \begin{pmatrix} 0 \\ \cdots \\ 0 \\ C_{jp}^{-1} - C_{qp}^{-1} \\ 0 \\ \cdots \\ 0 \\ -C_{jp}^{-1} + C_{qp}^{-1} \\ 0 \\ \cdots \\ 0 \end{pmatrix} \tag{B.16}$$

See figure B.2 (steps 2 and 3) for the specific example.

Inserting equation B.16 back to equation B.11, we rewrite it as:

$$\frac{\partial V_{ip,p}}{\partial g_{jq}} = -\mathbf{V}_{ip}^T \begin{pmatrix} 0 \\ \cdots \\ 0 \\ C_{jp}^{-1} - C_{qp}^{-1} \\ 0 \\ \cdots \\ 0 \\ -C_{jp}^{-1} + C_{qp}^{-1} \\ 0 \\ \cdots \\ 0 \end{pmatrix} \tag{B.17}$$

where the only non zero elements of the vector in the right hand side are in rows j and q.

The operation in equation B.17 extracts voltages j and q with the suitable sign and a multiplicative factor:

$$\frac{\partial V_{ip,p}}{\partial g_{jq}} = -(C_{jp}^{-1} - C_{qp}^{-1})(V_{ip,j} - V_{ip,q}) \tag{B.18}$$

In figure B.2 (step 4) the final result is presented for the specific case described above.

$$\frac{\partial V_{3A,A}}{\partial g_{2B}} = -V_{3A}^T \frac{\partial C}{\partial g_{2B}} \mathbf{C}^{-1} 1_A$$

Step 1

$$-(V_{3A,2}, V_{3A,3}, V_{3A,A}, V_{3A,B}, V_{3A,C}) \begin{pmatrix} 1 & 0 & 0 & -1 & 0 \\ 0 & 0 & 0 & 0 & 0 \\ 0 & 0 & 0 & 0 & 0 \\ -1 & 0 & 0 & 1 & 0 \\ 0 & 0 & 0 & 0 & 0 \end{pmatrix} \begin{pmatrix} C_{22}^{-1} & C_{23}^{-1} & C_{2A}^{-1} & C_{2B}^{-1} & C_{2C}^{-1} \\ C_{32}^{-1} & C_{33}^{-1} & C_{3A}^{-1} & C_{3B}^{-1} & C_{3C}^{-1} \\ C_{A2}^{-1} & C_{A3}^{-1} & C_{AA}^{-1} & C_{AB}^{-1} & C_{AC}^{-1} \\ C_{B2}^{-1} & C_{B3}^{-1} & C_{BA}^{-1} & C_{BB}^{-1} & C_{BC}^{-1} \\ C_{C2}^{-1} & C_{C3}^{-1} & C_{CA}^{-1} & C_{CB}^{-1} & C_{CC}^{-1} \end{pmatrix} \begin{pmatrix} 0 \\ 0 \\ 1 \\ 0 \\ 0 \end{pmatrix}$$

Step 2

$$-(V_{3A,2}, V_{3A,3}, V_{3A,A}, V_{3A,B}, V_{3A,C}) \begin{pmatrix} 1 & 0 & 0 & -1 & 0 \\ 0 & 0 & 0 & 0 & 0 \\ 0 & 0 & 0 & 0 & 0 \\ -1 & 0 & 0 & 1 & 0 \\ 0 & 0 & 0 & 0 & 0 \end{pmatrix} \begin{pmatrix} C_{2A}^{-1} \\ C_{3A}^{-1} \\ C_{AA}^{-1} \\ C_{BA}^{-1} \\ C_{CA}^{-1} \end{pmatrix}$$

Step 3

$$-(V_{3A,2}, V_{3A,3}, V_{3A,A}, V_{3A,B}, V_{3A,C}) \begin{pmatrix} C_{2A}^{-1} - C_{BA}^{-1} \\ 0 \\ 0 \\ -C_{2A}^{-1} + C_{BA}^{-1} \\ 0 \end{pmatrix}$$ ← row "2"

← row "B"

Step 4

$$-(C_{2A}^{-1} - C_{BA}^{-1})(V_{3A,2} - V_{3A,B})$$

Figure B.2: Step by step calculation of $\partial V_{3A,A}/\partial g_{2B}$ for a 3 x 3 RSA. [149] (© 2022 IEEE)

In a similar manner, it can be shown that:

$$\frac{\partial V_{ip,i}}{\partial g_{jq}} = -(C_{ji}^{-1} - C_{qi}^{-1})(V_{ip,j} - V_{ip,q}) \tag{B.19}$$

Thus, we can introduce equations B.18 and B.19 into B.5 leading to:

$$\frac{\partial G_{ip}}{\partial g_{jq}} = \frac{I_{ref}}{(V_{ip,p} - V_{ip,i})^2} \left(C_{jp}^{-1} - C_{qp}^{-1} - C_{ji}^{-1} + C_{qi}^{-1}\right)(V_{ip,j} - V_{ip,q}) \qquad (B.20)$$

In the last equation B.20, some components of the solution $\mathbf{C}^{-1}\mathbf{I}_{ip}$ are obtained, recalling that the elements of vector $\mathbf{I}_{ip}$ are zero except for row i $(-I_{ref})$ and row p (I_{ref}). Therefore:

$$\left(C_{jp}^{-1} - C_{qp}^{-1} - C_{ji}^{-1} + C_{qi}^{-1}\right)I_{ref} =$$
$$\left(C_{jp}^{-1} - C_{ji}^{-1} - C_{qp}^{-1} + C_{qi}^{-1}\right)I_{ref} =$$
$$(\mathbf{C}^{-1}\mathbf{I}_{ip})_j - (\mathbf{C}^{-1}\mathbf{I}_{ip})_q = V_{ip,j} - V_{ip,q} \qquad (B.21)$$

For instance, in the 3x3 RSA example, we can identify $V_{3A,2} = (C_{2A}^{-1} - C_{23}^{-1})I_{ref}$ and $V_{3A,B} = (C_{BA}^{-1} - C_{B3}^{-1})I_{ref}$ in the formal solution:

$$\begin{pmatrix} V_{3A,2} \\ V_{3A,3} \\ V_{3A,A} \\ V_{3A,B} \\ V_{3A,C} \end{pmatrix} = \mathbf{C}^{-1}\mathbf{I}_{3A} =$$

$$\begin{pmatrix} C_{22}^{-1} & C_{23}^{-1} & C_{2A}^{-1} & C_{2B}^{-1} & C_{2C}^{-1} \\ C_{32}^{-1} & C_{33}^{-1} & C_{3A}^{-1} & C_{3B}^{-1} & C_{3C}^{-1} \\ C_{A2}^{-1} & C_{A3}^{-1} & C_{AA}^{-1} & C_{AB}^{-1} & C_{AC}^{-1} \\ C_{B2}^{-1} & C_{B3}^{-1} & C_{BA}^{-1} & C_{BB}^{-1} & C_{BC}^{-1} \\ C_{C2}^{-1} & C_{C3}^{-1} & C_{CA}^{-1} & C_{CB}^{-1} & C_{CC}^{-1} \end{pmatrix} \begin{pmatrix} 0 \\ -I_{ref} \\ I_{ref} \\ 0 \\ 0 \end{pmatrix} =$$

$$\begin{pmatrix} C_{2A}^{-1} - C_{23}^{-1} \\ C_{3A}^{-1} - C_{33}^{-1} \\ C_{AA}^{-1} - C_{A3}^{-1} \\ C_{BA}^{-1} - C_{B3}^{-1} \\ C_{CA}^{-1} - C_{C3}^{-1} \end{pmatrix} I_{ref} \qquad (B.22)$$

Thus, we finally get the equation used as the basis of the error propagation inserting equation B.21 into B.20:

$$\frac{\partial G_{ip}}{\partial g_{jq}} = \frac{(V_{ip,j} - V_{ip,q})^2}{(V_{ip,p} - V_{ip,i})^2} \tag{B.23}$$

There are several points that can be highlighted:

- Since node 1 has been set to ground, some of the parts of the derivation might seem to be meaningless if we had taken one of the indices as row 1 of the resistive array (node 1). For instance there is no row or column associated to node 1 in matrix $\mathbf{C}$ or vector $\mathbf{I}_{ip}$. However, the final result depends only on voltage differences, which are the only quantities physically relevant. By symmetry, the result must also be true even if node 1 is one of the indices.

- The partial derivative is always positive. This is expected because increasing the conductance of a particular cell will always increase the equivalent conductance of any pair of nodes.

- The case $j = i$, $q = p$ leads to $\frac{\partial G_{ip}}{\partial g_{ip}} = 1$. This is also expected since the equivalent resistance between row i and column p is the parallel circuit of r_{ip} and the rest of the network. Therefore, in terms of conductance:

$$G_{ip} = g_{ip} + \cdots \tag{B.24}$$

and then the partial derivative is 1.

Appendix C

Adaptation of IECM to QZPM

This section is based on [149] (© 2022 IEEE).

In this appendix we are going to show an example of the adaptation of IECM to other circuit configurations. In particular, we are going to adapt it to the kind of circuit shown in figure C.1a corresponding to QZPM. It was proposed by Hidalgo et al. [138]. It is a configuration derived from ZPM for sequential reading with few components. The switches can connect any row or column either to ground or to node V_{in}, the so-called connecting node. In figure C.1b the simultaneous connection of a row and a column is presented including the internal non zero switch resistances. It has been shown that a series of voltage measurements on the circuit output allows calculating cell conductances without the crosstalk due to non ideal switches. For an $N_R \times N_C$ matrix, the readings required are associated to different configurations of connections to the connecting node: i) column-row pairs ($N_R \cdot N_C$); ii) Only a single row at a time (N_R); iii) Only a single column at a time (N_C); iv) Different pairs column-column ($N_C \cdot (N_C - 1)/2$).

However, an assumption of QZPM is that the internal resistance of the switch is known and the same for all the components, $r_i = r^p = r_s$, where we have used the notation r_i/r^p for the internal resistance of the switch in row i/column p. The associated conductances are denoted as g_i and g^p. In this appendix, IECM is extended to the case in which the resistance is not known and even different for each switch. It is a more realistic situation because manufacturers provide typical values, but it would be hard to know them for a particular set of components unless a calibration procedure is devised.

For a given configuration of the switches when the row i and the column p are
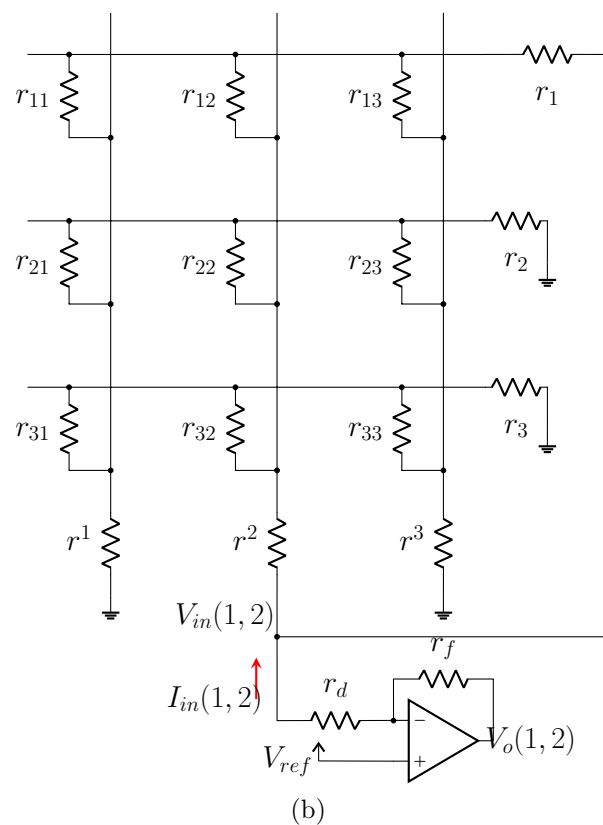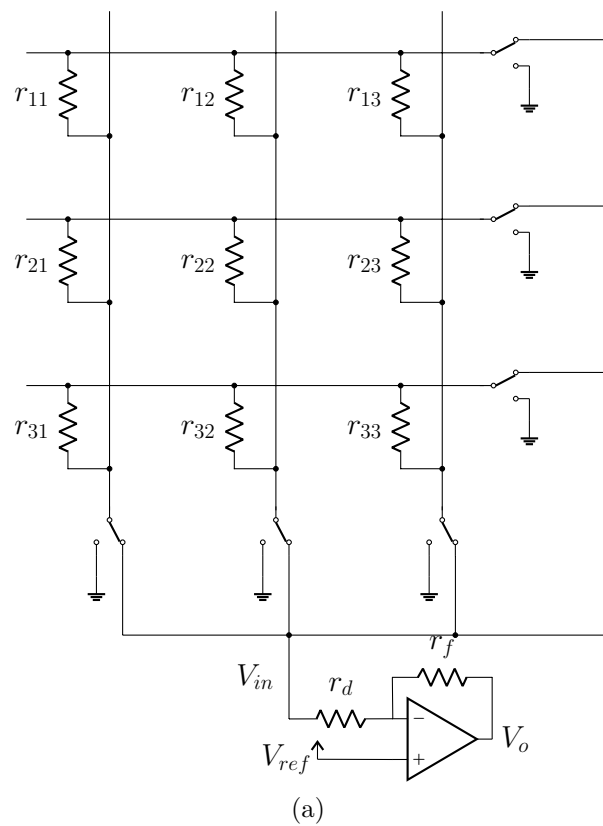
Figure C.1: (a) Circuit configuration of QZPM for a 3x3 array; (b) Example when row 1 and column 2 are connected to V_{in} (internal resistance of the switches included). [149] (© 2022 IEEE)

connected to the connecting node, the output voltage is measured, $V_o(i, p)$. The following convention is used: if either $i = 0$ or $p = 0$ it means that there is no row or column connected to it respectively. The equivalent conductance of the network between the connecting node and ground can be obtained by considering an ideal OA (figure C.1b). Firstly, the intensity that flows into the network, I_{in}, and the voltage at the connecting node, V_{in} can be calculated as:

$$I_{in}(i, p) = \frac{V_o(i, p) - V_{ref}}{r_f} \tag{C.1}$$

$$V_{in}(i, p) = V_{ref} - I_{in}(i, p) \cdot r_d \tag{C.2}$$

Then, the equivalent conductance of the network for that particular configuration is:

$$G_{exp,ip} = \frac{I_{in}(i, p)}{V_{in}(i, p)} \tag{C.3}$$

Thus, a set of equivalent conductances, which we denote globally as $\mathbf{G}_{exp}$, can be obtained experimentally from the set of measured voltages for different switch configurations.

On the other hand, if the set of conductances in the array and in the switches were known, another set of equivalent conductances could be obtained by solving Kirchhoff's laws in the corresponding configuration. For instance, formally the equivalent conductance can be obtained from the kind of circuit shown in figure C.2 for a 3x3 array. There are $N_R + N_C + 1$ nodes in the circuit, corresponding to row voltages, V_i, column voltages, V^p, and the connecting node V_{in}. If row i and column p are connected to the connecting node through the switches, then the equations to be solved are:

$$g_j(V_j - V_{in}\delta_{ji}) + \sum_{q=1}^{N_C} g_{jq}(V_j - V^q) = 0 \tag{C.4}$$

for row nodes $j = 1, \ldots, N_R$,

$$g^q(V^q - V_{in}\delta_{qp}) + \sum_{j=1}^{N_R} g_{jq}(V^q - V_j) = 0 \tag{C.5}$$

for column nodes $q = 1, \ldots, N_C$, and
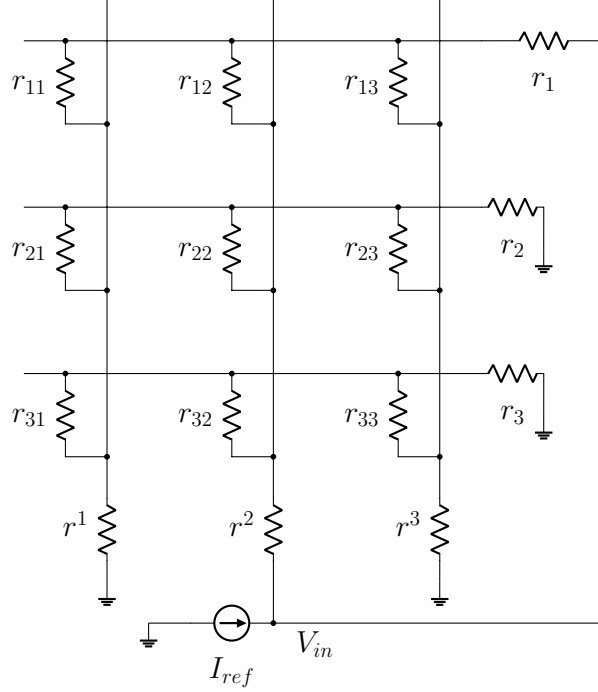
Figure C.2: Theoretical circuit to find the equivalent resistance of a 3x3 array when row 1 and column 2 are connected to the connecting node. [149] (© 2022 IEEE)

$$\sum_{j=1}^{N_R} \delta_{ij} g_j (V_{in} - V_j) + \sum_{q=1}^{N_C} \delta_{qp} g^q (V_{in} - V^q) = I_{ref} \qquad \text{(C.6)}$$

for the connecting node.

In equations C.4, C.5 and C.6, δ_{nm} is the Kronecker delta (1 if $n = m$, 0 otherwise). The notation is a bit succinct but allows considering the following cases: a row-column pair, a single row, or a single column connected to V_{in}. For instance, if $i = 0$, which means that there is no row connected to V_{in}, then δ_{ji} is always zero in equation C.4. This effectively removes V_{in} from the equation according to the lack of connection. The current injected, I_{ref}, is just a multiplicative constant and can be set to 1 in the implementation.

We note that the number of unknown parameters is $N_R \cdot N_C + N_R + N_C$. Therefore, for the adaptation of IECM only the row-column pairs, the single column and the single row connections were taken into account. The column-column connection readings were not required. If they were two columns, p_1 and p_2, connected to V_{in}, then the substitution of δ_{qp} by $\delta_{qp_1} + \delta_{qp_2}$ in equations C.5

Input: cell conductances g_{jq}, row switch conductances, g_j and column switch conductances, g^q with $j = 1, \cdots, N_R$ $q = 1, \cdots, N_C$

Output: Equivalent conductances G_{ip}, with $i = 0, \cdots, N_R$ $p = 0, \cdots, N_C$ for the configuration in which row i and column p are connected to the connecting node (0 index means no connection):

for all pairs (i, p) except $(0, 0)$ **do**

Solve equations C.4, C.5 and C.6

$G_{ip} \leftarrow \frac{I_{ref}}{V_{in}}$

end for

Figure C.3: Algorithm to find equivalent conductances for several configurations of the network. [149] (© 2022 IEEE)

and C.6 would be enough to get the right equations in this case.

Once equations C.4, C.5 and C.6 are solved, the equivalent conductance can be found as:

$$G_{ip} = \frac{I_{ref}}{V_{in}} \tag{C.7}$$

To sum up, a formal relation between the set of conductances, denoted globally as $\mathbf{g}$, and the set of equivalent conductances, $\mathbf{G}$, can be deduced using the algorithm in figure C.3. This relation is denoted $\mathbf{G} = \mathbf{F}(\mathbf{g})$ in short.

The numerical relation between $\mathbf{g}$ and $\mathbf{G}$ allows stating the problem of finding the unknown conductances as an optimization problem. The elements of $\mathbf{g}$ are found by minimizing the following cost function:

$$\|\mathbf{G}_{exp} - \mathbf{F}(\mathbf{g})\|^2 \tag{C.8}$$

subject to the constraints:

$$0 \leq g_{ip},\ 0 \leq g_i,\ 0 \leq g^p \tag{C.9}$$

To test the adaptation of IECM to QZPM we have considered a set of simulations. For different arrays sizes, random arrays of sensor resistances were obtained in the range $100\,\Omega$-$10\,k\Omega$. The resistances of the switches were also randomly distributed in the ranges $10 \pm 5\,\Omega$ or $10 \pm 1\,\Omega$. Firstly, the procedure explained in figure C.3 was applied to extract the equivalent conductances, which play the role of $\mathbf{G}_{exp}$ (in other words, an ideal set of experimental values). Then, we applied a least square approach to solve the minimization of the objective function C.8 and to test if the cell conductances could be recovered. Two kinds of simulations were

performed. On the one hand, a set of simulations were run with circuits having a single unknown switch resistance, the same for all the switches. In the implementation we forced $g_i = g^p = g_s$, a single parameter to be optimized other than the sensor matrix itself. On the other hand, we considered circuits in which each g_i and g^p was allowed to take its own value ($N_R + N_C$ additional free parameters).

Moreover, we also implemented the equations of QZPM [138] considering an ideal OA (equations C.1 and C.2) with $r_d = 100\,\Omega$, $r_f = 400\,\Omega$ and $V_{ref} = 1\,V$. QZPM assumes the same internal resistance for all the switches, which we took as $10\,\Omega$. In this way we could check the output of QZPM when the assumption is not true. The values of resistances are also taken from typical values shown in [138].

If the solution found by an algorithm for a cell is denoted as g'_{ip}, the absolute relative error (ARE) was obtained as:

$$\epsilon_{ip} = \left| \frac{g'_{ip} - g_{ip}}{g_{ip}} \right| \tag{C.10}$$

Ten simulations were repeated for each of the conditions considered above. The values of the ARE 95th percentile are reported in tables C.1 and C.2 for a single switch resistance (the same for all the switches) or for $N_R + N_C$ different switch resistances respectively. For QZPM a range of $\pm 1\,\Omega$ in $10\,\Omega$ induces errors in the system above 4%. The error increases with the size of the array. If the internal resistance range is $\pm 5\,\Omega$ the situation is even worse. On the other hand, IECM is able to recover cell values with high accuracy.

Nonetheless, comparing tables C.2 and C.1, it is clear that the IECM error is large when all the switch resistances are allowed to get a different value. This is likely to be related to the associated extra number of free parameters. It is known that optimization problems are much harder when the number of parameters increases and there might be several minima of the cost function. The errors for a particular simulation configuration are shown in figure C.4 (10x10 array, every switch allowed to get its own internal resistance in the range $10\pm5\,\Omega$). No trend is visually seen with respect to the x-axis, except for a slight increase in the QZPM error for very low values of conductance. The IECM errors are mainly below $1e-9$, but some points reach higher values. They are responsible for achieving a 95th percentile value of $8.7e-5$, table C.2. This fact also supports the idea that often the optimization algorithm ends at a point very close to the exact solution but that sometimes the distance to the solution is far larger, probably another

Table C.1: ARE for the adaptation of IECM to QZPM and the original QZPM implementation. The 95th percentile across all the simulation is provided. All the switches have the same resistance value, r_s, which was varied in two different ranges. QZPM assumed a fixed value ($10\,\Omega$). [149] (© 2022 IEEE)

| | Range $r_s = 10 \pm 5\Omega$ | | Range $r_s = 10 \pm 1\Omega$ | |
| | IECM 95th PCTL | QZPM 95th PCTL | IECM 95th PCTL | QZPM 95th PCTL |
size				
4x4	1.9e-10	0.28	2.0e-10	4.5e-2
6x6	5.3e-10	0.35	1.8e-12	7.7e-2
8x8	2.6e-10	0.53	1.0e-12	0.10
10x10	6.9e-11	0.89	2.6e-12	0.12
12x12	1.7e-11	1.4	2.0e-11	0.13

Table C.2: ARE for the adaptation of IECM to QZPM and the original QZPM implementation. The 95th percentile across all the simulation is provided. The switches in the circuit are allowed to have different values, which were varied in two different ranges. QZPM assumed a fixed value ($10\,\Omega$). [149] (© 2022 IEEE)

| | Range $r_s = 10 \pm 5\Omega$ | | Range $r_s = 10 \pm 1\Omega$ | |
| | IECM 95th PCTL | QZPM 95th PCTL | IECM 95th PCTL | QZPM 95th PCTL |
size				
4x4	4.7e-5	0.19	5.9e-10	4.2e-2
6x6	3.4e-11	0.24	1.4e-11	4.6e-2
8x8	1.7e-4	0.37	5.0e-10	6.5e-2
10x10	8.7e-5	0.40	6.5e-11	7.9e-2
12x12	8.0e-6	0.75	8.7e-4	0.11

minimum.

In conclusion, in our opinion it is worth studying numerical optimization methods within the context of crosstalk in RSA. They are more flexible and can overcome some of the assumptions of analytical methods. If the assumptions of the later are not fulfilled, relevant errors can appear in the system. In particular, we have adapted IECM to QZPM when the internal resistance of the switches is not known. Other aspects such as processing speed, effect of non-ideal OA, quantization error in ADC and noise were left out for future research because they are out of the scope of the present document.
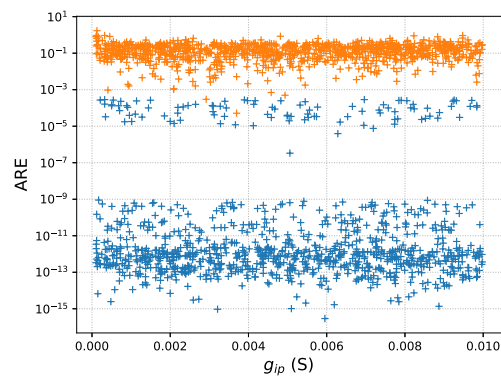
Figure C.4: ARE for a particular set of simulations: 10x10 array, every switch allowed to get its own internal resistance in the range $10 \pm 5\,\Omega$. Blue symbols refer to IECM, orange symbols to the original QZPM. [149] (© 2022 IEEE)

Appendix D

PCBs
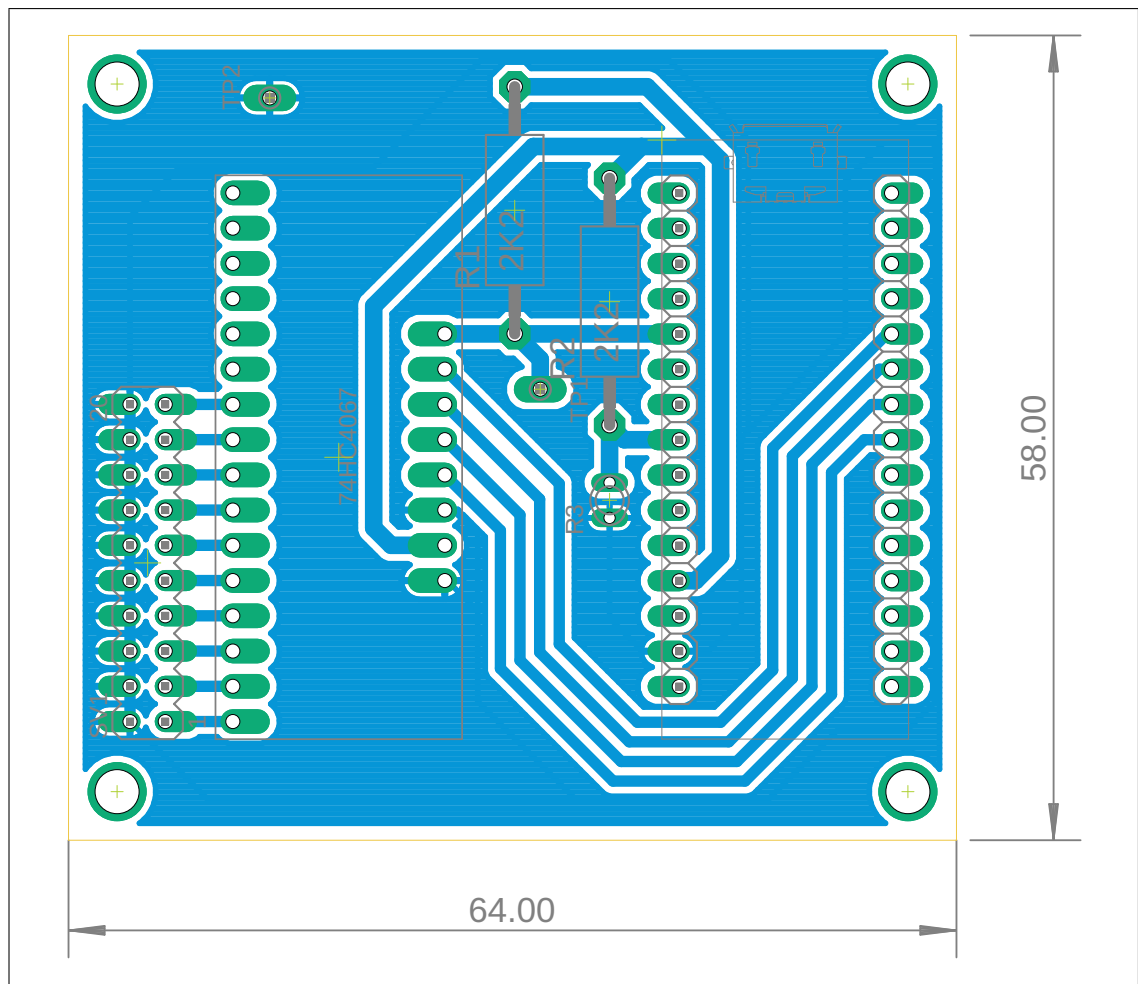
Figure D.1: PCB of the DAQ of the PCB used for the Comparison of Materials (units in mm)
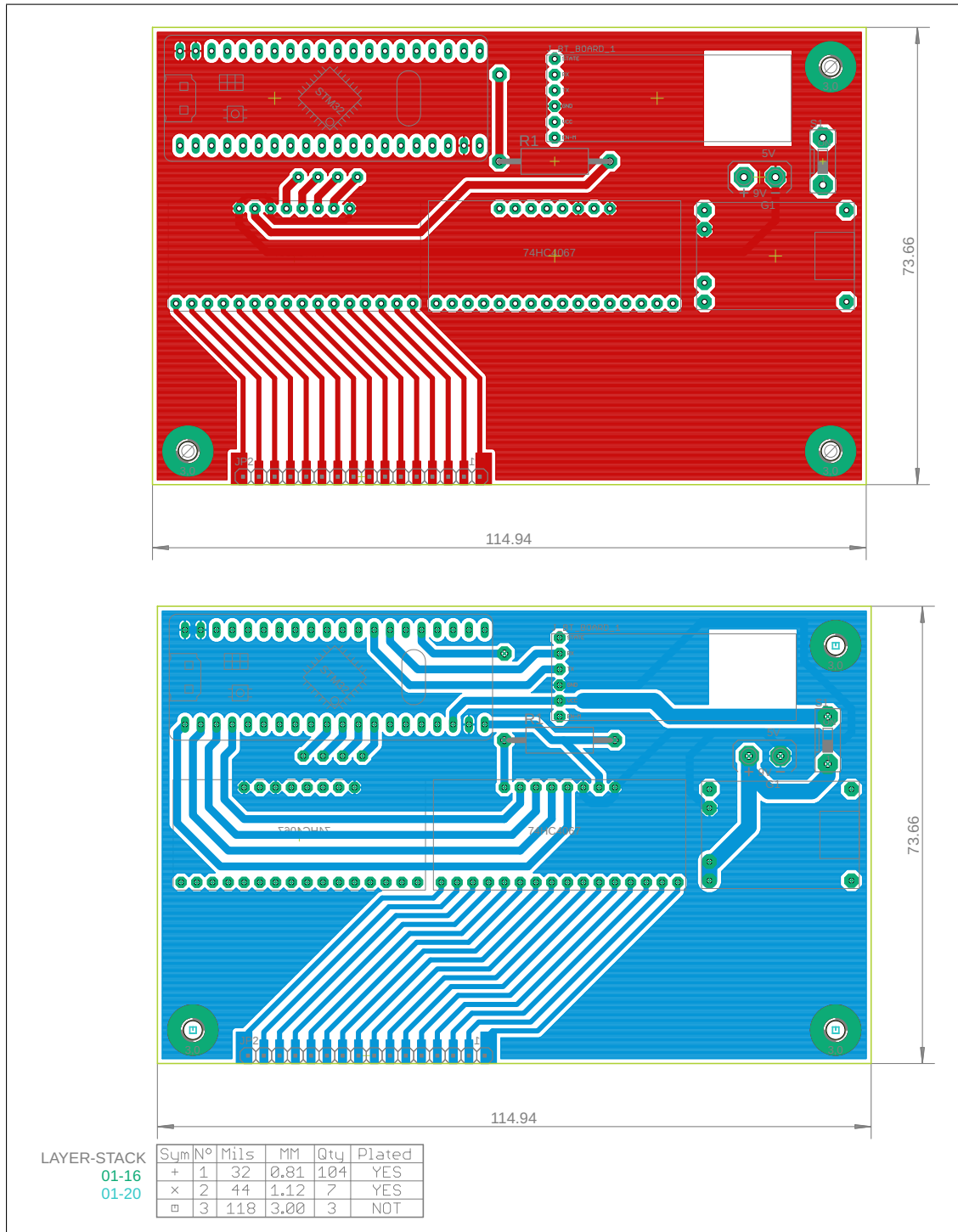
Figure D.2: PCB of the DAQ of the PSM (units in millimeters)
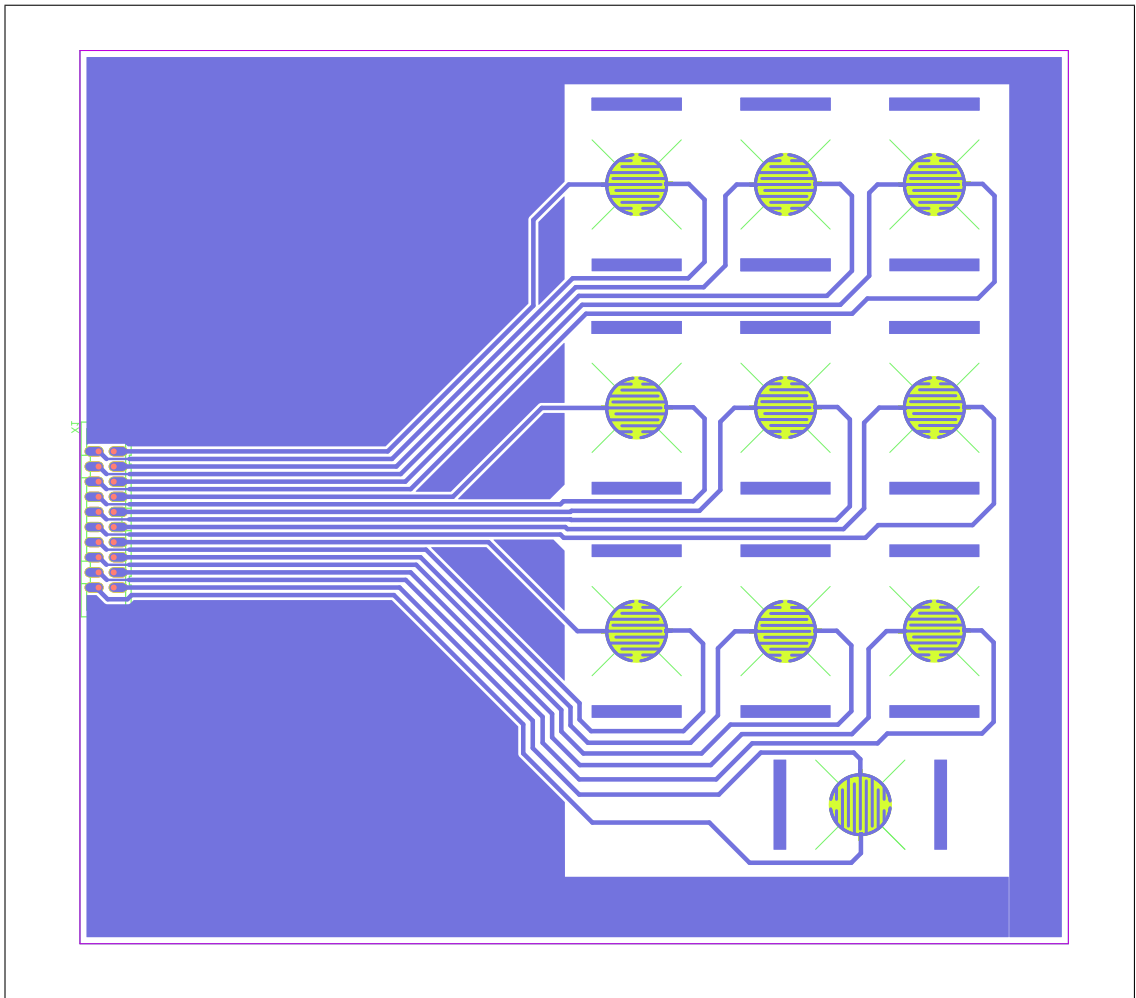
Figure D.3: Last PCB model used for the Comparison of Materials
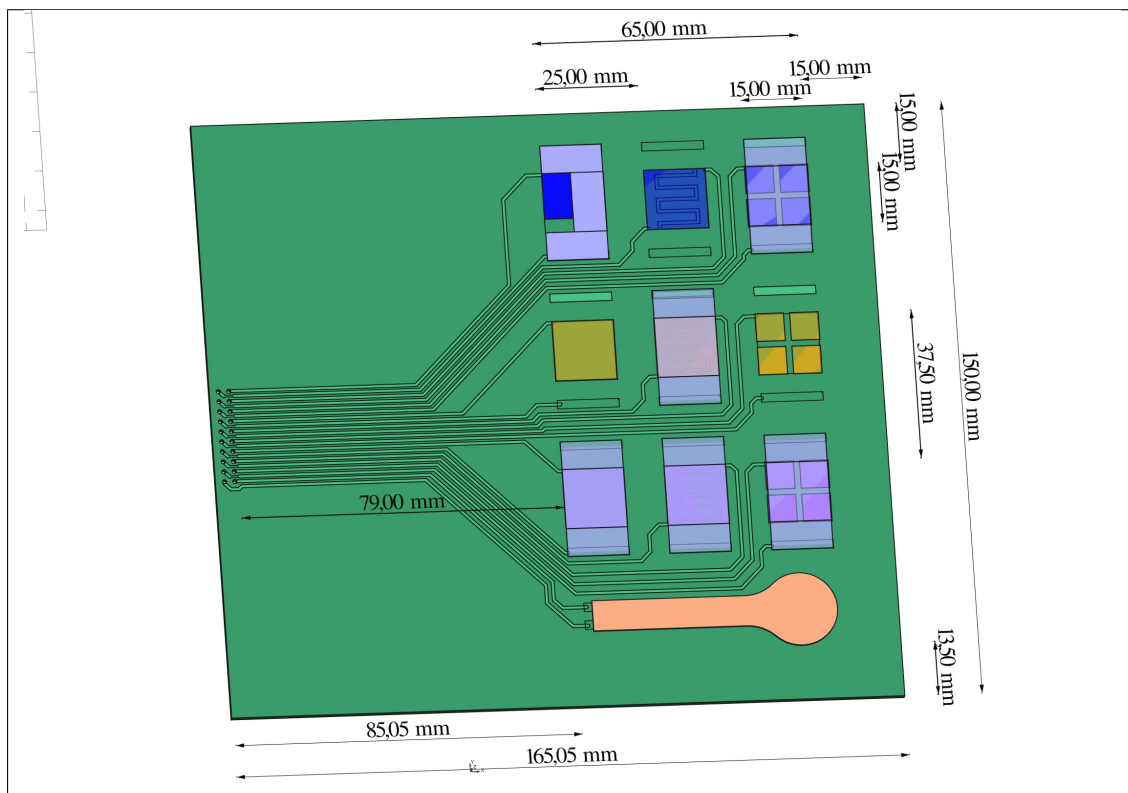
Figure D.4: 3D view of first PCB model used for the Comparison of Materials (units in mm)

Appendix E

Configuration of the STM32F103C8Tx (bluepill)

In this appendix we are going to show how to program the μC used in the PhD from two different environments, including several configuration tips.

E.1 STM32CubeIDE starting Guide

In this subsection the STM32CUBE IDE, shown in figure E.1, is considered for programming and debugging.

Figure E.1: STM32CubeIDE loading screen

After installing the software a new STM32 project has to be created, see figure E.2.
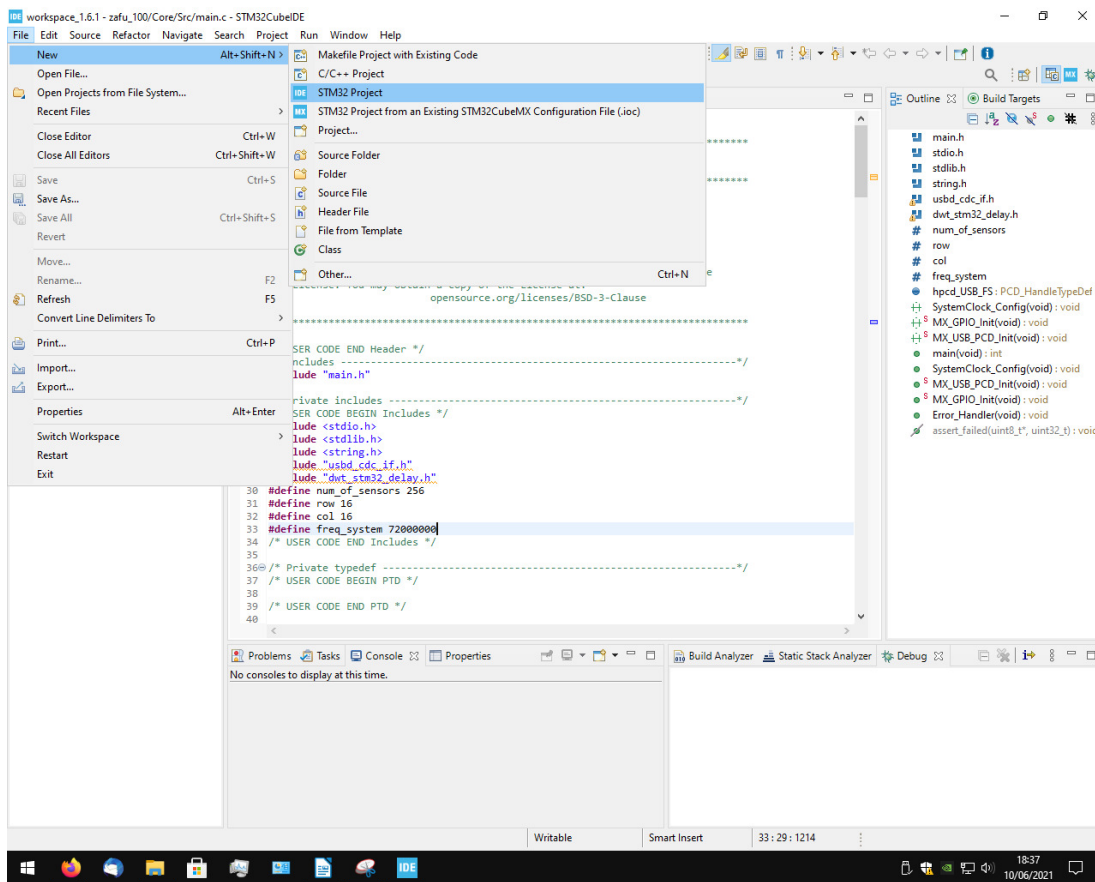
Figure E.2: Creation of a new project

The component name "stm32" can be used as a filter to find the components faster, see figure E.3:
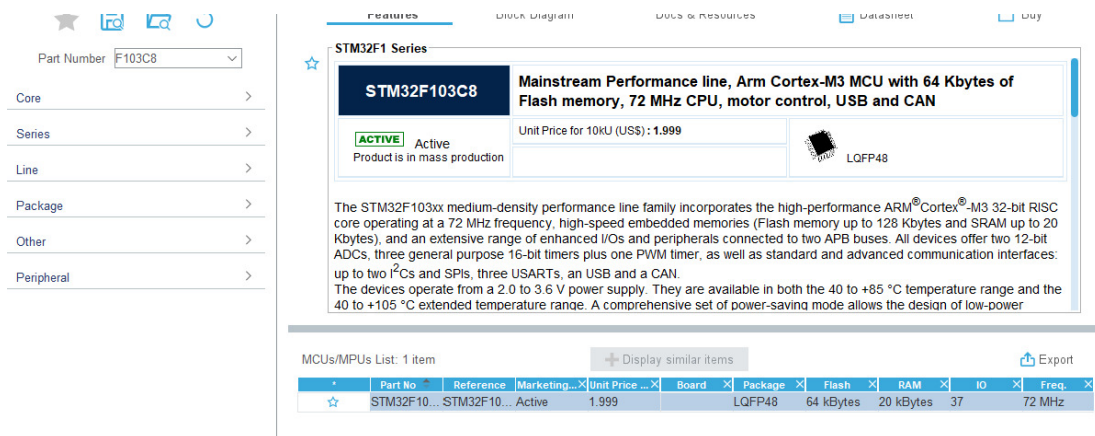
Figure E.3: Filter by component name

A name is assigned to the project and the process ends, shown in figure E.4.
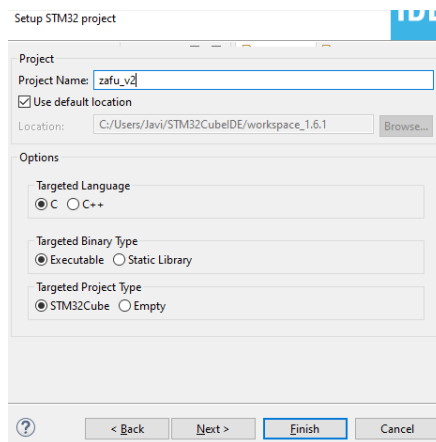
Figure E.4: Assignation of name to our project

A graphical window starts up in which the configuration pins are set. We can come back to it later by clicking on the file with extension ".ioc".

It is very important to configure the debugging pins, illustrated in figure E.5a, to make it easier to upload the programs and avoid further complications.
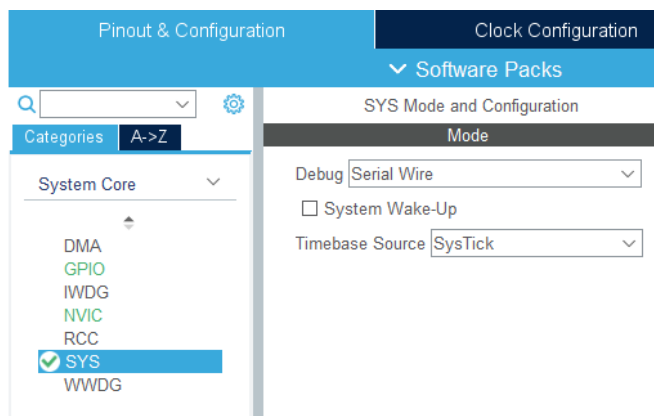
(b) Jumpers Boot0 and Boot1

(a) Enable debug of μC

Figure E.5: (**a**)Procedure to enable debug of μC; (**b**) Jumper of Boot0 and Boot1 in the μC.

If we forget the last step, we could set the BOOT0 jumper to 1, press the reset button and relaunch the program, see figure E.5b.

It is also important to enable the external clock included on the development board (BluePill) to be able to use it, see figure E.6:

(a) Enable clock of µC
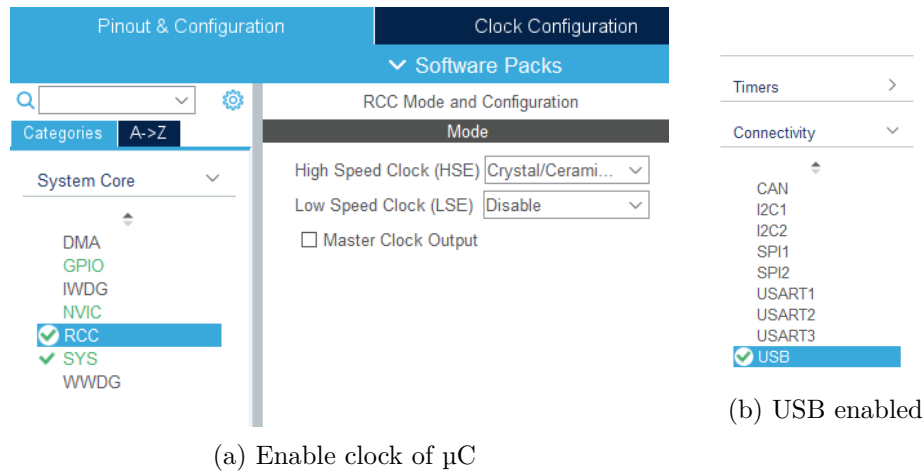
(b) USB enabled

Figure E.6: (**a**)Procedure to enable clock of µC; (**b**) USB enabled in the µC.

Then in the clock configuration tab we can select the external clock. Changing a few parameters we could obtain the following configuration at 72 MHz (look at figure E.7). It allows higher frequency with "overclocking" but it is not recommended.
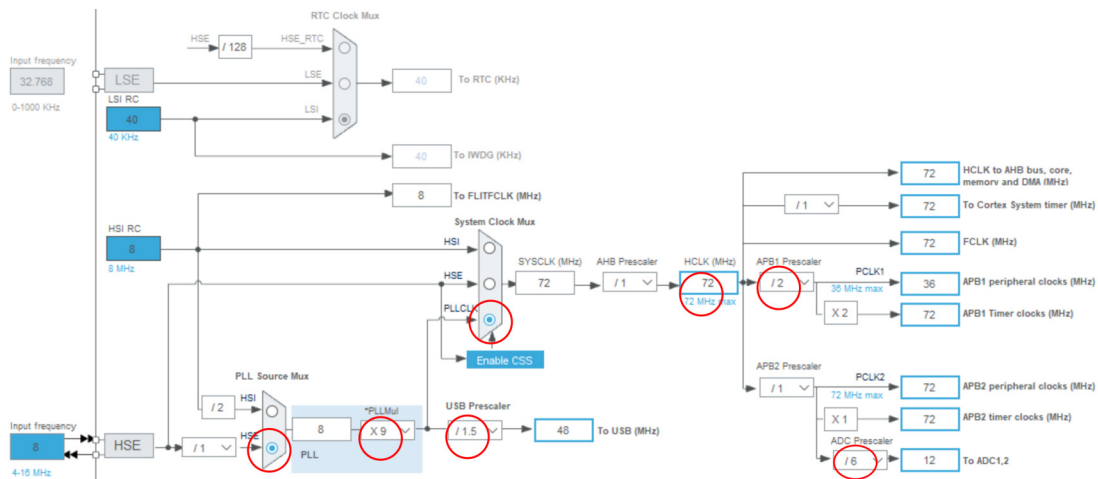
Figure E.7: µC clock configuration

Going back to the PinOut and Configuration screen we could configure the peripherals that we want to use.

Once the peripherals have been configured, the corresponding code is generated in the gear icon E.8. An important point is to be highlighted: this action resets files such as the Core/Src/main.c. Therefore, all the modifications that we could have done in them will be erased.
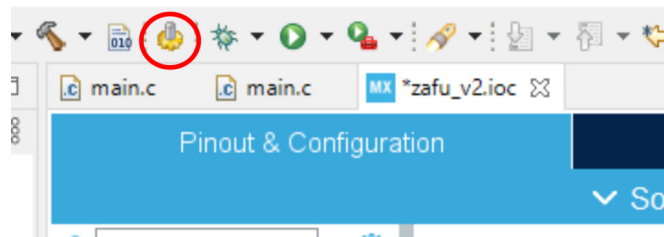
Figure E.8: Generate code according to PinOut

Then, it will generate the code and will take us to Core/Src/main.c where we will write our code and where the autocompletion is done with CTRL+space.

A simple example would be to make the on-board LED connected to pin 13 blink. For this we would additionally configure pin 13 as a general purpose digital output (GPIO_Output, similar to figure E.9).
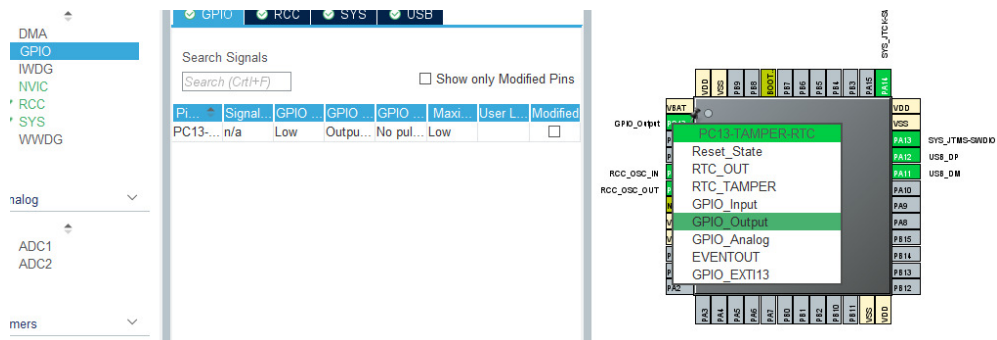
Figure E.9: Configuration of Pin as Output.

We would generate the configuration file, and in the main block of the chip we would tell it to switch the value of pin 13 and wait a time for example 3000 milliseconds. Afterwards the code is compiled to verify that there are no errors In order to upload the code to the µC through the Stlink-v2 (or in our case its economic version, previous image) it is necessary to modify two parameters of the default configuration (see figure E.10):
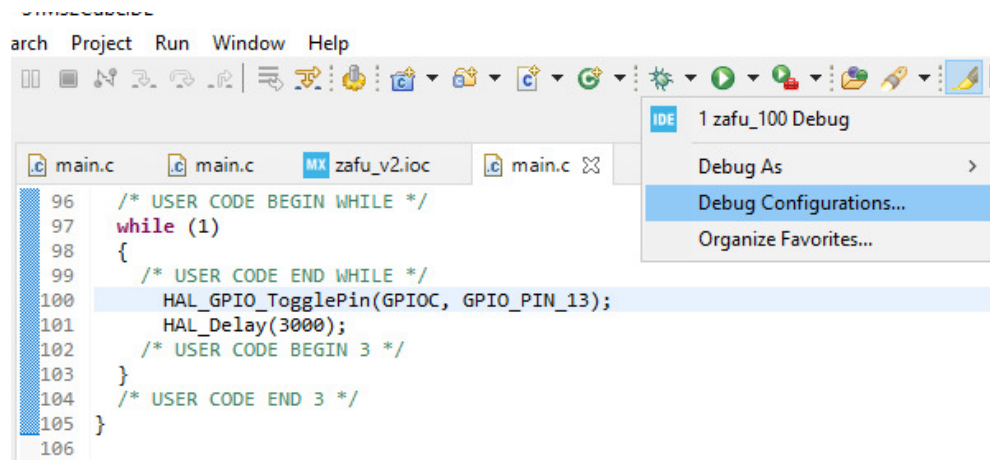
Figure E.10: Access to the Debug Configuration Menu

If we want to use the non official programmer/debugger, in the debug tab (see figure E.11), it is necessary to select "ST-LINK (OpenOCD)" in the "Debug probe" dropdown. Besides, in "showing the option generator" we can enable the "Software Reset" (shown in figure E.12).
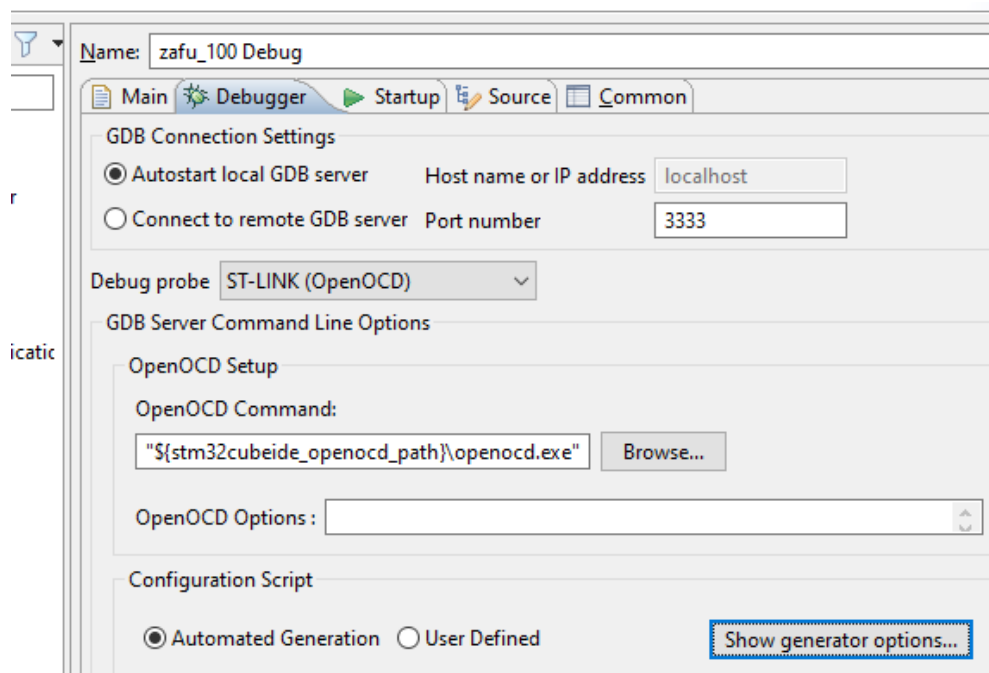
Figure E.11: Access to the Debug Configuration Menu
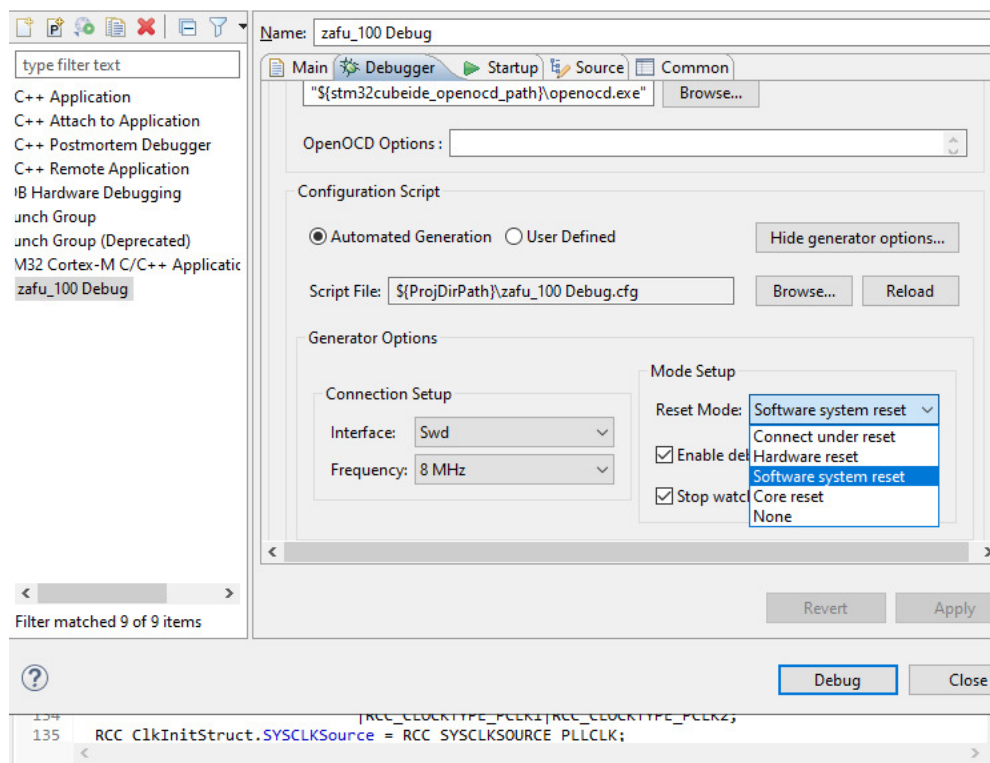
Figure E.12: Enable software reset in the Debug Configuration Menu

With these options if we start the debugging, the software will first complain showing red messages in the console. It will ask us if we want to change to the debug mode. Once in the debug mode we can start the debugging execution and set breakpoints (using for it the palette of the figure E.13).
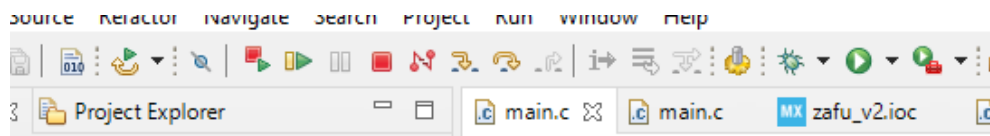
Figure E.13: Debug Menu Palette

If instead of debugging we simply want to execute the program we can click on the run icon (see figure E.14). The configuration of the debugging is also useful for the execution, so it would not be necessary to choose again ST-LINK (OpenOCD).
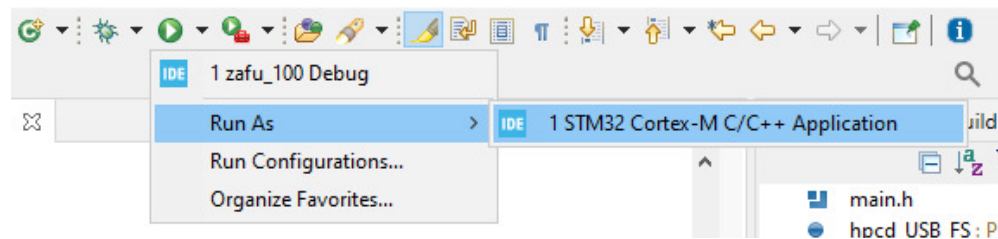
Figure E.14: Run menu in the application

If the software complains about GDP it means that the ST-LINK (OpenOCD) is not set. In principle and in spite of the red messages of the console our LED should blink. We must not forget that when compiling the software indicates the errors in the code. For the case of the PSM it is necessary to configure some more peripherals:
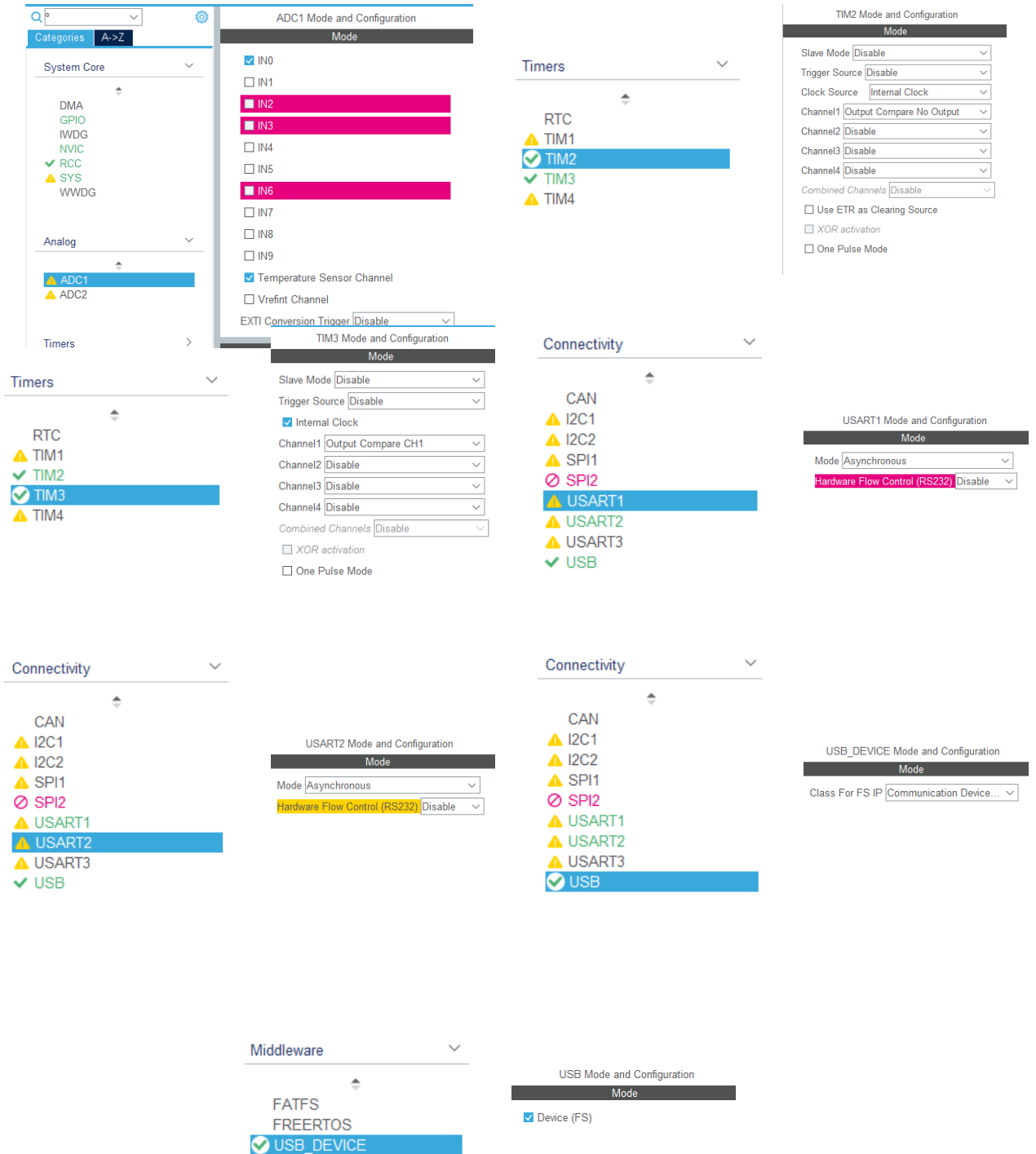
Figure E.15: Additional configuration for employing it on a PSM

E.2   STM32Duino Configuration Guide

In this section, we are going to show how to configure the STM32F103C8Tx (bluepill) as an Arduino via USB.

To upload the Arduino bootloader, the programming software STM32 ST-LINK 004 Utility is required (`https://my.st.com/content/my_st_com/en/products/ development-tools/software-development-tools/stm32-software-development-tools/stm32-programmers/stsw-link004.html`) (see figure E.16).
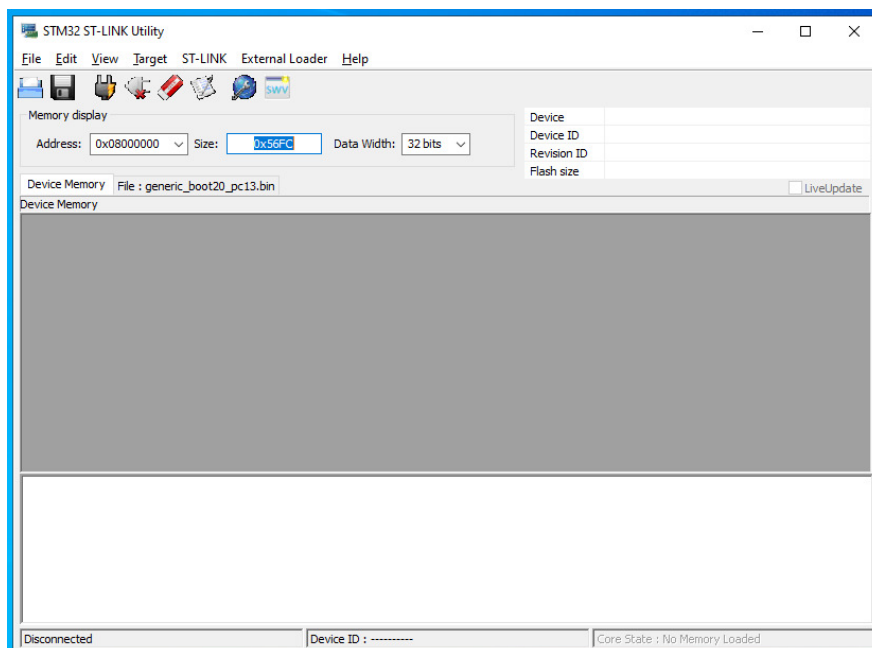
Figure E.16: ST-Link004 main screen

The ST-Link V2 module (shown in figure E.5b) is also required to upload the Arduino. However, once the Arduino is uploaded and the USB programming is enabled it will only be necessary in case of failure.

We will also need to install the ST-Link V2 Drivers on Windows (`https://my. st.com/content/my_st_com/en/products/development-tools/software-development-tools/stm32-software-development-tools/stm32-utilities/stsw-link009. html`).

Of course, the Arduino bootloader has to be downloaded from the repository (`https://github.com/rogerclarkmelbourne/STM32duino-bootloader/ blob/master/binaries/generic_boot20_pc13.bin`)

We should never connect the STM32F103C8Tx (BluePill) board to several

power supplies simultaneously, otherwise it may melt ports, from the STM32, the ST-Link and even the PC.

Using the STM32 ST-LINK Utility we proceed to upload the Arduino Boot-Loader. For this purpose, we have to connect the ST-Link V2 to the BluePill board (normal wiring, SWCLK with SWCLK, SWDIO with SWDIO, Vcc with Vcc and GND with GND, pin view in figure E.17).
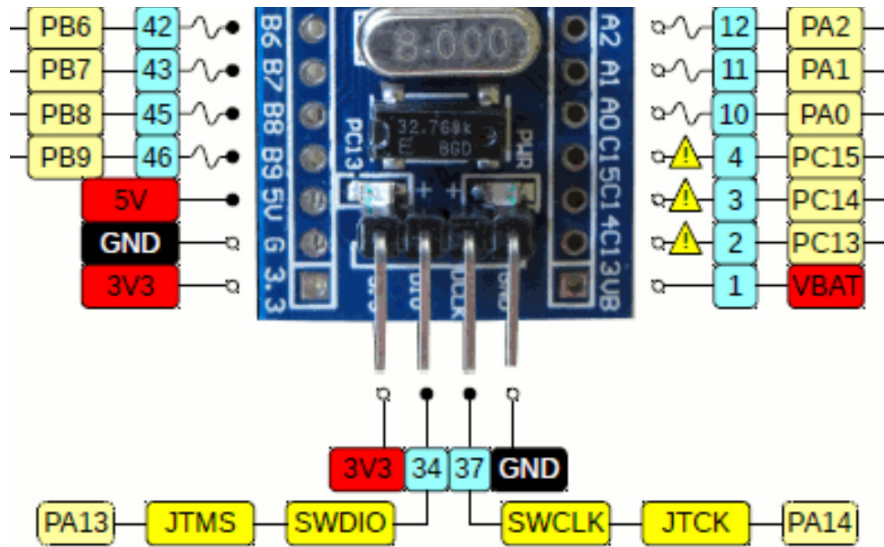
Figure E.17: ST-Link004 main screen

The ST-Link V2 is then connected to the computer and the ST-LINK Utility program is opened. Once inside the ST-LINK Utility, we should connect to the BluePill board (see figure E.18, it may be necessary to press and hold the RESET button on the board when connecting, and release it shortly after):
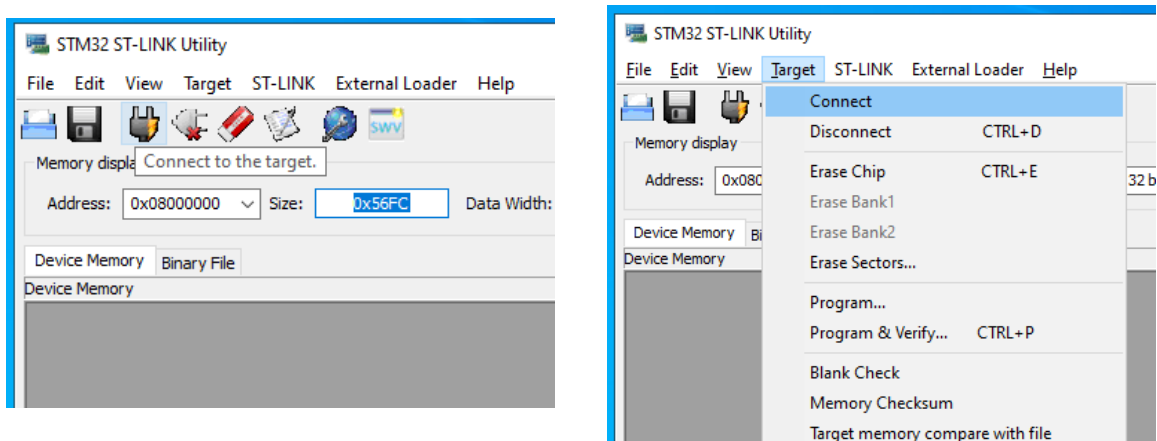
Figure E.18: Procedure to connect to the device

Once connected, we set the Boot0 Jumper to position 1, which will allow us to upload the Arduino in memory (shown in figure E.19):
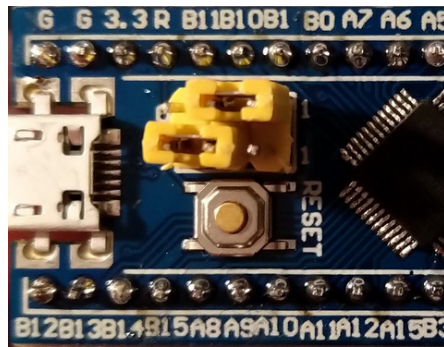
Figure E.19: Jumpers setting to upload in memory

From the ST-LINK Utility, the bootloader Arduino file for this board has to be opened (generic_boot20_pc13.bin, illustrated in figure E.20):

(a)

(b)
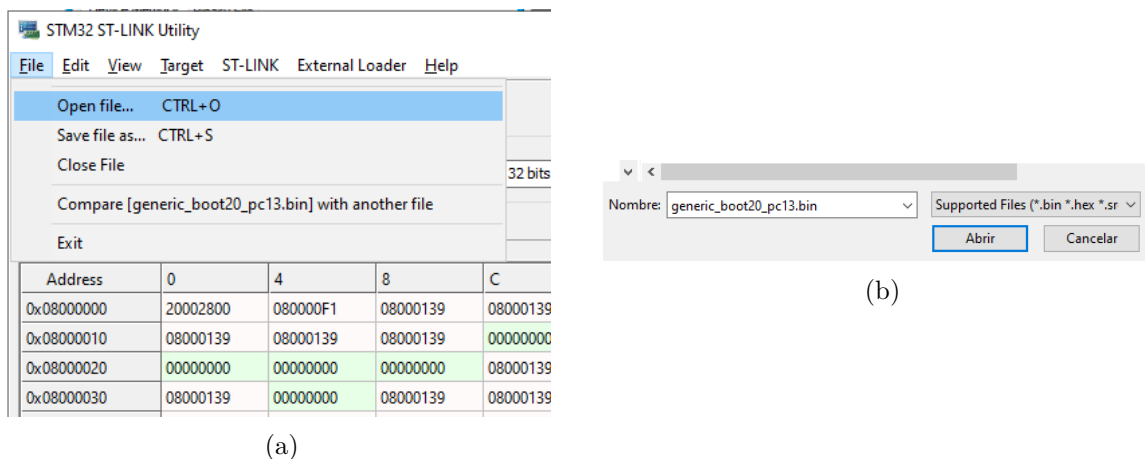
Figure E.20: Upload Bootloader in the ST-LINK004

Opening the file will change the colors of the cells and their values. To program the Arduino Bootloader on the BluePill board we should click on Target/ Program (see figure E.21) and on Start in the popup window (shown in figure E.22).
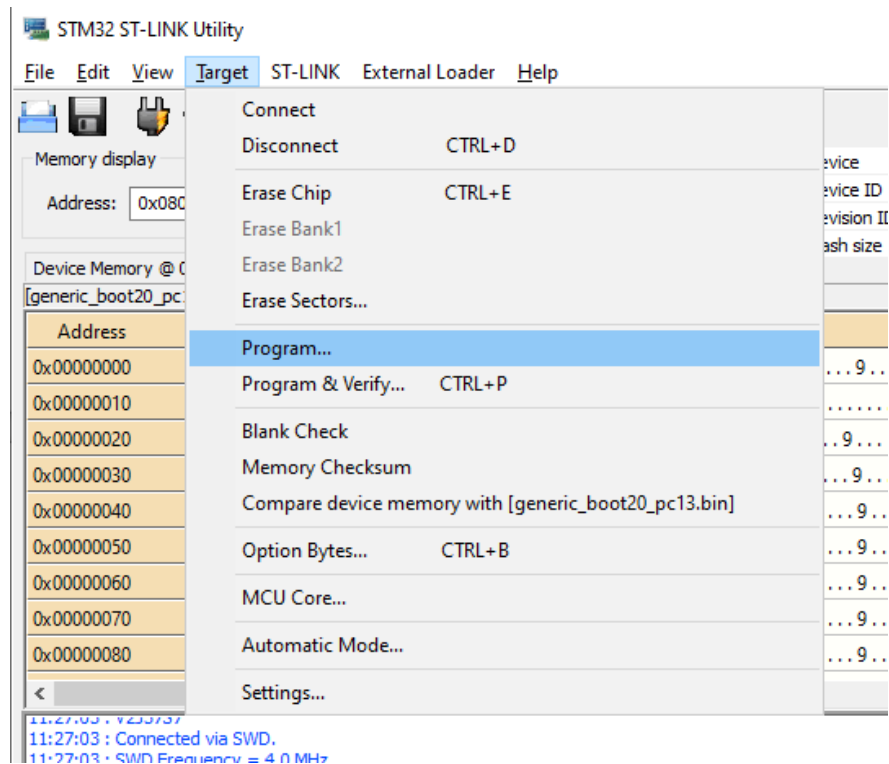
Figure E.21: Upload the Bootloader in the device
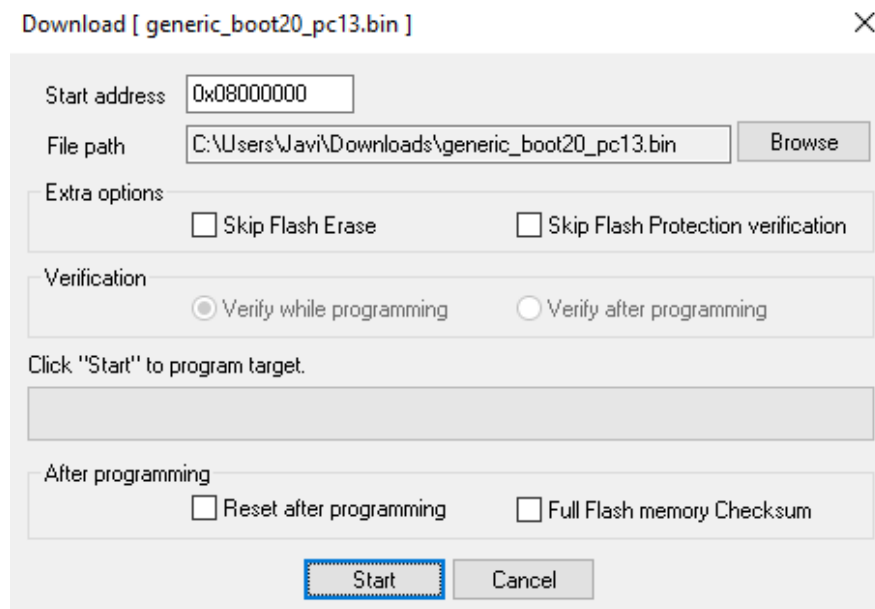
Figure E.22: Start the programming of the device

Once the bootloader has been successfully uploaded, the Boot0 jumper has to be set to 0 (like in figure E.23). Then it has to remain in that state. With the

jumper in the initial state, we have to press on the RESET button.
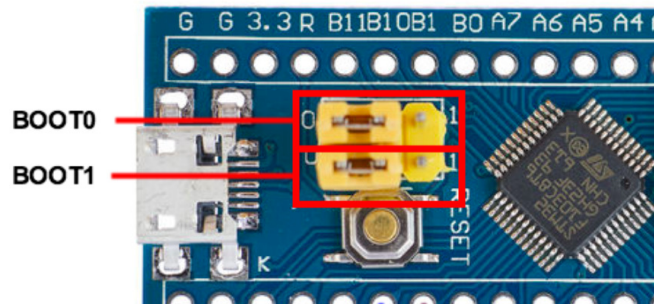
Figure E.23: Jumper settings to keep data in memory

Once the Jumper is in its original state, and the RESET button is pressed, we can close ST-LINK Utility, eject the USB corresponding to ST-Link V2 and disconnect the ST-Link V2 from the BluePill Board. The ST-Link V2 is no more required if everything is alright.

If the Boot0 Jumper is disconnected while the BluePill board is powered on, the Arduino BootLoader will be erased and if we want to use the Arduino we will have to repeat the uploading process with the ST-Link Utility.

Once the cables are disconnected, we can connect the BluePill board to the computer directly through its miniUSB port, and it will detect the device as a Maple Serial (COMx) port (shown in figure E.24).
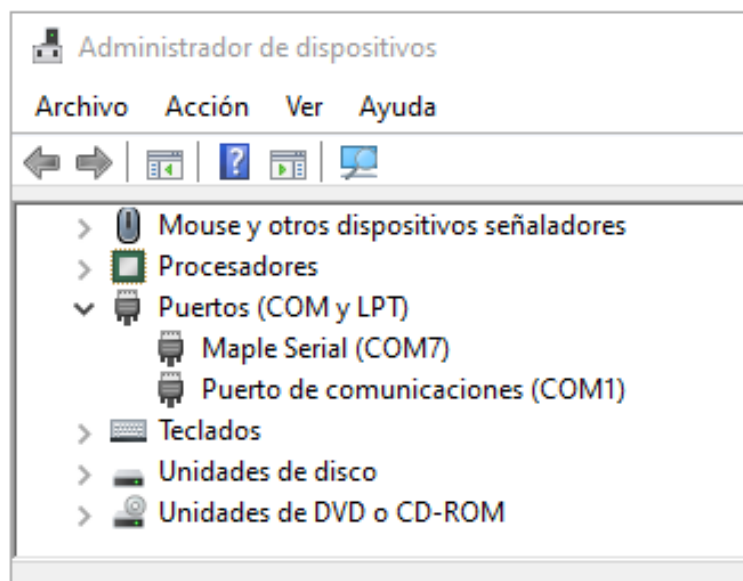
Figure E.24: Detected devices by the system

In order for Arduino to be able to upload new regular programs on our board, we must install a number of additional libraries and changes to it, which requires having installed Arduino from the installer, rather than from the software store. This is because the board does not come in the list of standard ones.

In the Arduino IDE, from preferences, in the management of URL additional boards, shown in figure E.25, we must insert the following text in two new lines and accept to exit preferences (see figure E.26):

`http://dan.drown.org/stm32duino/package_STM32duino_index.json`
`https://github.com/stm32duino/BoardManagerFiles/raw/master/STM32/package_`
`stm_index.json`

(a)

(b)
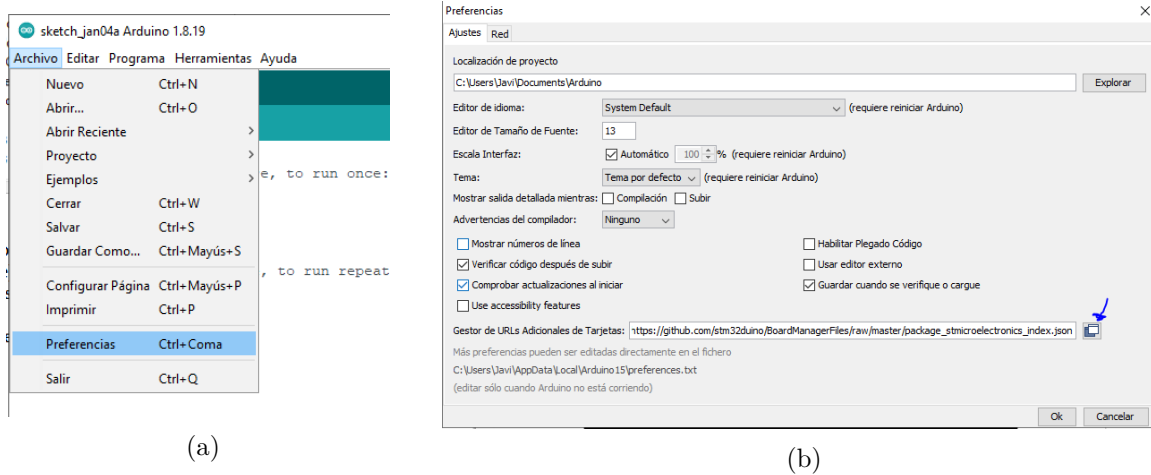
Figure E.25: Installation of STM libraries
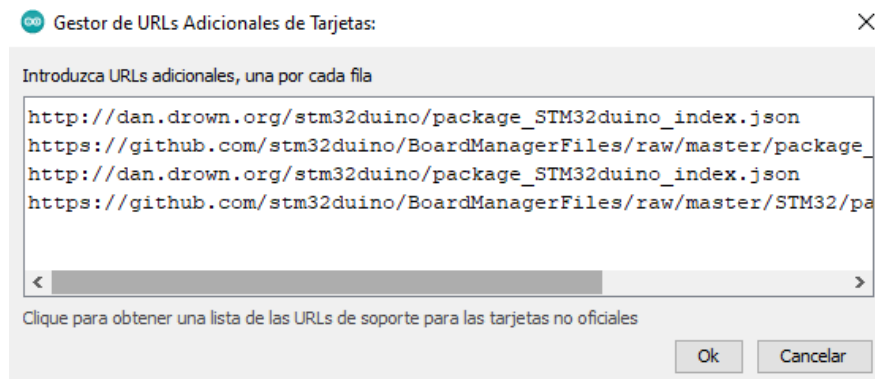
Figure E.26: Arduino URL manager

Then, from Tools/ Library management, we must look for STM32F1 (see figure E.27):
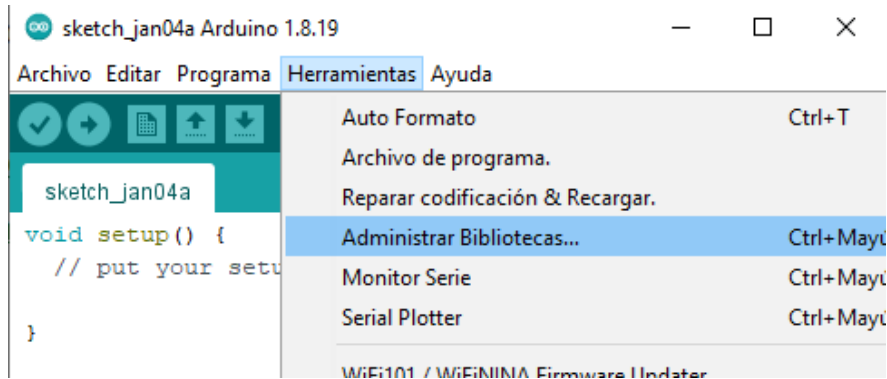
Figure E.27: Arduino Library manager

Then, among the list we have to install "FlashStorage_STM32F1" y "STM32F1_RTC" (all that include STM32F1 in their name, shown in figure E.28)
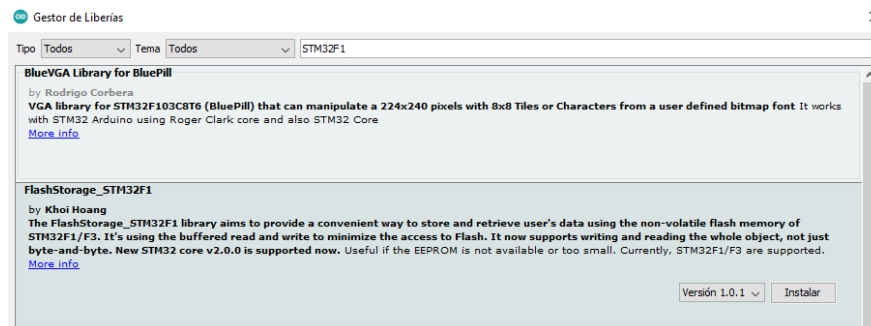
(a)
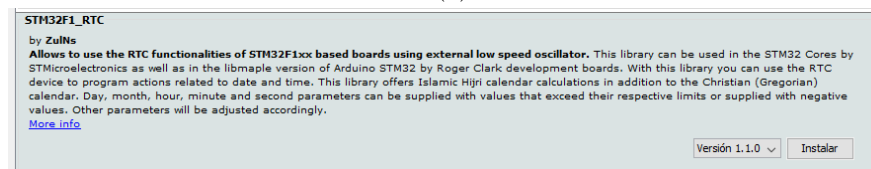
(b)

Figure E.28: Installation of STM32F1 libraries

Finally, we are ready to program the BluePill from Arduino IDE. When connecting the BluePill it detects the configuration of the board, so we only have to choose the port where it is connected, see figure E.29:
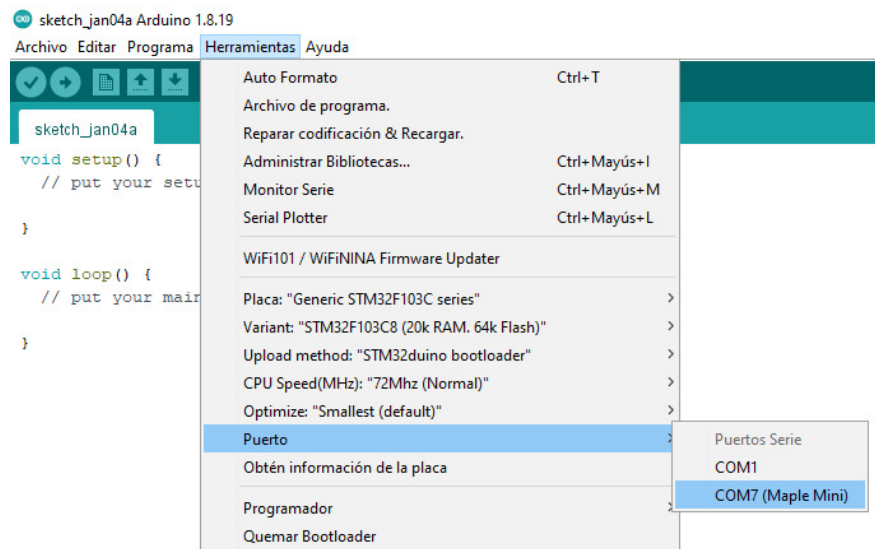
Figure E.29: Select the device in the ArduinoIDE

For the configuration of the modules in a simple way from Arduino IDE, we can use some of the functions already available in the menus, but we can also integrate functions in C in a simple way. For the configuration in other operating systems it would be similar.

Bibliography

[1] buildmywheelchair.com boditrak2 lt, includes pressure mat & tablet. `https://buildmywheelchair.com/comfort-company-boditrak2-lt-includes-pressure-mat-tablet/`. Accessed: 2023-01-17.

[2] Tekscan pressure mapping sensor 5315. `https://www.tekscan.com/products-solutions/pressure-mapping-sensors/5315`. Accessed: 2023-01-17.

[3] Official website of amti. `https://www.amti.biz/`. (accessed on 30 January 2023).

[4] ebay.co.uk gaitrite electronic walkway system map/cir inc + software gait walking lab. `https://www.ebay.co.uk/itm/266069253862`. Accessed: 2023-01-17.

[5] Materialise pressure plates & 3d scanners. `https://www.materialise.com/en/healthcare/phits-suite/pressure-plates-3d-scanners`. Accessed: 2023-01-17.

[6] 1704 36x150. - FILM, VELOSTAT, 36 x 150 ROLL 67y8891, . URL `https://es.farnell.com/scs/1704-36x150/film-velostat-36-x-150-roll-67y8891/dp/3218528`.

[7] Arduino reference - arduino reference, . URL `https://www.arduino.cc/reference/en/`.

[8] Arduino for STM32 - index page, . URL `https://www.stm32duino.com/`.

[9] CD74hc4067 data sheet, product information and support | TI.com, . URL `https://www.ti.com/product/CD74HC4067`.

[10] Complete language index maple v0.0.12 documentation, . URL http://docs.leaflabs.com/static.leaflabs.com/pub/leaflabs/maple-docs/0.0.12/language-index.html.

[11] EX-STATIC CONDUCTIVE FABRIC, . URL https://www.filteremf.com/buy/ex-static-conductive-fabric/.

[12] Filaflex 82a 'original' | filamento flexible TPU para impresión 3d, . URL https://recreus.com/es/filamentos/9-684-filaflex-82a.html.

[13] FT232rl (NRND), . URL https://ftdichip.com/products/ft232rl/.

[14] human spine length - wolfram|alpha, . URL https://es.wolframalpha.com.

[15] Smart sensor BNO055, . URL https://www.bosch-sensortec.com/products/smart-sensors/bno055/.

[16] ST-LINK/v2, . URL https://estore.st.com/en/st-link-v2-cpn.html.

[17] STM32cubeide - integrated development environment for STM32 - STMicroelectronics, . URL https://www.st.com/en/development-tools/stm32cubeide.html.

[18] STM32f103c8 - mainstream performance line, arm cortex-m3 MCU with 64 kbytes of flash memory, 72 MHz CPU, motor control, USB and CAN - STMicroelectronics, . URL https://www.st.com/en/microcontrollers-microprocessors/stm32f103c8.html.

[19] TCA9548a data sheet, product information and support | TI.com, . URL https://www.ti.com/product/TCA9548A.

[20] Official website of pasco. https://www.pasco.com/products/sensors/force/ps-2141. (accessed on 30 December 2022).

[21] Sensing Tex seating mat for wellness dev kit 1.8. https://sensingtex.com/product/seating-mat-dev-kit/. Accessed: 2023-01-17.

[22] Official website of sensing-tex. http://sensingtex.com/product/seating-mat-dev-kit/. (accessed on 30 December 2022).

[23] Official website of spartan. `https://success.spartascience.com/en/knowledge/force-plate-technology`. (accessed on 30 January 2023).

[24] Metrological regulation for load cells., January 2000. URL `https://www.oiml.org/en/files/pdf_r/r060-e00.pdf/@@download/file/R060-e00.pdf`.

[25] Evaluation of measurement data guide to the expression of uncertainty in measurement. `https://www.bipm.org/documents/20126/2071204/JCGM_100_2008_E.pdf`, 2008. Working Group 1 of the Joint Committee for Guides in Metrology,.

[26] Evaluation of measurement data supplement 1 to the "guide to the expression of uncertainty in measurement" propagation of distributions using a monte carlo method. `https://www.bipm.org/documents/20126/2071204/JCGM_101_2008_E.pdf`, 2008. Accessed: 2021-09-23.

[27] *Design and Evaluation of a Touch Activated Glove System for Upper Extremity Rehabilitation Studies*, volume Volume 3: Biomedical and Biotechnology Engineering of *ASME International Mechanical Engineering Congress and Exposition*, January 2015. doi: 10.1115/IMECE2015-52240. V003T03A090.

[28] Adafruit unified BNO055 driver (AHRS/orientation), February 2023. URL `https://github.com/adafruit/Adafruit_BNO055`. original-date: 2015-04-04T23:43:22Z.

[29] F. Aghazadeh, N. Arjmand, and A. M. Nasrabadi. Coupled artificial neural networks to estimate 3d whole-body posture, lumbosacral moments, and spinal loads during load-handling activities. *Journal of Biomechanics*, 102: 109332, March 2020. ISSN 0021-9290. doi: 10.1016/j.jbiomech.2019.109332.

[30] Dahbia Agher, Karima Sedki, Sylvie Despres, Jean-Pierre Albinet, Marie-Christine Jaulent, and Rosy Tsopra. Encouraging behavior changes and preventing cardiovascular diseases using the prevent connect mobile health app: Conception and evaluation of app quality. *J Med Internet Res*, 24(1): e25384, Jan 2022. ISSN 1438-8871. doi: 10.2196/25384.

[31] Csaba Antonya, Silviu Butnariu, and Claudiu Pozna. Real-time representation of the human spine with absolute orientation sensors. In *2016 14th International Conference on Control, Automation, Robotics and Vision (ICARCV)*, pages 1–6, January 2016. doi: 10.1109/ICARCV.2016.7838745.

[32] Rachael A. Ard, Jake A. Melaro, Alex M. Carnall, Alexis K. Nelson, Sarah E. Blackmore, Victoria A. White, Max R. Paquette, and Douglas W. Powell. Validation of the tekscan strideway plantar pressure mat compared to a force platform: 1348 board #110 may 30 10:30 AM - 12:00 PM. *Medicine & Science in Sports & Exercise*, 51(6):357, June 2019. ISSN 0195-9131. doi: 10.1249/01.mss.0000561580.36179.b1.

[33] R.P. Areny. *Instrumentos electrónicos básicos*. Marcombo, 2006. ISBN 9788426713902. URL https://books.google.es/books?id=pMfgL_SimNQC.

[34] A Arndt. Correction for sensor creep in the evaluation of long-term plantar pressure data. *Journal of Biomechanics*, 36(12):1813–1817, 2003. ISSN 0021-9290. doi: https://doi.org/10.1016/S0021-9290(03)00229-X.

[35] Gabriela L. Atanasova and Nikolay T. Atanasov. Impact of electromagnetic properties of textile materials on performance of a low-profile wearable antenna backed by a reflector. In *2020 International Workshop on Antenna Technology (iWAT)*, pages 1–4, February 2020. doi: 10.1109/iWAT48004.2020.1570609739.

[36] Musa L. Audu, Brooke M. Odle, and Ronald J. Triolo. Control of standing balance at leaning postures with functional neuromuscular stimulation following spinal cord injury. *Medical & Biological Engineering & Computing*, 56(2):317–330, February 2018. ISSN 1741-0444. doi: 10.1007/s11517-017-1687-x.

[37] Branko Babusiak, Stefan Borik, and Ludmila Balogova. Textile electrodes in capacitive signal sensing applications. *Measurement*, 114:69–77, January 2018. ISSN 0263-2241. doi: 10.1016/j.measurement.2017.09.024.

[38] Jeff M. Barrett, Daniel Viggiani, Jonathan Park, and Jack P. Callaghan. Expressing angles relative to reference postures: A mathematical compar-

ison of four approaches. *Journal of Biomechanics*, 104:109733, May 2020. ISSN 0021-9290. doi: 10.1016/j.jbiomech.2020.109733.

[39] Antonio Barrientos, Luís Felípe Peñín, Carlos Balaguer, and Rafael Aracil. *Fundamentos de Robótica*. McGraw-Hill, 1997. ISBN 84-481-0815-9.

[40] Tito Bassani, Elena Stucovitz, Zhihui Qian, Matteo Briguglio, and Fabio Galbusera. Validation of the AnyBody full body musculoskeletal model in computing lumbar spine loads at l4l5 level. *Journal of Biomechanics*, 58: 89–96, June 2017. ISSN 0021-9290. doi: 10.1016/j.jbiomech.2017.04.025.

[41] George Beckham, Tim Suchomel, and Satoshi Mizuguchi. Force plate use in performance monitoring and sport science testing. *New Studies in Athletics*, 29(3):25–37, 2014.

[42] Christina Bickley, Judith Linton, Elroy Sullivan, Katy Mitchell, Greg Slota, and Douglas Barnes. Comparison of simultaneous static standing balance data on a pressure mat and force plate in typical children and in children with cerebral palsy. *Gait & Posture*, 67:91 – 98, 2019. ISSN 0966-6362. doi: https://doi.org/10.1016/j.gaitpost.2018.08.012.

[43] Christopher M. Bishop. *Pattern Recognition and Machine Learning (Information Science and Statistics)*. Springer, 1 edition, 2007. ISBN 0387310738.

[44] Mark G. Boocock, Grant A. Mawston, and Steve Taylor. Age-related differences do affect postural kinematics and joint kinetics during repetitive lifting. *Clinical Biomechanics*, 30(2):136–143, February 2015. ISSN 0268-0033. doi: 10.1016/j.clinbiomech.2014.12.010.

[45] Angela Brenton-Rule, Joshua Mattock, Matthew Carroll, Nicola Dalbeth, Sandra Bassett, Hylton Menz, and Keith Rome. Reliability of the tekscan matscanő system for the measurement of postural stability in older people with rheumatoid arthritis. *Journal of foot and ankle research*, 5:21, August 2012. doi: 10.1186/1757-1146-5-21.

[46] Jessa M. Buchman-Pearle, Kayla M. Fewster, Brendan L. Pinto, and Jack P. Callaghan. Moving toward individual-specific automotive seat design: How individual characteristics and time alter the selected lumbar support prominence. *Human Factors*, page 00187208211042776, September 2021. ISSN

0018-7208. doi: 10.1177/00187208211042776. Publisher: SAGE Publications Inc.

[47] Iris Busscher, Joris J. W. Ploegmakers, Gijsbertus J. Verkerke, and Albert G. Veldhuizen. Comparative anatomical dimensions of the complete human and porcine spine. *European Spine Journal*, 19(7):1104–1114, July 2010. ISSN 1432-0932. doi: 10.1007/s00586-010-1326-9.

[48] Tomas Bystricky, Daniela Moravcova, Petr Kaspar, Radek Soukup, and Ales Hamacek. A comparison of embroidered and woven textile electrodes for continuous measurement of ECG. In *2016 39th International Spring Seminar on Electronics Technology (ISSE)*, pages 7–11, May 2016. doi: 10.1109/ISSE.2016.7562871. ISSN: 2161-2064.

[49] Wenyu Cai, Dongyang Zhao, Meiyan Zhang, Yinan Xu, and Zhu Li. Improved self-organizing map-based unsupervised learning algorithm for sitting posture recognition system. *Sensors*, 21(18):6246, January 2021. ISSN 1424-8220. doi: 10.3390/s21186246. Number: 18 Publisher: Multidisciplinary Digital Publishing Institute.

[50] Roberto Cardoso, Eduardo de Souza, Luiz Camano, and José Roberto Leite. Meditation in health: an operational definition. *Brain research protocols*, 14(1):58–60, 2004.

[51] H. Carvalho, Y. Yao, and L. M. Gonçalves. Flexible force sensors for e-textiles. *IOP Conference Series: Materials Science and Engineering*, 254 (7):072007, October 2017. ISSN 1757-899X. doi: 10.1088/1757-899X/254/7/072007. Publisher: IOP Publishing.

[52] Pedro Carvalho, Sandro Queirós, António Moreira, José Henrique Brito, Fernando Veloso, Miguel Terroso, Nuno F. Rodrigues, and João L. Vilaça. Instrumented vest for postural reeducation. In *2017 IEEE 5th International Conference on Serious Games and Applications for Health (SeGAH)*, pages 1–8, April 2017. doi: 10.1109/SeGAH.2017.7939300.

[53] Julián Castellanos-Ramos. Caracterización, modelado y diseño de sensores táctiles piezorresistivos, 2016. URL https://riuma.uma.es/xmlui/handle/10630/11333. Accepted: 2016-05-11T10:08:04Z Publisher: Servicio de Publicaciones y Divulgación Científica.

[54] Julián Castellanos-Ramos, Rafael Navas-González, Haritz Macicior, Tomasz Sikora, Estíbalitz Ochoteco, and Fernando Vidal-Verdú. Tactile sensors based on conductive polymers. *Microsystem Technologies*, 16(5): 765–776, May 2010. ISSN 1432-1858. doi: 10.1007/s00542-009-0958-3.

[55] Robert D. Catena, Joshua P. Bailey, Nigel Campbell, and Hallie E. Music. Stand-to-sit kinematic changes during pregnancy correspond with reduced sagittal plane hip motion. *Clinical Biomechanics*, 67:107–114, July 2019. ISSN 0268-0033. doi: 10.1016/j.clinbiomech.2019.05.014.

[56] Shanty Chacko and Srinivasan M. Sivakumar. A procedure for correction of creep in foam rubber optical pressure measurement techniques. *Experimental Mechanics*, 39:125–131, 1999.

[57] Baoliang Chen, Peng Liu, Feiyun Xiao, Zhengshi Liu, and Yong Wang. Review of the upright balance assessment based on the force plate. *International Journal of Environmental Research and Public Health*, 18(5), 2021. ISSN 1660-4601. doi: 10.3390/ijerph18052696.

[58] Jingyuan Cheng, Mathias Sundholm, Bo Zhou, Marco Hirsch, and Paul Lukowicz. Smart-surface: Large scale textile pressure sensors arrays for activity recognition. *Pervasive and Mobile Computing*, 30:97 – 112, 2016. ISSN 1574-1192. doi: https://doi.org/10.1016/j.pmcj.2016.01.007.

[59] Guillaume Christe, Lucy Redhead, Thomas Legrand, Brigitte M. Jolles, and Julien Favre. Multi-segment analysis of spinal kinematics during sit-to-stand in patients with chronic low back pain. *Journal of Biomechanics*, 49(10):2060–2067, July 2016. ISSN 0021-9290. doi: 10.1016/j.jbiomech.2016.05.015.

[60] Yang Chuan and Li Chen. The compensation for hysteresis of silicon piezoresistive pressure sensor. *IEEE Sensors Journal*, 11(9):2016–2021, 2011. doi: 10.1109/JSEN.2011.2105474.

[61] Andrew P. Claus, Julie A. Hides, G. Lorimer Moseley, and Paul W. Hodges. Thoracic and lumbar posture behaviour in sitting tasks and standing: Progressing the biomechanics from observations to measurements. *Applied Ergonomics*, 53:161–168, March 2016. ISSN 0003-6870. doi: 10.1016/j.apergo.2015.09.006.

[62] Henry M. Clever, Ariel Kapusta, Daehyung Park, Zackory Erickson, Yash Chitalia, and Charles C. Kemp. 3d human pose estimation on a configurable bed from a pressure image. In *2018 IEEE/RSJ International Conference on Intelligent Robots and Systems (IROS)*, pages 54–61, October 2018. doi: 10.1109/IROS.2018.8593545. ISSN: 2153-0866.

[63] Ilaria Conforti, Ilaria Mileti, Zaccaria Del Prete, and Eduardo Palermo. Measuring biomechanical risk in lifting load tasks through wearable system and machine-learning approach. *Sensors*, 20(6):1557, January 2020. ISSN 1424-8220. doi: 10.3390/s20061557. Number: 6 Publisher: Multidisciplinary Digital Publishing Institute.

[64] Ravinder S. Dahiya and Maurizio Valle. *Tactile Sensing: Definitions and Classification*, pages 13–17. Springer Netherlands, Dordrecht, 2013. ISBN 978-94-007-0579-1. doi: 10.1007/978-94-007-0579-1_2.

[65] Quoc Khanh Dang, Han Gil Seo, Duy Duong Pham, and Youngjoon Chee. Wearable sensor based stooped posture estimation in simulated parkinsons disease gaits. *Sensors*, 19(2):223, January 2019. ISSN 1424-8220. doi: 10.3390/s19020223. Number: 2 Publisher: Multidisciplinary Digital Publishing Institute.

[66] Ankur Desai, Valerie Goodman, Naaz Kapadia, Barbara L. Shay, and Tony Szturm. Relationship Between Dynamic Balance Measures and Functional Performance in Community-Dwelling Elderly People. *Physical Therapy*, 90 (5):748–760, May 2010. ISSN 0031-9023. doi: 10.2522/ptj.20090100.

[67] Jonathan S. Dufour, Alexander M. Aurand, Eric B. Weston, Christopher N. Haritos, Reid A. Souchereau, and William S. Marras. Dynamic joint motions in occupational environments as indicators of potential musculoskeletal injury risk. *Journal of Applied Biomechanics*, 37(3):196–203, March 2021. ISSN 1065-8483, 1543-2688. doi: 10.1123/jab.2020-0213. Publisher: Human Kinetics Section: Journal of Applied Biomechanics.

[68] Stacey C. Dusing, Anastasia Kyvelidou, Vicki S. Mercer, and Nick Stergiou. Infants Born Preterm Exhibit Different Patterns of Center-of-Pressure Movement Than Infants Born at Full Term. *Physical Therapy*, 89(12):1354–1362, February 2009. ISSN 0031-9023. doi: 10.2522/ptj.20080361.

[69] Juliane Eberth and Peter Sedlmeier. The effects of mindfulness meditation: a meta-analysis. *Mindfulness*, 3(3):174–189, 2012.

[70] SparkFun Electronicső. EeonTex conductive fabric - COM-14110 - Spark-Fun electronics. URL https://www.sparkfun.com/products/14110. 6333 Dry Creek Parkway, Niwot, Colorado 80503.

[71] A. H. Eskandari, N. Arjmand, A. Shirazi-Adl, and F. Farahmand. Subject-specific 2d/3d image registration and kinematics-driven musculoskeletal model of the spine. *Journal of Biomechanics*, 57:18–26, May 2017. ISSN 0021-9290. doi: 10.1016/j.jbiomech.2017.03.011.

[72] Cesar Tregón Esteban. Comparación de coste y consumo entre varios sistemas de adquisición de datos para una malla sensible a la presión. Trabajo fin de grado, Escuela Universitaria Politécnica de Teruel, Universidad de Zaragoza, 2022.

[73] M. Galassi et al. Gnu scientific library reference manual, 2018. URL https://www.gnu.org/software/gsl/.

[74] Fawwaz Eniola Fajingbesi, Amelia Wong Azman, Zuraida Ahmad, Rashidah Funke Olanrewaju, Muhammad Ibn Ibrahimy, and Yasir Mohd Mustafah. Low cost piezoresistive pressure sensor matrix for pressure ulcer prevention and management. In *2019 7th International Conference on Mechatronics Engineering (ICOM)*, pages 1–4, October 2019. doi: 10.1109/ICOM47790.2019.8952007.

[75] A. G. Ferreira, A. P. Catarino, J. L. Monteiro, and A. M. Rocha. Textile-based pressure sensors for step detection: a preliminary assessment. *IOP Conference Series: Materials Science and Engineering*, 459(1):012041, February 2018. ISSN 1757-899X. doi: 10.1088/1757-899X/459/1/012041. Publisher: IOP Publishing.

[76] Python Software Foundation. The python standard library, 2001. URL https://docs.python.org/3/library/index.html.

[77] M. Frey, M. Barrett, and D. De Carvalho. Effect of a dynamic seat pan design on spine biomechanics, calf circumference and perceived pain during prolonged sitting. *Applied Ergonomics*, 97:103546, January 2021. ISSN 0003-6870. doi: 10.1016/j.apergo.2021.103546.

[78] Mona Frey, Alison Poynter, Keisha Younge, and Diana De Carvalho. The relationship between lumbopelvic flexibility and sitting posture in adult women. *Journal of Biomechanics*, 84:204–210, February 2019. ISSN 0021-9290. doi: 10.1016/j.jbiomech.2018.12.048.

[79] Mona Frey, Ryan Greene, and Diana De Carvalho. What is the best way to collect maximum forward lumbar spine flexion values for normalizing posture to range of motion? *Journal of Biomechanics*, 103:109706, April 2020. ISSN 0021-9290. doi: 10.1016/j.jbiomech.2020.109706.

[80] Wataru Fukui, Futoshi Kobayashi, Fumio Kojima, Hiroyuki Nakamoto, Nobuaki Imamura, Tadashi Maeda, and Hidenori Shirasawa. High-speed tactile sensing for array-type tactile sensor and object manipulation based on tactile information. *Journal of Robotics*, 2011:691769, Dec 2011. ISSN 1687-9600. doi: 10.1155/2011/691769.

[81] Kaitlin M. Gallagher, Michael Sehl, and Jack P. Callaghan. A radiographic assessment of lumbar spine posture in four different upright standing positions. *Clinical Biomechanics*, 37:131–136, August 2016. ISSN 0268-0033. doi: 10.1016/j.clinbiomech.2016.07.004.

[82] Aurélien Geéron. *Hands-on machine learning with Scikit-Learn and Tensor-Flow : concepts, tools, and techniques to build intelligent systems*. O'Reilly Media, Sebastopol, CA, 2017. ISBN 978-1491962299.

[83] A. Gholipour and N. Arjmand. Artificial neural networks to predict 3d spinal posture in reaching and lifting activities; applications in biomechanical models. *Journal of Biomechanics*, 49(13):2946–2952, September 2016. ISSN 0021-9290. doi: 10.1016/j.jbiomech.2016.07.008.

[84] Davide Giovanelli and Elisabetta Farella. Force sensing resistor and evaluation of technology for wearable body pressure sensing. *Journal of Sensors*, 2016:e9391850, February 2016. ISSN 1687-725X. doi: 10.1155/2016/9391850. Publisher: Hindawi.

[85] John Goetschius, Mark A. Feger, Jay Hertel, and Joseph M. Hart. Validating center-of-pressure balance measurements using the matscan® pressure mat. *Journal of Sport Rehabilitation*, 27(1):1 – 5, 2018. ISSN 10566716. doi: https://doi.org/10.1123/jsr.2017-0152.

[86] Hong Gong, Chen-Xu Ni, Yun-Zi Liu, Yi Zhang, Wen-Jun Su, Yong-Jie Lian, Wei Peng, and Chun-Lei Jiang. Mindfulness meditation for insomnia: A meta-analysis of randomized controlled trials. *Journal of Psychosomatic Research*, 89:1–6, 2016.

[87] Ian J. Goodfellow, Yoshua Bengio, and Aaron Courville. *Deep Learning.* MIT Press, Cambridge, MA, USA, 2016. `http://www.deeplearningbook.org`.

[88] Runyu L. Greene, Yu Hen Hu, Nicholas Difranco, Xuan Wang, Ming-Lun Lu, Stephen Bao, Jia-Hua Lin, and Robert G. Radwin. Predicting sagittal plane lifting postures from image bounding box dimensions. *Human Factors*, 61(1):64–77, February 2019. ISSN 0018-7208. doi: 10.1177/0018720818791367. Publisher: SAGE Publications Inc.

[89] D. W. Grieve and T. Rashdi. Pressures under normal feet in standing and walking as measured by foil pedobarography. *Annals of the Rheumatic Diseases*, 43:816–818, 1984. doi: https://doi.org/10.1136/ard.43.6.816.

[90] Guo-Ying Gu, Li-Min Zhu, Chun-Yi Su, Han Ding, and Sergej Fatikow. Modeling and control of piezo-actuated nanopositioning stages: A survey. *IEEE Transactions on Automation Science and Engineering*, 13(1):313–332, 2016. doi: 10.1109/TASE.2014.2352364.

[91] Guoying Gu, Limin Zhu, and ChunYi Su. Modeling and compensation of asymmetric hysteresis nonlinearity for piezoceramic actuators with a modified prandtlishlinskii model. *IEEE Transactions on Industrial Electronics*, 61:1583–1595, 2014.

[92] Megan Hamilton, Kamran Behdinan, and Jan Andrysek. Evaluating the effects of load area and sensor configuration on the performance of pressure sensors at simulated body-device interfaces. *IEEE Sensors Journal*, 20 (10):5187–5194, May 2020. ISSN 1530-437X, 1558-1748, 2379-9153. doi: 10.1109/JSEN.2020.2970964.

[93] Kaiming He, Xiangyu Zhang, Shaoqing Ren, and Jian Sun. Delving deep into rectifiers: Surpassing human-level performance on ImageNet classification. In *2015 IEEE International Conference on Computer Vision (ICCV),*

pages 1026–1034, February 2015. doi: 10.1109/ICCV.2015.123. ISSN: 2380-7504.

[94] José A. Hidalgo-López, Óscar Oballe-Peinado, Julián Castellanos-Ramos, José A. Sánchez-Durán, Raquel Fernández-Ramos, and Fernando Vidal-Verdú. High-accuracy readout electronics for piezoresistive tactile sensors. *Sensors*, 17(11), 2017. ISSN 1424-8220. doi: 10.3390/s17112513.

[95] José A. Hidalgo-López, Raquel Fernández-Ramos, Jorge Romero-Sánchez, José F. Martín-Canales, and Francisco J. Ríos-Gómez. Improving accuracy in the readout of resistive sensor arrays. *Journal of Sensors*, 2018. doi: 10.1155/2018/9735741.

[96] José A. Hidalgo-López, Jorge Romero-Sánchez, and Raquel Fernández-Ramos. New approaches for increasing accuracy in readout of resistive sensor arrays. *IEEE Sensors Journal*, 17(7):2154–2164, 2017. doi: 10.1109/JSEN.2017.2662803.

[97] Lara Hilton, Susanne Hempel, Brett A Ewing, Eric Apaydin, Lea Xenakis, Sydne Newberry, Ben Colaiaco, Alicia Ruelaz Maher, Roberta M Shanman, Melony E Sorbero, et al. Mindfulness meditation for chronic pain: systematic review and meta-analysis. *Annals of behavioral medicine*, 51(2): 199–213, 2017.

[98] Matthew Hopkins, Ravi Vaidyanathan, and Alison H. Mcgregor. Examination of the performance characteristics of velostat as an in-socket pressure sensor. *IEEE Sensors Journal*, 20(13):6992–7000, July 2020. ISSN 1558-1748. doi: 10.1109/JSEN.2020.2978431.

[99] Bin Hu, Guo-Ping Gao, Le-Le He, Xiao-Dong Cong, and Jin-Ning Zhao. Bending and on-arm effects on a wearable antenna for 2.45 GHz body area network. *IEEE Antennas and Wireless Propagation Letters*, 15:378–381, 2016. ISSN 1548-5757. doi: 10.1109/LAWP.2015.2446512.

[100] Robert Hudec, Miroslav Benco, Slavomir Matuska, Patrik Kamencay, and Martina Zachariasova. Utilization of electro-conductive blended ag/PA textile rayon yarns as data and power wires in an intelligent textile structures. In *2014 ELEKTRO*, pages 658–661, May 2014. doi: 10.1109/ELEKTRO.2014.6848982.

[101] Babar Jamil, Seulah Lee, and Youngjin Choi. Conductive knit-covered pneumatic artificial muscle (k-PAM) actuator. In *2018 IEEE/RSJ International Conference on Intelligent Robots and Systems (IROS)*, pages 1476–1481, October 2018. doi: 10.1109/IROS.2018.8594510. ISSN: 2153-0866.

[102] Sangeun Jin and Gary A. Mirka. A systems-level perspective of the biomechanics of the trunk flexion-extension movement: Part i normal low back condition. *International Journal of Industrial Ergonomics*, 46:7–11, March 2015. ISSN 0169-8141. doi: 10.1016/j.ergon.2015.01.008.

[103] Seong-Hun Jo. How to sit in sitting meditation. *Mindfulness*, 10(11):2468–2471, 2019.

[104] Masoud Kalantari, Javad Dargahi, Jozsef Kövecses, Mahmood Ghanbari Mardasi, and Shahrzad Nouri. A new approach for modeling piezoresistive force sensors based on semiconductive polymer composites. *IEEE/ASME Transactions on Mechatronics*, 17(3):572–581, June 2012. ISSN 1941-014X. doi: 10.1109/TMECH.2011.2108664.

[105] Martin Kaltenbrunner, Tsuyoshi Sekitani, Jonathan Reeder, Tomoyuki Yokota, Kazunori Kuribara, Takeyoshi Tokuhara, Michael Drack, Reinhard Schwödiauer, Ingrid Graz, Simona Bauer-Gogonea, Siegfried Bauer, and Takao Someya. An ultra-lightweight design for imperceptible plastic electronics. *Nature*, 499:458–63, July 2013. doi: 10.1038/nature12314.

[106] Wern Kam, Kieran O'Sullivan, Mary O'Keeffe, Sinead O'Keeffe, Waleed S. Mohammed, and Elfed Lewis. Low cost portable 3-d printed optical fiber sensor for real-time monitoring of lower back bending. *Sensors and Actuators A: Physical*, 265:193–201, October 2017. ISSN 0924-4247. doi: 10.1016/j.sna.2017.08.044.

[107] Sung-Won Kang, Hyeob Choi, Hyung-Il Park, Byoung-Gun Choi, Hyobin Im, Dongjun Shin, Young-Giu Jung, Jun-Young Lee, Hong-Won Park, Sukyung Park, and Jung-Sim Roh. The development of an IMU integrated clothes for postural monitoring using conductive yarn and interconnecting technology. *Sensors*, 17(11):2560, January 2017. ISSN 1424-8220. doi: 10.3390/s17112560. Number: 11 Publisher: Multidisciplinary Digital Publishing Institute.

[108] Kyong Kim, Mi Yeon Shin, Woo Suk Chong, and Chang Ho Yu. Study on the spine health management of the elderly using center of pressure data. *Journal of Mechanics in Medicine and Biology*, 20(10):2040041, February 2020. ISSN 0219-5194. doi: 10.1142/S0219519420400412. Publisher: World Scientific Publishing Co.

[109] P. Krejci and K. Kuhnen. Inverse control of systems with hysteresis and creep. *IEE Proceedings - Control Theory and Applications*, 148:185–192(7), May 2001. ISSN 1350-2379. URL https://digital-library.theiet.org/content/journals/10.1049/ip-cta_20010375.

[110] Ute Kreplin, Miguel Farias, and Inti A Brazil. The limited prosocial effects of meditation: A systematic review and meta-analysis. *Scientific reports*, 8 (1):2403, 2018.

[111] John A. Kreuz. Characterization of kaptonő polyimide film for use in flexible circuitry. In *1973 EIC 11th Electrical Insulation Conference*, pages 231–233, September 1973. doi: 10.1109/EIC.1973.7468695.

[112] Alex Krizhevsky, Ilya Sutskever, and Geoffrey E. Hinton. ImageNet classification with deep convolutional neural networks. *Communications of the ACM*, 60(6):84–90, May 2017. ISSN 0001-0782. doi: 10.1145/3065386.

[113] H.H. Ku. Notes on the use of propagation of error formulas. *Journal of Research of the National Bureau of Standards*, 70C(4):263–273, 1966. doi: 10.6028/jres.070c.025.

[114] Roman Peter Kuster, Christoph Markus Bauer, Sarah Oetiker, and Jan Kool. Physiological motion axis for the seat of a dynamic office chair. *Human Factors*, 58(6):886–898, September 2016. ISSN 0018-7208. doi: 10.1177/0018720816646508. Publisher: SAGE Publications Inc.

[115] Microcontrollers Lab. STM32f103c8t6 blue pill development board, January 2021. URL https://microcontrollerslab.com/stm32f103c8t6-blue-pill-pinout-peripherals-programming-features/.

[116] Kelly Ka-Lee Lai, Timothy Tin-Yan Lee, Michael Ka-Shing Lee, Joseph Chi-Ho Hui, and Yong-Ping Zheng. Validation of scolioscan air-portable radiation-free three-dimensional ultrasound imaging assessment system for

scoliosis. *Sensors*, 21(8):2858, January 2021. ISSN 1424-8220. doi: 10.3390/s21082858. Number: 8 Publisher: Multidisciplinary Digital Publishing Institute.

[117] Kathleen A. Lamkin-Kennard and Marko B. Popovic. 4 - sensors: Natural and synthetic sensors. In Marko B. Popovic, editor, *Biomechatronics*, pages 81–107. Academic Press, 2019. ISBN 978-0-12-812939-5. doi: https://doi.org/10.1016/B978-0-12-812939-5.00004-5.

[118] Y. Langeron, M. Doussot, D. J. Hewson, and J. Duchêne. Classifying NIR spectra of textile products with kernel methods. *Engineering Applications of Artificial Intelligence*, 20(3):415–427, April 2007. ISSN 0952-1976. doi: 10.1016/j.engappai.2006.07.001.

[119] R. Lazzarini, R. Magni, and P. Dario. A tactile array sensor layered in an artificial skin. In *Proceedings 1995 IEEE/RSJ International Conference on Intelligent Robots and Systems. Human Robot Interaction and Cooperative Robots*, volume 3, pages 114–119 vol.3, 1995. doi: 10.1109/IROS.1995.525871.

[120] Kam Leang, Qingze Zou, and Santosh Devasia. Feedforward control of piezoactuators in atomic force microscope systems. *IEEE Control Systems*, 29:70–82, 2009.

[121] Hoonyong Lee, Kanghyeok Yang, Namgyun Kim, and Changbum R. Ahn. Detecting excessive load-carrying tasks using a deep learning network with a gramian angular field. *Automation in Construction*, 120:103390, February 2020. ISSN 0926-5805. doi: 10.1016/j.autcon.2020.103390.

[122] Hyosang Lee, Haedo Cho, Sangjoon J Kim, Yeongjin Kim, and Jung Kim. Dispenser printing of piezo-resistive nanocomposite on woven elastic fabric and hysteresis compensation for skin-mountable stretch sensing. *Smart Materials and Structures*, 27(2):025017, jan 2018. doi: 10.1088/1361-665x/aaa5e3.

[123] Jaehyun Lee, Hyosung Joo, Junglyeon Lee, and Youngjoon Chee. Automatic classification of squat posture using inertial sensors: Deep learning approach. *Sensors*, 20(2):361, January 2020. ISSN 1424-8220. doi:

10.3390/s20020361. Number: 2 Publisher: Multidisciplinary Digital Publishing Institute.

[124] N. K. S. Lee, R. S. Goonetilleke, Y. S. Cheung, and Geommi M. Y. So. A flexible encapsulated MEMS pressure sensor system for biomechanical applications. *Microsystem Technologies*, 7(2):55–62, May 2001. ISSN 1432-1858. doi: 10.1007/s005420100092.

[125] R. Leenen. *The modelling and identification of an hysteretic system: the wire as a nonlinear shock vibration isolator*. DCT rapporten. Technische Universiteit Eindhoven, 2002.

[126] Chun-Ting Li, Chih-Hsien Chen, Yen-Nien Chen, Chih-Han Chang, and Kuen-Horng Tsai. Biomechanical evaluation of a novel wheelchair backrest for elderly people. *BioMedical Engineering OnLine*, 14(1):1–10, February 2015. ISSN 1475-925X. doi: 10.1186/s12938-015-0008-6. Number: 1 Publisher: BioMed Central.

[127] Erfeng Li, Xiaoyou Lin, Boon-Chong Seet, Frances Joseph, and Jono Neville. Low profile and low cost textile smart mat for step pressure sensing and position mapping. In *2019 IEEE International Instrumentation and Measurement Technology Conference (I2MTC)*, pages 1–5, May 2019. doi: 10.1109/I2MTC.2019.8826892. ISSN: 2642-2077.

[128] Nan Li, Dapeng Yang, Li Jiang, Hong Liu, and Hegao Cai. Combined use of fsr sensor array and svm classifier for finger motion recognition based on pressure distribution map. *Journal of Bionic Engineering*, 9(1):39–47, Mar 2012. ISSN 2543-2141. doi: 10.1016/S1672-6529(11)60095-4.

[129] Wei Li, Chenglu Sun, Wei Yuan, Weibing Gu, Zheng Cui, and Wei Chen. Smart mat system with pressure sensor array for unobtrusive sleep monitoring. In *2017 39th Annual International Conference of the IEEE Engineering in Medicine and Biology Society (EMBC)*, pages 177–180. IEEE, July 2017. ISBN 978-1-5090-2809-2. doi: 10.1109/EMBC.2017.8036791.

[130] Yutian Li, Xuhong Miao, and Rafiu King Raji. Flexible knitted sensing device for identifying knee joint motion patterns. *Smart Materials and Structures*, 28(11):115042, October 2019. ISSN 0964-1726. doi: 10.1088/1361-665X/ab4afe. Publisher: IOP Publishing.

[131] Zhen Li, Yan-Yi Liang, Lei Wang, Jing Sheng, and Shao-Jun Ma. Reliability and validity of center of pressure measures for balance assessment in older adults. *Journal of Physical Therapy Science*, 28(4):1364–1367, 2016. doi: 10.1589/jpts.28.1364.

[132] An Liang, Rebecca Stewart, and Nick Bryan-Kinns. Analysis of sensitivity, linearity, hysteresis, responsiveness, and fatigue of textile knit stretch sensors. *Sensors*, 19(16):3618, January 2019. ISSN 1424-8220. doi: 10.3390/s19163618. Number: 16 Publisher: Multidisciplinary Digital Publishing Institute.

[133] Craig Liebenson, Amy M. Karpowicz, Stephen H.M. Brown, Samuel J. Howarth, and Stuart M. McGill. The active straight leg raise test and lumbar spine stability. *PM&R*, 1(6):530–535, 2009. ISSN 1934-1563. doi: 10.1016/j.pmrj.2009.03.007.

[134] H. Liu, E. Sanchez, J. Parkerson, and A. Nelson. Poster abstract: Unobtrusive sleep monitoring with low-cost pressure sensor array. In *2019 IEEE/ACM International Conference on Connected Health: Applications, Systems and Engineering Technologies (CHASE)*, pages 17–18, Sep. 2019. doi: 10.1109/CHASE48038.2019.00014.

[135] Hangxin Liu, Xu Xie, Matt Millar, Mark Edmonds, Feng Gao, Yixin Zhu, Veronica J. Santos, Brandon Rothrock, and Song-Chun Zhu. A glove-based system for studying hand-object manipulation via joint pose and force sensing. In *2017 IEEE/RSJ International Conference on Intelligent Robots and Systems (IROS)*, pages 6617–6624, September 2017. doi: 10.1109/IROS.2017.8206575. ISSN: 2153-0866.

[136] Haoyan Liu, Enrique Sanchez, James Parkerson, and Alexander Nelson. Poster abstract: Unobtrusive sleep monitoring with low-cost pressure sensor array. In *2019 IEEE/ACM International Conference on Connected Health: Applications, Systems and Engineering Technologies (CHASE)*, pages 17–18, September 2019. doi: 10.1109/CHASE48038.2019.00014.

[137] Weifeng Liu, Dongkai Shangguan, and Jeffrey ChangBing Lee. Evaluation of launderability of electrically conductive fabrics for e-textile applications. *IEEE Transactions on Components, Packaging and Manu-*

facturing Technology, 10(5):763–769, May 2020. ISSN 2156-3985. doi: 10.1109/TCPMT.2020.2981902.

[138] José A. Hidalgo López, Óscar Oballe-Peinado, and José A. Sánchez-Durán. A proposal to eliminate the impact of crosstalk on resistive sensor array readouts. *IEEE Sensors Journal*, 20(22):13461–13470, 2020. doi: 10.1109/ JSEN.2020.3005227.

[139] Fan-Zhe Low, Matthew Chin-Heng Chua, Pan-Yin Lim, and Chen-Hua Yeow. Effects of mattress material on body pressure profiles in different sleeping postures. *Journal of Chiropractic Medicine*, 16(1):1–9, March 2017. ISSN 1556-3707. doi: 10.1016/j.jcm.2016.09.002.

[140] Ming-Lun Lu, Thomas Waters, and Dwight Werren. Development of human posture simulation method for assessing posture angles and spinal loads. *Human Factors and Ergonomics in Manufacturing & Service Industries*, 25 (1):123–136, 2015. ISSN 1520-6564. doi: 10.1002/hfm.20534.

[141] Tony Luczak, Reuben F. Burch V, Brian K. Smith, Daniel W. Carruth, John Lamberth, Harish Chander, Adam Knight, J. E. Ball, and R. K. Prabhu. Closing the wearable gappart v: Development of a pressure-sensitive sock utilizing soft sensors. *Sensors*, 20(1):208, January 2020. ISSN 1424-8220. doi: 10.3390/s20010208. Number: 1 Publisher: Multidisciplinary Digital Publishing Institute.

[142] Christina Zong-Hao Ma, Long-Jun Ren, Connie Lok-Kan Cheng, and Yong-Ping Zheng. Mapping of back muscle stiffness along spine during standing and lying in young adults: A pilot study on spinal stiffness quantification with ultrasound imaging. *Sensors*, 20(24):7317, January 2020. ISSN 1424-8220. doi: 10.3390/s20247317. Number: 24 Publisher: Multidisciplinary Digital Publishing Institute.

[143] Willem Maes. How to make an arduino fast enough to... April 2018. URL https://es.scribd.com/document/396171556/speeding-arduino.

[144] Sara Mahallati, Hossein Rouhani, Richard Preuss, Kei Masani, and Milos R. Popovic. Multisegment kinematics of the spinal column: Soft tissue artifacts assessment. *Journal of Biomechanical Engineering*, 138(7), June 2016. ISSN 0148-0731. doi: 10.1115/1.4033545.

[145] Ramesh Manocha. Why meditation? *Australian Family Physician*, 29(12): 1135–1138, 2000.

[146] Elvira Maranesi, Giacomo Ghetti, Rosa Anna Rabini, and Sandro Fioretti. Functional reach test: Movement strategies in diabetic subjects. *Gait & Posture*, 39(1):501 – 505, 2014. ISSN 0966-6362. doi: https://doi.org/10.1016/j.gaitpost.2013.08.035.

[147] Arnas Martinaitis and Kristina Daunoraviciene. Low cost self-made pressure distribution sensors for ergonomic chair: Are they suitable for posture monitoring? *Technology and Health Care*, 26:655–663, January 2018. ISSN 0928-7329. doi: 10.3233/THC-182512. Publisher: IOS Press.

[148] Javier Martinez-Cesteros, Carlos Medrano-Sanchez, Inmaculada Plaza-Garcia, Raul Igual-Catalan, and Sergio Albiol-Pérez. A velostat-based pressure-sensitive mat for center-of-pressure measurements: A preliminary study. *International Journal of Environmental Research and Public Health*, 18(11), 2021. ISSN 1660-4601. doi: 10.3390/ijerph18115958.

[149] Javier Martinez-Cesteros, Carlos Medrano-Sanchez, Inmaculada Plaza-Garcia, and Raul Igual-Catalan. Uncertainty analysis in the inverse of equivalent conductance method for dealing with crosstalk in 2-d resistive sensor arrays. *IEEE Sensors Journal*, 22(1):373–384, 2022. doi: 10.1109/JSEN.2021.3129668.

[150] Carlos Medrano-Sánchez, Raul Igual-Catalán, Victor H. Rodríguez-Ontiveros, and Inmaculada Plaza-García. Circuit analysis of matrix-like resistor networks for eliminating crosstalk in pressure sensitive mats. *IEEE Sensors Journal*, 19(18):8027–8036, September 2019. ISSN 1558-1748. doi: 10.1109/JSEN.2019.2918592.

[151] Jan Meyer, Bert Arnrich, Johannes Schumm, and Gerhard Troster. Design and modeling of a textile pressure sensor for sitting posture classification. *IEEE Sensors Journal*, 10(8):1391–1398, August 2010. ISSN 1558-1748. doi: 10.1109/JSEN.2009.2037330.

[152] P.A. Misiewicz, K. Blackburn, T.E. Richards, J.L. Brighton, and R.J. Godwin. The evaluation and calibration of pressure mapping system for the

measurement of the pressure distribution of agricultural tyres. *Biosystems Engineering*, 130:81 – 91, 2015. ISSN 1537-5110. doi: https://doi.org/10.1016/j.biosystemseng.2014.12.006.

[153] Niels C. C. M. Moes. Variation in sitting pressure distribution and location of the points of maximum pressure with rotation of the pelvis, gender and body characteristics. *Ergonomics*, 50(4):536–561, April 2007. ISSN 0014-0139. doi: 10.1080/00140130601138585. Publisher: Taylor & Francis.

[154] Yousef Mohammadi, Navid Arjmand, and Aboulfazl Shirazi-Adl. Comparison of trunk muscle forces, spinal loads and stability estimated by one stability- and three EMG-assisted optimization approaches. *Medical Engineering & Physics*, 37(8):792–800, August 2015. ISSN 1350-4533. doi: 10.1016/j.medengphy.2015.05.018.

[155] Babak Mokaberi and Aristides A. G. Requicha. Compensation of scanner creep and hysteresis for afm nanomanipulation. *IEEE Transactions on Automation Science and Engineering*, 5:197–206, 2008.

[156] Dafne Zuleima Morgado Ramirez, Maria del Pilar Garcia Souto, Benjamin M. Oldfrey, Peter Smitham, Mark Miodownik, and Catherine Holloway. Characterization of bespoke force sensors for tailored applications. *IEEE Sensors Journal*, 17(6):1727–1734, March 2017. ISSN 1530-437X, 1558-1748, 2379-9153. doi: 10.1109/JSEN.2016.2644378.

[157] Seiyed Hamid Mousavi, Hassan Sayyaadi, and Navid Arjmand. Prediction of the thorax/pelvis orientations and l5s1 disc loads during various static activities using neuro-fuzzy. *Journal of Mechanical Science and Technology*, 34(8):3481–3485, August 2020. ISSN 1976-3824. doi: 10.1007/s12206-020-0740-0.

[158] Seyed Javad Mousavi, Rebecca Tromp, Matthew C. Swann, Andrew P. White, and Dennis E. Anderson. Between-session reliability of opto-electronic motion capture in measuring sagittal posture and 3-d ranges of motion of the thoracolumbar spine. *Journal of Biomechanics*, 79:248–252, October 2018. ISSN 0021-9290. doi: 10.1016/j.jbiomech.2018.08.033.

[159] Falk Mörl, Michael Günther, Julia M. Riede, Maria Hammer, and Syn Schmitt. Loads distributed in vivo among vertebrae, muscles, spinal liga-

ments, and intervertebral discs in a passively flexed lumbar spine. *Biomechanics and Modeling in Mechanobiology*, 19(6):2015–2047, February 2020. ISSN 1617-7940. doi: 10.1007/s10237-020-01322-7.

[160] M. Narimani and N. Arjmand. Three-dimensional primary and coupled range of motions and movement coordination of the pelvis, lumbar and thoracic spine in standing posture using inertial tracking device. *Journal of Biomechanics*, 69:169–174, March 2018. ISSN 0021-9290. doi: 10.1016/j.jbiomech.2018.01.017.

[161] Robert Needham, Roozbeh Naemi, Aoife Healy, and Nachiappan Chockalingam. Multi-segment kinematic model to assess three-dimensional movement of the spine and back during gait. *Prosthetics and Orthotics International*, 40(5):624, October 2016. ISSN 0309-3646. doi: 10.1177/0309364615579319.

[162] Joanna L. Ng, Vina D. L. Putra, and Melissa L. Knothe Tate. In vitro biocompatibility and biomechanics study of novel, microscopy aided designed and ManufacturEd (MADAME) materials emulating natural tissue weaves and their intrinsic gradients. *Journal of the Mechanical Behavior of Biomedical Materials*, 103:103536, March 2020. ISSN 1751-6161. doi: 10.1016/j.jmbbm.2019.103536.

[163] Bradford Nichols, Dick Buttlar, and Jacqueline Proulx Farrell. *Pthreads programming - a POSIX standard for better multiprocessing.* O'Reilly, 1996. ISBN 978-1-56592-115-3.

[164] Shermeen Nizami, Madison Cohen-McFarlane, James R. Green, and Rafik Goubran. Comparing metrological properties of pressure-sensitive mats for continuous patient monitoring. In *2017 IEEE Sensors Applications Symposium (SAS)*, pages 1–6, March 2017. doi: 10.1109/SAS.2017.7894054.

[165] Shermeen Nizami, Amente Bekele, Mohamed Hozayen, Kimberley J. Greenwood, JoAnn Harrold, and James R. Green. Measuring uncertainty during respiratory rate estimation using pressure-sensitive mats. *IEEE Transactions on Instrumentation and Measurement*, 67(7):1535–1542, July 2018. ISSN 0018-9456, 1557-9662. doi: 10.1109/TIM.2018.2805154.

[166] Kunihiko Nomura, Kei Fukada, Teruaki Azuma, Toshimitsu Hamasaki, Saburo Sakoda, and Taishin Nomura. A quantitative characterization of postural sway during human quiet standing using a thin pressure distribution measurement system. *Gait & Posture*, 29(4):654 – 657, 2009. ISSN 0966-6362. doi: https://doi.org/10.1016/j.gaitpost.2009.02.001.

[167] Kunihiko Nomura, Kei Fukada, Teruaki Azuma, Toshimitsu Hamasaki, Saburo Sakoda, and Taishin Nomura. A quantitative characterization of postural sway during human quiet standing using a thin pressure distribution measurement system. *Gait & Posture*, 29(4):654–657, June 2009. ISSN 09666362. doi: 10.1016/j.gaitpost.2009.02.001.

[168] Mykola Novik. torch-optimizer collection of optimization algorithms for PyTorch., January 2020. URL https://github.com/jettify/pytorch-optimizer. original-date: 2020-01-03T03:16:39Z.

[169] Óscar Oballe-Peinado, Fernando Vidal-Verdú, José A. Sánchez-Durán, Julián Castellanos-Ramos, and José A. Hidalgo-López. Improved circuits with capacitive feedback for readout resistive sensor arrays. *Sensors*, 16(2), 2016. ISSN 1424-8220. doi: 10.3390/s16020149.

[170] Andrés Ramiro Osorio Cantor, Jaime Eduardo Manchola Romero, Juan Sebastian Rubiano Labrador, and William Daniel Moscoso Barrera. Estudio y caracterización de telas conductivas para uso en ECG utilizando procedimientos analíticos. In *2018 IEEE ANDESCON*, pages 1–5, August 2018. doi: 10.1109/ANDESCON.2018.8564623.

[171] Satu Pajala, Pertti Era, Markku Koskenvuo, Jaakko Kaprio, Timo Törmäkangas, and Taina Rantanen. Force Platform Balance Measures as Predictors of Indoor and Outdoor Falls in Community-Dwelling Women Aged 6376 Years. *The Journals of Gerontology: Series A*, 63(2):171–178, February 2008. ISSN 1079-5006. doi: 10.1093/gerona/63.2.171.

[172] Pragna Paladugu, Alejandra Hernandez, Karlie Gross, Yi Su, Ahmet Neseli, Sara Gombatto, Kee Moon, and Yusuf Ozturk. A sensor cluster to monitor body kinematics. In *2016 IEEE 13th International Conference on Wearable and Implantable Body Sensor Networks (BSN)*, pages 212–217, June 2016. doi: 10.1109/BSN.2016.7516262. ISSN: 2376-8894.

[173] Davide Paloschi, Marco Bravi, Emiliano Schena, Sandra Miccinilli, Michelangelo Morrone, Silvia Sterzi, Paola Saccomandi, and Carlo Massaroni. Validation and assessment of a posture measurement system with magneto-inertial measurement units. *Sensors*, 21(19):6610, January 2021. ISSN 1424-8220. doi: 10.3390/s21196610. Number: 19 Publisher: Multidisciplinary Digital Publishing Institute.

[174] Un Jin Park and Seong Ho Jang. The influence of backrest inclination on buttock pressure. *Annals of Rehabilitation Medicine*, 35(6):897–906, February 2011. ISSN 2234-0645, 2234-0653. doi: 10.5535/arm.2011.35.6. 897. Publisher: Korean Academy of Rehabilitation Medicine.

[175] K. B. Petersen and M. S. Pedersen. The matrix cookbook, nov 2012. URL http://www2.compute.dtu.dk/pubdb/pubs/3274-full.html. Version 20121115.

[176] A. Plamondon, A. Delisle, C. Larue, D. Brouillette, D. McFadden, P. Desjardins, and C. Larivière. Evaluation of a hybrid system for three-dimensional measurement of trunk posture in motion. *Applied Ergonomics*, 38(6):697–712, January 2007. ISSN 0003-6870. doi: 10.1016/j.apergo.2006. 12.006.

[177] Inmaculada Plaza, Marcelo Marcos Piva Demarzo, Paola Herrera-Mercadal, Javier García-Campayo, et al. Mindfulness-based mobile applications: literature review and analysis of current features. *JMIR mHealth and uHealth*, 1(2):e2733, 2013.

[178] David Poulard, Damien Subit, John-Paul Donlon, and Richard W. Kent. Development of a computational framework to adjust the pre-impact spine posture of a whole-body model based on cadaver tests data. *Journal of Biomechanics*, 48(4):636–643, February 2015. ISSN 0021-9290. doi: 10. 1016/j.jbiomech.2014.12.050.

[179] M. Baran Pouyan, J. Birjandtalab, M. Heydarzadeh, M. Nourani, and S. Ostadabbas. A pressure map dataset for posture and subject analytics. In *2017 IEEE EMBS International Conference on Biomedical & Health Informatics (BHI)*, pages 65–68, February 2017. doi: 10.1109/BHI.2017.7897206.

[180] Celestine Preetham, Girish Ramakrishnan, Sujan Kumar, Anish Tamse, and Nagendra Krishnapura. Hand talk-implementation of a gesture recognizing glove. In *2013 Texas Instruments India Educators' Conference*, pages 328–331, April 2013. doi: 10.1109/TIIEC.2013.65.

[181] T.E. Prieto, J.B. Myklebust, R.G. Hoffmann, E.G. Lovett, and B.M. Myklebust. Measures of postural steadiness: differences between healthy young and elderly adults. *IEEE Transactions on Biomedical Engineering*, 43(9): 956–966, 1996. doi: 10.1109/10.532130.

[182] Flavien Quijoux, Aliénor Vienne-Jumeau, François Bertin-Hugault, Philippe Zawieja, Marie Lefèvre, Pierre-Paul Vidal, and Damien Ricard. Center of pressure displacement characteristics differentiate fall risk in older people: A systematic review with meta-analysis. *Ageing Research Reviews*, 62:101117, 2020. ISSN 1568-1637. doi: https://doi.org/10.1016/j.arr.2020. 101117.

[183] Jakub Rafl, Thomas E Bachman, Veronika Rafl-Huttova, Simon Walzel, and Martin Rozanek. Commercial smartwatch with pulse oximeter detects short-time hypoxemia as well as standard medical-grade device: Validation study. *DIGITAL HEALTH*, 8:20552076221132127, 2022. doi: 10.1177/ 20552076221132127.

[184] Mohammad Shamim Reza, Kevin Ray Ayag, Mi Kyong Yoo, Kap Jin Kim, and Hongdoo Kim. Electrospun spandex nanofiber webs with ionic liquid for highly sensitive, low hysteresis piezocapacitive sensor. *Fibers and Polymers*, 20(2):337–347, February 2019. ISSN 1875-0052. doi: 10.1007/s12221-019-8778-2.

[185] C.P. Robert and G. Casella. *Monte Carlo statistical methods*. Springer Verlag, 2004.

[186] Xavier Robert-Lachaine, Philippe Corbeil, Antoine Muller, Jasmin Vallée-Marcotte, Hakim Mecheri, Denys Denis, and André Plamondon. Combined influence of transfer distance, pace, handled mass and box height on spine loading and posture. *Applied Ergonomics*, 93:103377, May 2021. ISSN 0003-6870. doi: 10.1016/j.apergo.2021.103377.

[187] Alvaro Rodriguez, Juan R. Rabuñal, Alejandro Pazos, Antonio Rodríguez Sotillo, and Norberto Ezquerra. Wearable postural control system for low back pain therapy. *IEEE Transactions on Instrumentation and Measurement*, 70:1–10, 2021. ISSN 1557-9662. doi: 10.1109/TIM.2021.3057935.

[188] Victor H Rodriguez, Carlos T Medrano, and Inmaculada Plaza. Wearable sensors for measuring movement in short sessions of mindfulness sitting meditation: a pilot study. *Journal of Healthcare Engineering*, 2018, 2018.

[189] Sabrina Rose, Ethan Zell, and Jason E Strickhouser. The effect of meditation on health: A metasynthesis of randomized controlled trials. *Mindfulness*, 11:507–516, 2020.

[190] D.V. Sabarianand, P. Karthikeyan, and T. Muthuramalingam. A review on control strategies for compensation of hysteresis and creep on piezoelectric actuators based micro systems. *Mechanical Systems and Signal Processing*, 140:106634, 2020. ISSN 0888-3270. doi: https://doi.org/10.1016/j.ymssp.2020.106634.

[191] Jose Francisco Saenz-Cogollo, Massimiliano Pau, Beatrice Fraboni, and Annalisa Bonfiglio. Pressure mapping mat for tele-home care applications. *Sensors*, 16(3), 2016. ISSN 1424-8220. doi: 10.3390/s16030365.

[192] K. Safi, S. Mohammed, Y. Amirat, and M. Khalil. Postural stability analysis a review of techniques and methods for human stability assessment. In *2017 Fourth International Conference on Advances in Biomedical Engineering (ICABME)*, pages 1–4, 2017.

[193] Sravan Salibindla, Brice Ripoche, Daniel T. H. Lai, and Simon Maas. Characterization of a new flexible pressure sensor for body sensor networks. In *2013 IEEE Eighth International Conference on Intelligent Sensors, Sensor Networks and Information Processing*, pages 27–31, April 2013. doi: 10.1109/ISSNIP.2013.6529758.

[194] S Samadi and N Arjmand. A novel stability-based EMG-assisted optimization method for the spine. *Medical Engineering & Physics*, 58:13–22, August 2018. ISSN 1350-4533. doi: 10.1016/j.medengphy.2018.04.019.

[195] Cynthia Vieira Sanches Sampaio, Manuela Garcia Lima, and Ana Marice Ladeia. Meditation, health and scientific investigations: review of the literature. *Journal of religion and health*, 56:411–427, 2017.

[196] José A. Sánchez-Durán, Fernando Vidal-Verdú, Óscar Oballe-Peinado, Julián Castellanos-Ramos, and José A. Hidalgo-López. A new model based on adaptation of the external loop to compensate the hysteresis of tactile sensors. *Sensors*, 15(10):26170–26197, 2015. ISSN 1424-8220. doi: 10.3390/s151026170.

[197] Jose Antonio Sanchez-Duran. Propuesta y evaluación de algoritmos para la corrección de errores en sensores táctiles, 2016. URL https://riuma.uma.es/xmlui/handle/10630/12213. Accepted: 2016-10-13T12:18:24Z Publisher: Servicio de Publicaciones y Divulgación Científica.

[198] José Antonio Sánchez-Durán, Óscar Oballe-Peinado, Julián Castellanos-Ramos, and Fernando Vidal-Verdú. Hysteresis correction of tactile sensor response with a generalized prandtlishlinskii model. *Microsystem Technologies*, 18:1127–1138, 2012.

[199] Tatiana de Oliveira Sato, Gert-Åke Hansson, and Helenice Jane Cote Gil Coury. Goniometer crosstalk compensation for knee joint applications. *Sensors*, 10(11):9994–10005, January 2010. ISSN 1424-8220. doi: 10.3390/s101109994. Number: 11 Publisher: Molecular Diversity Preservation International.

[200] R. S. Saxena, N. K. Saini, and R. K. Bhan. Analysis of crosstalk in networked arrays of resistive sensors. *IEEE Sensors Journal*, 11(4):920–924, 2011.

[201] Katsuki Sekida. *Za zen*. Editorial Kairós, 2016.

[202] Liba Sheeran, Rebecca Hemming, Robert van Deursen, and Valerie Sparkes. Can different seating aids influence a sitting posture in healthy individuals and does gender matter? *Cogent Engineering*, 5(1):1442109, January 2018. ISSN null. doi: 10.1080/23311916.2018.1442109. Publisher: Cogent OA.

[203] Iman Shojaei, Cazmon Suri, Jaap H. van Dieën, and Babak Bazrgari. Alterations in trunk bending stiffness following changes in stability and equilib-

rium demands of a load holding task. *Journal of Biomechanics*, 77:163–170, August 2018. ISSN 0021-9290. doi: 10.1016/j.jbiomech.2018.07.005.

[204] Lin Shu, Tao Hua, Yangyong Wang, Qiao Li, David Dagan Feng, and Xiaoming Tao. In-shoe plantar pressure measurement and analysis system based on fabric pressure sensing array. *bioinformatics and bioengineering*, 14(3):767–775, 2010. URL https://academic.microsoft.com/paper/2139973231.

[205] Lauren Simpson, Monish M. Maharaj, and Ralph J. Mobbs. The role of wearables in spinal posture analysis: a systematic review. *BMC Musculoskeletal Disorders*, 20(1):1–14, February 2019. ISSN 1471-2474. doi: 10.1186/s12891-019-2430-6. Number: 1 Publisher: BioMed Central.

[206] W. E. Snyder and J. St. Clair. Conductive elastomers as sensor for industrial parts handling equipment. *IEEE Transactions on Instrumentation and Measurement*, 27(1):94–99, March 1978. ISSN 0018-9456. doi: 10.1109/TIM.1978.4314628.

[207] Katharina Stollenwerk, Jonas Müller, André Hinkenjann, and Björn Krüger. Analyzing spinal shape changes during posture training using a wearable device. *Sensors*, 19(16):3625, January 2019. ISSN 1424-8220. doi: 10.3390/s19163625. Number: 16 Publisher: Multidisciplinary Digital Publishing Institute.

[208] Zhiyong Sun, Bo Song, Ning Xi, Ruiguo Yang, Lina Hao, and Liangliang Chen. Scan range adaptive hysteresis/creep hybrid compensator for afm based nanomanipulations. In *2014 American Control Conference*, pages 1619–1624, 2014. doi: 10.1109/ACC.2014.6859376.

[209] Mathias Sundholm, Jingyuan Cheng, Bo Zhou, Akash Sethi, and Paul Lukowicz. Smart-mat: recognizing and counting gym exercises with low-cost resistive pressure sensing matrix. In *Proceedings of the 2014 ACM International Joint Conference on Pervasive and Ubiquitous Computing*, UbiComp '14, pages 373–382. Association for Computing Machinery, September 2014. ISBN 978-1-4503-2968-2. doi: 10.1145/2632048.2636088.

[210] S.S. Suprapto, A.W. Setiawan, H. Zakaria, W. Adiprawita, and B. Supartono. Low-cost pressure sensor matrix using velostat. In *2017 5th*

International Conference on Instrumentation, Communications, Information Technology, and Biomedical Engineering (ICICI-BME), pages 137–140, January 2017. doi: 10.1109/ICICI-BME.2017.8537720. ISSN: 2158-0456.

[211] Shunsuke Suzuki, Mineichi Kudo, and Atsuyoshi Nakamura. Sitting posture diagnosis using a pressure sensor mat. In *2016 IEEE International Conference on Identity, Security and Behavior Analysis (ISBA)*, pages 1–6, February 2016. doi: 10.1109/ISBA.2016.7477236.

[212] Mária Takács, Ervin Rudner, Attila Kovács, Zsanett Orlovits, and Rita M. Kiss. The assessment of the spinal curvatures in the sagittal plane of children using an ultrasound-based motion analysing system. *Annals of Biomedical Engineering*, 43(2):348–362, February 2015. ISSN 1573-9686. doi: 10.1007/s10439-014-1160-z.

[213] Yaguang Tao, Alan Both, Rodrigo I. Silveira, Kevin Buchin, Stef Sijben, Ross S. Purves, Patrick Laube, Dongliang Peng, Kevin Toohey, and Matt Duckham. A comparative analysis of trajectory similarity measures. *GIScience & Remote Sensing*, 58(5):643–669, 2021. doi: 10.1080/15481603. 2021.1908927.

[214] Bernd Tessendorf, Bert Arnrich, Johannes Schumm, Cornelia Setz, and Gerhard Troster. Unsupervised monitoring of sitting behavior. In *2009 Annual International Conference of the IEEE Engineering in Medicine and Biology Society*, pages 6197–6200, September 2009. doi: 10.1109/IEMBS. 2009.5334620. ISSN: 1558-4615.

[215] Thingiverse.com. Side release buckle 3/4 inch by thatburritoth0. URL https://www.thingiverse.com/thing:2591485.

[216] Madhavi Thomas, Joseph Jankovic, Monthaporn Suteerawattananon, Sharmin Wankadia, Kavitha Salomi Caroline, Kevin Dat Vuong, and Elizabeth Protas. Clinical gait and balance scale (GABS): validation and utilization. *Journal of the Neurological Sciences*, 217(1):89–99, January 2004. ISSN 0022-510X. doi: 10.1016/j.jns.2003.09.005.

[217] Amina Tihak and Duanka Bokovi. Experimental evaluation of challenges in designing a resistive pressure sensors. In *IEEE EUROCON 2019 -18th*

International Conference on Smart Technologies, pages 1–6, July 2019. doi: 10.1109/EUROCON.2019.8861803.

[218] Ferdews Tlili, Rim Haddad, Ridha Bouallegue, and Neila Mezghani. A real-time posture monitoring system towards bad posture detection. *Wireless Personal Communications*, 120(2):1207–1227, September 2021. ISSN 1572-834X. doi: 10.1007/s11277-021-08511-2.

[219] Jarkko Tolvanen, Jari Hannu, and Heli Jantunen. Hybrid foam pressure sensor utilizing piezoresistive and capacitive sensing mechanisms. *IEEE Sensors Journal*, 17(15):4735–4746, August 2017. ISSN 1558-1748. doi: 10.1109/JSEN.2017.2718045.

[220] A. Tonazzini, J. Shintake, C. Rognon, V. Ramachandran, S. Mintchev, and D. Floreano. Variable stiffness strip with strain sensing for wearable robotics. In *2018 IEEE International Conference on Soft Robotics (RoboSoft)*, pages 485–490, April 2018. doi: 10.1109/ROBOSOFT.2018. 8405373.

[221] Sergio Valdivia, Robin Blanco, Alvaro Uribe-Quevedo, Lina Penuela, David Rojas, and Bill Kapralos. Development and evaluation of two posture-tracking user interfaces for occupational health care. *Advances in Mechanical Engineering*, 10(6):1687814018769489, June 2018. ISSN 1687-8132. doi: 10.1177/1687814018769489. Publisher: SAGE Publications.

[222] Martin Valis, Jakub Drsata, David Kalfert, Pavel Semerak, and Jan Kremlacek. Computerised static posturography in neurology. *Open Medicine*, 7 (3):317–322, 2012. doi: doi:10.2478/s11536-011-0152-8.

[223] S. M. Van Niekerk, S. M. Fourie, and Q. A. Louw. Postural dynamism during computer mouse and keyboard use: A pilot study. *Applied Ergonomics*, 50:170–176, September 2015. ISSN 0003-6870. doi: 10.1016/j.apergo.2015. 03.009.

[224] Erik Vanegas, Raul Igual, and Inmaculada Plaza. Piezoresistive breathing sensing system with 3d printed wearable casing. *Journal of Sensors*, 2019: 1–19, 2019.

[225] Igor Vehec and Lubomir Livovsky. Flexible resistive sensor based on velo-stat. In *2020 43rd International Spring Seminar on Electronics Technology (ISSE)*, pages 1–6, May 2020. doi: 10.1109/ISSE49702.2020.9121009. ISSN: 2161-2536.

[226] Pauli Virtanen, Ralf Gommers, Travis E. Oliphant, Matt Haberland, Tyler Reddy, David Cournapeau, Evgeni Burovski, Pearu Peterson, Warren Weckesser, Jonathan Bright, Stéfan J. van der Walt, Matthew Brett, Joshua Wilson, K. Jarrod Millman, Nikolay Mayorov, Andrew R. J. Nelson, Eric Jones, Robert Kern, Eric Larson, CJ Carey, İlhan Polat, Yu Feng, Eric W. Moore, Jake VanderPlas, Denis Laxalde, Josef Perktold, Robert Cimrman, Ian Henriksen, E. A. Quintero, Charles R Harris, Anne M. Archibald, Antônio H. Ribeiro, Fabian Pedregosa, Paul van Mulbregt, and SciPy 1. 0 Contributors. SciPy 1.0: Fundamental Algorithms for Scientific Computing in Python. *Nature Methods*, 17:261–272, 2020. doi: https://doi.org/10.1038/s41592-019-0686-2.

[227] Gheorghe-Daniel Voinea, Silviu Butnariu, and Gheorghe Mogan. Measurement and geometric modelling of human spine posture for medical rehabilitation purposes using a wearable monitoring system based on inertial sensors. *Sensors*, 17(1):3, January 2017. ISSN 1424-8220. doi: 10.3390/s17010003. Number: 1 Publisher: Multidisciplinary Digital Publishing Institute.

[228] Linh Q. Vu, K. Han Kim, Lawrence J. H. Schulze, and Sudhakar L. Rajulu. Lumbar posture assessment with fabric strain sensors. *Computers in Biology and Medicine*, 118:103624, March 2020. ISSN 0010-4825. doi: 10.1016/j. compbiomed.2020.103624.

[229] Linh Q. Vu, Han Kim, Lawrence J. H. Schulze, and Sudhakar L. Rajulu. Evaluating lumbar shape deformation with fabric strain sensors. *Human Factors*, 64(4):649–661, June 2022. ISSN 0018-7208. doi: 10.1177/ 0018720820965302. Publisher: SAGE Publications Inc.

[230] Hongbo Wang, Greg de Boer, Junwai Kow, Mazdak Ghajari, Ali Alazmani, Robert Hewson, and Peter Culmer. A low-cost soft tactile sensing array using 3d hall sensors. *Procedia Engineering*, 168:650–653, 2016. ISSN 1877-7058. doi: https://doi.org/10.1016/j.proeng.2016.11.237. Proceedings

of the 30th anniversary Eurosensors Conference Eurosensors 2016, 4-7. Sepember 2016, Budapest, Hungary.

[231] Peng Wang and Tianhuai Ding. Creep of electrical resistance under uniaxial pressures for carbon blacksilicone rubber composite. *Journal of Materials Science*, 45(13):3595–3601, July 2010. ISSN 1573-4803. doi: 10.1007/s10853-010-4405-8.

[232] Qi Wang, Panos Markopoulos, Bin Yu, Wei Chen, and Annick Timmermans. Interactive wearable systems for upper body rehabilitation: a systematic review. *Journal of NeuroEngineering and Rehabilitation*, 14(1): 1–21, February 2017. ISSN 1743-0003. doi: 10.1186/s12984-017-0229-y. Number: 1 Publisher: BioMed Central.

[233] Xiaying Wang, Fabian Geiger, Vlad Niculescu, Michele Magno, and Luca Benini. Leveraging tactile sensors for low latency embedded smart hands for prosthetic and robotic applications. *IEEE Transactions on Instrumentation and Measurement*, 71:1–14, 2022. doi: 10.1109/TIM.2022.3165828.

[234] Zhelong Wang, Jiaxin Wang, Hongyu Zhao, Sen Qiu, Jie Li, Fengshan Gao, and Xin Shi. Using wearable sensors to capture posture of the human lumbar spine in competitive swimming. *IEEE Transactions on Human-Machine Systems*, 49(2):194–205, April 2019. ISSN 2168-2305. doi: 10.1109/THMS.2019.2892318.

[235] Zheyao Wang, Yonggui Dong, Huizhong Zhu, and Guanping Feng. Creep characteristics of combined bulk acoustic wave quartz resonator force sensors. *Sensors and Actuators A: Physical*, 111(2):203–209, March 2004. ISSN 0924-4247. doi: 10.1016/j.sna.2003.10.036.

[236] Anjana Wijekoon. MEx - multi-modal exercise dataset for human activity recognition. 2, August 2019. doi: 10.17632/p89fwbzmkd.2. Publisher: Mendeley Data.

[237] Boena Wojciechowska-Maszkowska, Ryszard Marcinów, Janusz Iskra, and Rafa Tataruch. Postural stability in athletes during special hurdle tests without a definite dominant leg. *International Journal of Environmental Research and Public Health*, 18(1), 2021. ISSN 1660-4601. doi: 10.3390/ijerph18010172.

[238] J Woodburn and PS Helliwell. Observations on the f-scan in-shoe pressure measuring system. *Clinical Biomechanics*, 11(5):301–304, July 1996. ISSN 0268-0033. doi: 10.1016/0268-0033(95)00071-2.

[239] J. Wu. Scanning approaches of 2-d resistive sensor arrays: A review. *IEEE Sensors Journal*, 17(4):914–925, 2017.

[240] JianFeng Wu, Lei Wang, and JianQing Li. Vf-nse method measurement error analysis of networked resistive sensor array. *Sensors and Actuators A: Physical*, 211:45–50, 2014. ISSN 0924-4247. doi: https://doi.org/10. 1016/j.sna.2014.02.033.

[241] Jianfeng Wu, Lei Wang, Jianqing Li, and Aiguo Song. A novel crosstalk suppression method of the 2-d networked resistive sensor array. *Sensors*, 14 (7):12816–12827, 2014. ISSN 1424-8220. doi: 10.3390/s140712816.

[242] Jiayu Wu, Hong Yuan, and Xin Li. A novel method for comfort assessment in a supine sleep position using three-dimensional scanning technology. *International Journal of Industrial Ergonomics*, 67:104–113, September 2018. ISSN 0169-8141. doi: 10.1016/j.ergon.2018.05.012.

[243] W. Xu, M. Huang, N. Amini, L. He, and M. Sarrafzadeh. ecushion: A textile pressure sensor array design and calibration for sitting posture analysis. *IEEE Sensors Journal*, 13(10):3926–3934, Oct 2013. ISSN 1530-437X. doi: 10.1109/JSEN.2013.2259589.

[244] Wenyao Xu, Ming-Chun Huang, Navid Amini, Lei He, and Majid Sarrafzadeh. eCushion: A textile pressure sensor array design and calibration for sitting posture analysis. *IEEE Sensors Journal*, 13(10):3926–3934, October 2013. ISSN 1530-437X, 1558-1748. doi: 10.1109/JSEN.2013.2259589.

[245] Lee Yu-Chi, Lee Chih-Yun, and Wang Mao-Jiun. Better combination of thickness and hardness of mattress topper for supine sleeping posture: A physiological measurements evaluation. *International Journal of Industrial Ergonomics*, 78:102979, July 2020. ISSN 0169-8141. doi: 10.1016/j.ergon. 2020.102979.

[246] Shichao Yue and Walied A. Moussa. A piezoresistive tactile sensor array for touchscreen panels. *IEEE Sensors Journal*, 18(4):1685–1693, 2018. doi: 10.1109/JSEN.2017.2776936.

[247] Martina Zaltieri, Carlo Massaroni, Daniela Lo Presti, Marco Bravi, Riccardo Sabbadini, Sandra Miccinilli, Silvia Sterzi, Domenico Formica, and Emiliano Schena. A wearable device based on a fiber bragg grating sensor for low back movements monitoring. *Sensors*, 20(14):3825, January 2020. ISSN 1424-8220. doi: 10.3390/s20143825. Number: 14 Publisher: Multidisciplinary Digital Publishing Institute.

[248] Jackie D. Zehr, Kayla M. Fewster, Chad E. Gooyers, Robert J. Parkinson, and Jack P. Callaghan. Partitioning the total seatback reaction force amongst the lumbar spine motion segments during simulated rear-impact collisions. *International Journal of Occupational Safety and Ergonomics*, 27(2):613–619, April 2021. ISSN 1080-3548. doi: 10.1080/10803548.2019. 1617455. Publisher: Taylor & Francis.

[249] Yu Zeng, Yafei Qin, Youpeng Yang, and Xinyu Lu. A low-cost flexible capacitive pressure sensor for health detection. *IEEE Sensors Journal*, 22 (8):7665–7673, April 2022. ISSN 1530-437X, 1558-1748, 2379-9153. doi: 10.1109/JSEN.2022.3158354.

[250] Rui Zhang, Hua Deng, Renata Valenca, Junhong Jin, Qiang Fu, Emiliano Bilotti, and Ton Peijs. Carbon nanotube polymer coatings for textile yarns with good strain sensing capability. *Sensors and Actuators A: Physical*, 179:83–91, June 2012. ISSN 0924-4247. doi: 10.1016/j.sna.2012.03.029.

[251] Yunong Zhao, Ying Huang, Wei Hu, Xiaohui Guo, Yang Wang, Ping Liu, Caixia Liu, and Yugang Zhang. Highly sensitive flexible strain sensor based on threadlike spandex substrate coating with conductive nanocomposites for wearable electronic skin. *Smart Materials and Structures*, 28(3):035004, February 2019. ISSN 0964-1726. doi: 10.1088/1361-665X/aaf3ce. Publisher: IOP Publishing.